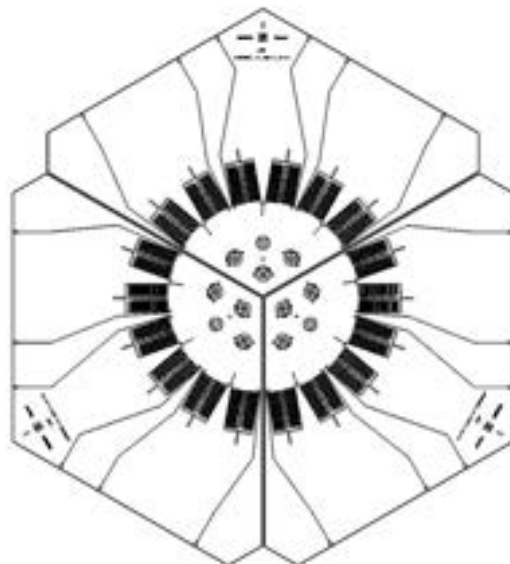

The Focal Plane Development of SPT-SLIM,
an On-Chip Superconducting Filter-Bank Spectrometer
Pathfinder for Millimetre Line Intensity Mapping

by

Gethin Robson



A Thesis submitted to Cardiff University
for the degree of Doctor of Philosophy

September 2024

Abstract

Millimetre wave line intensity mapping (LIM) of carbon monoxide (CO) rotational transitions and the carbon fine structure (CII) spectral lines is a new, complimentary and efficient approach to map the large scale structure of the Universe between red-shifts of $0 < z < 10$, which could provide further constraints on our cosmological model of the Universe. To utilise the full potential of LIM, a new kilo-pixel scalable, photon noise limited detecting technology is required with moderate spectral resolving powers ($R \approx 1000$) and minimal integration times for fast mapping. This thesis presents the focal plane development for a superconducting on-chip filter-bank spectrometer (FBS) technology pathfinder for LIM at millimetre wavelengths called SPT-SLIM as it prepares for the first deployment on the South Pole Telescope in November 2024. The motivations which lead to a focal plane of 9 pixels and $18 \times R = 100$ spectrometers are presented, most notably are the efficiency concerns due to mm-wave dielectric losses and microwave detector multiplexing constraints due to high cross-coupling between neighbouring lumped element kinetic inductance detectors (LEKIDs). The LEKID design is shown to be on the cusp of the expected photon noise limit, limited in responsivity by the aluminium inductor thickness and the geometric inductance of the large interdigital capacitors (IDC) required for frequency scheduling in a suitable range for the readout bandwidth. The parallel plate capacitor (PPC) is presented as an alternative to remove many of the IDC limitations, however, currently the PPC suffers significantly from two level systems in the dielectric resulting in excess noise. FBS devices that were tested have successfully demonstrated optical measurements of spectra at millimetre wave (≈ 100 GHz to 200 GHz), however, the spectral resolution of the spectrometers are shown to be limited ($R = 100 \rightarrow \approx 67$) which we attribute to the dielectric loss tangent. Despite this, SPT-SLIM will provide cutting edge LIM measurements and pave the way for future experiments.

Publications

First Author Publications

Robson, G., Anderson, A.J., Barry, P.S. et al. The Simulation and Design of an On-Chip Superconducting Millimetre Filter-Bank Spectrometer. *J Low Temp Phys* 209, 493–501 (2022).

Co-Author Publications

Karkare, K.S., Anderson, A.J., Barry, P.S. et al. SPT-SLIM: A Line Intensity Mapping Pathfinder for the South Pole Telescope. *J Low Temp Phys* 209, 758–765 (2022).

Barry, P.S., Anderson, A., Benson, B. et al. Design of the SPT-SLIM Focal Plane: A Spectroscopic Imaging Array for the South Pole Telescope. *J Low Temp Phys* 209, 879–888 (2022).

T. Cecil et al., "Fabrication Development for SPT-SLIM, a Superconducting Spectrometer for Line Intensity Mapping," in *IEEE Trans. Appl. Supercond.*, vol. 33, no. 5, pp. 1-6, Aug. 2023, Art no. 1101406.

Contents

Abstract	v
Publications	vii
List of Tables	x
List of Figures	xii
Symbols Used	xvii
Abbreviations	xix
Acknowledgements	xxiii
1 Introduction	1
1.1 A brief introduction to millimetre and sub-millimetre astronomy	1
1.2 Millimetre and sub-millimetre spectrometers	2
1.3 Millimetre line intensity mapping	6
2 SPT-SLIM Overview	9
2.1 Cryostat	9
2.2 Focal plane overview	11
3 The Millimetre Perspective	15
3.1 The Millimetre Perspective	15
3.2 Circular waveguide	15
3.3 The OMT antenna	17
3.4 Filter-bank design	20
3.4.1 Filter channel geometry and characterisation	21
3.4.2 Dielectric loss tangent	26
3.5 Fabrication error tolerance	29
3.6 Filter-bank simulation	30
3.6.1 Microstrip transmission line model	31
3.6.2 Filter capacitor model	34
3.6.3 Parasitic stub	35
3.6.4 Filter model	37
3.6.5 Filter-bank model and results	39
3.7 Millimetre perspective conclusion	43

4 The Microwave Perspective	45
4.1 LEKID design	45
4.1.1 Design constraints	45
4.1.2 Microstrip-coupled inductor	47
4.1.3 Inter-digital capacitor design	51
4.2 Detector Cross-coupling	53
4.2.1 Cross-coupling as a function of frequency spacing	55
4.2.2 Cross-coupling as a function of physical separation	57
4.3 Parallel plate capacitor LEKID	61
4.4 Detector Multiplexing	64
4.4.1 Multiplexing algorithm	65
4.4.2 Focal plane variations	67
4.5 Microwave perspective conclusion	71
5 Fabrication	75
6 Dark Detector Characterisation	81
6.1 Detector yield, scatter and quality factors	83
6.2 Homodyne noise measurement	89
6.3 Kinetic inductance fraction and dark responsivity	96
6.4 Multitone Dark NEP	99
6.5 Summary and discussion	103
7 Optical Filter-Bank Characterisation	107
7.1 Experimental set-up and procedure	107
7.1.1 Martin-Puplett interferometer set-up	107
7.1.2 Interferogram analysis of a Lorentzian spectrum	109
7.2 Loss tangent measurement at mm-wave	111
7.3 Optical sub-module measurements	117
7.4 Summary and discussion	122
8 Conclusion	127
8.1 Thesis Overview	127
8.2 Key Results	129
8.3 Future work and concluding remarks	131

List of Tables

2.1	Summary of the devices tested whose results are presented in this Thesis.	14
3.1	Material and simulation parameters used to simulate the filter geometries in Sonnet.	23
3.2	Table of filter tuning relations.	27
4.1	Key focal plane attributes for the three variations considered.	70
6.1	Summary table of dark detector characterisation results.	105
7.1	Summary of measured results from FTS data taken from 6 filter-banks from the SLIM23-1, SLIM23-3 and SLIM24-1 channels.	121

List of Figures

1.1	An example line intensity map.	7
1.2	Simulated mean spectral line brightness temperatures and source redshift as a function of observed frequency for mm-wave ground based detection.	8
2.1	Overview of the SPT-SLIM instrument.	10
2.2	Overview of the full SPT-SLIM focal plane.	12
2.3	Schematic of a single SPT-SLIM $R = 100$ sub-module.	13
2.4	Full wafer fabrication stack cartoons for IDC and PPC LEKID devices.	13
2.5	An $R = 100$ sub-module in a testing holder.	14
3.1	1.6mm diameter circular waveguide cut-off frequencies and supported TEM modes. .	16
3.2	Schematic and micrograph of an orthomode transducer (OMT) antenna.	17
3.3	180° Hybrid schematic and power throughput.	18
3.4	Microscope images of OMT membrane stress with varying deposited dielectric. . . .	19
3.5	Basic principle of a filter-bank spectrometer.	20
3.6	Single $\lambda/2$ filter circuit and geometry.	22
3.7	Filter input coupling capacitor tuning.	24
3.8	Filter output capacitor tuning.	25
3.9	Filter resonator length tuning.	26
3.10	Trade-off between filter resolution and single filter efficiency due to dielectric loss. .	29
3.11	Single filter fabrication tolerance.	30
3.12	RF Transmission line circuit model.	32
3.13	Z_0 and ε_r interpolation surfaces.	33
3.14	Sonnet and Scikit-RF microstrip S_{21} simulation comparison.	34
3.15	Filter coupling capacitor lumped element modelling.	36
3.16	Coupling capacitor interpolation surfaces.	37
3.17	Modelling of filter parasitic stub and its cascaded impact on filter bank throughput. .	37
3.18	Sonnet and Scikit-RF filter simulation comparisons.	38
3.19	Scikit-RF filter simulation f_0 and Q_{filt} accuracy test.	39
3.20	Scikit-RF filter-bank simulations for $R = 100, 200, 300$ with $\frac{1}{4}\lambda$ spacing.	40
3.21	Total FBS throughput as a function of filter spacing.	42
3.22	$R = 200, \frac{3}{8}\lambda$ spaced filter-bank simulation at varying dielectric loss tangents.	43
4.1	2D mask design of the IDC microstrip-coupled LEKID.	46
4.2	Schematic of the filter-detector microstrip coupling.	48
4.3	Impedance matching of the filter coupling to the microstrip inductor.	49

4.4	Predicted performance of the microstrip-coupled LEKID as a function of inductor volume.	51
4.5	Current density simulations for three potential IDC LEKID designs.	53
4.6	Example cross-coupled detector level crossing simulations.	54
4.7	Configurations considered during detector cross-coupling study.	55
4.8	Cross coupling simulation S_{21} results.	57
4.9	Interpolation method used to find the frequency separation required for a 1% shift for a 2 linewidth shift in the first three nearest neighbour positions.	58
4.10	Diagram showing the variation in the physical separation of two detectors.	59
4.11	Physical separation impact on cross-coupling.	60
4.12	The required frequency separation for an IDC detector as a function of neighbour position.	61
4.13	3D schematic of the parallel plate LEKID design.	62
4.14	Level crossing plots for IDC detectors compared to parallel plates.	63
4.15	LEKID design tolerance to a $0.2\text{ }\mu\text{m}$ increase in either the inductor or capacitor geometries.	64
4.16	Frequency space and physical space illustration of the multiplexing algorithm used on the SPT-SLIM devices.	66
4.17	Flow chart visualising the logic used in the Python script to find suitable mixing sequences for a given number of filter-banks on a channel.	68
4.18	Schematics of three sub-modules for focal plane variations.	70
4.19	Simulated filter-bank transmission for the three focal plane variations.	72
4.20	Summary bar plots for the efficiency metrics of each focal plane variation.	73
5.1	Fabrication process flow cartoons for SPT-SLIM sub-modules and prototypes.	77
5.2	Device micrographs for a SPT-SLIM device, showing regions of a filter-bank (filter geometries, LEKIDs and the step-down).	79
6.1	Image of the SLIM10 prototype and diagrams of the three detector architectures (IDC, IDC NS and PPC).	82
6.2	RF readout schematic and cryostat configuration.	84
6.3	Broadband S_{21} S_{21} sweeps for each SLIM10 channel.	85
6.4	Bias power sweeps and non-linear Lorentzian fitting of an IDC and PPC resonator.	86
6.5	SIIM10 Frequency scatter results.	87
6.6	SLIM10 plots of f_0 separations resulting in the full and useful yield.	88
6.7	SLIM10 quality factor histograms.	90
6.8	Breakdown of the three components considered in the fitting algorithm of the noise power spectrum for an MKID.	92
6.9	Example homodyne timestream noise data for an IDC resonator from the SLIM10 device.	93
6.10	Homodyne fractional frequency noise spectra and roll-off time constant fit to an IDC resonator at various temperatures.	94
6.11	Noise roll-off time constant fits as a function of temperature for the different LEKID architectures.	95
6.12	Example S_{21} of IDC, IDC NS and PPC resonances at various temperatures.	97

6.13	Mean fractional frequency shifts vs. Temperature and N_{qp} for different LEKID architectures	98
6.14	Violin plots for α_k and responsivities for different LEKID architectures.	99
6.15	Scatter plots for α_k and responsivities vs. f_0 at base temperature for different LEKID architectures.	100
6.16	Multitone fractional frequency noise measurements for the IDC and PPC channels on the SLIM10 prototype.	101
6.17	Comparison of the average S_{xx} and NEP spectra for the different architectures.	103
6.18	Principal component analysis impact on noise spikes in IDC noise spectrum.	104
7.1	Cardiff cryostat optical set-up and FTS schematic.	110
7.2	Demonstration of $\lambda/2$ filter interferogram fitting on generated exponentially decaying cosine.	111
7.3	Design of the Mini FBS test chip and mounted device.	112
7.4	SLIM30 Mini FBS variable resolution interferograms.	113
7.5	Spectra from the SLIM30 Mini FBS variable resolution filter-banks.	114
7.6	SLIM30 Mini FBS Comparison of measured spectral ν_0 and Q_{filt} to the designed values.	115
7.7	SLIM30 Mini FBS spectral ν_0 deviation from design and measure of stochastic scatter.	115
7.8	Mm-wave loss tangent measurement: Measured Q_{filt} vs. designed Q_c	116
7.9	Blue Sky Martin-Puplett FTS set-up and an example processed interferogram from a SLIM23 resonator.	118
7.10	An example of applying a linear phase correction to a measured interferogram.	119
7.11	Filter-bank spectra from SLIM23 channel 3.	119
7.12	Spectral coverage of both filter-banks from channel 3 of SLIM23 compared to their corresponding broadband detector spectrum.	120
7.13	SLIM23-3 and simulated $\tan \delta = 7 \times 10^{-3}$ filter-bank fit values for Q_{filt} and spectral f_0	121
7.14	Mean simulated FBS Q_{filt} as a function of dielectric loss tangent compared to the measured result from six filter-banks.	122
7.15	Colormaps showing the possible material parameter combinations that result in a simulated filter matching the measured results.	124
7.16	Simulated spectrum of a realistic $R = 100$ filter-bank with the expected loss tangent of 7×10^{-3}	125

Symbols Used

- f : Frequency or specifically microwave frequency (Hz) .
- ν : Spectral/optical or mm-wave frequency in chapters when both detector and spectral frequencies are discussed (Hz) .
- f_0 or ν_0 : Resonant frequency (Hz).
- ω : Angular frequency (rad s^{-1}).
- L : Inductance (H or H m^{-1}).
- L_s : Surface inductance (H or H m^{-1}).
- L_k : Kinetic Inductance (H or often $\text{H} \square^{-1}$).
- L_G : Geometric Inductance (H or often $\text{H} \square^{-1}$).
- G : Conductance (S or S m^{-1}). Or an integer count in Section 4.4.
- γ : Complex propagation constant (m^{-1})
- α : Attenuation constant (dB m^{-1}).
- β : Phase constant (rad m^{-1}).
- $\tan \delta$: Loss tangent.
- V : Voltage (V) or Volume (m^3).
- I : Current (A) or the in-phase component of two modulated sinusoids (V).
- Q : The quadrature or out of phase components of two modulated sinusoids.
- x_{res} : Resonator Length (m)
- x : Fractional frequency shift (FFS).
- C : Capacitance (F).
- α_k : Kinetic inductance fraction.
- NEP_{GR} : Generation-recombination noise equivalent power ($\text{W}/\sqrt{\text{Hz}}$)

- NEP_γ : Photon noise equivalent power ($\text{W}/\sqrt{\text{Hz}}$)
- Q_r : Total resonator quality factor.
- Q_i : Quality factor for losses.
- Q_c : Coupling quality factor.
- R : Spectrometer resolution or detector responsivity (W^{-1}).
- dx : Filter spacing (m or wavelengths)
- λ : Wavelength (m).
- $\Delta\nu$: Spectral bandwidth (Hz)
- η_{filt} : Single filter efficiency.
- η_{feedline} : Feedline efficiency from OMT to FBS.
- $\eta_{\text{total, filt}}$: Single filter efficiency including the feedline efficiency.
- η_{pb} : Cooper pair breaking efficiency.
- η_{opt} : Optical efficiency.
- \bar{n}_{ph} : Mean photon occupation number.
- μ : Permeability (H m^{-1}).
- ε : Permittivity (F m^{-1})
- T_c : Superconducting Critical Temperature (K)
- Δf_R : Readout bandwidth (Hz) or frequency resolution (Hz).
- N_{qp} : Number of quasiparticles in a given volume.
- Δ_{sc} : Superconductor energy gap (J), generally approximated as the superconducting energy gap at 0 K. Where $2\Delta_{\text{sc}}$ is the energy required to break a Cooper pair.
- k_B : Boltzmann constant.
- ds : FTS mechanical step size.
- k_0 : Wavenumber at the resonant frequency.

Abbreviations

To help in a field littered with abbreviations:

- SPT-SLIM: South Pole Telescope - Summertime Line Intensity Mapper.
- CMB: Cosmic Microwave Background
- ISM: Interstellar Medium.
- IGM: Intergalactic Medium.
- LSS: Large Scale Structure.
- TES: Transition Edge Sensor.
- LO: Local Oscillator.
- CPW: Co-Planar Waveguide
- TE: Transverse Electric.
- TM: Transverse Magnetic.
- TEM: Transverse Electro-Magnetic.
- LEKID: Lumped Element Kinetic Inductance Detector.
- MKID: Microwave Kinetic Inductance Detector.
- LIM: Line Intensity Mapping.
- IDC: Inter-Digital Capacitor.
- IDC NS: Inter-Digital Capacitor, No Step-down.
- PPC: Parallel Plate Capacitor.
- NFP: Nearest Frequency Neighbour Position.
- TLS: Two-Level System.
- OMT: Ortho-Mode Transducer.
- FBS: Filter-Bank Spectrometer.

- RIE: Reactive Ion Etch.
- NEP: Noise Equivalent Power.
- FFS: Fractional frequency shift.
- SNR: Signal-to-Noise Ratio.
- FPI: Fabry-Pérot interferometer.
- FTS: Fourier Transform Spectrometer.
- MPI: Martin-Puplett Interferometer.
- ZPD: Zero Path Difference.
- OPD: Optical Path Difference.
- FF: Fold Factor.
- PTC: Pulsed Tube Cooler.
- SKRF: Scikit-RF (Python module).

For my Father, from whom I learnt hard work and perseverance.

Acknowledgements

Funding Bodies and Affiliations

I would like to personally thank all of my fellow collaborators, working on SPT-SLIM has been a deeply interesting, exciting and fulfilling project which I have been truly proud to be a part of and is testament to the support and culture within the group. I would also like to thank the continuing support from the Science and Technology Facilities Council Ph.D studentship programme under reference ST/S00033X/1.

Personal Thanks

Completing this PhD has been the biggest challenge I have faced so far, it would not be right to claim I achieved this alone.

First of all, to my Parents I wish to say the following: you have always provided me with all the support and encouragement I could need. My successes and achievements are testament to you both. Thank you.

I would also like to thank my supervisors Dr. Peter Barry and Prof. Simon Doyle, without whom this work simply could not exist. Pete, I cannot thank you enough for being a brilliant mentor, colleague and friend. Your dedication both to myself and your work has been inspiring and working with you has been a true pleasure. Simon, I couldn't have done this without your guidance and support through these years. Thank you for making the time for me and giving me this opportunity in the first place.

I want to also thank the members of my examining board, Professor Sean Giblin and Dr. Martino Calvo for taking the time to read this Thesis and provide insightful comments and discussion.

To my colleagues who have supported me in a variety of ways, thank you. Tom and Sam, for all your various bits of help, whether it be fixing the cryostat or readout, helping me with turning around the cryostats or discussions which have helped me understand something. Maclean, for being an excellent host in Montreal and giving me the opportunity to climb in Canada! Also, your patience and fast responses with me trying to operate the ICE board did not go unnoticed despite the time and location difference. You have always been a reliable call for aid... Potentially too reliable! Chris, for all your teaching and help in the cleanroom, particularly when the wire bonder gremlins come out to play. Kirit and Adam, despite being across the pond you made me feel welcome and valued within the collaboration. Your enthusiasm to your work and the field was infectious. Karia, Kira, Tyler and everyone else at Chicago University, thank you for bearing so much of the SPT-SLIM testing over the years, particularly for taking the sub-module measurements which provided the analysis included in this Thesis.

Freddie, for your help with various bits of code and programming, which has formed the foundation of my work.

To the rest of my friends and family, whilst you didn't contribute to this Thesis in an academic sense, your contribution is no less valued. Your ability to pull me away from research and remind me of life's joys made this process much more manageable and enjoyable. Whether through laughter, conversation, or climbing trips, you all provided the perfect reprieve when I needed it most. Thank you for being the wonderful distraction I often needed to recharge and continue on this academic journey.

Finally, I owe a special thanks to Tala. You have been patient, understanding and supportive throughout this writing period when I needed it most. Adventures with you have been among my most treasured memories during my time in Cardiff. You have been my rock and I couldn't have done it without you.

Chapter 1

Introduction

1.1 A brief introduction to millimetre and sub-millimetre astronomy

Millimetre and sub-millimetre astronomy, focusing on wavelengths from approximately 1 millimetre to 100 micrometers, plays a critical role in understanding a wide range of astrophysical phenomena, from the cold molecular clouds that birth stars to the Cosmic Microwave Background (CMB) radiation that offers insights into the early universe, to much of the Universe's evolution yet to be probed. However, making precise astronomical measurements at these wavelengths presents significant challenges, primarily due to the presence of the so-called "Terahertz gap". As such, this region of the spectrum remains to see the extensive investigations to which regions like the Cosmic Optical Background have experienced, despite the fact it is the largest contribution to the integrated spectral brightness of the Universe¹.

The Terahertz gap, spanning frequencies from around 0.1 THz to 10 THz, is a spectral region notoriously difficult to observe. Traditional electronic devices struggle with inefficiencies and noise at these frequencies, while photonic technologies are often insufficiently sensitive and frequency limited by the energy band gap, (E_g) of semiconductors corresponding to wavelengths typically around $hc/E_g = 1 \mu\text{m}$ ($\approx 300 \text{ THz}$) for silicon based detectors². The atmospheric absorption, dominated by water vapor, further exacerbates the difficulties by heavily attenuating the incoming signals, making ground-based observations particularly challenging. These obstacles necessitate the use of advanced techniques and materials to achieve the sensitivity required for millimetre and sub-millimetre astronomical observations.

In recent decades, superconducting detectors have emerged as the most viable solution to these challenges. These detectors, operating at cryogenic temperatures, leverage the unique properties of superconductors, such as zero DC electrical resistance and extremely low noise, to detect

faint astronomical signals with high sensitivity. In particular, superconducting technologies like Transition Edge Sensors (TES)³ and Microwave Kinetic Inductance Detectors⁴ (MKIDs) have proven to be indispensable tools in pushing the boundaries of observational astronomy within the Terahertz gap.

Despite their advantages, the implementation of superconducting detectors in millimetre and sub-millimetre spectroscopy is not without its challenges. Designing instrumentation that operates effectively at these wavelengths requires addressing several critical issues, including the precise control of detector noise, the need for ultra-low temperature environments, and the integration of these detectors with complex optical systems. Furthermore, the development of large-format detector arrays poses additional challenges related to fabrication, readout electronics, and thermal management. The inherent ease to which MKID detectors can be multiplexed in the thousands on one readout line has earmarked these devices as the likely path to achieving mm and sub-mm focal planes on the order of 1×10^5 detectors or more, as is the goal of CMB Stage 4⁵.

In the terahertz regime, there has been a wealth of advancements in these superconducting technologies thanks to the CMB community and many direct imaging instrument demonstrations of both the TES^{6–11} and more recently MKID^{12–17} all on the order of $\approx 10 \times 10^3$ pixels. Considerable amounts of information on the status of terahertz direct imaging superconducting detectors can be found in literature^{2,18–21}, yet is beyond the scope of this thesis. Rather, we will focus on the status and challenges of spectrometers at these wavelengths.

1.2 Millimetre and sub-millimetre spectrometers

For similar reasons as for direct imaging, spectrometers in the terahertz regime have also adopted superconducting technologies. The main considerations when designing an imaging spectrometer are the frequency resolution, R , instantaneous bandwidth, the sensitivity to the desired signals and the mapping speeds. The latter two parameters are not necessarily degenerate, for example, higher sensitivities can be achieved by longer integration times at the cost of reduced mapping speeds. Therefore the scalability of a technology plays a crucial role in its capability as an instrument since the more spectrometers or number of detectors for an Fourier Transform Spectrometer (FTS) on a focal plane increases the instantaneous sensitivity and thus, faster mapping speeds can be achieved. All current technologies compromise on some aspect to a certain degree and as such, there are yet to be equivalent terahertz devices to the integral field units found in the optical spectrum which provide data cubes of very sensitive light intensity measurements and high resolution spectral content as a function of direction without sacrificing large integration times. Hence, different choices are more suitable than others depending on the

science case and often one technology can compliment another.

Extremely high resolution measurements are made possible with heterodyne receivers, reaching values on the order of $R = 1 \times 10^7$ ^{22,23}. This class of spectrometer technology is able to measure both the amplitude and phase of incident signal which astronomers can use to extract a wealth of information. To reach the high sensitivities and resolutions, these systems generally use arrays of antenna covering hundreds or thousands of square meters, using a correlator and interferometry to compare between antenna. Each antenna is then typically equipped with superconductor-insulator-superconductor (SIS) mixers which limit the maximum observable frequency according to the superconducting gap frequency. Niobium being the best established in sub-millimetre instruments leads to an upper frequency limit of around 700 GHz²⁴, though higher can be achieved with niobium nitride for example. Due to the difficulties with generating sub-millimetre signals, the Local Oscillator (LO) is typically achieved by multiplication chains from microwave frequencies. As such, multiplexing mixers at these frequencies with a common LO without compromising on the purity of the LO signal and power balance is difficult and can contribute noise²². This leads to heterodyne sensitivities being limited to the quantum noise limit of the input noise temperature, above the photon noise²⁵. Current receivers are typically limited to a pixel count on the order of 10, with the biggest array reaching 64²². For this reason, and the fact that the instantaneous bandwidth is typically limited to a few gigahertz^{22,26}, heterodyne receivers are best suited for high resolution, single source measurements with large integration times rather than mapping large areas. It is also worth mentioning that, whilst incredibly successful, the strong reliance on heterodynes for millimetre to far infrared measurements has the potential for limiting what could possibly be discovered since only a small portion of the spectrum can be sampled at once compared to what could be found with a wide instantaneous bandwidth. Thus, complementary spectrally and physically wide fields of view are desired.

Conventional spectrometry techniques with dispersive elements have also been applied to this region of the spectrum. Most notably is ZEUS-2, and the instruments from Z-spec²⁷ heritage, most recently is the TIME instrument^{28,29} which combines 32 Z-spec-like grating spectrometers. These spectrometers disperse light with a diffraction grating, then the spectrum is measured with a 2-D array of TES detectors. This method has the advantage that the full frequency band is sampled instantaneously and simultaneously, rather than needing to scan each frequency individually, hence faster mapping speeds can be achieved. Furthermore, since only a few tens to a few hundreds of detectors (60 in the case of TIME) are currently required for each array per spectrometer, TES detectors can be used without reaching the logistical limitation due to readout wiring that is common in TES instruments pushing beyond 1×10^4 detectors, however as is described in J. Hunacek's thesis²⁹, it is still not trivial. Hence, with the heritage of consistent and precise TES fabrication from the CMB community, arrays of extremely sensitive detectors can be realised

Introduction

without too much difficulty relative to MKID fabrication which is less mature by comparison. Another advantage is that since each detector only receives a narrow band of light, there is less photon noise per detector which can further improve sensitivities and reduce integration times. However, these frequencies of light in a vacuum/air require that the size of the grating “grooves” are fairly large, e.g., comparable the wavelength of the light. Hence, only moderate groove densities and therefore resolutions can be achieved without making the size of the spectrometer too large which in turn requires cooling larger volumes to the cryogenic temperatures required for the detectors. Current vacuum grating spectrometers occupy approximately $\approx 700 \text{ cm}^3$ ²⁹. Hence, scaling this technology is ultimately limited beyond roughly 100 spectrometers.

Fourier Transform Spectrometers provide an alternative method that has also been demonstrated,³⁰⁻³³. Here, an FTS is placed in front of an array of superconducting detectors. High signal to noise ratios (SNR) can be achieved with an FTS instrument since the optical throughput, limited by collimating optics, is on the order of tens higher than for a grating monochromator with a comparative spectral resolution as is known as the Jacquinot advantage³⁴. This is beneficial in the case of weak signals as is the case in astronomy. In the case of a detector noise limited instrument, a similar advantage to the spectrograph’s multiplex advantage can also be achieved with an FTS known as the Felgett advantage which with the recent development of photon noise limited detectors is now becoming a disadvantage. For an FTS in front of a detector array, each detector sees a slightly different spectrum depending on the object it is looking at, thus a larger focal plane (and therefore larger optics) will yield in a larger field of view increasing mapping speeds. Furthermore, to reach high SNR and resolutions requires a large number of sample points for an FTS scan (precise mirror movements) and a long mirror stage (or large fold factor).. This is entirely plausible with spectral resolutions in the hundreds to thousands^{35,36} being easily achieved, however, since each detector in this system receives the full frequency band and hence suffers additional frequency noise, large detector counts are required to reduce integration times in order to allow efficient scanning. Additionally, since the FTS optics at millimetre and sub-millimetre are fairly large, this method is not easily scaled as increasingly large optics become difficult to make and problematic when incorporated with moving parts.

Given the size constraints on scalability with the aforementioned technologies, one is naturally drawn to the ability to reduce the wavelength of light and hence technology with the higher permittivities found in on-chip circuits and dielectrics relative to vacuum equivalents. On-chip spectrometers are currently being developed in a few different forms, typically trying to combine the multiplex advantage with a sensitive scalable technology, hence MKIDs are typically used for detectors. Micro-spec³⁷⁻³⁹ (μ -spec) is an on-chip equivalent of a grating spectrometer that would occupy a $\approx 10 \text{ cm}^3$ silicon chip and is the technology proposed for the EXCLAIM balloon mission⁴⁰ using six such devices. Designed to measure spectra between 300 GHz to 600 GHz, the

EXCLAIM spectrometers are expected to have a resolution of 512^{41} , with prototypes demonstrating $R = 64^{42,43}$. Another on-chip option is the on-chip filter-bank spectrometer (FBS), which is the subject of this thesis.

The FBS at its surface level is simple. A series of superconducting resonant filters tuned to a desired frequency and bandwidth are placed in parallel along an antenna coupled transmission line. These filters are then terminated in a superconducting detector, where the convenient frequency multiplexing of MKIDs along a separate feedline provides a natural choice. Hence, a compact highly sensitive spectrometer can be realised, only occupying a few cubic centimetres of silicon. Spectral resolving powers in the thousands are technically achievable, if not for the current limitation set by dielectric losses as will become clearly apparent throughout this thesis. These spectrometers are therefore extremely sensitive thanks to the MKIDs exposed only to a narrow bandwidth and could achieve fast mapping speeds as the full spectrum is sampled simultaneously. A further benefit is that since the spectral sorting structures are also constructed out of transmission line circuitry, the fabrication procedure can be carried out at the same time as the fabrication of the MKIDs. There are a few existing demonstrations of this technology, namely DESHIMA⁴⁴ ($R \approx 380$) and DESHIMA 2.0 ($R \approx 500$)⁴⁵ targeting 322 GHz to 377 GHz and 220 GHz to 440 GHz respectively, with on-sky observations successfully carried out with DESHIMA at the ASTE telescope^{46,47}. Another is Superspec^{48–50} aimed at the 195 GHz to 310 GHz band with an intended resolution of $R = 700$. However, whilst the concept may seem relatively simple, realising an on-chip FBS instrument with high resolution and optical efficiency remains a technical challenge such that multi-pixel instruments have not been deployed to a telescope yet. Recent progression with tuneable on-chip FTS devices has also shown a lot of promise for a millimetre IFU technology, yet is even more immature than the on-chip FBS⁵¹. However, for the purpose of this thesis the on-chip FBS will be the focus.

To summarise, heterodynes offer the unique ability for high resolution spatial interferometry since phase is preserved, however are limited by the narrow bandwidth, quantum noise temperatures and scalability with respect to imaging spectrometers. Conventional gratings offer a robust option, but will struggle to reach kilo-pixel arrays due to the size of components set by the free space wavelength of light in the terahertz spectrum. FTS instruments are a viable mapping option, however with the advent of the photon noise limited detector, FTS instruments pay a penalty for the full bandwidth being incident on each detector, however post dispersal would help this issue⁵². Furthermore, increased mapping speeds come at the cost of larger focal planes and larger optics which will likely become impractical. Hence, on-chip filter-bank spectrometers offer the benefits of photon noise limited detection, wide instantaneous bandwidths and the potential for kilo-pixel or larger detector arrays with wide field of views. Whilst currently limited to low to mid resolutions, there is still significant demand from various fields in astronomy and cosmology for a

sensitive instrument with fast mapping capabilities such as the on-chip FBS. This would provide complimentary observations to those measurements of high resolution yet very localised. Line intensity mapping is one such field.

For further details on the current millimetre to far infrared spectroscopy instrument landscape, an extensive review can be found in Farrah et. al. 2019²⁵.

1.3 Millimetre line intensity mapping

This section aims to provide an introductory description of the line intensity mapping (LIM) observing technique, specifically in the millimetre and submillimetre spectrum, in order to contextualise the SPT-SLIM instrument reported in this thesis. For more in-depth discussions, the reader is referred to the 2017 Status Report⁵³ and the 2021 Snowmass white paper⁵⁴.

Line intensity mapping is a cutting-edge observational technique used in astrophysics to study the large-scale structure (LSS) of the universe. It focuses on measuring the integrated emission from specific atomic or molecular spectral lines over large volumes of space. Instead of resolving individual galaxies or sources, LIM captures the collective signal from many sources, providing a three-dimensional map of the intensity distribution of these lines across the sky. LIM at these wavelengths offers a unique way to explore the evolution of galaxies and the intergalactic medium (IGM) over cosmic time, especially during key epochs like the Epoch of Reionization ($5 < z < 27$)⁵³ and the peak of galaxy assembly and star formation ($2 < z < 10$)⁵³. Such high redshift portions of the Universe's history have typically only been probed with missions which are unable to survey large areas due to integration times. Furthermore, those missions with large field of views such as optical galaxy surveys are limited to low redshifts. Therefore, with the complimentary low resolution and large field of views that can be achieved with LIM, scientists can gain insights into the distribution of matter and dark matter, the processes governing galaxy formation, and the thermal history of the universe, potentially providing significant constraints on cosmological parameters beyond the ability of current CMB and galaxy surveys.

At millimetre and submillimetre wavelengths, LIM is particularly effective for probing the cosmic web, which includes the interstellar medium (ISM) and the intergalactic medium of galaxies. These wavelengths are sensitive to molecular and atomic transitions, such as carbon monoxide rotational transitions ($\text{CO}(J \rightarrow J - 1)$) or ionised carbon (CII) fine structure lines, which are tracers of star formation and the cold gas content in the Universe. Depending on the redshift of the source, the rest frame frequency of these spectral lines is shifted down into the millimetre and submillimetre range. Therefore, by spatially mapping the integrated mean brightness at multiple frequencies over a wide bandwidth, one could effectively map the matter distribution as a function

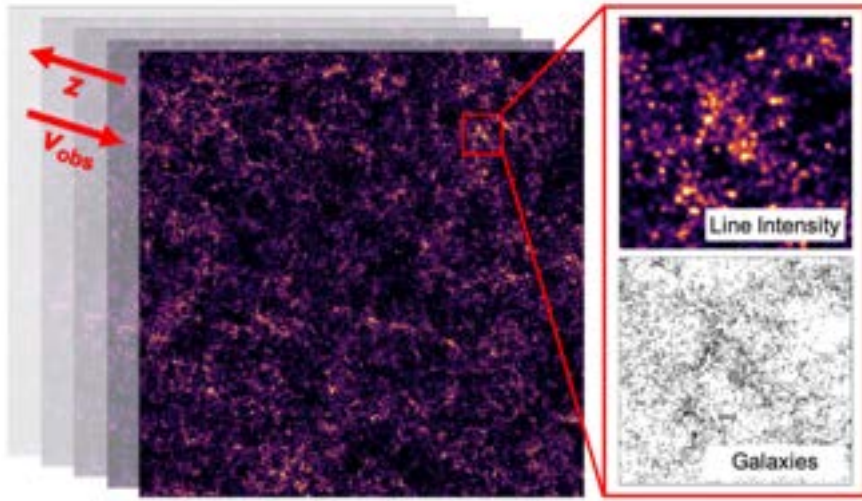


Figure 1.1. Schematic image of a 100 deg^2 line intensity map from Karkare et. al.⁵⁴. Each layer represents the three dimensional intensity map of an example spectral line at different observed frequencies, ν_0 . The zoom-in panels show the intensity map (top) and a map of what would be the corresponding galaxies if each were fully resolved.

of time and space, this concept is illustrated in Figure 1.1.

There are a number of complementary spectral lines for LIM that are being targeted in other frequency ranges such as the 21 cm hydrogen line⁵⁵. This hydrogen line is of particular interest due to the abundance of hydrogen throughout the history of the Universe, hence mapping this line provides significant redshift reach even through the so-called Dark Age ($z \approx 100 - 1000$). However, there is additionally significant interest in millimetre and submillimetre spectral lines due to the reduced galactic foregrounds⁵⁶. In this range, a combination of various CO rotational transitions and the CII ionised fine structure lines can be used to obtain intensity maps within the frequency range $\approx 60 \text{ GHz}$ to 370 GHz to probe LSS between redshifts of $0 < z < 10$. The simulated mean brightness temperatures of the spectral line as a function of frequency for the different lines are shown in Figure 1.2, where the color of each line indicates the redshift of the source if the spectral line were measured at that frequency. Also overplotted is the atmospheric transmission at the South Pole, indicating the ground based observation windows.

The spectral resolving power of the LIM measurements effectively dictates the “thickness” of the time slice that can be resolved, as it provides the accuracy and precision to which line’s source redshift (epoch) is known. As such, higher resolution instruments (up to the limit of the spectral linewidth itself) are always preferred. However, competitive cosmological constraints are expected to be delivered with $R \approx 100$ to 1000 instruments⁵⁴, provided that a large field of view can be mapped. Hence, an instrument capable of a wide instantaneous bandwidth with low- to mid-resolution capabilities combined with photon noise-limited detection that can be scaled to

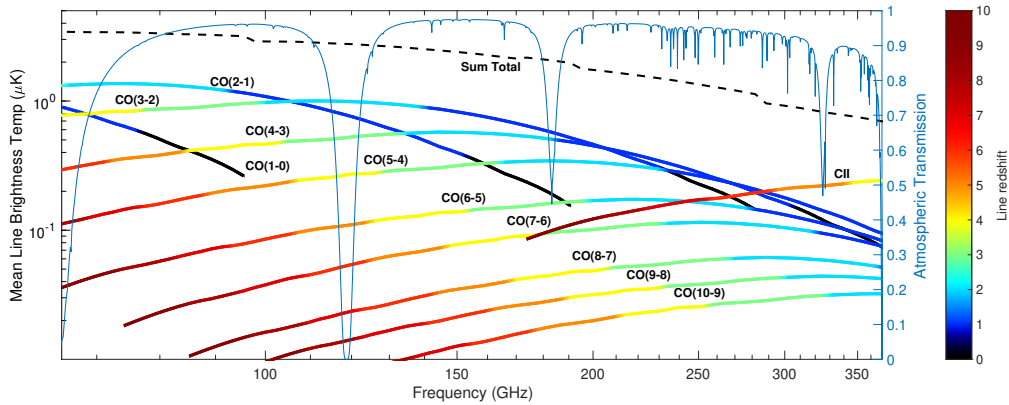


Figure 1.2. Simulated mean spectral line brightness temperatures and source redshift as a function of observed frequency for mm-wave ground based detection. Over-plotted in blue is the atmospheric transmission at the South Pole, highlighting the ground based observation windows. *Model and plot credit:*^{54,57}.

large pixel counts to provide rapid mapping is best suited for measurements such as these. Whilst current grating LIM experiments (TIM⁵⁸ and TIME²⁸) as well as FTS (CONCERTO³¹) and Fabry-Pérot interferometers (FPI) (CCAT-prime⁵⁹) based LIM experiments will provide cutting edge measurements for line intensity mapping across the millimetre spectrum, yet for the reasons discussed in Section 1.2, the capability of these technologies ultimately lack the required scale and sensitivities to achieve the potential of LIM cosmological constraints, largely due to the required spectrometer hours on the sky^{53,54}. Hence, it is no surprise that there is significant interest in the development of on-chip spectrometers for this purpose (among others). Current on-chip spectrometers being developed for millimetre LIM are EXCLAIM⁴⁰ which, as mentioned previously, consists of six $R \approx 512$ μ -spec spectrometers to measure the CO $J = 4 \rightarrow 3$, CII and CI emission lines between 420 GHz to 540 GHz and SPT-SLIM, the focus of this thesis.

Chapter 2

SPT-SLIM Overview

As discussed in Sections 1.2 and 1.3, multi-pixel superconducting on-chip filter-bank spectrometers (FBS) should be capable of satisfying many of the technology requirements to enable line intensity mapping of spectral lines in the millimetre region of the spectrum. As such, the main goal of SPT-SLIM is to serve as a technological pathfinder for future line intensity mapping missions, principally demonstrating the sensitivity and scalability of this technology. Nevertheless, SPT-SLIM will be cutting-edge and aims to conduct novel measurements of large-scale structure that will be beneficial to progressing our cosmological models. The instrument is designed to target the carbon monoxide (CO) rotational transitions from galaxies with high redshift. The intended sensitivities of SPT-SLIM should make observations of CO(2-1), CO(3-2) and CO(4-3) possible within the 120 GHz to 180 GHz atmospheric window, thus allowing sources with red-shifts of approximately $0.3 < z < 2.8$ to be measured⁶⁰, recalling that the redshift span that can be achieved for a given intensity map is set by the accuracy and precision to which a molecular line can be resolved, largely set by the resolution of the spectrometer.

Section 2.1 presents the SPT-SLIM cryostat in which the superconducting focal plane will be placed, providing the context and the physical design constraints that motivated many of the choices for the focal plane architecture. Section 2.2 then introduces the overview for the full 9 pixel, $R = 100$ spectrometer focal plane as will be deployed in November 2024.

2.1 Cryostat

The south pole telescope is a 10m off-axis Gregorian telescope and has a smooth surface down to roughly $25 \mu\text{m}$ ^{61,62}, hence it's suitability for mm-wave observations. The SPT-SLIM cryostat will occupy the space in the receiver cabin that the Event Horizon Telescope (EHT) also uses⁶³

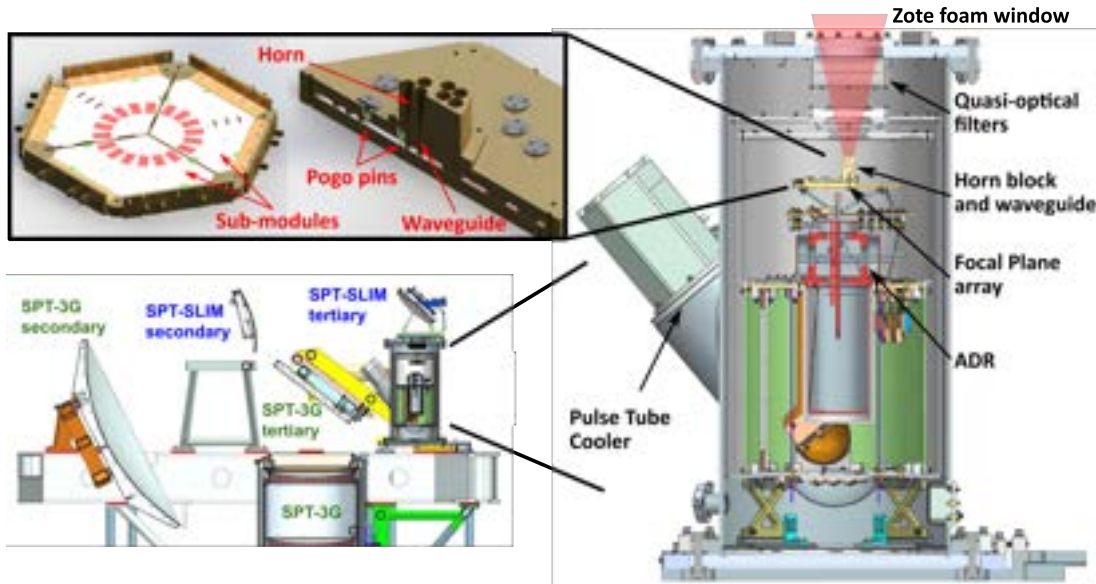


Figure 2.1. Overview of the full SPT-SLIM instrument: (upper left) Cross-Section view of the proposed sub-module holder and coupled waveguide and horn block. (right) CAD rendering of the cryostat and the location of the focal plane within. (lower left) Diagram of the location of the SPT-SLIM cryostat in the receiver cabin relative to main SPT-3G cryostat.

and the beam from the primary mirror will be picked off by a custom SPT-SLIM secondary mirror to direct the beam that would otherwise go to the main SPT-3G cryostat as shown in Figure 2.1a. To cool the detectors to the desired temperature (≈ 100 mK), a Cryomech PT407 will provide the cooling to 4 K and then sub-Kelvin cooling will be achieved with a High Precision Devices 155 adiabatic demagnetization refrigerator (ADR). The dominant thermal loading is expected to be from the coaxial lines used to readout the detectors, hence a maximum of 9 readout channels can be installed, which along with the physical size of the focal plane stage, ultimately leads to two of the main constraints imposed on the focal plane layout and design as will be discussed throughout.

The optics result in a 32 mm diameter diffraction-limited area at the plane of the horn-blocks. A compromise between the detector cross-coupling requirements on multiplexing within the 9 microwave readout channels (see Section 4.4), focal plane efficiency and maximising scientific impact lead to 12 horn pixels each with a collecting diameter of ≈ 9.69 mm.

The band pass reaching the focal plane is defined as follows. The infrared filter stack consists of Zote foam filters at 300 K, HDPE and nylon filters at 50 K and a nylon and metal-mesh filter at 4 K⁶⁰ resulting in a low pass cut-off at ≈ 180 GHz. Then the high-pass frequency of the coupling scheme is set by the size of the waveguide between the horn and the orthomode transducer (OMT) probes, as is discussed further in Section 3.2.

2.2 Focal plane overview

In short, the overall aim of the SPT-SLIM focal plane is to realise a compact spectrometer with preferably as many pixels as possible to increase mapping speeds, connected to filter-bank spectrometers of as high a resolution as achievable without sacrificing too much optical efficiency and non-uniformity across the frequency band. The proposal at the inception of SPT-SLIM consisted of plans to develop a 18 pixel spectrometer camera with each pixel feeding two moderate resolution, $R = f_0/\Delta f = 300$, superconducting microchip on-chip FBS sensitive between 120 GHz to 180 GHz⁶⁰. Lumped Element Kinetic Inductance Detectors (LEKID)⁶⁴ were chosen as the mm-wave detectors that each filter channel would be terminated in. However, as mentioned in the previous section we eventually moved to a 9 pixel design, but we also reduced the resolution of the filter-bank to $R = 100$. The motivation for this change was derived from various studies of both the millimetre and microwave aspects of this device. After characterising the focal plane design via simulation, we first revised the focal plane to a 12 pixel, $R = 200$ design. Tests on prototypes and would-be deployment grade sub-modules then pushed us to the lower-risk $R = 100$ design shown in Figure 2.2. As such, the focus of the following chapters is to provide understanding of what directed the design of the focal plane to that presented here. Figure 2.2 shows the full focal plane consisting of 9 OMT pixels coupled to 18 filter-banks. Each filter bank has a resolution of $R = 100$, spanning 120 GHz to 180 GHz with a channel oversampling factor of 1.6, leading to 65 filter-channels each terminated in a microstrip coupled LEKID. The full focal plane of 1170 LEKIDs is split into three sub-modules, each fabricated on it's own 6 inch silicon wafer.

The sub-module design is shown in more detail in Figure 2.3. Each sub-module contains three microwave CPW readout channels, each consisting of two filter-banks.

To better understand the functionality of the device, it is beneficial to consider the path of an incident photon starting as the signal from sky signal which is directed to the horn array of the focal plane via the telescope optics system. From this point, the signal propagates through a circular waveguide before coupling to the focal plane mm-wave circuitry via the OMT antenna (1). Following this, the signal passes down a mm-wave microstrip that feeds the filter-bank channels (2). After passing through the filter-bank channel according to the frequency of the signal, the signal is then absorbed into and detected by the microwave detectors resulting in a detector response which is measured via the CPW readout line (4). As such, the focal plane is split into two main subsystems: The mm-wave circuitry (1-2) and the microwave circuitry (3-4), covered respectively in the Millimetre Perspective, Chapter 3, and the Microwave Perspective in Chapter 4. In each chapter, details specific to each subsystem are provided as well as many of the design considerations, challenges and solutions that were experienced throughout the design process.

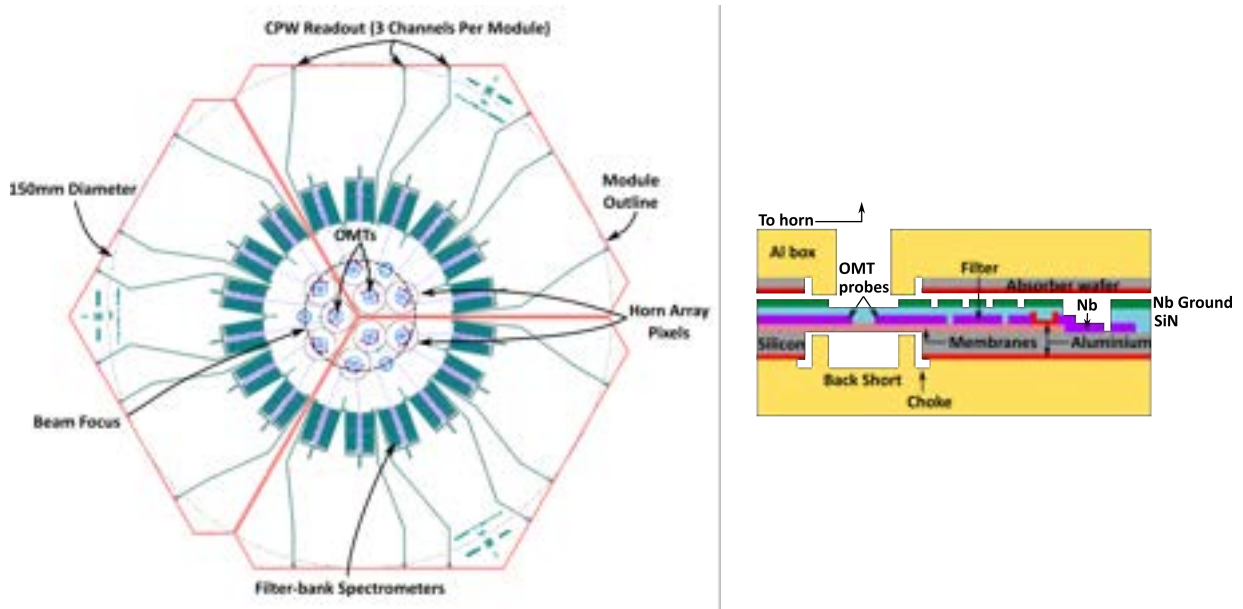


Figure 2.2. (Left) A schematic of the full focal plane layout consisting of three sub-modules, each with four, dual polarisation OMT antennas and eight $R = 100$ filter-bank spectrometers. (Right) Cross Section view of the dielectric and wafer stack when mounted in the test package with a waveguide and horn block.

A detailed view of the material stack of a sub-module is presented in Figure 2.4. The OMT architecture requires a suspended low stress membrane SiN layer to give structure to the antenna probes after removing the back-side silicon via a back etch, with an etch-stop oxide layer. To maximise coupling to the probes, a $\frac{1}{4}\lambda$ backshort is built into the packaging. We then use an inverted microstrip architecture for the mm-wave circuitry up to and including the absorbing microstrip inductor of the LEKID. The inverted design allows the detector to be fabricated on a minimally processed surface, as well as providing extra shielding for the sensitive LEKID inductors from stray light. All non-absorbing sections of the circuitry are patterned in a niobium device layer since the cut-off frequency is well above that of our target millimetre frequency range²⁴, thus providing an efficient transmission line. Aluminium is then used for all components that require the absorption of millimetre signals since the pair breaking frequency is approximately 100 GHz and will therefore be lossy within our band. The microwave readout transmission line uses a bridged CPW geometry.

In this thesis, two variations of the LEKID are explored for the detectors on SPT-SLIM, one with an Inter-Digital Capacitor (IDC), and the other with Parallel Plate Capacitors (PPC). The two geometries have slightly differing fabrication processes where the former requires the niobium to step down off of the membrane layers to prevent two-level system noise from the dielectric materials being present in the dense electric field regions of the IDC, hence the two separate diagrams. Further details of the detector geometries are presented in Section 4.1 and the

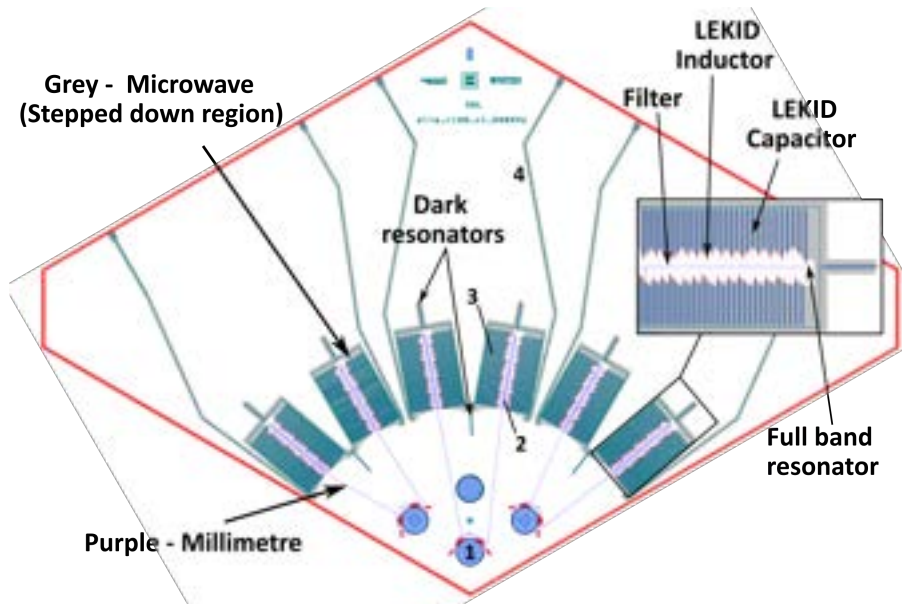


Figure 2.3. A schematic of a single sub-module, highlighting the two sides of the device, the microwave and millimetre regions. The numbers indicate the key subsystems: (1) The OMT Antenna, (2) the filter-bank and filter channels, (3) the detectors, (4) the microwave readout line.

fabrication process and considerations are discussed in Chapter 5.

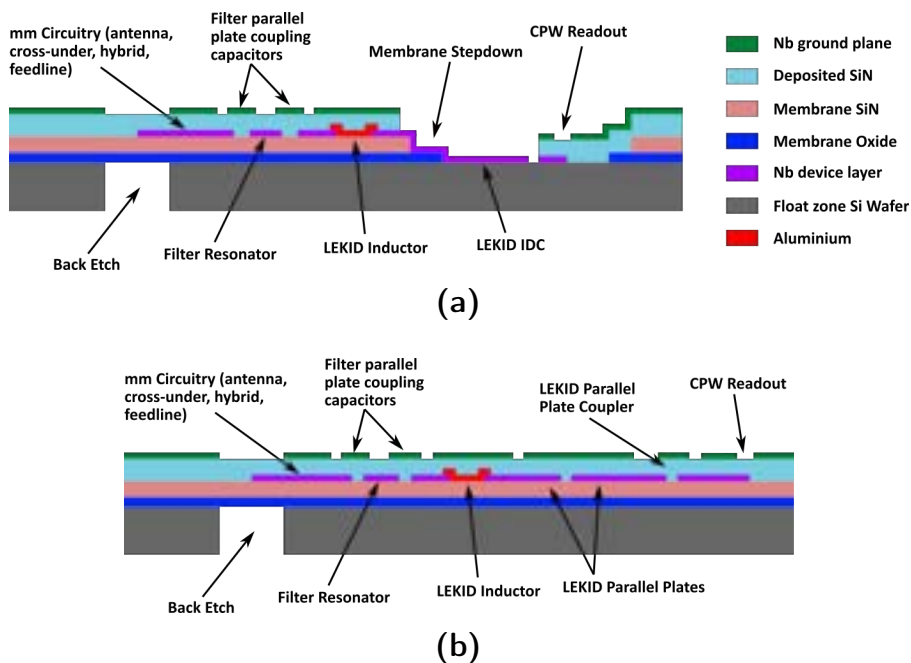


Figure 2.4. A diagram of the material stack of an SPT-SLIM-like optical device with either an IDC LEKID or a PPC LEKID. Figure (a) demonstrates the need for a processing step in which the two membrane layers are removed around the IDC of the LEKIDs, requiring the niobium to step down off of the membrane layers.

Fabrication Run	Device Name	Test Location	Purpose	Date Tested
SLIM10	IDC	Cardiff	Dark characterisation	September 2023 / June 2024
SLIM10	IDC NS	Cardiff	Dark characterisation	September 2023 / June 2024
SLIM10	PPC	Cardiff	Dark characterisation	September 2023 / June 2024
SLIM23	Channel 1	Chicago	Optical characterisation	May 2024
SLIM23	Channel 3	Chicago	Optical characterisation	May 2024
SLIM24	Channel 1	Chicago	Optical characterisation	May 2024
SLIM30	Mini FBS	Cardiff	Mm-wave loss tangent measurement	July 2024

Table 2.1. Summary of the devices tested whose results are presented in this Thesis.

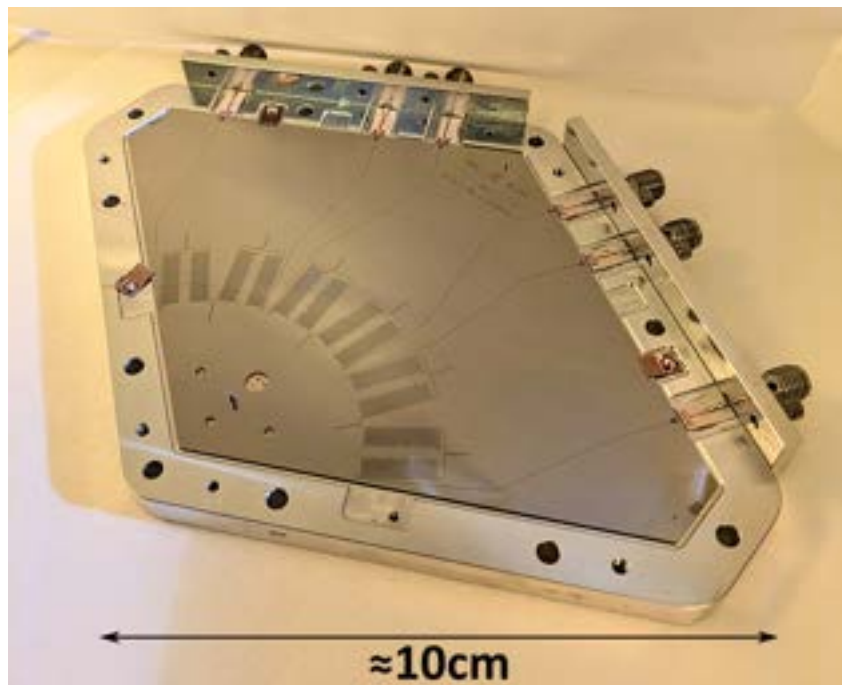


Figure 2.5. An $R = 100$ sub-module in a testing holder.

The final two chapters before the conclusion present measured results. To help provide clarity and a timeline, Table 2.1 provides a summary of the devices tested which contributed to the results that are included in this thesis. Chapter 6 presents dark detector characterisations for three LEKID geometries from a prototype device from the SLIM10 fabrication run. Chapter 7 then presents optical results firstly from a SLIM30 test device used to obtain millimetre dielectric loss tangent measurements and secondly spectra and analysis of some channels from deployment grade sub-module devices from the SLIM23 and SLIM24 fabrication runs, similar to the sub-module shown in a test holder in Figure 2.5.

The Millimetre Perspective

3.1 The Millimetre Perspective

This section presents the various millimetre circuit components, following the path of the optical signal once it is incident within a horn of the horn block to the termination of a photon within the sensitive inductor of the LEKID after passing through a mm-wave filter in the filter-bank.

3.2 Circular waveguide

The circular waveguide is well understood and described by solving Maxwell's equations within a cylindrical cavity⁶⁵. The Transverse Electric (TE) and Transverse Magnetic (TM) modes that can propagate through the circular waveguide have a cut-off frequency below which the waveguide is unable to support them and can be calculated according to

$$\text{TE: } f_{c_{nm}} = \frac{p'_{nm}}{\pi D \sqrt{\mu\epsilon}} \quad (3.1)$$

$$\text{TM: } f_{c_{nm}} = \frac{p_{nm}}{\pi D \sqrt{\mu\epsilon}}, \quad (3.2)$$

where p'_{nm} and p_{nm} are values of the roots to Bessel differential equations for the TE and TM modes respectively and D is the diameter of the circular waveguide. The first five cut-off frequencies for a 1.6 mm diameter waveguide are shown in Figure 3.1a and their corresponding electric field lines within the circular waveguide are depicted in Figure 3.1b. These depictions also have two

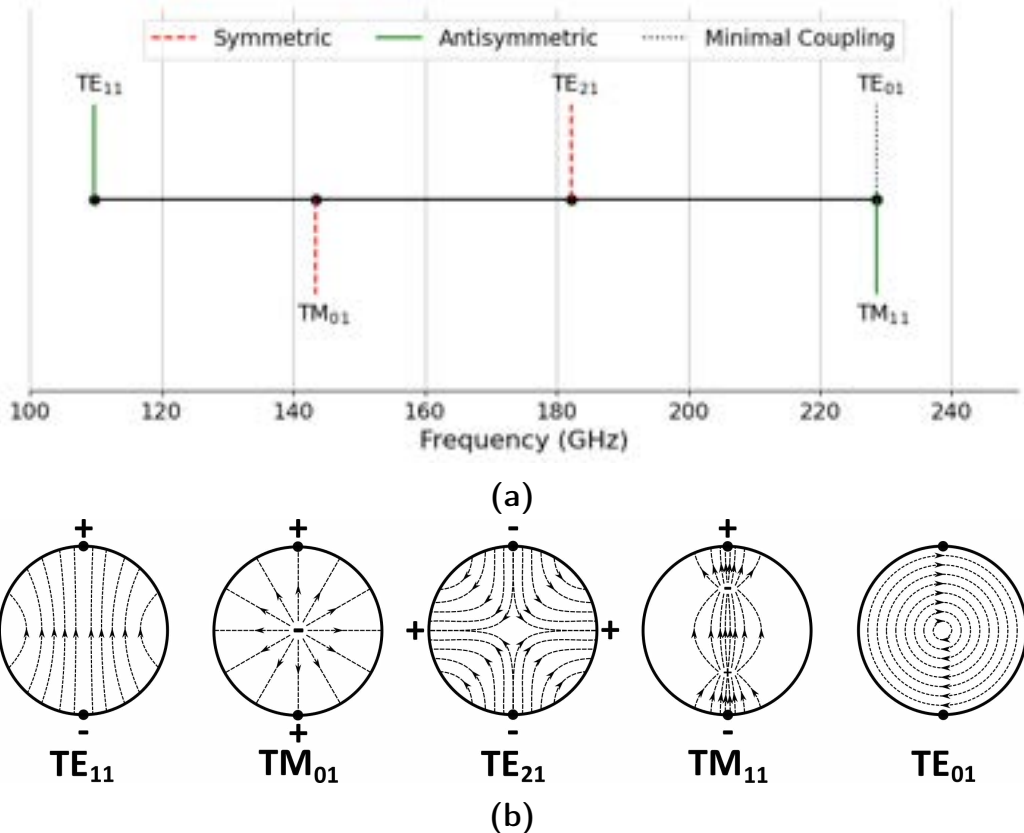


Figure 3.1. (a) Calculated cut-off frequencies for the first few lowest frequency $D = 1.6$ mm circular waveguide TEM modes. (b) Top down view of a single polarisation's electric field lines supported in a circular waveguide for the first few modes.

dots on the perimeter, indicating that if planar probes were positioned there then the phase relative to each other is indicated by the “+” and “-” symbol. If both probes are plus then the coupled signal will be in phase (symmetric), if instead one is plus and the other minus then they are 180° out of phase (anti-symmetric). For example, the lowest frequency mode is the TE₁₁ mode which conveniently has a well-controlled symmetric Gaussian beam pattern with low side-lobe levels for a circular horn antenna⁶⁶. This mode is analogous to a quarter wavelength standing wave, and each polarisation will couple to probes on opposite sides out of phase. The symmetry of these couplings can be taken advantage of such that only the desired TE₁₁ mode can propagate to detectors; this is discussed further in Section 3.3. In the case of a circular waveguide with a diameter of $D = 1.6$ mm, the TE₁₁ mode comes in at 109.8 GHz, and the next anti-symmetric mode is supported over an octave later at 228.5 GHz. Hence, providing the symmetric modes can be removed, this is an effective optical coupling scheme providing a distinct cut-off frequency.

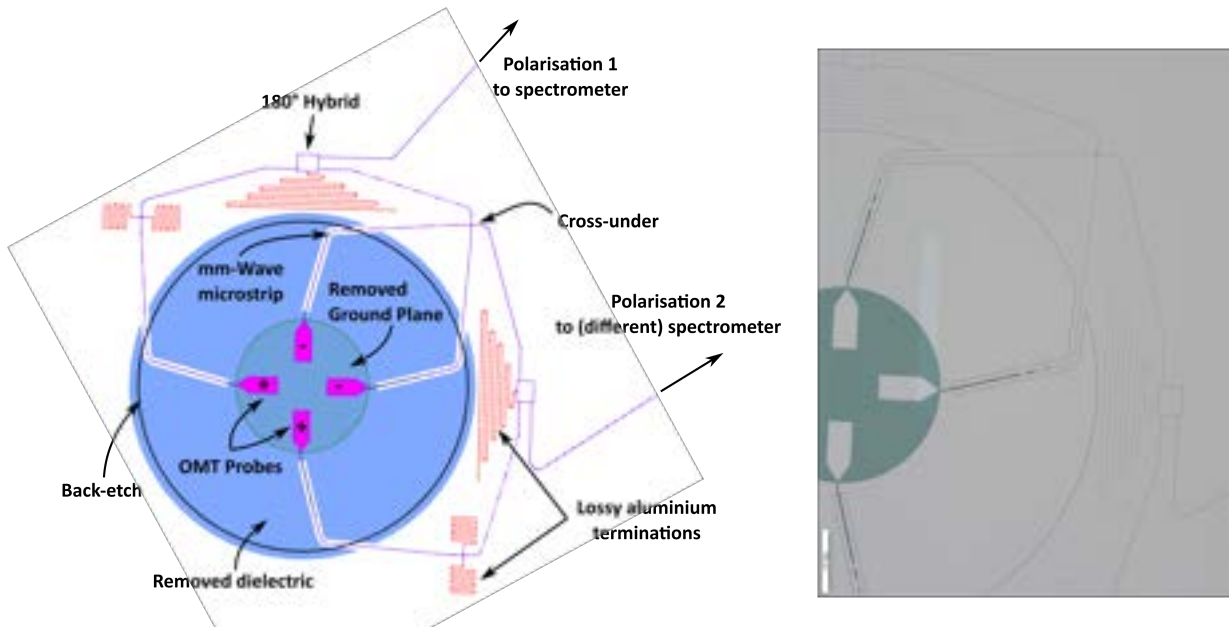


Figure 3.2. (Left) A schematic of the full OMT architecture, showing how the coupled TE_{11} signal at the probes for each polarisation are combined via the 180° hybrid before continuing on to the filter-banks. (Right) Micrograph of a portion of a realised OMT antenna.

3.3 The OMT antenna

Although each pixel is polarisation sensitive, this is not necessary for the line intensity planned for SPT-SLIM and is rather used to maximise the signal per pixel, effectively to collect as much light as possible within the focal plane. The schematic of the optical coupling scheme via a planar orthomode transducer (OMT) can be seen in Figure 3.2.

OMT coupling schemes of this nature have become a popular choice for optical coupling in CMB and other millimetre astronomy instruments^{21,66–71} for a multitude of reasons. To name a few: OMTs provide high co-polar and minimal cross-polar coupling⁷², polarisation sensitivity within one pixel, practical methods of minimising waveguide leakage^{73,74} and suitability for integration into large arrays due to the ease of combining with a horn block and waveguide as demonstrated by Figure 2.2.

As previously shown in Section 3.2, the circular waveguide still allows the higher order TEM modes (TM_{01} , TM_{21}) to propagate within our observing band and potentially couple to the antenna probes. One may think that more power coupling to the antenna would improve signal to noise, however these higher order modes typically have non-Gaussian beam patterns⁷⁵ which is undesirable in spatial imaging. Therefore, we use a 180° Hybrid coupler to discard the undesired higher order modes whilst preserving the Gaussian TE_{11} mode.

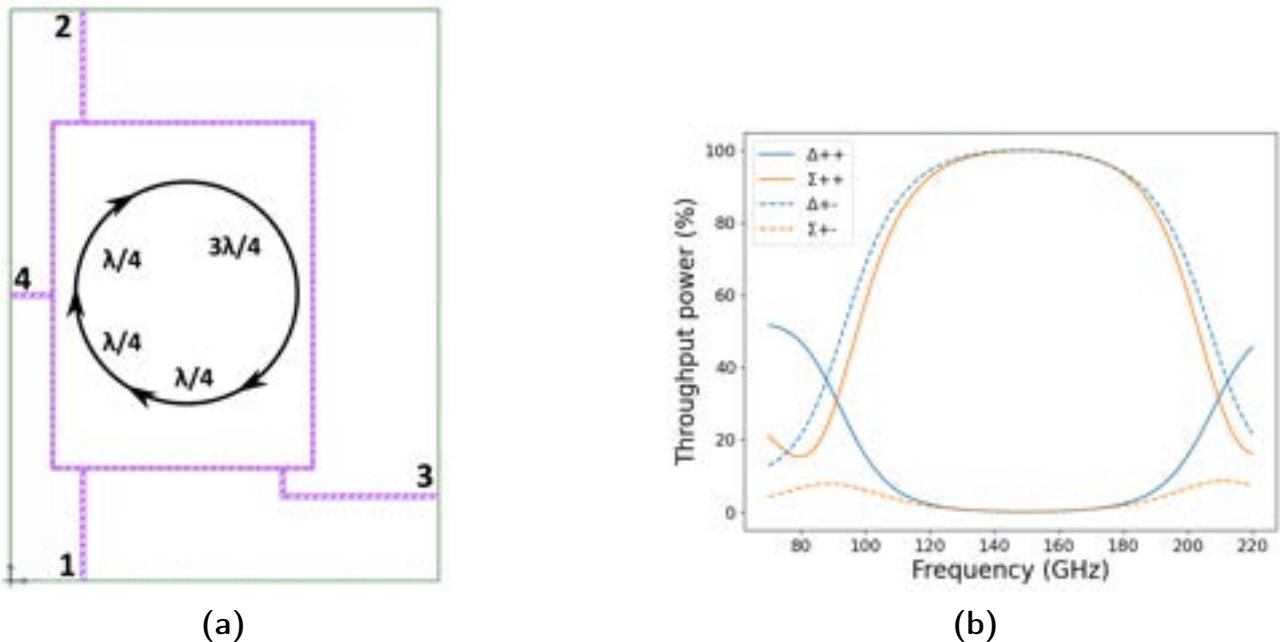


Figure 3.3. (a) Schematic of a Sonnet simulation of a 180° hybrid where ports 1 and 2 are the input signal ports, 3 is the Difference port and 4 is the Sum port. (b) Simulation results of the hybrid optimised for 150 GHz ($\lambda \approx 560 \mu\text{m}$) showing the difference in the output power between the difference (Δ) and the sum (Σ) ports depending on whether the input ports are in phase (++) or out of phase (+-).

The hybrid is a simply a resonating loop of transmission line that uses constructive and destructive interference between input signals. Referring to Figure 3.3a, ports 1 and 2 are the input signal ports and the output at ports 3 and 4 depends on their relative phase. For reasons that will soon become apparent, port 3 is called the “Difference” port and 4 is the “Summation” or “Sum” port. If we first consider the case where the input ports are perfectly in phase with each other (++)¹, as would be the case for the symmetric coupled modes, then signal arriving at the Difference (Δ) port from port 1 would have travelled half a wavelength further than that from port 2 and thus interfere destructively, whereas at the Sum port, signal from port 2 travels $\frac{5}{4}\lambda$ thus arriving in phase with that from port 1 to produce constructive interference.

The same logic can be applied for when the input ports are perfectly out of phase (+-), which would be the case when coupled to anti-symmetric modes within the circular waveguide, producing constructive interference at the Difference port and destructive at the Sum port. The throughput power to each port in these two scenarios is presented in Figure 3.3b for a hybrid optimised for 150 GHz. Thus, using the hybrid will only allow the anti-symmetric TE_{11} mode to propagate through the Difference port and on to the filter-bank. The symmetric modes are terminated in a long lossy aluminium line at the Sum port to dissipate the unwanted power and prevent it from radiating elsewhere.

Between each probe and the edge of the membrane (the black perimeter labelled as “back-etch” in Figure 3.2) there is a CPW to microstrip transition. The purpose of this is that CPW can reach higher characteristic impedances than a microstrip for realistic dimensions. Due to fabrication constraints, the smallest practical linewidth is $2\text{ }\mu\text{m}$ and therefore with CPW a closer match to the impedance of the circular wave guide can be achieved which is typically larger than free space ($377\text{ }\Omega$), thus improving the throughput from the antenna probe. However, due to the geometry of the filter-bank a microstrip feedline is preferable and therefore the transition acts as both an impedance transformer from free-space to that of the microstrip line but also as a convenient geometry transition.

The fabrication team at Argonne National laboratory found that the deposited SiN layer used as the dielectric for the circuitry added significant stress to the membrane which either caused a higher chance of the membrane rupturing or wrinkling which would affect the coupling performance in some unknown/unpredictable way. We therefore moved to removing the dielectric from the membrane region except from along the path of the microstrip/ CPW. The improvement on the membrane surface tension can be visually seen in Figure 3.4. Here the black contours due to the membrane wrinkles are significantly reduced in regions without any deposited dielectric.

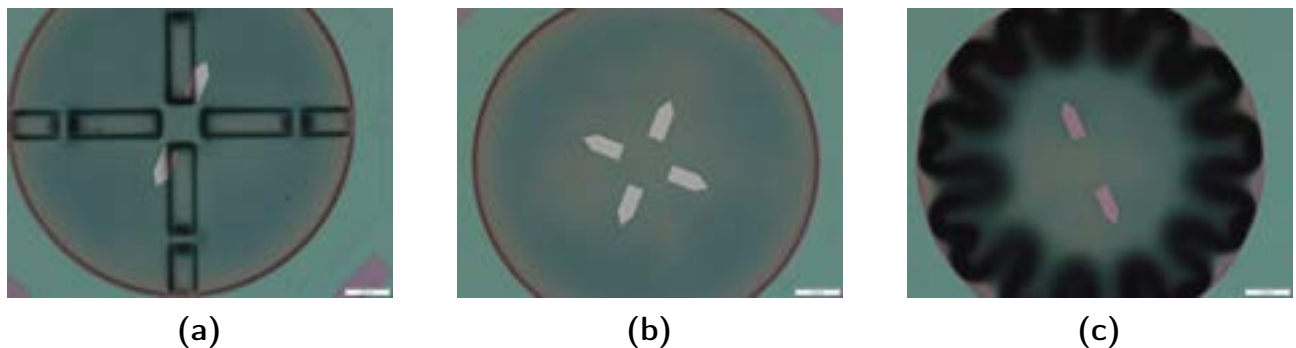


Figure 3.4. Microscope images of three released OMT membranes on the same device (a) with SiN deposited in a cross-hair-like pattern, (b) without any deposited SiN and (c) with SiN deposited everywhere. The black marks are caused by the microscope failing to focus due to the change in depth of field from membrane wrinkling.

The final feature of the OMT is the cross-under. Since it is necessary to combine the co-polar signals, the feedline from one probe (the “-” probes) must cross the feedline of the other polarisation as shown in Figure 3.2. To achieve this, one of the feedlines has a via through the dielectric to an isolated path in the ground plane before passing through another via back down on to the device layer, forming a bridge for the other polarisation to pass under. This is only necessary for one of the feedlines from each polarisation. However, the phase length of each co-polar feedline must be identical for the TE_{11} mode to pass through the hybrid and onwards to the filter-bank. Thus, dummy step-overs are added as well (to the “+” probes).

3.4 Filter-bank design

The design for an on-chip FBS makes use of the low-loss properties of superconductors operating well below the superconducting critical temperature (T_c), integrated microwave circuitry, and the sensitive and multiplexing capabilities of MKIDs to create an efficient, compact, and sensitive spectrometer that does not need large dispersive optical components, complex readout systems, or noise limiting amplifiers and local oscillators.

The output of the hybrid is then connected to the filter-bank by a microstrip transmission line. The filter-bank is made up of a series of capacitively-coupled half-wave ($\lambda/2$) resonators each with a different resonant frequency, f_0 , set by the length, and spectral bandwidth, Δf , set by the coupling strength to the feedline.

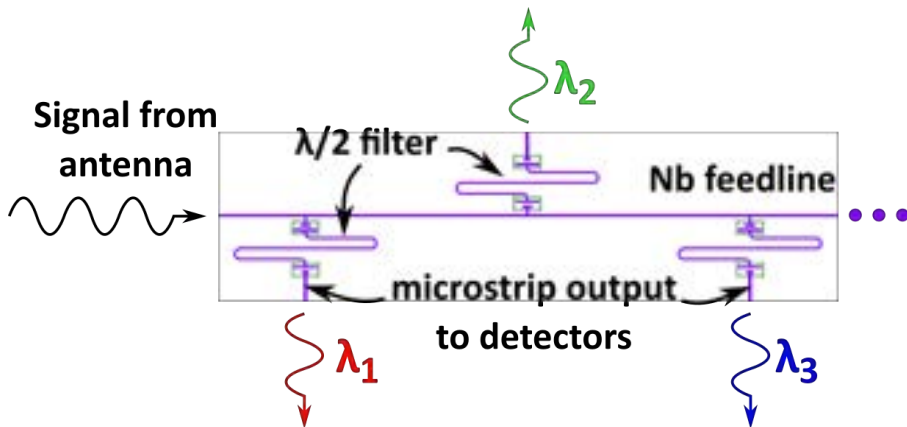


Figure 3.5. Schematic presenting the basic principle of an FBS. Multiple colours from the incident signal are filtered according to the quarter wavelength of the microstrip resonators before passing to the detector.

The two key performance metrics of an on-chip spectrometer are the spectral resolution, R , and the total spectral throughput efficiency of the FBS, η_{FBS} . The resolution is equivalent to the quality factor, Q_{filt} , of each filter channel's resonator, which is proportional to the ratio of energy stored in the electromagnetic fields to that lost per second in the resonator circuit,

$$R = Q_{\text{filt}} = \frac{f_0}{\Delta f} = \omega \frac{\text{Energy Stored}}{\text{Energy Loss/Second}}. \quad (3.3)$$

The total FBS efficiency is defined as the ratio of the total signal output through the channels to that at the input of the FBS. η_{FBS} is a product of the single filter efficiency and the spectral sampling density or oversampling factor, Σ . The oversampling comes at the cost of increasing the number of filters/detectors, which for log spaced filters between f_{min} and f_{max} is given by

$$N_{\text{channels}} = \Sigma R \log \frac{f_{\text{max}}}{f_{\text{min}}}. \quad (3.4)$$

It is worth noting that having more filter-channels is not always possible due to constraints on the readout and the footprint of the FBS. Furthermore, it has also been found that there are diminishing gains to be had by pushing the oversampling beyond Nyquist sampling ($\Sigma = 2$) as one begins to pay a penalty in the Noise Equivalent Power (NEP) of spectrometer for splitting the signal at a single frequency between more and more detectors⁷⁶.

The maximum power transferred through the single filter to the detector that can be achieved for a lossless feedline-filter T-junction such as this is 50% of the incident signal^{65,77,78}. However, by oversampling the spectral band with overlapping spectral channels, η_{FBS} can reach the upper quartiles of efficiency as seen in studies such as Kovács et. al.⁷⁷. Additionally, the physical spacing between channels can also impact the total efficiency. This is explored further in this chapter, particularly as a means of finding a compromise between instrument efficiency and detector readout cross-talk mitigation.

3.4.1 Filter channel geometry and characterisation

A filter channel is created by coupling a $\lambda/2$ resonator to the main filter-bank feedline. On resonance, the current distribution results in a current node at each end of the resonator. This enables two coupling methods: inductively, by exploiting the current maximum in the centre as demonstrated by SuperSpec^{79,80}; or capacitively, using the voltage maximum at the ends, as seen in the DESHIMA^{46,78,81} devices. Both examples tune the coupling quality factors, Q_C , via the separation between feedline and resonator. Due to fabrication tolerances, the tuning precision of Q_C is somewhat limited for such proximity couplings, particularly without the use of E-beam lithography. Figure 3.6 presents an alternative coupling scheme that uses a pseudo-lumped element capacitor island in the ground plane to form parallel plate capacitors; two at either end of the resonator. This allows for a highly tuneable capacitive coupling using a microstrip architecture to minimize losses due to radiation^{78,82}. One potential issue with this geometry is that off resonance, the microstrip between the feedline and the first capacitor (C_{in}) will appear as a very short stub. For the single filter this has no impact other than acting as a small parasitic capacitance to ground, however when multiple of these exist on a feedline they can produce an undesirable effect which is studied in Section 3.6.

The spectral resolution of a single channel can be written as the inverse sum of the quality factors due to losses within resonator, Q_{loss} , the coupling to the feedline, Q_{feed} , and detector coupling, Q_{det} ⁷⁹,

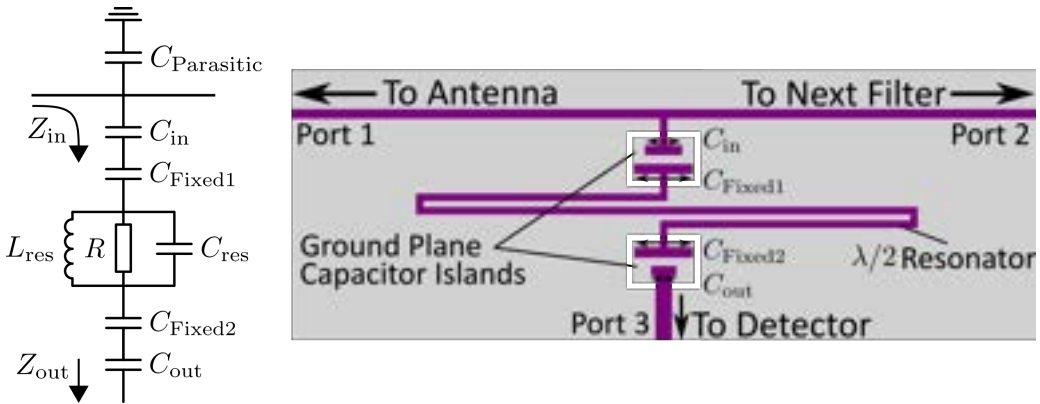


Figure 3.6. (Left) lumped-element circuit diagram of the filter where the $\lambda/2$ resonator has been modelled as an LRC circuit with the resistor representing the loss mechanisms. (Right) Top-down view of a filter channel microstrip geometry. The purple geometry is the Niobium device layer and the grey background indicates the niobium ground plane separated by the 300 nm thick dielectric.

$$\frac{1}{R} = \frac{1}{Q_{filt}} = \frac{1}{Q_C} + \frac{1}{Q_{loss}} = \frac{1}{Q_{feed}} + \frac{1}{Q_{det}} + \frac{1}{Q_{loss}}. \quad (3.5)$$

Q_{feed} and Q_{det} can be controlled by changing the overlapping surface area of the parallel plates. For this design, Q_{filt} is largely controlled by the capacitor widths C_{in} and C_{out} and f_0 by the resonator length (see Figure 3.6).

To characterise this design, the geometry in Figure 3.6 was simulated using Sonnet EM⁸³. Table 3.1 shows the simulation parameters used. The aim here was to obtain a parameter mapping whereby a desired f_0 can be converted into the C_{in} , C_{out} and resonator length, x_{res} , values which result in a maximally efficient filter at the desired Q_{filt} and f_0 . The following process demonstrates this characterisation for $R = 200$ filters. In the lossless case where the dielectric loss tangent is set to zero, this is achieved by tuning $Q_{feed} = Q_{det} = 400$ such that the inverse sum results in $Q_C = 200$.

The fixed capacitors are set to a width which roughly allows variable capacitors widths such that the filter at each extreme (low and high frequency) can obtain the desired quality factor range. This was originally motivated to keep the geometry of the resonating length identical across the filterbank, however this did limit the range of Q_{filt} that could be achieved. Later the design was changed to keep the paddles within each pair the same size and vary both as well as the ground island to provide a more flexible and versatile filter that can achieve whichever filter resolution was desired. The following characterisation process remained the same.

Parameter	Value
Cell size	$0.1 \mu\text{m} \times 0.1 \mu\text{m}$
Simulation box size	$200 \mu\text{m} \times 90 \mu\text{m}$
SiN ϵ_r	10
SiN thickness	300 nm
Niobium L_k	$0.1 \text{ pH} \square^{-1}$
SiN membrane ϵ_r	7.0
SiN membrane thickness	$2.0 \mu\text{m}$
Oxide membrane ϵ_r	4.0
Oxide membrane thickness	450 nm
Si substrate ϵ_r	7.5
Si substrate thickness	525 μm

Table 3.1. Material and simulation parameters used to simulate the filter geometries in Sonnet.

Feedline Capacitor

Firstly, a simulation sweeping C_{in} at multiple resonator length values was carried out with the port 3 impedance set high enough to resemble an open circuit. This effectively turns off port 3 and therefore Q_{det} , allowing the feedline coupling to be tuned in isolation. However, due to the geometry of the filter, it is not possible to fully remove the contribution of C_{out} , even when port 3 is de-embedded up to the output paddle. The impact of this presents itself when tuning C_{out} , and is discussed further in the next sub-section.

The results from the second iteration of Q_{feed} tuning are shown in figures 3.7. To extract the value for Q_{feed} , the S_{21} data from each simulation was fit with a Lorentzian curve for an open circuit parallel $\lambda/2$ resonator for frequencies, f , near resonance of the form⁸⁴,

$$S_{21} = 1 - \frac{Q_{\text{filt}}}{\text{Re}(Q_{\text{feed}}) + j\text{Im}(Q_{\text{feed}})} \left(\frac{1}{1 + 2jQ_{\text{filt}}x_0} \right) \quad \text{where} \quad x_0 = \frac{f - f_0}{f_0}. \quad (3.6)$$

Detector Capacitor

With the quality factor of the feedline coupling tuned to $Q_{\text{feed}} = 400$, the output capacitor is then tuned by setting the impedance of port 3 to the characteristic impedance of the microstrip. The total power transferred from port 1 to port 3, $|S_{31}|^2$, was simulated for a range of C_{out} values at each resonator length with the tuned C_{in} value.

The S_{31} power spectrum ($|S_{31}|^2$) for these filters can be fit with a lorentzian of the form below in order to extract Q_{filt} (or Q_C in the lossless case)⁸¹

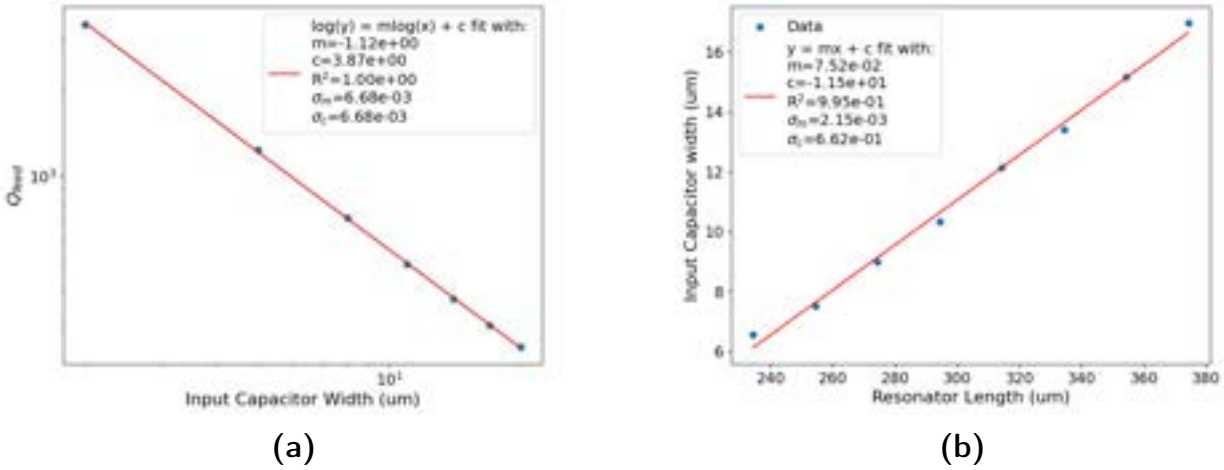


Figure 3.7. Feedline coupler tuning: (a) A linear fit in log space of the feedline quality factor at a range of input capacitor widths for a filter with $x_{\text{res}} = 334.4 \mu\text{m}$. (b) The summary of the interpolated C_{in} values at multiple resonator lengths which give $Q_{\text{feed}} = 400$.

$$|S_{31}|^2 = \left| \frac{Q_{\text{filt}}}{\sqrt{\frac{2Q_{\text{loss}}^2 Q_{\text{filt}}^2}{(Q_{\text{loss}} - Q_{\text{filt}})^2} (1 + 2jQ_{\text{filt}}x_0)}} \right|^2. \quad (3.7)$$

As mentioned previously, considering the filter simulation as a matched 3 port T-junction, the theoretical maximum efficiency that can be achieved for a filter is 50% to port 3 and an equal 25% split to port 1 and port 2⁶⁵. This should occur when $Q_{\text{feed}} = Q_{\text{det}}$, however, the C_{out} value resulting in the peak in $|S_{31}|^2$ does not match the value that gives the desired Q_{filt} as shown in Figures 3.8c and 3.8e. To improve this, the complete characterisation can be carried out a second time, where the maximally efficient C_{out} from the first run is used for the Q_{feed} tuning. As shown in the figures 3.8d and 3.8f, the maximally efficient C_{out} occurs at a closer value to that which gives the desired Q_{C} . One might expect that to achieve $Q_{\text{feed}} = Q_{\text{det}}$ the input and output capacitors should have identical geometries, note that this isn't the case due to the output linewidth being larger than on the input (due to the microstrip coupling to the detector, see 4.1.2), hence the filter also acts as an impedance transformer on resonance.

Fortunately, the peak efficiency has a rather broad peak as a function of C_{out} relative to sub-micron fabrication tolerances. Hence, the value at the peak efficiency was preferred to the capacitor widths that provide the desired Q_{C} for this fabrication/design latitude.

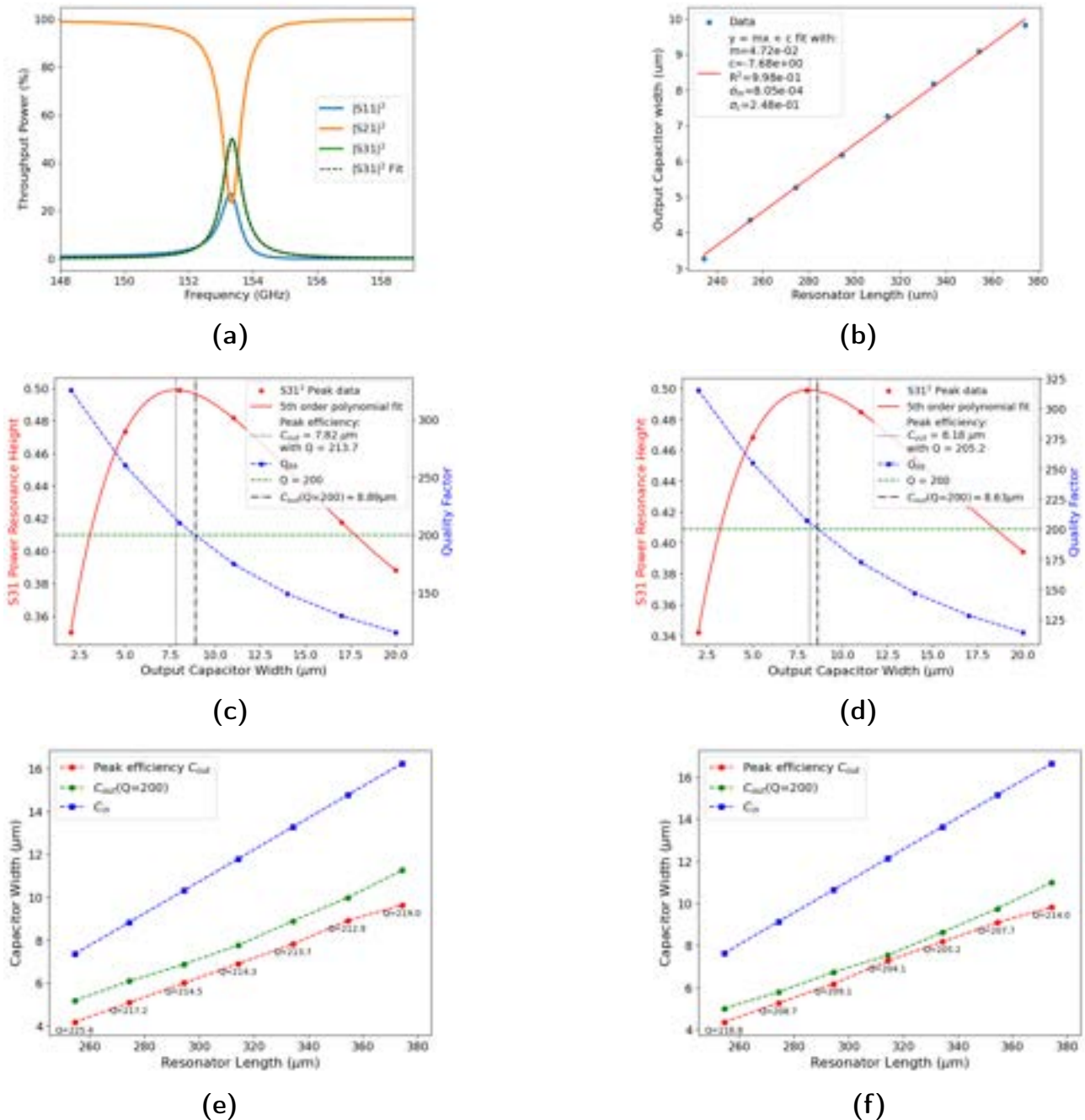


Figure 3.8. Q_{det} tuning: (a) Sonnet simulation S-parameter power spectrum data for a single filter near peak efficiency with a fit of $|S_{31}|^2$ using Equation 3.7. (b) Shows the tuned relationship between the peak efficiency C_{out} value and the resonator length. (c) Fit extracted parameters for a C_{out} sweep of a filter with $x_{res} = 334.4 \mu m$ from the first iteration of tuning and (d) the second iteration. Finally (e) and (f) show the tuned capacitor widths across the range of resonator lengths for the first and second iteration respectively. Note the improvement in matching between the peak efficiency C_{out} value and that which gives $Q_C = 200$ between the first and second iteration of tuning.

Resonator Length

Finally, with the relationship between the resonator length and the optimal capacitor widths determined, a simulation was performed over the range of x_{res} values that cover the frequency window with the capacitor model functions in use. These results are shown in Figure 3.9, where Figure 3.9a clearly shows the capacitor width functions successfully working with the power resonance peaks reaching the optimal efficiency at 0.5 across the band. Furthermore, Figure 3.9c shows how the relationship between resonant frequency and the resonator length can be obtained with a linear fit in log-space. The quality factor for each filter is also shown with the mean value being $Q_{\text{filt}} = 209.1 \pm 4.5$ where the uncertainty is the half range. It would have been possible to continue iterating on this, but with diminishing improvements. Furthermore, the fluctuations in the filter quality factor were suitably small and would likely be dominated by the effects of fabrication tolerances (see Section 3.6), loss tangents, and uncertainty around the precise material properties used in the simulations. This would also be true for the single filter efficiency, which is particularly affected by the dielectric loss tangent.

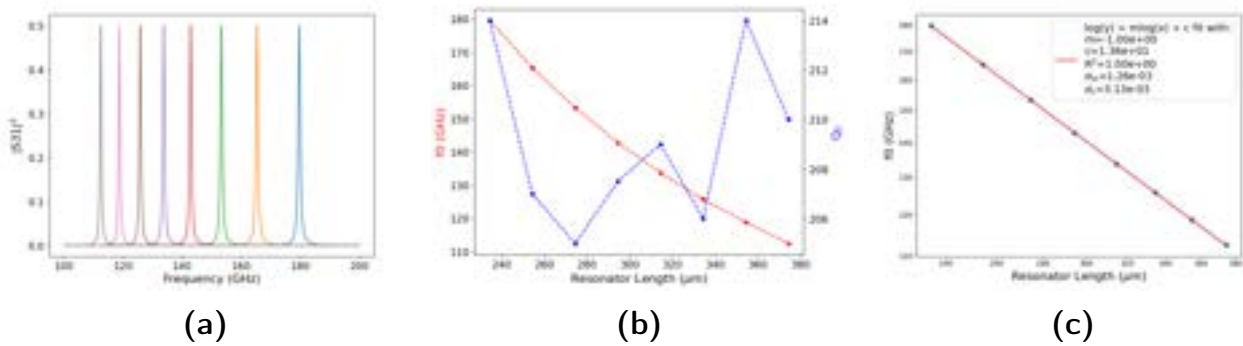


Figure 3.9. Resonator f_0 tuning: (a) Simulations across the observing band of filters using the second iteration expressions for the peak efficiency capacitor widths. (b) Resonator f_0 s and Q_C at each resonator length, showing a smooth function in f_0 and a noisy distribution in Q_C with a mean value of 209.1 with a half-range of 4.5. (c) Linear fit in log-space of filter f_0 and resonator length.

The full filter model for the layout defined by the material simulation parameters in Table 3.1 is summarised in Table 3.2, where the variable capacitor widths depend on the resonator length and the resonator length on the desired f_0 .

3.4.2 Dielectric loss tangent

The presence of a dielectric layer introduces a loss mechanism due to parasitic two level systems (TLS), which has been extensively studied^{85,86}. The dielectric loss tangent, $\tan \delta$, is a measure of

Variable	Function
x_{res}	$10^{-\log(f_0) - 13.6}$
C_{in}	$0.0752(x_{\text{res}}) - 11.5$
C_{out}	$0.0472(x_{\text{res}}) - 7.68$

Table 3.2. Filter geometry model functions which yield geometry sizes in microns for a filter with a quality factor of $Q_C = 209.1 \pm 4.5$ for a given filter frequency, f_0 in Hertz.

the energy dissipated through this mechanism and hence can be expressed as a quality factor and is considered to be the dominant contribution to Q_{loss} in Equation 3.5, thus $\tan \delta = 1/Q_{\text{loss}}$. As will become apparent further in this thesis, the loss tangent governs the ultimate performance of this mm-wave on-chip FBS technology and is currently the main limiting factor on improving device efficiency and spectrometer resolution.

The precise microscopic mechanisms that lead to a materials loss tangent are not well understood and typical dielectrics exhibit a wide range of loss tangents at microwave frequencies, where most deposited dielectrics, usually silicon composites, in use for high quality factor resonators are somewhere within the range of 0.1×10^{-3} to 10×10^{-3} . As we will see, variations in this range have a significant effect on the filter performance. It is also worth noting that, as per Equation 3.5, if the loss tangent is large enough such that it becomes a significant percentage of $1/Q_C$ then the materials loss tangent should be accurately known to suitably account for it whilst characterising the filters, e.g. if $\tan \delta = 3 \times 10^{-3}$ then $Q_C = 143$ is required to achieve a filter with a resolution of $R = 100$, note however this would reduce the efficiency of the filter as will be discussed shortly. Dielectric properties, including the loss tangent, seem to depend strongly on the specific material as well as the particular growth technique and conditions. In the first couple of years of developing the SPT-SLIM focal plane there were limited published results for the high frequency loss tangents of composite silicon dielectrics, those that were found in literature were measured at microwave frequencies below 10 GHz^{87,88}. Approximate extrapolations and inferred values from resonator losses suggested that a SiN dielectric might have a loss tangent around 7×10^{-4} ⁸⁹. As such, the SPT-SLIM focal plane was developed with this as the baseline since our architecture and fabrication process would be similar, hence a $\tan \delta = 1 \times 10^{-3}$ was assumed. Due to the importance of the loss tangent in a device such as SPT-SLIM, Argonne was motivated to develop a robust technique for measuring the loss at millimetre frequencies where a study⁹⁰ later showed three methods of measuring the loss tangent at 150 GHz where values vary from 1×10^{-3} to 4×10^{-3} between the measurements.

The maximal fraction of power, η_{filt} , that passes through the $\lambda/2$ filter towards the detector (single filter efficiency) depends on the ratio of Q_{filt} to Q_{loss} as⁸⁰,

$$\eta_{\text{filt}} = 2 \frac{Q_{\text{filt}}}{Q_{\text{filt, lossless}}} \left[1 - \frac{Q_{\text{filt}}}{Q_{\text{filt, lossless}}} - \frac{Q_{\text{filt}}}{Q_{\text{loss}}} \right], \quad (3.8)$$

where terms denoted by “lossless” refer to values where the loss tangent is zero. The optimisation process in the previous section has the effect of maximising this expression by tuning the coupling capacitors until $Q_{\text{filt}}/Q_{\text{filt, lossless}} = 0.5(1 - Q_{\text{filt}}/Q_{\text{loss}})$. This results in the maximum filter efficiency being dependent on the loss quality factor as

$$\eta_{\text{filt, max}} = \frac{1}{2} \left[1 - \frac{Q_{\text{filt}}}{Q_{\text{loss}}} \right]^2. \quad (3.9)$$

For the lossless case, $Q_{\text{loss}} \gg Q_{\text{filt}}$ hence $\eta_{\text{max}} = 0.5$, which is what was observed from optimising the coupling capacitors in Figure 3.9a. According to Equation 3.9, higher Q_{filt} filters have increasingly poorer efficiencies, this is effectively because at resonance, the signal oscillates more times along the length of the microstrip, thus allowing more energy to dissipate into the dielectric with each pass. To demonstrate the dependence on the loss tangent, Figure 3.10b shows the the impact that the loss tangent has on the filter efficiency for a range of $Q_{\text{filt, lossless}}$ predicted by Equation 3.9, as well as good agreement with a Sonnet simulation for an optimised filter with $Q_{\text{filt, lossless}} = 337$ filter at 148 GHz. Since there are no other loss mechanisms in the Sonnet simulation besides the input loss tangents, fitting to the S_{31} power spectrum with Equation 3.7 will extract the true value for Q_{loss} experienced by the filter, which inverted is $\tan \delta$. For the results from Equation 3.9 to agree with the simulated results, it was necessary to scale Q_{loss} by the gradient shown in Figure 3.10a. This is because in this filter simulation the the filter microstrip is on top of the low stress SiN layer which is expected to have negligible loss relative to that of the SiN layer separating the microstrip from the ground plane. This has the small effect of reducing the the dielectric loss tangent due to the fringing fields which pass through the membrane en-route to the ground plane, giving an effective loss tangent similar to an effective dielectric constant.

Figure 3.10b shows that there is a significant trade-off between the spectrometer resolution and the single filter efficiency which similarly translates to a reduced device efficiency, which is shown in further detail in Section 3.6. For $\tan \delta = 1 \times 10^{-3}$, filter efficiency could vary by $\approx 10\%$ between $R = 100$ and $R = 300$ filters, thus it is clear what stands to be gained from low loss dielectrics, particularly ones that are below 2×10^{-3} . However, until these are found on-chip FBS spectrometers will be limited as low to medium resolution millimetre spectrometers. Fortunately, this is currently still beneficial in astronomy instrumentation, particularly for line intensity mapping.

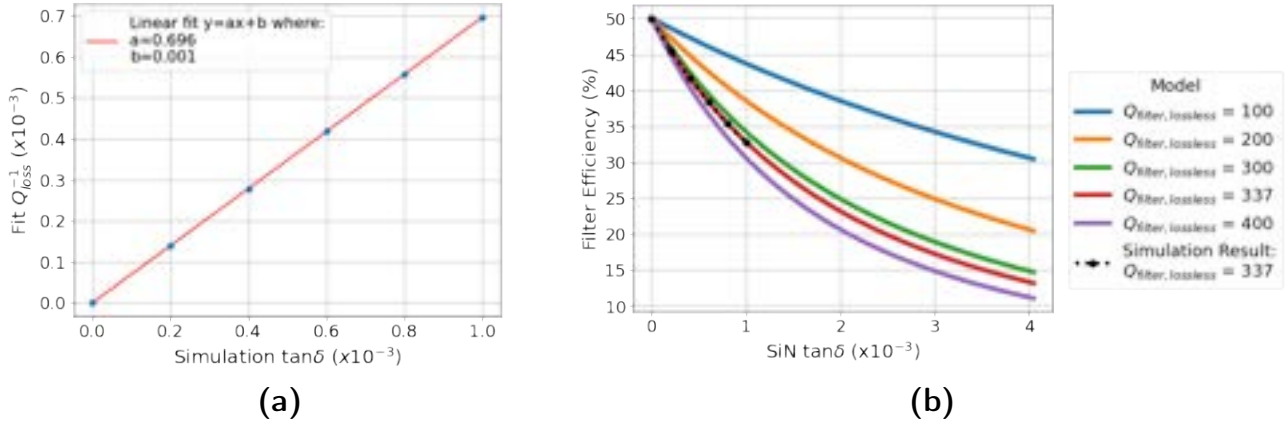


Figure 3.10. (a) Plot showing the conversion between the SiN loss tangent used in a filter simulation and the inverted Q_{loss} extracted from the sonnet simulated S_{31} , representing the actual loss of the filter. (b) The trade-off between the filter resolution, R and efficiency, η_{filt} for a range of initial lossless filter quality factors, $Q_{\text{filt, lossless}}$ and $\tan \delta$ values. Note, to compare to the simulation, the model $\tan \delta$ has been appropriately scaled by the gradient in (a).

3.5 Fabrication error tolerance

The largest source for disagreement between simulated and fabricated filters is generally due to fabrication error, a somewhat unavoidable aspect of nano-fabrication. Deviations in the kinetic inductance, L_k , of the superconducting film, the dielectric thickness/constant, and over or under etching, have all been shown to have a considerable impact on the filter properties, and this is particularly the case for etch sensitivity with proximity-coupled filters⁷⁸. Therefore it was necessary to understand the tolerance of a design to a variety of fabrication errors. Figure 3.11 shows the filters' $Q_{\text{filt, lossless}}$ and f_0 sensitivity to variations in key features of our architecture using the Python model described in Section 3.6 for the $R = 300$ FBS, to study the impact of typical deposition and lithography error based on un-optimised fabrication runs at Cardiff. Note, the results for varying the niobium kinetic inductance were obtained from simulating the filters in Sonnet and then changing the kinetic inductance to measure the shift in Q_{filt} and f_0 .

These results demonstrate that this design has a good tolerance to fabrication error, particularly given that worst case errors were used. The resonant frequency is most sensitive to variations in L_k , however this is only approximately 3.5 % and suitably constant across the band. Thus, all filters should shift by the same amount. Note, changes in L_k due to a variation in niobium thickness were not considered as L_k for niobium is expected to vary slowly with thickness for ≈ 300 nm thick niobium with a magnetic penetration depth of ≈ 135 nm. It is worth noting that a change in L_k is an analog for a change in wave velocity, hence variations in dielectric constant will also impact the f_0 , however, at the time the impact of dielectric constant variation was not

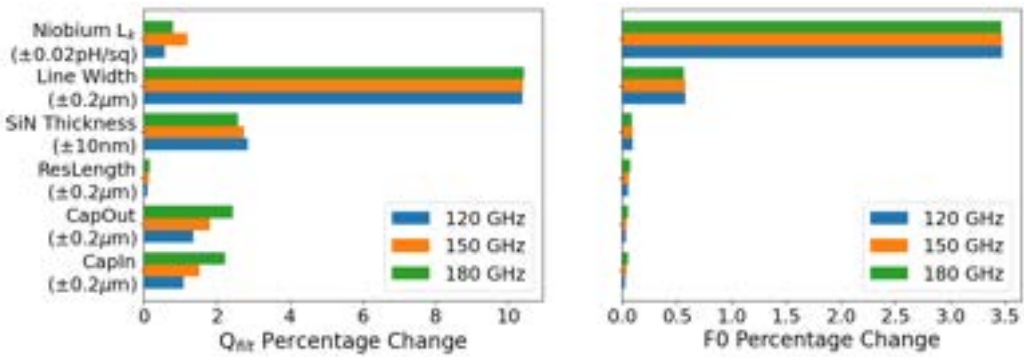


Figure 3.11. Simulated single-filter quality factor, Q_{filt} , (Left) and resonant frequency, f_0 , (Right) tolerance to the worst-case fabrication errors for different variables.

considered. Furthermore, we saw a promising forecast for the tolerance of the geometry to the variables that are the main controllers of Q_C , namely the input and output capacitor geometries (“CapIn” & “CapOut”), and “SiN Thickness” since these control the capacitance of the coupling capacitors, each resulting in a shift in Q between 2-3%. One can in fact see the Q_{filt} and f_0 latitude to changes in the coupling capacitance from the curves in Figures 3.7 and 3.8. By comparison, proximity-coupled filters demonstrate a far higher sensitivity to etch error at the coupling geometry where a change in 100 nm can triple the value of Q_C ⁷⁸. This low tolerance removes the need to use electron-beam lithography, a more precise but time-consuming etching method, reducing the cost, and speed of device turn around.

3.6 Filter-bank simulation

To take the characterisation of the design further, it was necessary to understand the performance of the filter-bank. Simulations carried out in Sonnet EM capture electromagnetic behaviour otherwise overlooked by lumped-element simulation software. This is at the cost of simulation run time which gets increasingly longer the larger the size of the simulation, and therefore unsuitable for simulating the performance of an FBS with more than three filters if a high simulation accuracy is desired. Furthermore, niche issues start to become a problem such as larger box sizes result in dimensions that are a similar size to the signal wavelength creating interfering box modes. As such, an alternative simulation method which achieved similar accuracy to Sonnet without the simulation time penalty was sought. We developed a Python model based on Scikit-RF, an open source module to create a series of cascaded lumped-element networks connected by transmission lines to simulate an N-channel filter-bank. In the following sections, comparisons between simulated S-parameters from Sonnet, ADS and Scikit-RF (SKRF) are used to build the model. Similar methods have already been developed to simulate and analyse FBSs^{76,91} but

only from the perspective of resonator parameters, rather than using physical properties as the simulation handles, such as geometry dimensions and dielectric thickness. As discussed in the Section 3.5, we wanted to be able to simulate the filter-bank in such a way that could account for common fabrication deviants (linewidth / dielectric thickness) as well as being able to vary the parameters from Equation 3.4, (R , Σ , and the frequency bounds, f_{\min} and f_{\max}) and the dielectric loss-tangent.

This section describes the process used to build this simulation tool via a well understood circuit model that became a crucial utility throughout the focal plane development. It is worth noting that at the time of developing this simulation, the mm-wave feedline was planned to step-down off of the membrane layers before reaching the filter-bank and therefore the simulations presented here are derived from Sonnet simulations with the layer stack shown in Figure 2.4 without the membrane layers.

This filter-bank simulation code can be accessed from the following GitLab repository:
https://gitlab.com/Grobson97/skrf_filter_bank_simulation.

3.6.1 Microstrip transmission line model

To begin, a brief introduction into transmission lines is necessary, however, for an in-depth understanding, one should refer to Pozar's *Microwave Engineering*⁶⁵. An infinitesimal length of transmission line is represented in Figure 3.12 as the standard two conductor model including the circuit model for a unit length of transmission line. The series inductance L represents the total-self inductance, C represents the capacitance between the two conductors and then R and G represent resistive losses due to the conductor itself and the dielectric loss respectively.

The voltage, V and current, I for an alternating current signal of frequency ω propagating down a length of wire as a function of position z can be solved as travelling waves of the form

$$V(z) = V_0^+ e^{-\gamma z} + V_0^- e^{\gamma z}, \quad (3.10)$$

$$I(z) = I_0^+ e^{-\gamma z} + I_0^- e^{\gamma z}, \quad (3.11)$$

where the $e^{-\gamma z}$ terms represent that quantity travelling in the $+z$ direction and $e^{\gamma z}$ terms in the $-z$ direction. γ is the complex propagation constant with real and imaginary components α and β (the attenuation and phase constants) as given by

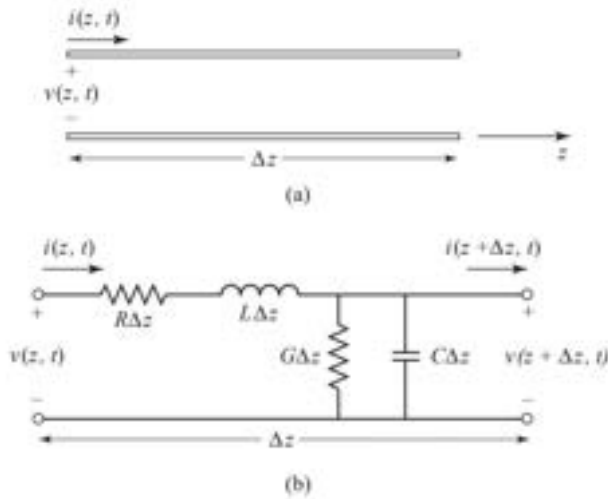


Figure 3.12. (a) Voltage and Current definitions and (b) Lumped-element equivalent circuit for a unit length (δz) of transmission line as presented in Pozar⁶⁵.

$$\gamma = \alpha + j\beta = \sqrt{(R + j\omega L)(G + j\omega C)}. \quad (3.12)$$

The phase constant represents the change in phase per unit length and as such is expressed as $\beta = 2\pi/\lambda$ which is trivially converted in terms of the phase velocity, v_p as $\beta = \omega/v_p$. Since the phase velocity is simply the velocity of the travelling wave in a medium, this can be easily calculated as a reduction in the vacuum speed of light by the effective relative permittivity, ϵ_r , and the relative permeability, μ_r , hence

$$\beta = \frac{\omega}{c} \sqrt{\epsilon_r \mu_r}. \quad (3.13)$$

It is typical to use non-magnetic materials for transmission lines, hence $\mu_r = 1$. Furthermore, the attenuation constant for a TEM wave on a line with some loss tangent as is propagated on CPW and microstrip lines can be given by

$$\alpha = \frac{\beta \tan \delta}{2}. \quad (3.14)$$

Thus, γ can be obtained if the dielectric constant is known for a given frequency.

Finally, the wave coefficients in Equation 3.10 can also provide the definition of the characteristic impedance of the transmission line as the ratio of the voltage to the current which can also be given in terms of the circuit parameters as

$$Z_0 = \frac{V_0^+}{I_0^+} = -\frac{V_0^-}{I_0^-} = \frac{R + j\omega L}{\gamma}. \quad (3.15)$$

The takeaway here is that the electromagnetic wave travelling along a transmission line can be fully characterised if the characteristic impedance, dielectric constant, and the dielectric loss are known for a given frequency. Therefore, the transmission line model in the simulation uses the Scikit-RF *Media* object which can be instantiated as a *DefinedGammaZ0*, which can take arrays of Z_0 , γ and the corresponding frequencies as inputs. This media object can then be used to add a section of transmission line for any desired length. To allow our model the flexibility of simulating microstrips with a variety of linewidths it was necessary to therefore obtain values for the characteristic impedance and propagation constant for these geometries. This was achieved by simulating a lossless microstripline in Sonnet for a range of dielectric thicknesses and linewidths, extracting the mean port imadance over the frequency range in order to allow for a three dimensional interpolation of Z_0 and ϵ_r for the given geometry. These interpolation surfaces are shown in Figure 3.13. The agreement between the Sonnet and SKRF simulated S_{21} for a 50 μm long microstrip with two different geometries as seen by 50 Ω ports is shown in Figure 3.14. Note, the agreement is best at the frequency in the centre of the band (150 GHz) and it is slightly worst at the frequency extremes. This is because the average port parameters are used for the interpolation surfaces. However, it is only a very small difference and thus has effectively a negligible effect.

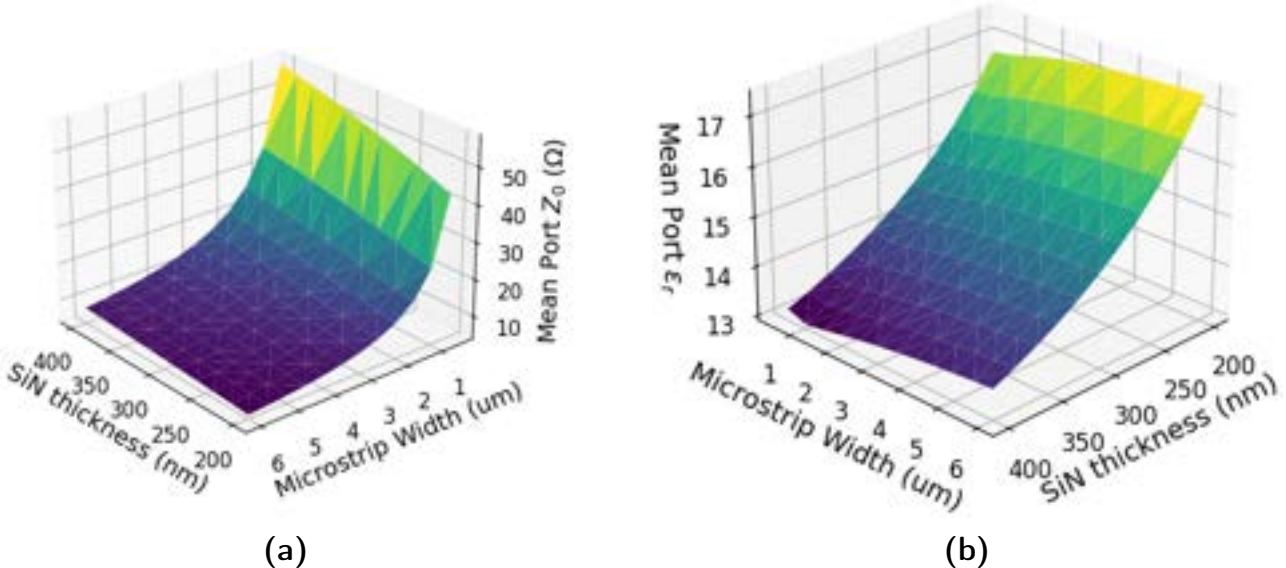


Figure 3.13. Microstrip interpolation surfaces used to extract the characteristic impedance Z_0 and effective relative permittivity ϵ_r , for a range of microstrip geometries.

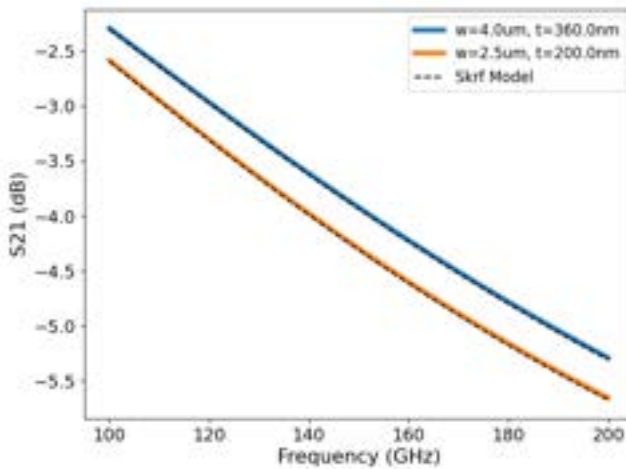


Figure 3.14. S_{21} comparison between Sonnet and the SKRF method for a simulated $50\text{ }\mu\text{m}$ long microstrip with microstrip widths of $w = 4.0\text{ }\mu\text{m}$ or $2.5\text{ }\mu\text{m}$ and SiN thicknesses of $t = 360\text{ nm}$ or $t = 200\text{ nm}$ as seen by 50Ω ports.

3.6.2 Filter capacitor model

Initial attempts at modelling the coupling capacitors as simple parallel plates proved to be unsuccessful. This lead to a study to find the lumped element circuit model which could accurately describe the physical component as is simulated in Sonnet. This process is summarised in Figure 3.15, where the coupling capacitor is gradually built up in complexity from a simple transmission line. At each stage a lumped element network including transmission lines as per Section 3.6.1 is built using SKRF and the S_{21} is simulated and compared to the Sonnet simulation. The circuit models shown are the ones that yielded the best results at each stage, however more were tested such as adding parasitic shunt capacitance or inductance to ground.

As a control, the first row shows the good agreement for a $50\text{ }\mu\text{m}$ long transmission line with the nominal filter microstrip geometry of $2\text{ }\mu\text{m}$ wide with a SiN thickness of 500 nm . Following this, a ground plane island is added and a lumped capacitor component with $C = 0.03\text{ pF}$ bridging the gap. As expected, this nicely agreed with the SKRF model using the same transmission line lengths and capacitance value. However, as it turned out, further complexity is added as the microstrip extends over the gap in the ground plane and on to the ground island. By allowing the component values to float in the SKRF models and fitting the SKRF S_{21} to the Sonnet simulation, the best model was one that suggested a parasitic series inductance is induced around the ground island of 3.605 pH as well as a slight increase in the series capacitance due to the overlap of the microstrip and the ground island as indicated by the optimal capacitance being $C = 30.93\text{ fF}$ rather than $C = 30.0\text{ fF}$. Also shown on the simulated S_{21} data for this step (third row) is the

slight disagreement if the parasitic inductance is not included. Finally, this circuit model was successfully fit to the complete coupling capacitor geometry and showed a slight increase in the parasitic inductance.

Once the lumped element model was obtained, the coupling capacitor geometry was simulated for a variety of capacitor paddle widths (according to the simulations from the filter characterisation) and SiN thicknesses where the ports were de-embedded up to the edge of the ground plane. Each data file was fit with the model and the capacitance and parasitic inductance values were extracted to form interpolation surfaces in a similar manner as in the previous section for the microstrip parameters. These surfaces are shown in Figure 3.16.

3.6.3 Parasitic stub

On each filter there is a small section of microstrip between the feedline and the input coupling capacitor, which, off-resonance acts as a very short stub. It was found that this stub is well modelled as a parasitic shunt capacitance to ground, hence the inclusion of a shunt capacitance to ground shown in the filter circuit diagram shown in Figure 3.6. The parasitic capacitance was fit to and was found to be 12.96 fF. Figure 3.17a shows the agreement between the Scikit-RF models which do and do not include the parasitic shunt capacitance and the Sonnet simulation shown in the inset. For a single filter, the impact of this stub is negligible. However, as the number of stubs increases an effect somewhat analogous to the impedance engineering in superconducting parametric amplifiers⁹² occurs when multiple small mismatches are present along the feedline. This creates a fairly effective stop-band, which could occur within or close to the band of operation depending on the electrical length between the filters (stubs). From our simulations (Figure 3.17b), the stop-band is kept out of the operational frequency band as long as the filters are separated by an electrical length that is suitably smaller than half a wavelength. Alternatively, a more well defined stop-band is produced if a fixed separation length is used, and this should be significantly smaller than the half-wavelength of the highest frequency. This however would impose a very impractical constraint on the physical size of the detectors, forcing even larger footprints perpendicular to the filter-bank feedline. Additionally, one could imagine engineering the fixed stop-bands such that the filter-bank is placed between the first and second order modes (providing the filter-bank frequencies span suitably less than an octave). Although, there are residual “ripples” that extend away from the stop-band which can and do impact the filter-bank transmission with a magnitude that is a function of the proximity in frequency space between the filters and the stop-band, as will be shown in Section 3.6.5.

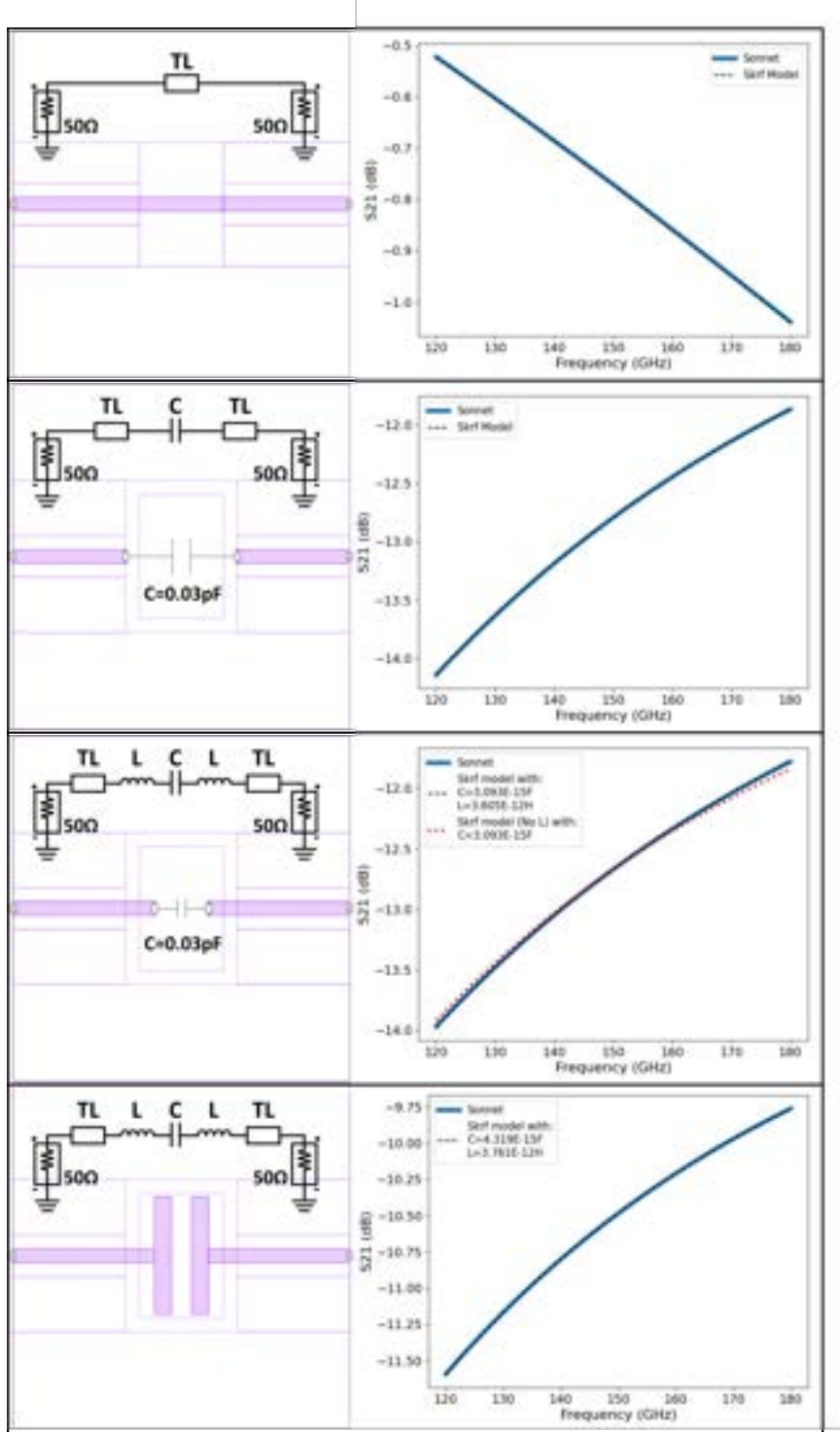


Figure 3.15. Developing the lumped element model for the coupling capacitor. The left hand side of each row shows the Sonnet simulation overlaid with the lumped element circuit model which gave the best agreement with the SKRF model. Then the right hand side shows the simulated S_{21} output by both simulations. In the bottom two rows the values for C and L are fit to in order to find the optimal values. “TL” indicates transmission lines.

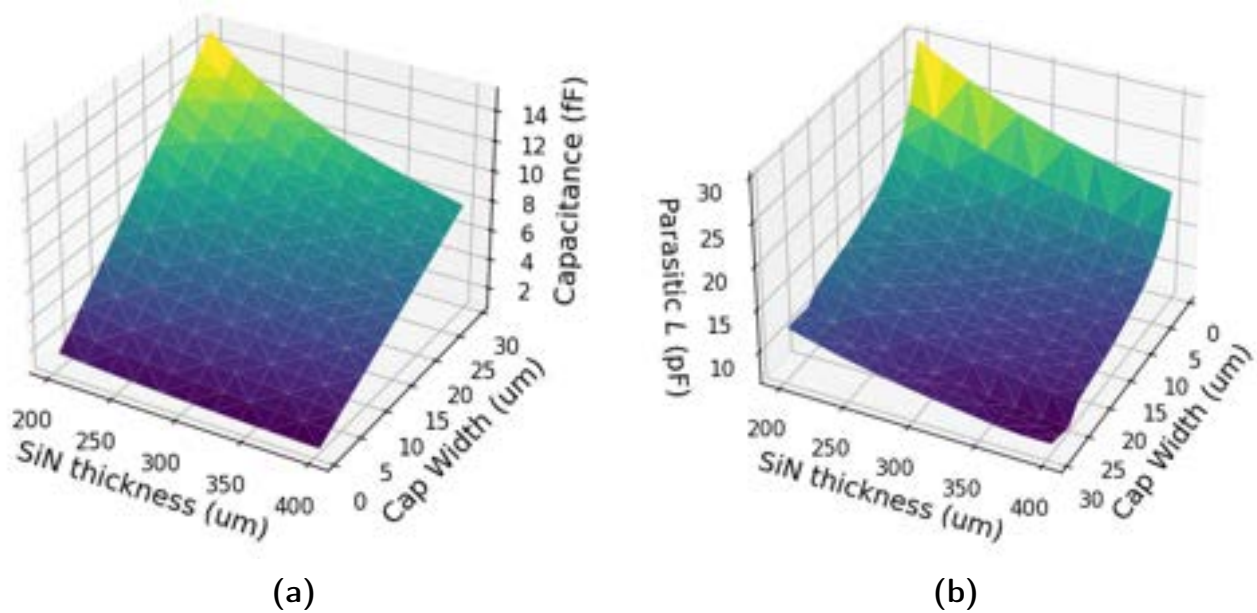


Figure 3.16. Interpolation surfaces used to obtain the capacitance, C and parasitic inductance, L of the coupling capacitor for a range of capacitor widths and SiN thicknesses.

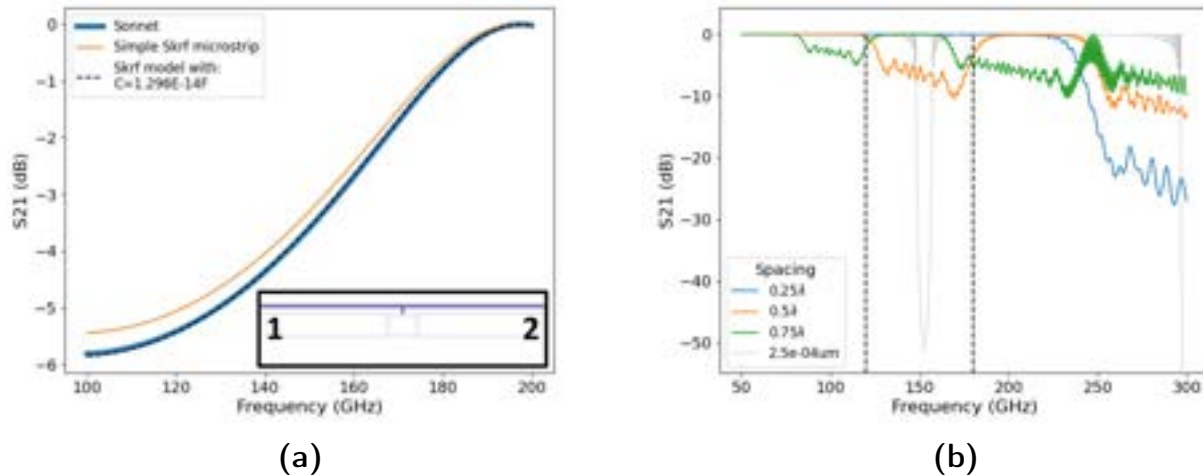


Figure 3.17. (a) A comparison between the Scikit-RF model using just microstrip transmission lines and one with an additional parasitic shunt capacitance to ground and the corresponding Sonnet simulation shown in the inset. The inset shows the Sonnet simulation of a microstrip of length 250 μm which is comparable to the wavelength corresponding to 150 GHz. (b) S₂₁ simulations of a 195 series parasitic stub cascade for different separations.

3.6.4 Filter model

With the components of the filters fully characterised, it is possible to create a filter within the Scikit-RF framework. First a series cascade of the filter components is built (microstrip + input

capacitor + resonator microstrip + output capacitor + output microstrip) then this series network is converted into a three port shunt network allowing input and output feedline microstrips to be connected. The filter geometries (capacitor widths and resonator lengths) can be derived using the interpolation expressions obtained in Section 3.4.1 to achieve the desired resonant frequencies. Filter models with identical physical parameters to Sonnet simulations were compared and demonstrated excellent agreement for both a single filter and a simulation of three filters in series, see Figure 3.18. This suggests that our model captures the electromagnetic environment well and gives confidence in the accuracy of results obtained by adding fabrication uncertainties such as deviations to microstrip linewidths, capacitor widths or dielectric thickness.

Furthermore, the consistency of the resonant frequency placements and desired lossless resonator quality factors is presented in Figure 3.19. The resonant frequencies of the Scikit-RF model do match the target frequency fairly well. However, there does seem to be a slight frequency dependence, where the agreement is best at 150 GHz and deviates more towards the extremes. This is likely an artifact from the fact that the microstrip characteristic impedance and effective relative permittivity is interpolated from a surface of mean values taken across the frequency band, which would thus favour the central frequencies. A similar small but existent frequency dependence can also be seen in the quality factors. Since the effect is very minor and given the agreement with the Sonnet filter simulations, this was not explored further. However it could be possible to improve the microstrip agreement using a 4D interpolation method to also incorporate the frequency dependence of the microstrip parameters.

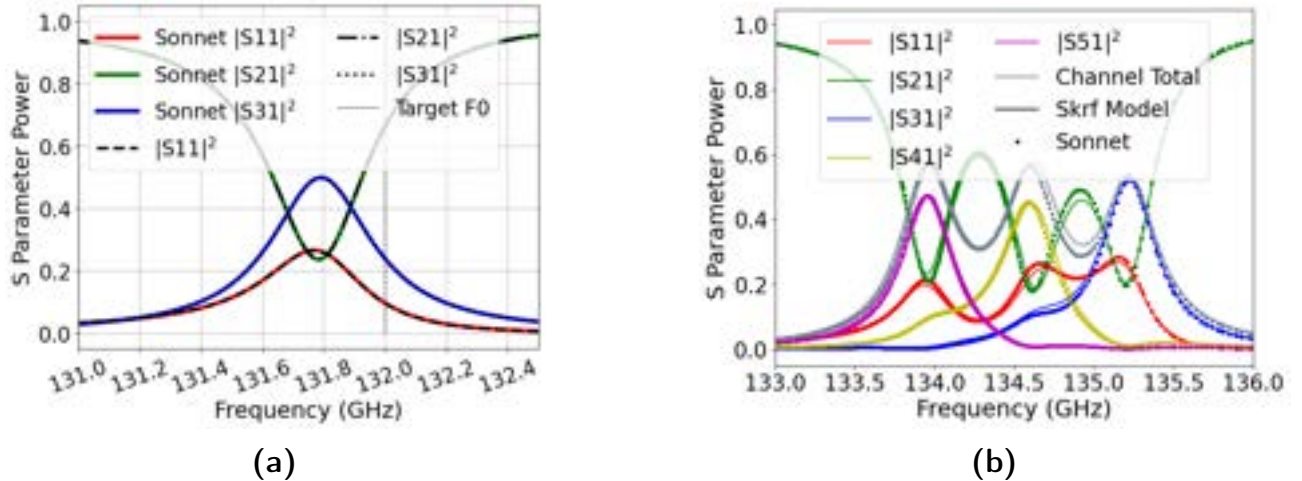


Figure 3.18. (a) Comparison of the S-Parameters simulated by the Scikit-RF Python model to that output by Sonnet for (a) a single $R = 300$ filter with an intended f_0 of 132 GHz and (b) a three $R = 300$ filter filter-bank with $f_0 = 134.0$ GHz, 134.5 GHz, and 135.0 GHz.

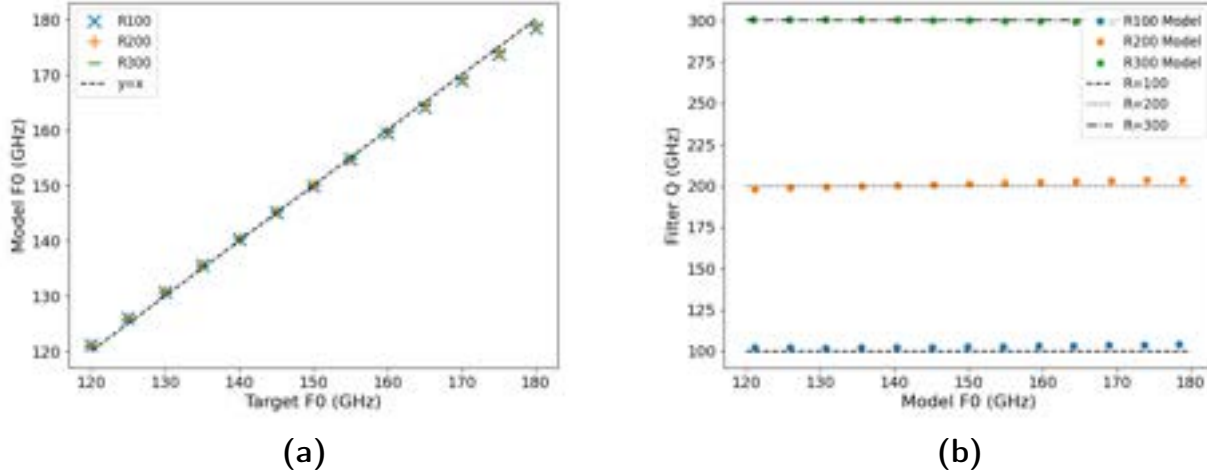


Figure 3.19. Comparison of the (a) resonant frequency and (b) lossless filter quality factor for filters simulated across the operational frequency band to that of the desired values for filters with resolutions of $R = 100, 200$, and 300 .

3.6.5 Filter-bank model and results

The filter-bank is then simulated by cascading all the different filters along the feedline. The filter-bank is in fact simulated multiple times, each time creating a 2-port network, one where the output is the end of the filter-bank and each of the filter-channels is terminated in a matched load and then also N more times for N channels where only the N th channel is the second output port. Each time the forward transmission coefficient is extracted. This means only the S-parameters of interest (from port 1 to the output of each filter, S_{N1} , and also to the end of the filter-bank, after all the filters, S_{21}) are kept, preventing large amounts of data to be stored in memory. This simulation framework allows a 65 channel filter-bank ($\Sigma = 1.6$, $R = 100$) to be simulated in less than 5 minutes (4.6 s per filter), which is roughly the same amount of time a single filter is simulated in Sonnet. This time scales to about 45 minutes for a 195 channel filter-bank ($\Sigma = 1.6$, $R = 300$). Thus, we are able to simulate the entire filter-bank quickly with high accuracy and flexibility on the physical parameters.

One of the main motivations for simulating the FBS with physical parameters as inputs was to include fabrication errors. Therefore, to include the errors in the simulation, each filter is given an etch error which is generated from a normal distribution to mimic a stochastic error between $\pm 0.2 \mu\text{m}$, which is approximately what is observed in our fabrication. This etch error is added to the nominal physical dimensions of all of the filters microstrip linewidths and also the capacitor widths. Additionally, each filter is given an adjustment to the dielectric thickness. The dielectric thickness variations across a wafer is typically a systematic variation due to deposition techniques

and has been seen to vary by approximately 2% from the centre of a 6-inch wafer to the edge. We chose to emulate this by giving the filter at the start of the filter-bank the nominal dielectric thickness (300 nm), and then subsequent filters are given a slight reduction in thickness depending on its physical distance from the first filter (wafer center) with the extremes at the edges (for very long filter-banks) having a 2% reduction in dielectric thickness.

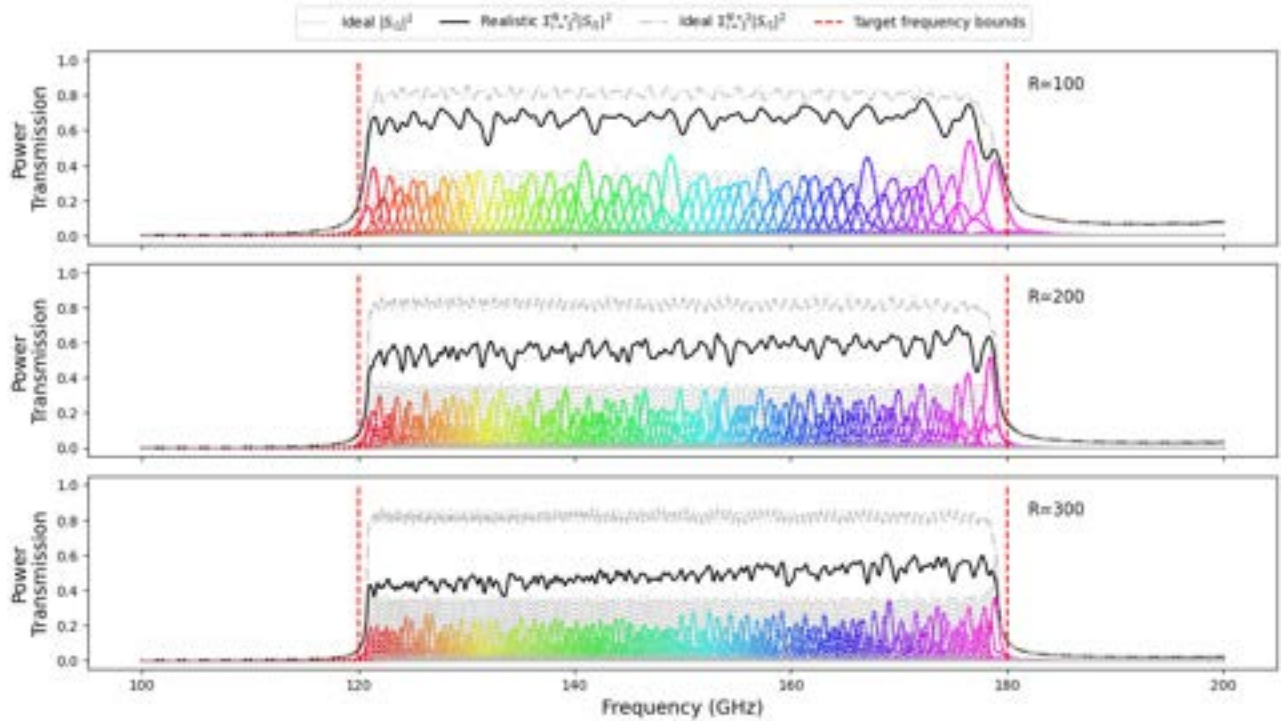


Figure 3.20. Scikit-RF filter-bank simulations for $R = 100, 200, 300$ with $\frac{1}{4}\lambda$ spacing, $\Sigma = 1.6$ oversampling between 120 GHz to 180 GHz, showing the single and total channel power transmission for the ideal and realistic cases. The “Realistic” simulation includes etch and dielectric thickness error as well as a loss tangent of $\tan \delta = 1.0 \times 10^{-3}$. The “Ideal” results do not include either fabrication error or loss tangent.

Figure 3.20 presents six filter-bank simulations for the single and total channel power transmissions, where each of the three panels are for the resolutions indicated. All filter-banks are $\frac{1}{4}\lambda$ wave-spaced with an oversampling of $\Sigma = 1.6$. The difference between the “Ideal” filter-bank (one without fabrication error and loss-tangent) and the “Realistic” filter-bank can be seen in each panel. The realistic filter-banks use a loss tangent of $\tan \delta = 1 \times 10^{-3}$ as this was a reasonable approximate value for our dielectrics according to some preliminary measurements. These simulated results present a few conclusions worth discussing.

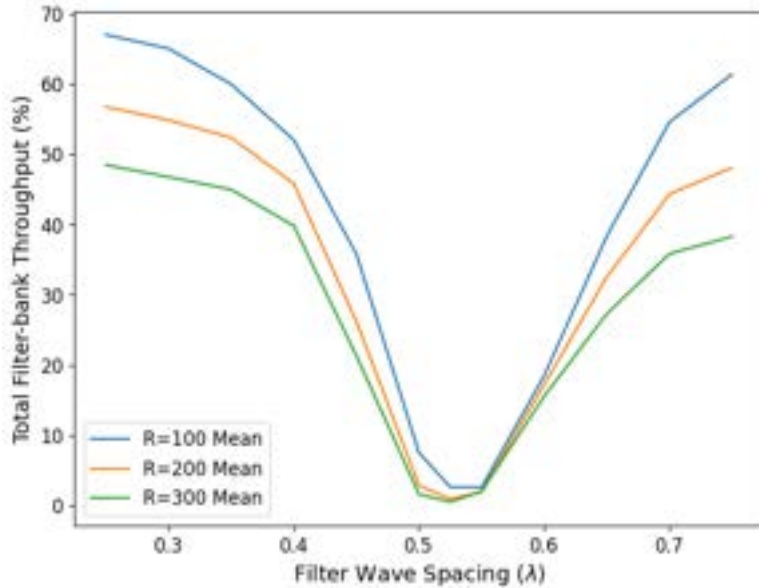
Firstly, viewing each total power transmission as a simple top-hat and comparing the realistic to the ideal we see that power is lost with an increasing percentage as the resolution of the filter-bank becomes larger. This is to be expected and agrees with Equation 3.9 and Figure 3.10b

since the EM wave in higher quality factor filters can be considered to pass along the length of the resonator more times during resonance, which is analogous to passing along a larger length of lossy transmission line. Furthermore, the higher resolution filter-banks consist of more filter channels which thus increases the total length of the FBS. This means the waves with frequencies that are filtered towards the end of the FBS must travel further along the lossy feedline and therefore the detectors placed here would receive less power than those at the start of the filter-bank. Note, we assume a frequency invariant loss tangent across the optical band. This is the motivation for placing the highest frequency filter first since this experiences the most loss per unit length. Despite this, whilst the dielectric loss tangent is not negligible, higher resolution and longer filter-banks will always exhibit a non-uniform and sloped efficiency across the band as is most obvious for the $R = 300$ simulation. The total efficiencies shown here have approximate mean values of $\eta_{\text{FBS}} = 68\%$, 57% , and 49% for $R = 100$, 200 , and 300 respectively, relative to the 80% ideal total efficiency which absent of loss is entirely determined by the oversampling factor.

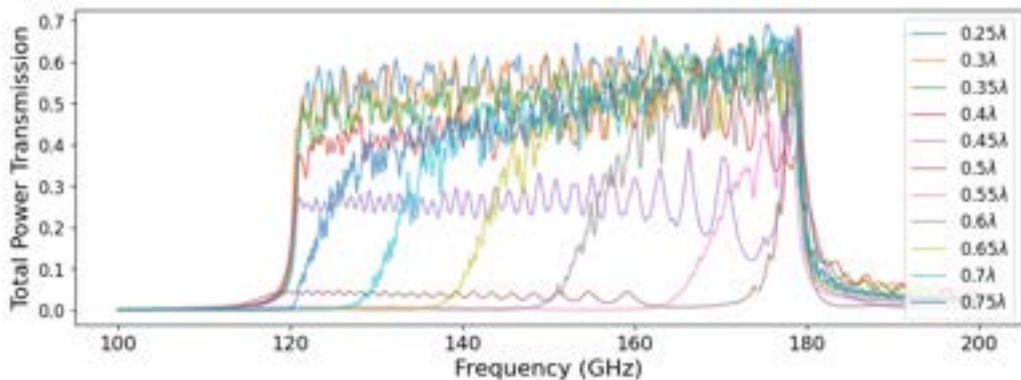
Another aspect worth noting is the level of the peak height for the single channel power transmission. Firstly, since the channels overlap in frequency (as designed) due to the oversampling, even in the ideal case each spectral channel does not receive the maximal 50% at resonance. This peak throughput is further reduced by the dielectric loss, and therefore one could foresee a situation where the individual channel throughput to a detector becomes small enough that the signal is within the noise, and thus the filter-bank would appear to not detect anything. However, it has been shown that with noise limited MKID detectors, an FBS is capable of detecting light with a total system efficiency of less than 6% , thus this is an unlikely issue but still a situation worth considering.

Later in Section 4.2, the motivation for easing the microwave detector multiplexing requirements is presented. This concludes that multiplexing becomes easier and/or possible if the detectors (filters) are spaced further apart. To find a suitable compromise that maximises the FBS performance, which can be observed with the total FBS power transmission, whilst also providing the necessary reduction in detector cross-coupling to make detector multiplexing possible. Thus, characterising the total throughput as a function of filter spacing becomes necessary, and the results are shown in Figure 3.21. For each filter-bank simulation the mean value of the total channel throughput is taken between 130 GHz to 170 GHz , this mean value is then plotted as a function of the filter spacing. As is apparent in both of these figures, there is a significant reduction in the FBS efficiency around the region of destructive interference at half wave-spacing. Furthermore, the uniformity or top-hat-likeness becomes worse around the destructive condition and is also an issue at the longer spacings between $\frac{1}{2}\lambda - \frac{3}{4}\lambda$. Interestingly, Figure 3.21b shows how the stop-band (which was first shown in Figure 3.17b) enters and passes through the operational band as the filter spacing

increases. The proximity of the stop-band also brings with it the “ripple” effect that manifests itself within the spectra. These results demonstrate why keeping the filter spacing small relative to half a wavelength is important for the filter-bank performance, but also that the FBS efficiency does not drop off too drastically until about $\frac{2}{5}\lambda$ spacing nor is the profile of the total throughput particularly non-uniform.



(a)



(b)

Figure 3.21. (a) Approximate mean total in-band FBS efficiency as a function of filter spacing for $R = 100, 200, 300$. (b) Total FBS throughput spectra for a variety of filter spacings with a resolution of $R = 200$ and oversampling $\Sigma = 1.6$.

Section 4.4.2 provides a detailed account of the design variations that were considered at the stage where it was necessary to commit to certain design choices. The outcome was to initially go with a $R = 200, \frac{3}{8}\lambda$ spaced FBS using an oversampling of $\Sigma = 1.6$. For further details on the motivation, see the aforementioned section. However, Figure 3.22 presents simulated performance of the chosen filter-bank for a small range of possible loss tangents. These results

further demonstrate the importance of low-loss dielectrics. The FBS efficiency is a reasonable 50 % for a loss of 1.0×10^{-3} , however this quickly drops off by a rate that is best observed in Figure 3.10b.

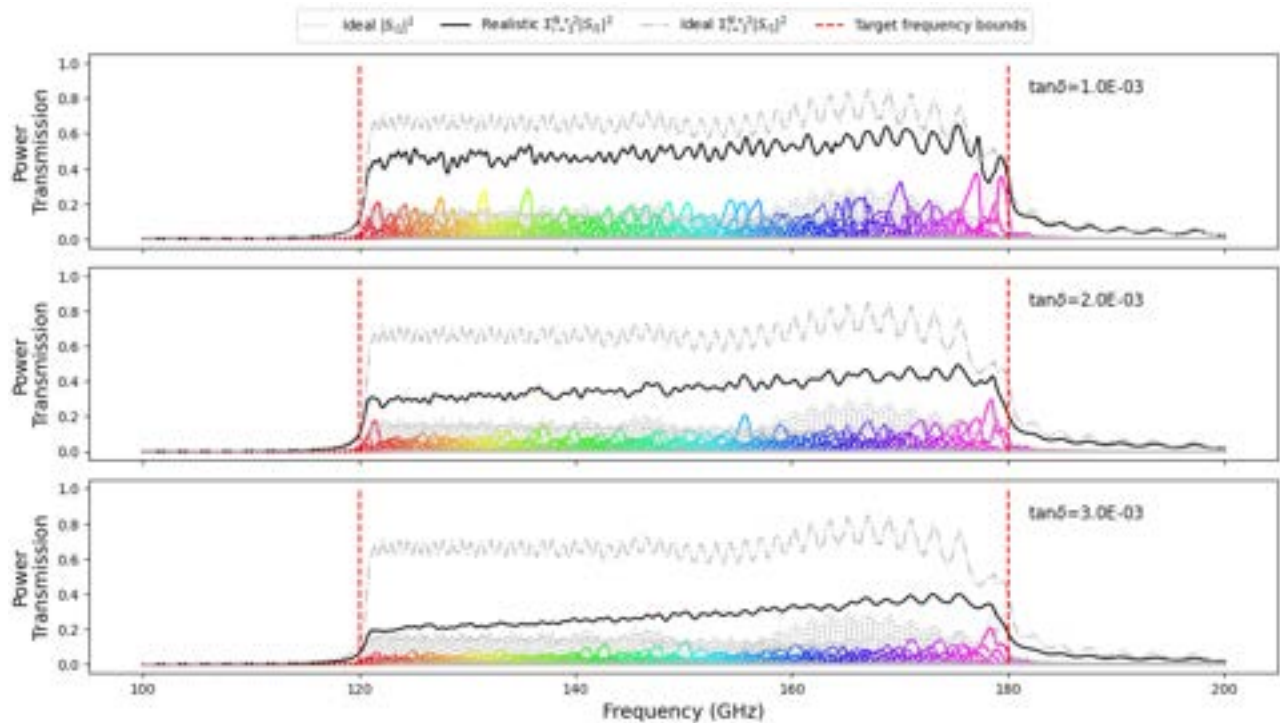


Figure 3.22. Scikit-RF filter-bank simulations for the single and total channel power transmissions of filter-banks with $R = 200$, $\frac{3}{8}\lambda$ spacing, $\Sigma = 1.6$ oversampling between 120 GHz to 180 GHz for different loss tangents, $\tan \delta = 1.0 \times 10^{-3}$, 2.0×10^{-3} , and 3.0×10^{-3}

3.7 Millimetre perspective conclusion

This section presented the details of the millimetre circuit, showing how the polarisations of a signal from the telescope incident to the horn array couple to an OMT antenna, then a 180° hybrid is used to reject all TEM modes except the dominant TE_{11} mode, which then propagates to the filter-back via a $2.5\ \mu\text{m}$ wide microstrip where finally the signal is split into N spectral channels via capacitively coupled $\lambda/2$ resonators before terminating in the inductive section of an lumped element MKID.

The design and principles for the filter-bank and $\lambda/2$ filters were then presented leading to the characterisation of the filters. We presented an effective interpolation method used to tune a filter within the observing band to any spectral frequency and resolution by controlling the resonator lengths and coupling quality factors via the capacitors. Following this, the impact of dielectric

loss tangent on a single filter efficiency was discussed, demonstrating the criticality of low loss dielectrics ($< 1 \times 10^{-4}$) if on-chip filter-bank spectrometers are to reach high resolutions ($R > 1000$) as is desired for high-redshift mm-wave LIM and other millimetre astronomy applications.

With the aid of Sonnet simulations and a custom built Python model allowing fast simulations of filters with varying filter properties and geometries, the filter quality factor and resonant frequency tolerance of the filter geometry to variations in aspects of the design were quantified and shown to be suitable. It was discovered that the resonant frequency was most sensitive to changes in the kinetic inductance at 3.5 % for $\pm 0.02 \text{ pH} \square^{-1}$. The quality factor (resolution) of the filter was less tolerant. Results suggested that fabricating the correct dimensions on the resonator geometry was the main area of concern, particularly, the microstrip linewidth presenting a $\approx 10\%$ change for $\pm 0.2 \mu\text{m}$, but also additional changes around $\approx 2\%$ for analogs of changes in the capacitance of the coupling capacitors: dielectric thickness ($\pm 10 \text{ nm}$), and input and output capacitor dimensions ($\pm 0.2 \mu\text{m}$).

The final part of this section then presented the process used to build the Python simulation model for the filter-banks, demonstrating good component agreement with equivalent Sonnet simulations. With the tool, it was found that a small microstrip stub-like section of the filter geometry added an off-resonance parasitic capacitance to ground. For the single filter this had a negligible impact, however when multiple stubs are placed along the feedline (one for each filter) a stop-band would generate due to interference at frequencies corresponding to the half-wavelength of the physical spacing between filters. Thus, one must ensure filters are spaced suitably apart to ensure the stop-band is far enough away in frequency to have minimal impact on the filter-bank in-band spectrum. This lead to understanding the parameter space of the total filter-bank throughput as a function of filter spacing, showing that for lossy dielectrics, more spectrally uniform and efficient throughputs were obtained with filter spacing below 0.4λ with increasingly better performance towards $\lambda/4$ spacing as the stop-band is further away in frequency, reducing a ripple effect which can extend tens of GHz from the main stop-band feature. A comparison between realistic filter-banks with nominal design parameters ($\tan \delta = 1.0 \times 10^{-3}$, $\Sigma = 1.6$, $\frac{1}{4}\lambda$ filter spacing) was also presented. This nicely demonstrated the trade-off of spectrometer resolution and filter-bank efficiency for an FBS on a lossy medium with an additional impact at higher resolutions of non-uniformity in the spectrum as the frequencies with channels further down the filter-bank experience more dielectric loss. The importance of low loss dielectrics was further illustrated with a comparison of identical simulated filter-bank with varying degrees of dielectric loss, which showed that by $\tan \delta = 3 \times 10^{-3}$ the single filter-efficiency is less than 5 %. The utility of this filter-bank simulation tool is further demonstrated in subsequent sections, both for aiding in instrument design choices in Section 4.4.2 and attempting to understand measured results in Section 7.3.

Chapter 4

The Microwave Perspective

The microwave aspect of the device is focused on the device readout circuit. This section will therefore cover the Lumped Element Kinetic Inductance Detector (LEKID) design considerations including details and discussions of the comparative benefits of two capacitor geometries, the Inter-Digital Capacitor (IDC) and the Parallel Plate Capacitor (PPC). Whilst the IDC design (Section 4.1) was the nominal architecture from the start of the project, the PPC resonator was also explored as it could provide significant benefits as will become apparent in Section 4.3. Following the details of the IDC design, study of the cross-coupling between resonators is presented in Section 4.2, the results from which were very formative for the multiplexing strategy (detailed in Section 4.4) and ultimately the interplay between the mm-wave and microwave circuits leading to the focal plane variations that were considered as discussed in Section 4.4.2.

4.1 LEKID design

The following sections describe the details and motivation for the design choices that lead to the IDC LEKID architecture presented in Figure 4.1.

4.1.1 Design constraints

For the reasons outline in Section 1.1, MKIDs are an extremely convenient technology to combine with on-chip filter-banks. Furthermore, one of the key advantages to the lumped element design for an MKID rather than the distributed version is the ability to separate the control of the detector characteristics between the inductor geometry and the capacitor geometry⁹³. The

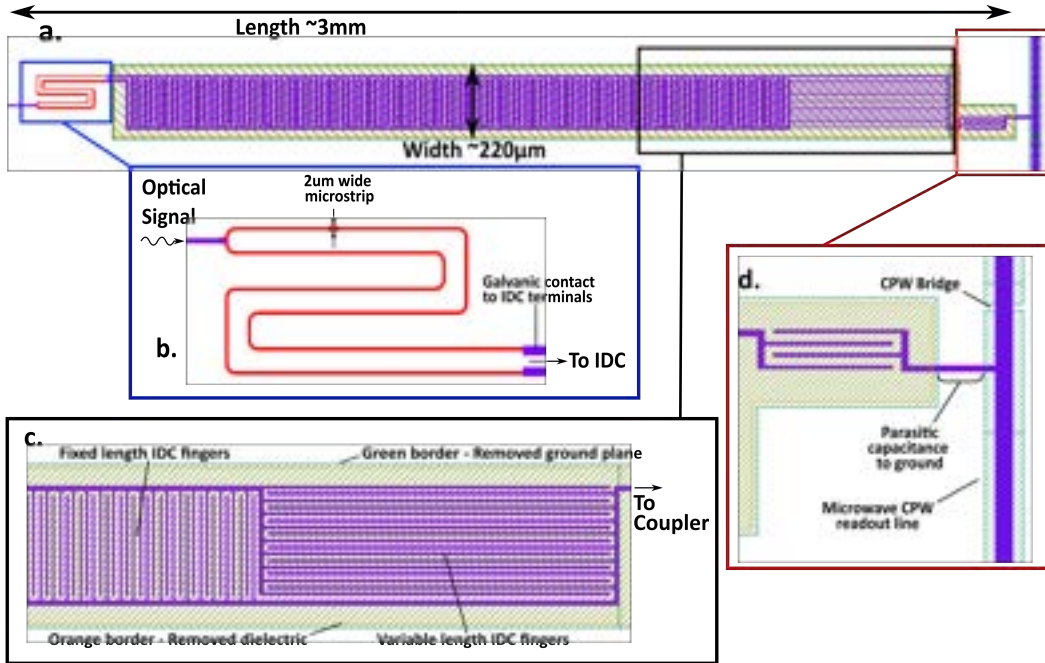


Figure 4.1. 2D mask design of the IDC microstrip-coupled LEKID showing *a.* the full LEKID and zoomed in portions of *b.* the inductor, *c.* the capacitor region and *d.* the coupling capacitor.

inductor geometry can be focused on the photon absorbing mechanics, the capacitor can be focused on the f_0 placement and the coupling geometry provides the control of the quality factor.

Before describing the details of the LEKIDs, it is necessary to highlight some of the design constraints imposed on the detector design. There were a number of factors that needed to be considered when designing the LEKIDs. Firstly, whilst the science case always pushes for higher spectral resolutions (up to the intrinsic resolution of the spectral line on the order of $R \approx 1 \times 10^3$) for LIM), the initial target spectral resolution was designed for a moderate $R = 300$ as this was expected to be achievable with suitable efficiencies considering the anticipated dielectric loss as well as recognising the trade-off between sensitivity and the fact that SPT-SLIM was intended as a technological pathfinder. Secondly, the size of the cryostat and optics, constrained by the space in the receiver cabin, and expected thermal loading limited the number of readout channels to 9 pairs of coaxial lines as well as 18 dual polarisation pixels. Finally, the RF-ICE readout system would have an approximate readout bandwidth of 500 MHz⁹⁴ per readout channel. Hence, the nominal focal plane was designed to consist of 36 filter-banks (one per polarisation) split across the 9 readout channels (four filter-banks per channel). For filter-banks with $R = 300$ and an oversampling of $\Sigma = 1.6$, resulting in ≈ 200 detectors per FBS led to a limited frequency spacing between $Q_c = 5 \times 10^4$ detectors of 500 kHz.

Furthermore, the physical space available inside the cryostat limited the size the focal plane

could occupy. Opting for a modular design, whereby the focal plane would be split into three sub-modules (see Figure 2.2) each fabricated on six-inch wafers meant that certain configurations were not possible. In certain cases it was technically possible from a footprint point of view to use up to $\frac{3}{4}\lambda$ spacing of the mm-wave filters in the filter-bank. However, this was not as desirable as closer spacing due to the impact on filter-bank efficiencies discussed in Section 3.6. Thus a detector design that is compatible with $\frac{1}{4}\lambda$ spacing was necessary. Therefore, to push the LEKID resonant frequencies, f_0 , below 3.0 GHz (another readout limitation), naturally, a tall and narrow geometry was adopted, where the dimension parallel to the filter-bank feedline needed to be $\approx 250\mu\text{m}$ for the smallest $\frac{1}{4}\lambda$ spacing (highest frequency).

4.1.2 Microstrip-coupled inductor

The inductor design is based on enabling a means of coupling radiation from the microstrip feedline from the antenna directly to the detector. A schematic of this coupling is presented in Figure 4.2. The output of each mm-wave filter feeds the detector at the voltage null of the LEKID inductor such that any photons that reach the inductor will be absorbed by the superconducting material via the breaking of Cooper pairs. As with any MKID⁴, the breaking of Cooper pairs will change the surface impedance of the superconductor by altering the total inductance of the resonator. This is measurable as a change in resonator f_0 , or quality factor, Q_r . The inductor material was chosen so that the material would remain a high-Q superconductor at the resonant frequency of the detector (requiring the operating temperature to be an insignificant fraction of the critical temperature, $T \ll T_c$) whilst also having a small enough superconducting energy gap to allow pair breaking within the observing band of SPT-SLIM (120 GHz to 180 GHz). Thin film aluminium with a cut-off frequency of approximately 100 GHz and a typical $T_c = 1.3\text{ K}$ was the natural choice.

LEKIDs typically used for direct imaging work by coupling incident light directly to the inductor^{77,95}. This requires that the impedance is high to match the impedance of free space in order to be an efficient free space absorber. This motivates the use of materials with a high normal state sheet resistivity, which can be increased by reducing the thickness of the metal film. Some examples of high resistivity superconductors that have been explored for use in MKIDs are titanium nitride⁹⁶, platinum silicide⁹⁷, hafnium⁹⁸ and β -phase tantalum⁹⁹. As the sheet resistance increases as thickness decreases, these materials also have the added advantage of increasing the responsivity of the detector by reducing the volume and therefore increasing the kinetic inductance fraction, α_k , since the inductance per square is then increased for a fixed inductor geometry. However, in the case of the microstrip-coupled LEKID, a trade-off presents itself between increasing the surface resistivity to improve α_k , and maximising the transmission efficiency from the mm-wave

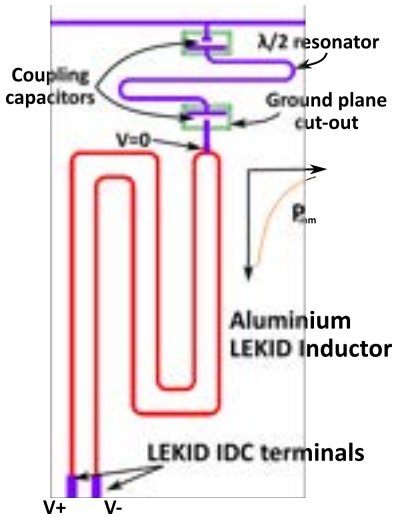


Figure 4.2. Schematic Showing how a single mm-wave resonator is terminated into the voltage node of a LEKID inductor. The inset plot shows an approximate power dissipation down the length of the absorbing aluminium inductor.

feedline into the inductor. Here, since the geometry at the signal input is equivalent to a T-junction, the optimal power transfer occurs when the impedance of the niobium microstrip matches the aluminium microstrip impedance such that $Z_{0,Nb} = Z_{0,Al}/2$. The right hand plots of Figure 4.3 show the simulated characteristic impedance of the combined aluminium and niobium microstrip lines over a range of linewidths as well as different aluminium sheet resistances. These show that for a given aluminium linewidth, it is possible to match the real component of the impedance by selecting the necessary niobium microstrip width. However, it is not possible to match the imaginary component of the lossy transmission line and thus there is a limit to the impedance match that can be achieved otherwise known as the Bode-Fano limit^{100,101}. In fact, the impedance match becomes increasingly worse with increased Al sheet resistance. The impact this has on the amount of signal reflected at the inductor is presented in the left hand plot of Figure 4.3. For a given sheet impedance, there is a minimum limit to the amount of reflected signal. This limit reduces as the the aluminium sheet resistance tends to that of the almost lossless niobium. A width of $2.0\ \mu\text{m}$ was chosen for the aluminium inductor as this provides the smallest inductor volume to reach the required sensitivities whilst remaining a reasonably achievable linewidth for direct imaging lithography. Therefore, a $2.0\ \mu\text{m}$ aluminium inductor can have a 96 % input efficiency across the optical bandwidth with a $3.0\ \mu\text{m}$ niobium input width and a sheet resistance of $0.6\ \Omega\ \square^{-1}$. It is worth noting that there are existing and well studied coupling architectures such as that employed by Superspec⁴⁸ that allow the use of high resistivity materials, as well as consistent power coupling between mm-wave filter and detector along the length of the LEKID inductor.

The geometry (surface area and thickness) is one of the most crucial parameters of the LEKID

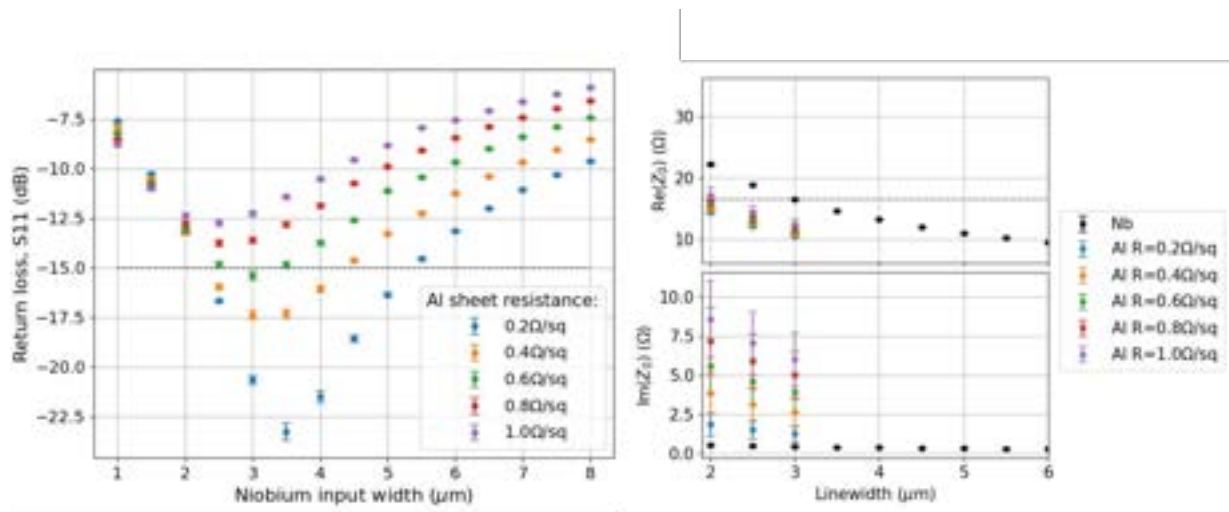


Figure 4.3. (Left) Simulated input reflections at the boundary between the niobium input line and the aluminium inductor for a 2.0 μm wide aluminium microstrip on 500 nm of SiN of varying sheet resistances. The black dotted line indicates the self-imposed minimum insertion loss constraint at -15 dB (96 % throughput). (Right) The real and imaginary components of the characteristic impedance of the niobium microstrip and the combined ($Z_{0,\text{Al}}/2$) aluminium microstrip at various linewidths. The black dotted line on the real impedance plot indicates the niobium width providing a suitable best real impedance match for a 2.0 μm Al microstrip which approximately corresponds to an $S_{11} = -15 \text{ dB}$ for a Al sheet resistance of $0.6 \Omega \square^{-1}$. Note the niobium has a slight reactance due to the loss tangent.

detector as it sets the overall sensitivity via the inductor volume and the impedance matching with the surface impedance via the film thickness as discussed above. As shown throughout the literature^{18,64,76,85,102}, the MKID sensitivity through quasiparticle recombination boils down to three key properties as defined by the figure of merit presented in Leduc, 2010⁹⁶. The first two being the number of quasiparticles, (N_{qp}) in the detecting volume and the time for the quasiparticles to recombine (quasiparticle lifetime, τ_{qp}) such that the noise equivalent power due to generation-recombination is proportional to the ratio $\text{NEP}_{\text{GR}} \propto \sqrt{N_{\text{qp}}/\tau_{\text{qp}}}$. Hence, a long quasiparticle lifetime in a small volume would result in a more sensitive detector. The third parameter is the ratio of kinetic inductance, L_k , to the total resonator inductance, commonly called the kinetic inductance fraction, α_k and given by

$$\alpha_k = \frac{L_k}{L_k + L_G}, \quad (4.1)$$

where L_G is the geometric inductance of the resonator. The significance and a thorough study of the kinetic inductance fraction can be found in Gao 2008⁸⁵. To summarise, since the resonator frequency depends on the inductance and capacitance (see Equation 4.3), a perturbation in L_k due to a Cooper pair separation will result in a larger frequency response for a larger α_k .

Therefore, a larger α_k can be achieved with a smaller geometric inductance, which further lends itself towards having a small inductor volume. However, it's worth noting that too much responsivity can cause difficulties with the on-sky readout technique used for MKIDs as the resonant frequency can move so far off of a probe tone through the variable optical load from the sky due to changes in atmospheric attenuation. This is not necessarily the case for SPT-SLIM however, as for mapping large areas of the sky, the most effective scanning method can be one that maintains the same elevation and hence a constant/similar atmospheric transmission, limiting the frequency of re-tuning.

An optical load of $P_{\text{opt}} \approx 25 \text{ fW}$ is expected for an $R = 300$ spectral channel under typical atmospheric conditions at the South Pole¹⁰². We can then compute the approximate photon noise equivalent power for an $\nu = 150 \text{ GHz}$ photon with^{85,102},

$$\text{NEP}_\gamma = 2\eta_{\text{opt}} P_{\text{opt}} \nu (1 + \eta_{\text{opt}} \bar{n}_{\text{ph}}), \quad (4.2)$$

where η_{opt} is the optical efficiency (amount of the incident power absorbed) and \bar{n}_{ph} is the mean photon occupation number at a source temperature, T , as per $\bar{n}_{\text{ph}} = (e^{hf/k_B T} - 1)^{-1}$. Taking the optical efficiency as 1 and a with a sky brightness temperature of $\approx 10 \text{ K}$, then the photon noise is calculated as $\text{NEP}_\gamma = 3.11 \times 10^{-18} \text{ W}/\sqrt{\text{Hz}}$. Given this value, and assuming a fixed two-level system noise power spectral density of $S_{xx} \approx 1 \times 10^{-18}$ as was representative of the current devices at the beginning of the project¹⁰³, the inductor volume was predicted to result in a photon noise limited detector if it was in the range of $20 \mu\text{m}^3$ to $70 \mu\text{m}^3$ ¹⁰⁴; this is shown in Figure 4.4¹⁰⁴. This was estimated by calculating an effective quasiparticle temperature and total quasiparticle density when considering various pair-breaking mechanisms. Further details are presented in Barry et. al.¹⁰⁴. In actuality, the inductor volumes used in the devices presented later in this thesis used a detector volume of $135 \mu\text{m}^3$ for two reasons, recognising that the inductor linewidth is already constrained by the impedance matching mentioned above. Firstly, the aluminium film was required to be thicker than desired to mitigate risks with fabrication (see Chapter 5). Secondly, the inductor length was chosen as a compromise to increase the geometric inductance sufficiently to prevent the detector capacitors becoming too large in order to bring the detector resonant frequencies around 2 GHz for the readout system. As such, this would bring the detector into a regime of more significant TLS noise, yet it was hoped that by implementing the stepped down capacitor design that the TLS noise would be reduced with our detectors.

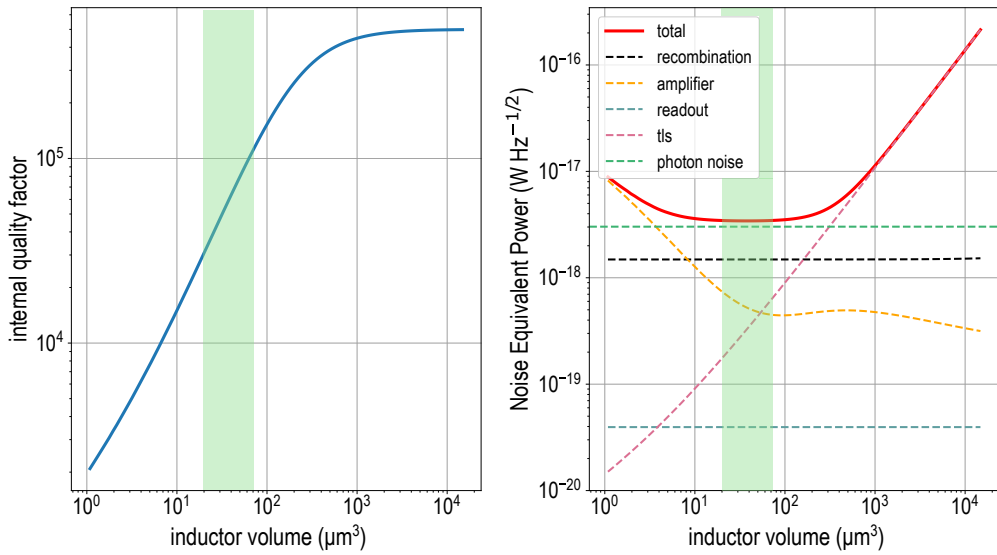


Figure 4.4. Predicted performance of a microstrip-coupled LEKID showing the estimated internal loss quality factor Q_i (Left) and the various contributing noise equivalent powers (right) as a function of inductor volume¹⁰⁴.

4.1.3 Inter-digital capacitor design

The original baseline for the capacitor was to use an inter-digital capacitor (IDC) geometry as it was expected that this design would provide better noise performance than a parallel plate.

To reduce the susceptibility to two-level system noise (TLS) from the dielectric and limit a reduction of responsivity whilst allowing for a microstrip transmission line coupling, the IDC regions of the detector should not be covered by dielectric materials. It has been demonstrated that the average noise power level for a detector with its IDC structure having bulk silicon substrate on one side and then exposed to air/vacuum on the other can be 25 times lower than if the IDC were covered by dielectric⁹³. Therefore, the dielectric layers are removed from the area indicated by the orange border in Figure 4.1, as is the ground plane (green border). This can also be seen in the material stack diagram shown in Figure 2.4a. This added an extra level of complexity to the fabrication as it requires the device niobium layer deposition to be compatible with a series of step-downs over the dielectrics. This is covered in greater detail in Chapter 5. Additionally, it has been reported that there is lower TLS noise levels for niobium grown on silicon compared to aluminium¹⁸, which, along with the fact that using a lower kinetic inductance material in the capacitor will improve the kinetic inductance fraction and responsivity of the detector is why niobium is used for the capacitor.

A somewhat unique aspect of this detector design is that the IDC has two sections to it. The majority of the capacitor area is made of fixed length fingers oriented parallel to the width of

the detector. Then towards the microwave side the orientation of the IDC fingers rotates 90 degrees to now be parallel to the length of the detector. The physical space restrictions along the length of the mm-feedline of the filter-bank set by the filter spacing, dx , meant the gradient of the change in f_0 to change in IDC width would be $\approx 2 \text{ MHz } \mu\text{m}^{-1}$ (≈ 45 linewidths per μm). This was not suitable with a lithography resolution of $1 \mu\text{m}$ and a target 500 kHz resonator spacing (≈ 10 linewidths). Therefore, a detector design that required variable IDC fingers along it's width was not ideal, see the horizontal design in Figure 4.5. Another option was to use IDC fingers parallel to the length of the detector, see the vertical design in Figure 4.5. This allowed the varying dimension to be limited by the amount of space on the focal plane, whereby an approximate length limit of 4.5 mm was given to fit twelve spectrometers on to the focal plane sub-module fabricated on a 6 inch wafer. This design required IDC finger lengths to be around 3.0 mm long, as such there was concern this would introduce some extra geometric inductance and would reduce the responsivity by diluting the total inductance. Values for α_k were obtained by simulating the detectors in Sonnet, once with the inductor metal with zero kinetic inductance, and a second time with $L_k = 0.6 \Omega \square^{-1}$. The resonant frequency of a LEKID is given by⁶⁴

$$f_0 = \frac{1}{2\pi\sqrt{(L_k + L_G)C}}, \quad (4.3)$$

where C is the geometric capacitance of the detector. Thus, one can extract an estimate for the geometric inductance of a design by equating the geometric capacitance between identical detectors with and without kinetic inductance in the inductor, resulting in

$$L_G = \frac{L_k f_{0,\text{kinetic}}^2}{f_{0,\text{geometric}}^2 - f_{0,\text{kinetic}}^2}, \quad (4.4)$$

where $f_{0,\text{kinetic}}$ and $f_{0,\text{geometric}}$ are the resonant frequencies of the detector with kinetic inductance in the inductor and without, respectively.

For the designs presented in Figure 4.5, the ortho-IDC design provided a compromise by allowing the variable length dimension to be orthogonal to the mm-wave feedline whilst also reducing the undesired geometric inductance within the capacitor which is particularly present in the vertical design due to the long IDC fingers and demonstrated by the lighter blue colour. The kinetic inductance fraction was 0.104, 0.122 and 0.117 for the horizontal, vertical and ortho-IDC designs respectively. Even though the ratios are improved for the horizontal and ortho-IDC designs, these results highlight an unavoidable issue that IDC LEKIDs for mm-wave filter-banks at this readout frequency have a significant geometric inductance which will limit the responsivity of the detector. Additionally, the coupler fingers were oriented as shown (perpendicular to the readout line) in order to minimise parasitic inductive coupling.

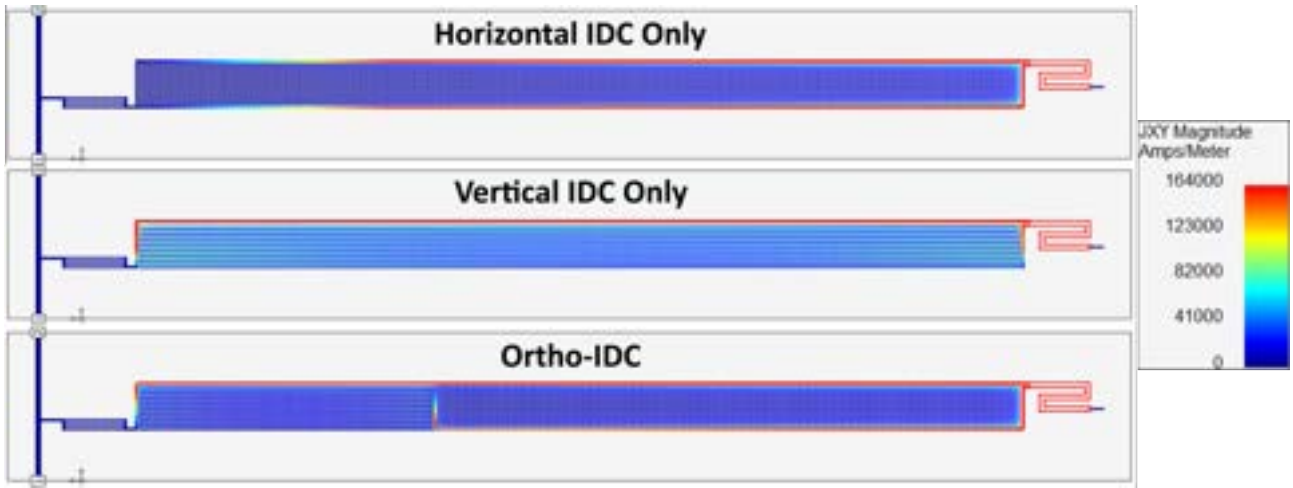


Figure 4.5. On resonance current density plots of Sonnet simulations of LEKIDs with three different capacitor geometries. Red represents areas of high current density. The horizontal model resulted in $\alpha_k = 0.122$, vertical $\alpha_k = 0.104$, and the ortho-IDC $\alpha_k = 0.117$. All resonators had the same $2\text{ }\mu\text{m}$ wide inductor geometry and 3.0 mm wide IDC fingers separated by 6.0 mm .

4.2 Detector Cross-coupling

To design a densely packed, large format array of MKIDs one must be aware of electro-magnetic microwave cross-coupling between detectors. This mechanism is distinct from carrier tone cross-talk due to overlapping resonances for the microwave readout. Electro-magnetic cross-coupling is where a change in the resonance of one detector can impact the resonance of a neighbouring one. Clearly, this causes detection confusion as absorbing a photon in one detector can simultaneously present itself as a detection in another. This effect has been well modelled as an electromagnetic coupling between the resonant circuit of one detector to another either by a coupling capacitance and/or inductance¹⁰⁵. The inset of Figure 4.6a shows a schematic of this model with a coupling capacitance.

Previous studies have also successfully demonstrated that the cross-coupling can be characterised and reduced by altering the geometry and layout of the detectors^{105,106}. Noroozian et. al.¹⁰⁵ use a parameter dubbed the splitting frequency (df_{split}) as the metric for the degree of detector cross-coupling. This is effectively the closest separation in frequency that the two detectors in the given geometry can be placed, or furthermore, the frequency spacing at which the two resonators become an entirely coupled system. A very small df_{split} implies little cross-coupling whereas a large df_{split} is found in highly coupled systems. As demonstrated in Figure 4.6, df_{split} is ≈ 10 resonator linewidths for two capacitively cross-coupled resonators with a capacitance close to that of a coupling capacitor and this will then tend to the un-coupled state with a $df_{\text{split}} = 0$ when the cross-capacitance is zero (in practice the readout then becomes limited by the overlapping

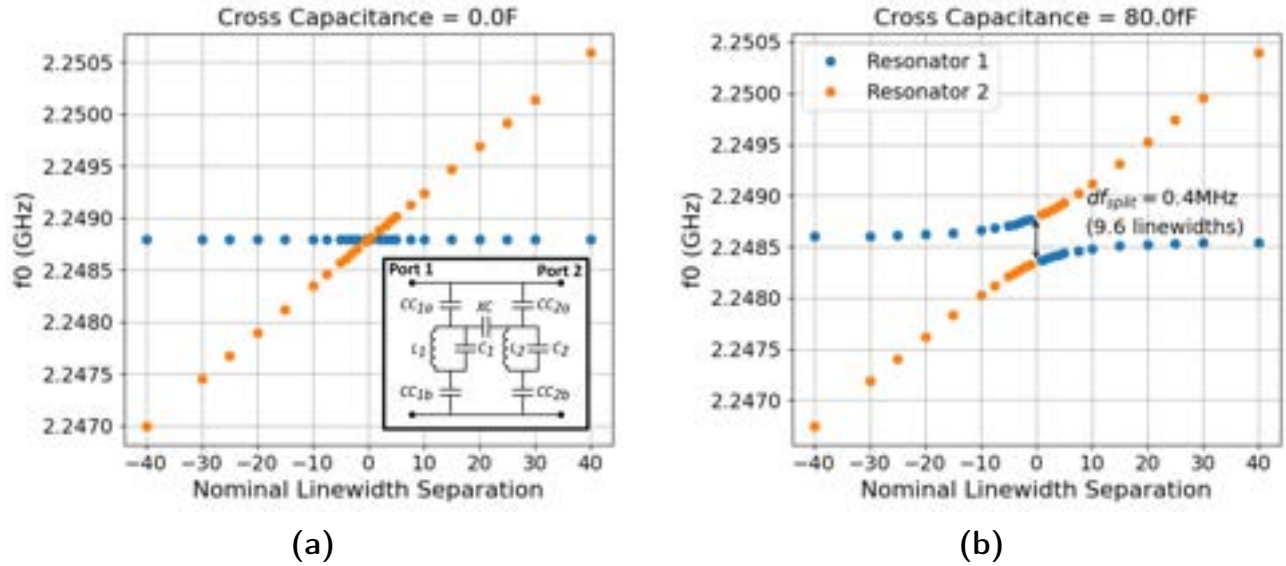


Figure 4.6. Simple Scikit-RF simulations of the inset circuit diagram for a capacitively cross-coupled two-resonator circuit. Here, L_N and C_N denotes the inductance and capacitance of resonator N (controlling f_0) whilst the quality factor ($Q_r = Q_c \approx 5 \times 10^4$ for these simulations) of the resonator is controlled by the combination of the CC_{Na} and CC_{Nb} coupling capacitors. In these simulations the The degree of cross coupling is then set by the capacitance of the cross-coupling capacitor XC . (a) Simulated resonant frequencies for the resonators in a capacitively cross-coupled circuit as a function of the f_0 separation in a single resonator circuit. Here, the cross-coupling capacitor XC is set to zero to represent the non-coupled state and $CC_{Na} = 0.116 \text{ pF}$, $CC_{Nb} = 0.1 \text{ pF}$, $C_1 = 50.0 \text{ pF}$, $L_1 = L_2 = 0.1 \text{ nH}$, C_2 is then varied to sweep the second resonator past the first resonator in frequency space. (b) Same as the left simulation except the cross-coupled capacitor is set to $XC = 80.0 \text{ fF}$.

Lorentzian lineshapes of the two resonators. Thus, this is a useful metric if comparing designs or trying to identify the mechanisms of the coupling between two detectors. This is demonstrated in Section 4.3. However, we found that the geometry of our detectors were in many ways already constrained due to the implications of the filter-bank and readout frequencies. Thus, we needed to explore how much our detectors would cross-couple with a metric that was related to their performance as optical detectors and try to optimise frequency and physical spacing of detectors to account for the cross-coupling. This lead us to a similar/extended approach of that shown by Yu et. al.¹⁰⁶, using the frequency shift of the resonators. Instead, we set a relatively conservative requirement on the cross-coupling: the frequency shift in the cross-coupled detector should be less than 1% for a two linewidth shift in the detecting resonator. In a simplified context relevant to LIM observations, this metric ensures that the detection of a photon from one spectral line, say 150 GHz, does not result in a false detection of another in its neighbouring detector. The following sections detail the the characterisation procedure of the relationship between the frequency spacing and the physical location of the detectors. All detectors in the following simulations were

tuned to have $Q_r = 5 \times 10^4$ and by normalising the resonance shifts to linewidths we make the assumption that the degree of shift in linewidths is constant as a function of Q_r .

4.2.1 Cross-coupling as a function of frequency spacing

To get a measurement of the percentage frequency shift in the neighbouring detector a simulation was set up as shown in Figure 4.7a. Here, the resonant frequencies of the two resonators are set by the IDC length to have a desired “dark” frequency separation when both inductors have the same kinetic inductance. Note, each resonator will be labelled with a number referring to its position from the left as shown in Figure 4.7. The simulations shown in this section were carried out using a physical spacing equivalent to the smallest mm-wave filter channel separation on the same side of the $\lambda/4$ spaced filter-bank. This was effectively a half wavelength of 180GHz on the microstrip, approximately 258 μm with our initial guesses at the mm-wave dielectric constant, see Section 3.4.

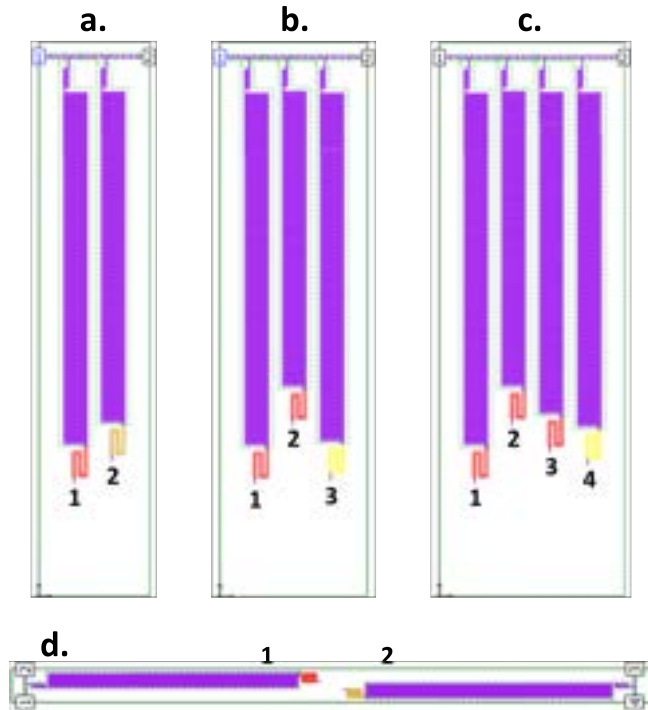


Figure 4.7. Sonnet simulation geometries for the cross coupling between the (a) first nearest frequency neighbour (NFNP), (b) second NFNP, (c) third NFNP, and (d) opposite neighbours. The kinetic inductance of the yellow inductors are varied and the f_0 relative to the “dark” f_0 is of the resonator of interest is observed. The numbers correspond to the resonator notations in the text and plots.

For a given dark frequency separation, the kinetic inductance of the resonator with the red inductor and labelled as resonator 1 in Figure 4.7 was fixed at $0.6 \text{ pH} \square^{-1}$ (the expected/desired

kinetic inductance of our aluminium films), and the resonators with yellow inductors have their kinetic inductance varied between $0.6 \text{ pH} \square^{-1}$ to $0.65 \text{ pH} \square^{-1}$. This is to effectively mimic a shift in f_0 due to the absorption of a photon, hence the name “dark frequency separation” when both are set to $0.6 \text{ pH} \square^{-1}$. The resonator quality factors and f_0 s are extracted by fitting a Lorentzian (see Equation 6.1) to the peaks of the S_{21} data and the shift in f_0 from the corresponding dark f_0 is calculated allowing the fractional shift, $\Delta f_0_1/\Delta f_0_2$, to be plotted as a function of the shift in f_0_2 in linewidths. This presents a linear relationship, which when fit can allow us to extrapolate the fractional shift for a 2 linewidth shift in f_0_2 . Unfortunately, we have to make an assumption that the linear relationship holds true to the lower linewidth shifts as the frequency shift in the coupled resonator become too small to measure due to simulation error. In the case of the plot shown in Figure 4.8d, a resonator with a frequency separation of 55 MHz to the first nearest frequency neighbour position (NFP) would have an 11.57 % shift of a 2 linewidth shift in its neighbour.

Thus, by repeating this process for a variety of frequency separations one can obtain a plot for the 2 linewidth percentage shift as a function of frequency spacing. Therefore, the required separation for a 1% shift in a 2 linewidth shift in the neighbouring resonator can be interpolated, as demonstrated in Figure 4.9c for the first, second and third NFNPs. In the simulations involving 3 or 4 resonators, the resonant frequencies of the resonators between the first detector and variable inductance detector were set to be suitably far away from any detectors to prevent them also cross-coupling and therefore confusing the results for the desired resonators.

The final step in this process was to plot the three interpolated required separations as a function of the neighbour position, then fit a linear regression in log space. Thus, for a given frequency separation, the required neighbour position can be extrapolated. This was an important tool for characterising the focal plane design and the spectrometer specifications as it presents a limit to the number of detectors that can be multiplexed within a 500 MHz readout bandwidth and therefore the number of spectrometer channels, which is directly linked to the resolution of the spectrometer as shown in Equation 3.4. For example, the $R = 300$, $\frac{1}{4}\lambda$ spaced filter-bank required 195 channels, the requirements set by the cryostat design at the time of this study, i.e. 9 readout lines and now 12 pixels, required at most, three spectrometers per 500 MHz readout line. Therefore, 585 detectors would be required within the readout bandwidth, hence a resonator frequency spacing of $\approx 850 \text{ kHz}$ needed to have the nearest frequency neighbour placed 1 resonators away if on the same side. Even if the nearest frequency resonator gets placed on the opposite side of the mm-wave feedline hence the same side frequency spacing becomes $\approx 1.70 \text{ MHz}$ (see Section 4.4.1), this resonator would need to be at least the 13th neighbour, which we were unable to find a suitable multiplexing procedure/algorith for.

4.2.2 Cross-coupling as a function of physical separation

Given the difficulties with the multiplexing of the $\frac{1}{4}\lambda$ spaced filter-bank imposed by the strong coupling parallel to the mm-wave feedline, it was necessary to explore the possibility of reducing

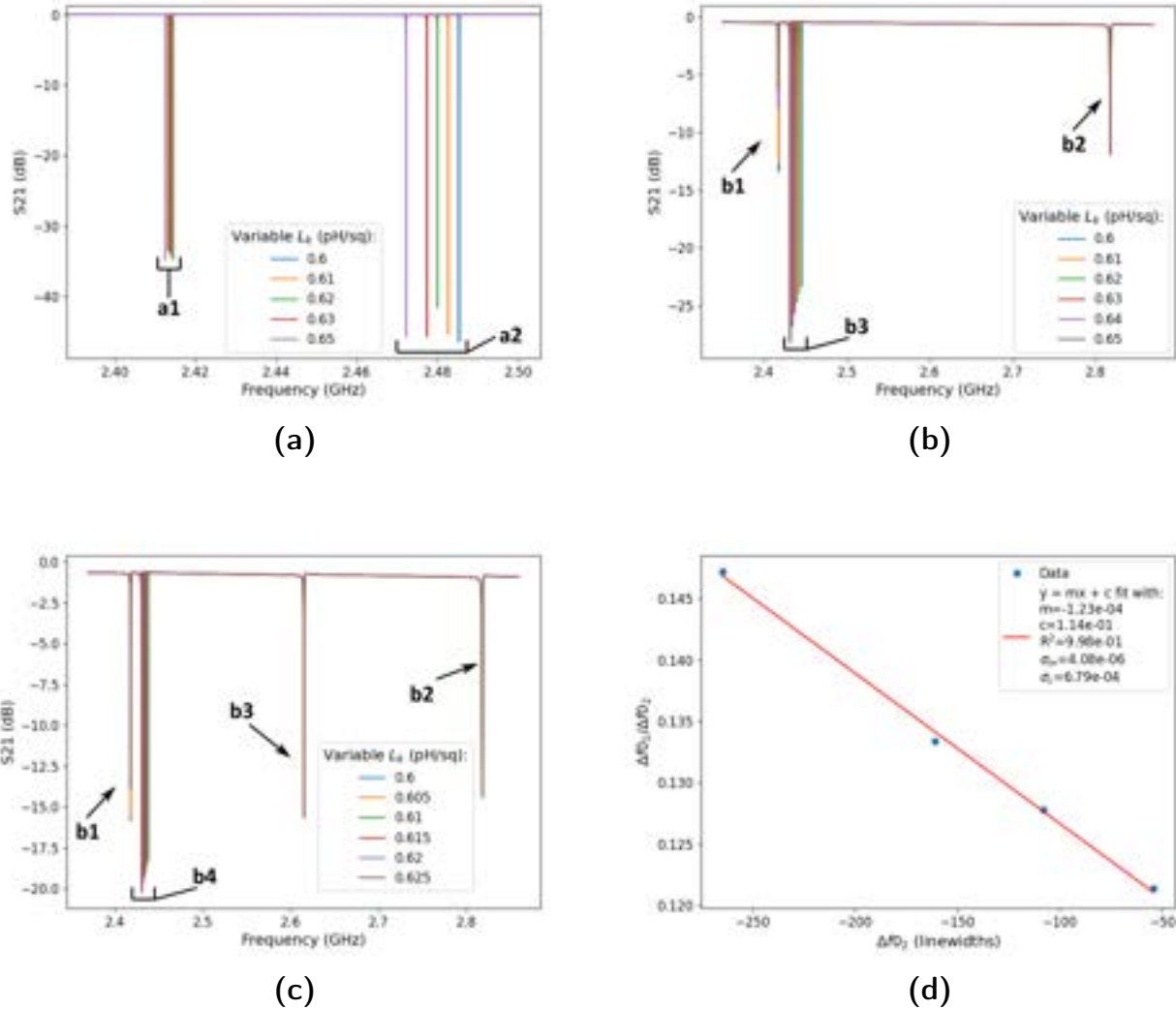


Figure 4.8. Plots showing the cross-coupling simulation results of two neighbouring LEKIDs, with an intended dark frequency separation of 55 MHz. (a) Shows the S_{21} data from each simulation, notably showing how the lower frequency resonance shifts to the left by some fraction as the higher resonance also shifts down in frequency due to the change in kinetic inductance. (b) and (c) show example S_{21} plots for the three and four resonator simulations with separations of 25 MHz and 20 MHz respectively between the detecting resonator and the coupled resonator. The letter in the annotated labels refer to the corresponding simulation then the numbers indicate the specific resonator responsible for the S_{21} notch. (d) Shows the linear fit to the ratio of the shift in the coupled resonator (Δf_01) to the shift in the detecting resonator (Δf_02) as a function of the detecting resonator shift in linewidths for the two neighbouring LEKID simulation.

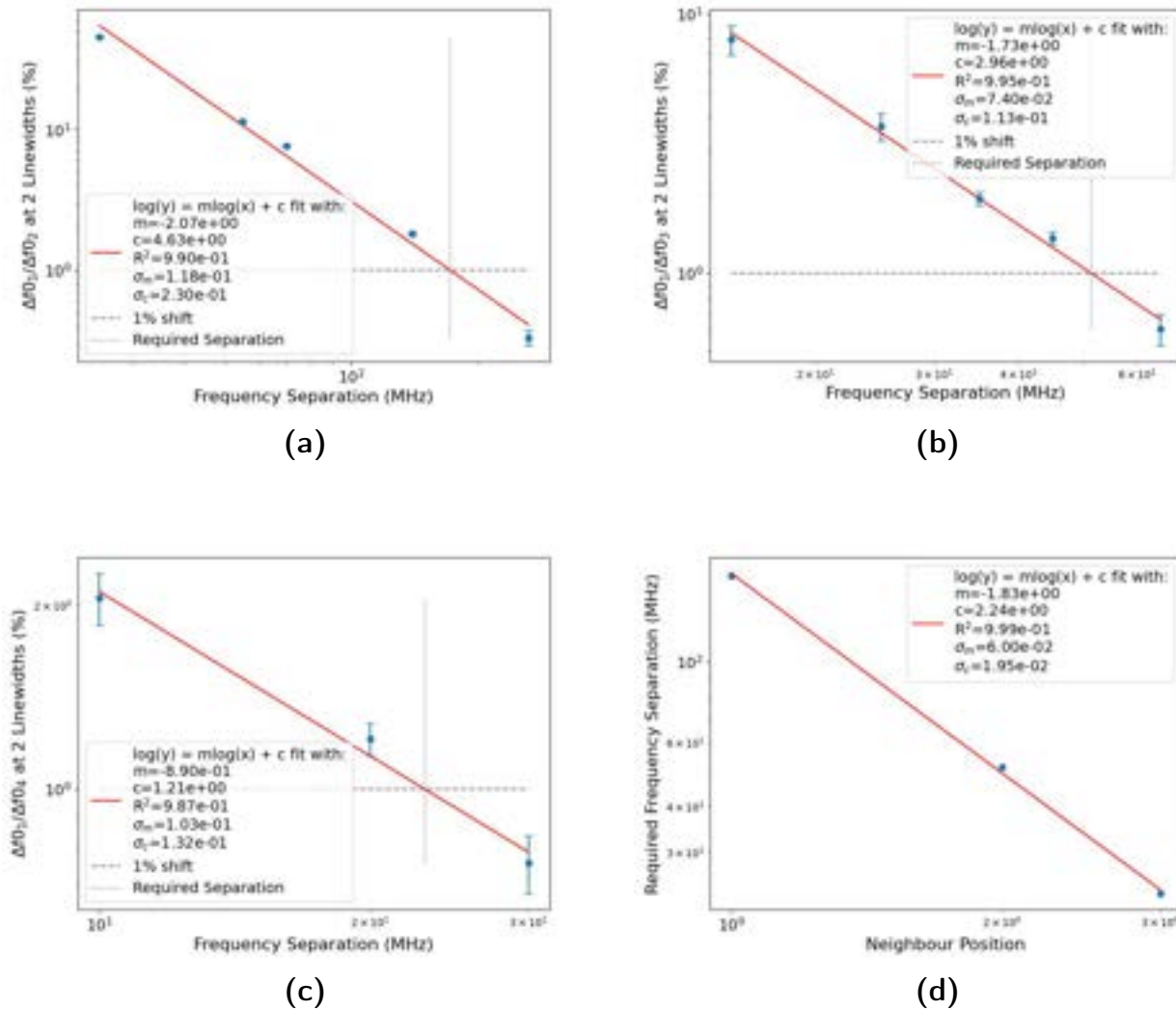


Figure 4.9. Plots demonstrating the interpolation method used to find the required frequency separation to obtain a cross coupling between two resonators with a 1% shift for a 2 linewidth shift in the (a) first NFN, (b) second NFN, (c) third NFN. The required separations were 173 MHz, 51.3 MHz, and 23.0 MHz respectively. The uncertainties are obtained from the uncertainties of the linear fits of the 2 linewidth extrapolations. (d) Shows the fit used to extrapolate the required position for a given frequency spacing, using the interpolated result from plots a, b and c.

the cross coupling by increasing the physical spacing of the detectors. This would of course have an impact on the millimetre performance of the filter-bank, hence the study presented in Section 3.6.5 was conducted in parallel to this work to allow us to find a suitable compromise between the filter-bank specifications required for the science case and a practical and low risk design for the microwave readout.

The simulations were set-up as shown in Figure 4.10. The physical separation was varied between $\frac{1}{4}\lambda$ and $\frac{3}{4}\lambda$ for the smallest wavelength in the filter-bank. For each separation, the kinetic

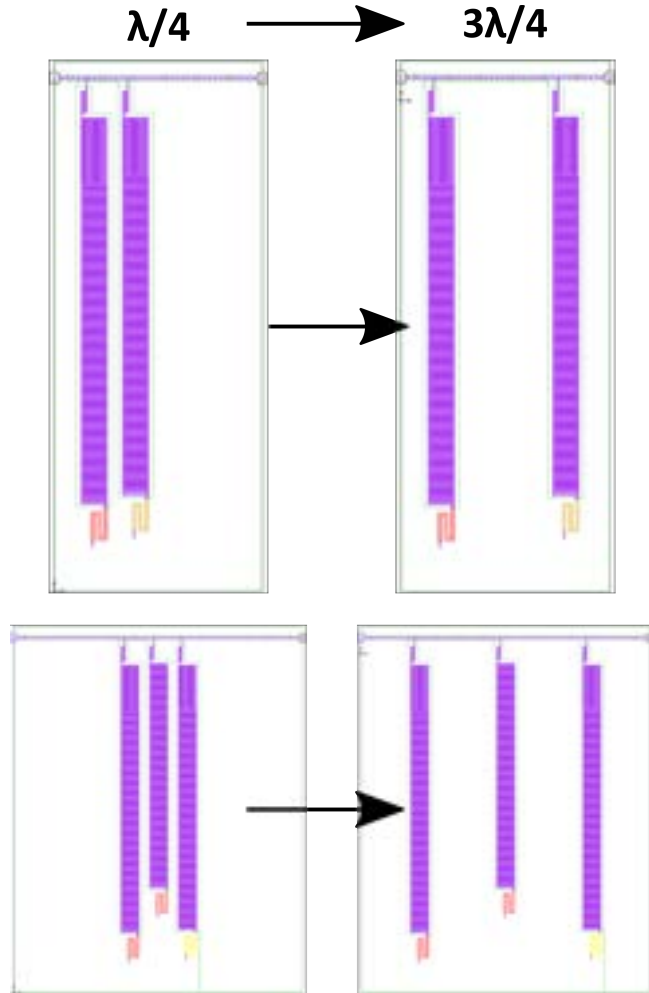


Figure 4.10. Sonnet simulations for studying the cross-coupling between the first nearest neighbour and second nearest neighbour as a function of physical separation between $\frac{1}{4}\lambda$ and $\frac{3}{4}\lambda$ for the smallest millimetre wavelength in the filter-bank.

inductance of the variable detector was changed to measure the fractional shift in the first resonator in the same way as described in Section 4.2.2. This allowed the fractional shift for a 2 linewidth shift in the variable detector to be compared at different separations, see Figure 4.11.

These results were used to approximate the reduction in frequency shift relative to that of the $\frac{1}{4}\lambda$ separated resonators. For example, for the first nearest neighbour, the 2 linewidth fractional shift was 10.70 % and 3.31 % for a $\frac{1}{4}\lambda$ and $\frac{3}{8}\lambda$ spacing respectively. Thus by moving to the latter spacing we see the cross-coupling reduce by 69.0 %. For the second nearest neighbour, this is 73.7 %. Hence, by approximating the cross-coupling reduction to be $\approx 70\%$, the NFPN for a separation of 850 kHz becomes 7 instead of 19. The impact this 70% reduction in cross-coupling has on the required frequency separation as a function of neighbour position is shown in Figure 4.9d. Unfortunately, radially fitting eight $R = 300$ filter-banks on a sub-module at this $\frac{3}{8}\lambda$ spacing did not fit on the 6 inch wafer as the filter-banks became too long. This was one of the reasons

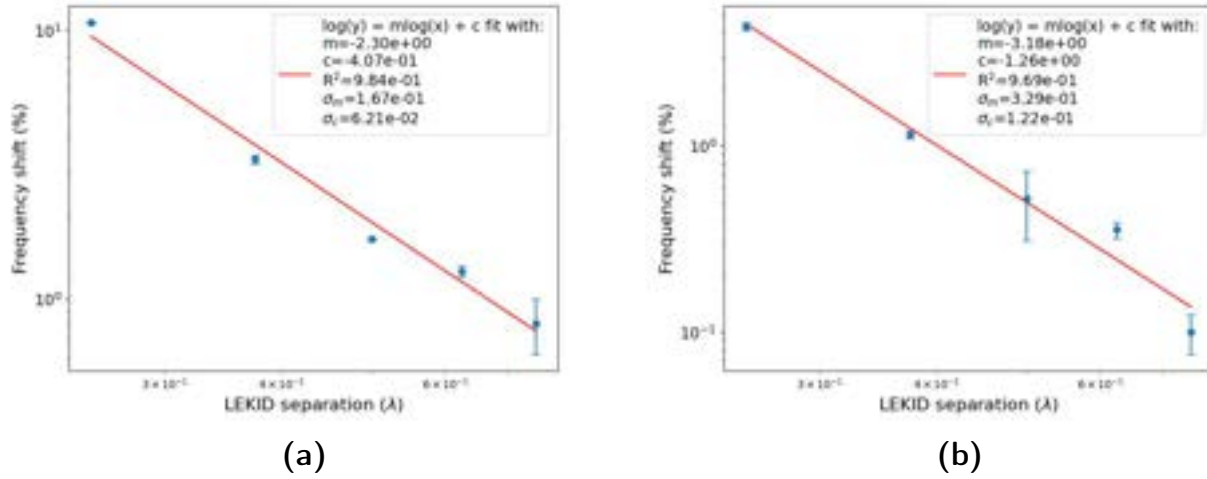


Figure 4.11. Plots obtained by extrapolating the 2 linewidth fractional at different resonator separations ($\frac{1}{4}\lambda$, $\frac{3}{8}\lambda$, $\frac{1}{2}\lambda$, $\frac{5}{8}\lambda$, $\frac{3}{4}\lambda$) for the first and second nearest neighbours with frequency separations of (a) 50 MHz and (b) 25 MHz respectively. Uncertainties are obtained from the linear fit uncertainties of the extrapolation to the fractional shift at 2 linewidth shift.

that lead us to de-scope our spectrometers to have a resolution of $R = 200$ to reduce the number of channels and ease the constraints on multiplexing.

To summarise, the extent of the cross-coupling between neighbouring IDC LEKIDs was characterised via Sonnet simulations measuring the degree of cross-coupling with the metric being the ratio of the resonant frequency shift of one “dark” detector relative to that of its neighbouring “loaded” detector. The relationship between the value of this ratio and frequency separation of the neighbouring detectors was observed for resonator pairs up to three positions away parallel to the readout line and opposite each other perpendicular to the readout line. For each scenario the frequency separation yielding a 1% frequency shift was extrapolated such that the required frequency separation could be approximated as a function of neighbour position. The results showed that this detector design cross-couples with neighbouring detectors significantly parallel to the mm-wave feedline but effectively zero coupling on opposite sides of the mm-wave feedline. It was also shown that by moving to $\frac{3}{8}\lambda$ spaced filters instead of $\frac{1}{4}\lambda$ spaced, the fractional shift due to cross coupling could be reduced by $\approx 70\%$. Despite the reduction, it was not possible to use the $R = 300$ $\frac{3}{8}\lambda$ spaced filter-banks with four pixels (8 spectrometers) due to limited space on a six-inch wafer. Further implications that this cross-coupling had on the multiplexing method for the microwave readout f_0 scheduling and ultimately the focal plane design is presented in Sections 4.4 and 4.4.2.

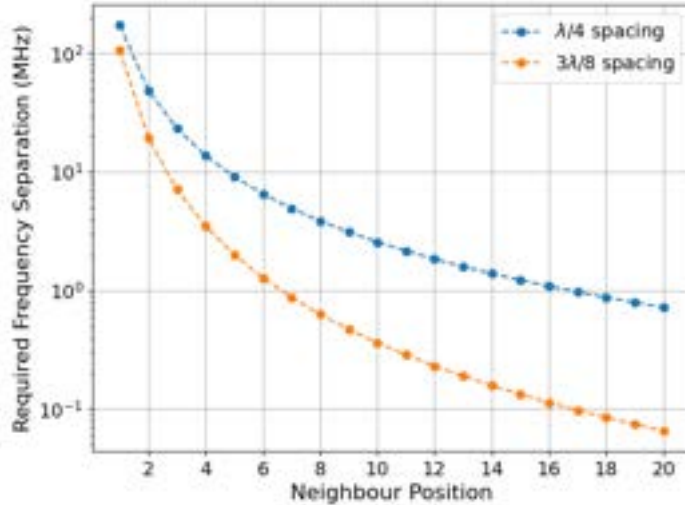


Figure 4.12. Plot showing the required resonant frequency separation between a detector and parallel neighbour depending on its neighbour position in order to achieve 1% or less cross-couplings. The blue line for $\frac{1}{4}\lambda$ spacing is equivalent to the linear fit shown in Figure 4.9d and the orange line for $\frac{3}{8}\lambda$ spacing assuming the 70% reduction in fractional shift achieved by increasing the separation between two detectors.

4.3 Parallel plate capacitor LEKID

An alternative design for the LEKID is to use a Parallel Plate Capacitor (PPC) instead of both the main IDC and the coupling IDC, yet still using the same inductor geometry. This design is presented in Figure 4.13. The PPC detector has a few advantages over its IDC counterpart. Firstly, a much larger capacitance per unit area can be achieved due to the ability to form the parallel plates on either side of a sub-micron deposited dielectric film, whereas the comparable length in the IDC (finger separation) is on the order of a few microns. This results in the detector footprint being roughly half that of the IDC detector, enabling a far more efficient use of space that would drastically ease constraints on the focal plane design that are a significant limitation of the IDC design as presented in Section 4.4.2.

Furthermore, the parallel plate has a significantly lower geometric inductance than the IDC, leading to a roughly four times higher α_k of 0.419, which was determined for the same resonant frequency detector as discussed in Section 4.1.3 using Equation 4.4. Thus, a PPC LEKID should be more responsive since the same change in kinetic inductance would result in a larger change in resonant frequency.

Additionally, in the case where the IDC cross-coupling is due to a capacitive coupling, the parallel plates having a very small separation relative to the detector separation (≈ 300 nm compared

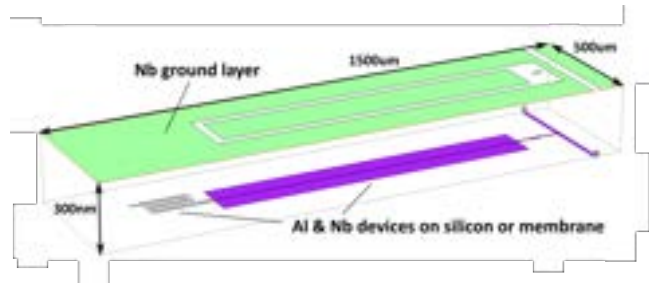


Figure 4.13. 3D diagram of a single parallel plate capacitor LEKID. The vertical separation between the two planes is not to scale relative to the in-plane dimensions. The device layers are separated from the niobium ground plane by a 300 nm SiN dielectric.

to $\approx 300 \mu\text{m}$), will result in the strength of the detector cross-coupling being minimal in comparison with the IDC design. Alternatively, if the IDC cross-coupling is inductive, the negligible geometric inductance in the PPC would also result in a much smaller effect. Hence, for the PPC, the cross-coupling was too small to extract out of simulations both with the level crossing method¹⁰⁵ and the variable kinetic inductance method.

Figure 4.14 shows a comparison between the level crossings of two series IDC detectors, two opposite IDC detectors (using similar simulations as shown in Figure 4.7a and 4.7d, respectively), and two series PPC detectors. In these simulations, the capacitor size of the neighbour is varied such that it sweeps through having the same capacitor length value, and the difference between the capacitor lengths (which is analogous to the non-coupled f_0) is plotted against the f_0 s of each resonator. The results show that the two series IDC resonators was the only situation in which a clear avoided level crossing could be seen suggesting the other two arrangements have an insignificant degree of cross-coupling, much like the un-coupled configuration of Figure 4.6. A similar conclusion was drawn from conducting the variable kinetic inductance simulations, whereby both the opposite IDCs and series PPCs showed only noisy results for the fractional shift as function of the variable kinetic inductance for a dark separation of approximately 1.0 MHz to 2.0 MHz, hence suggesting the strength of cross-coupling is below the simulation resolution and therefore significance.

Regarding fabrication, the parallel plate should firstly simplify the procedure by removing the need for the membrane step-down processes that the IDC LEKID recipe requires in order to place the IDC directly on to the surface of the silicon wafer; for further details see Chapter 5. Furthermore, the PPC should ease the tolerance on the lithography of the capacitors as a stochastic variation on geometry linewidths for a parallel plate should intuitively change the capacitance by a smaller degree than for an inter-digital capacitor. To test this, a simulation of an IDC resonator and a PPC resonator of similar f_0 and Q_r (of the architectures detailed in this thesis) were simulated first with the intended (“nominal”) geometries and then again

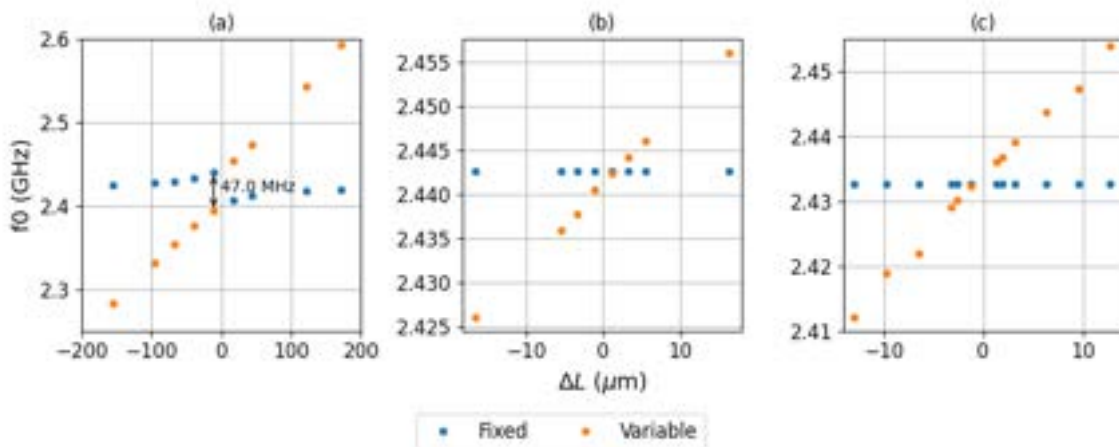


Figure 4.14. Level crossing plots for detector cross coupling simulations for (a) two series IDC resonators, (b) two IDC resonators on opposite sides of the mm-wave feedline and (c) two series PPC resonators. Here the capacitor of one resonator is a constant “fixed” value while its neighbour has a “variable” capacitor length, thus sweeping its resonant frequency over the fixed resonant frequency. The difference between the two capacitor lengths is denoted as ΔL .

with a $+0.2\text{ }\mu\text{m}$ dimension increase of either the inductor or capacitor. The results are shown in Figure 4.15, where as expected, the f_0 capacitor tolerance is significantly smaller for the PPC (-0.13%) compared to the IDC (-2.1%). Interestingly, the PPC is more sensitive to the inductor lithography (8.23% vs. 1.77%), however this is simply a manifestation of the difference in kinetic inductance fraction. Since the PPC design has minimal geometric inductance in the capacitor (unlike the IDC design) it will be more sensitive to geometric changes in the inductor. If this were an issue, more precise lithography on the inductor process should make an improvement, or alternatively one could add extra non-sensitive geometric inductance, though this would come with a responsivity penalty. The aluminium inductor is fabricated on a separate processing step to the niobium capacitor, hence the geometry variation will be different. Additionally, these values of fractional shift (on the order of 1×10^{-2}), are significantly larger than what is observed in measurements which are 2 orders of magnitude smaller around $\approx 1 \times 10^{-4}$, see Section 6.1 for more details relating to the measured performance of these designs.

Whilst there are many practical advantages to the PPC detector, the main drawback is the potential for poor $1/f$ noise at lower frequencies due to the field lines of the high charge areas (between the plates) propagating through a lossy dielectric¹⁰⁷, as is the somewhat unavoidable nature for this geometry. This is particularly problematic for our application as the lower frequencies is where the demodulated sky signal will reside. Limited to the speed of the telescope and scale of the spectral features to be reconstructed with the detector array brings the observation band around 15 Hz. The presence of this dielectric would therefore introduce TLS noise, which can make it difficult for detectors to achieve performance limited solely by the intrinsic photon noise.

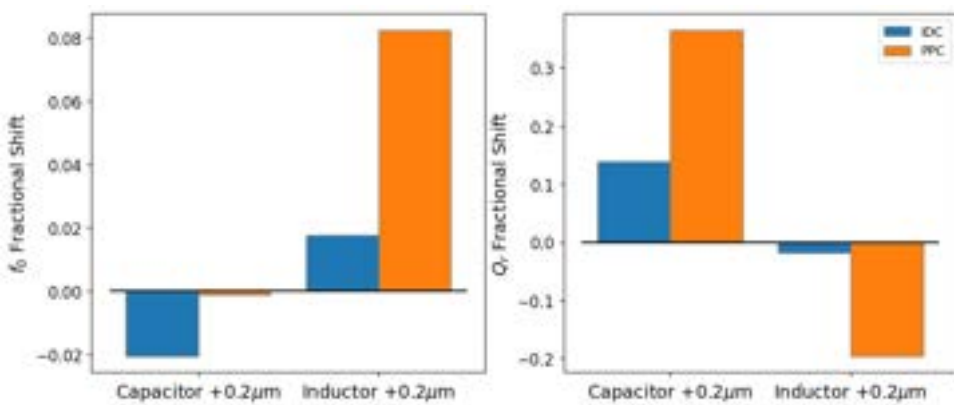


Figure 4.15. Simulated LEKID f_0 and Q_r tolerances to a $+0.2\text{ }\mu\text{m}$ increase to either the inductor or capacitor. These results compare simulations of a single IDC or PPC LEKID with nominal f_0 's of 2.467 GHz and 2.387 GHz , and Q_r 's of 4.59×10^4 and 4.98×10^4 respectively.

However, recent results from other groups have demonstrated photon noise limited PPC detectors^{107–109}. This can be made possible by using an extremely small inductor volume (on the order of $1\text{ }\mu\text{m}^3$ to $10\text{ }\mu\text{m}^3$ for example) since the detector NEP is inversely proportional to the the responsivity (discussed further in Chapter 6). Or by using very low loss dielectrics such as amorphous silicon or amorphous silicon carbide, both demonstrate low noise and loss. For our fabrication process however, these materials were unfortunately unsuitable and unavailable as is discussed in Chapter 5.

4.4 Detector Multiplexing

The level of cross-coupling presented in Section 4.2 creates difficulties with the frequency scheduling of the detectors in the microwave readout. The essence of the issue is that the limited readout bandwidth of 500 MHz imposes a maximum limit to the number of detectors that can be multiplexed on a single readout channel due to carrier tone cross-talk. An additional limit is also imposed due to the focal plane configurations which effectively depend on the number of filter-banks on the readout line as well as the parameters that govern the number of detectors on a filter-bank, i.e. filter resolution and oversampling (see Equation 3.4), and finally, the degree of detector cross-coupling which depends on the filter spacing, dx . As well as the nominal $\frac{1}{4}\lambda$ spacing, $dx = \frac{3}{8}\lambda$ was also considered due to the reduction in detector cross-coupling observed by moving whilst remaining to have a small FBS footprint relative to a $\frac{3}{4}\lambda$ spaced FBS and only inflicting a small reduction in total filter bank efficiency according to the FBS simulation results shown in Figure 3.21a. The relationship derived in Section 4.2 between the required frequency separation, δf as a function of neighbour position is shown in Figure 4.9d as a reference and also to visualise the difference between the two considered filter-spacings and the impact they have on multiplexing.

The oversampling was chosen to be fixed at $\Sigma = 1.6$, and constraints between the optics and cryostat imposed that at most 12 pixels would be split amongst 9 microwave readout channels thus in the most difficult case, 3 filter-banks would be readout on feedline. Channels consisting of three filter-banks will be referred to as “Trios” and two filter-bank channels as “Duos”. Understanding which combinations of this parameter space were logically possible and comparing their simulated performances ultimately became the motivator for de-scoping from $R = 300$ to $R = 200$. The following two sections present the multiplexing algorithm used to mitigate the cross-coupling (Section 4.4.1) and then Section 4.4.2 discusses the variations of possible focal plane layouts that were considered following this multiplexing study.

4.4.1 Multiplexing algorithm

Typically, the f_0 scheduling for multiplexed devices are designed to allow for the easy identification and mapping of detectors to their physical location. In the case for a Trio for example, being able to group the resonators into separated thirds of the readout bandwidth would allow us to separate out the three filter-banks. Unfortunately, this was not possible due to the strength of the cross-coupling. This meant that the full bandwidth range needed to be utilised equally for all the filter-banks on the channel.

The algorithm used to split the resonators amongst the number of filter-banks on a readout channel and then mix and arrange the detectors in physical space along the filter-bank is shown in Figure 4.16 and consists of the following steps:

1. First, N frequencies are equally spaced within the readout bandwidth Δf_R where N is the number of filters multiplied by the number of filter-banks.
2. The frequencies are then split into G groups, which is a number that needs to be determined.
3. Each group is then split into sub-groups dependent on the number of filter-banks in the channel (Trios or Duos). This allows for the spacing to be equal between filter-banks.
4. Within each sub-group every even other frequency is assigned as a “Top” and every odd other a “Bottom”. This utilises the fact that the detectors do not cross-couple across the mm-wave feedline, effectively making the minimum frequency spacing (as far as cross-coupling is concerned to be $2\Delta f_R/N$ rather than $\Delta f_R/N$.
5. Finally, the first Top and Bottom of each group (“a” and “a'”) are assigned to the first $2G$ filters for each filter-bank in a mixing sequence that satisfies the required frequency

separations shown in Figure 4.12. This process continues down the filter-bank until all frequencies from each group are assigned (b 's, c 's, d 's e 's...etc.).

Whilst this multiplexing method may not be ideal for diagnosing the devices, providing the device works end-to-end it is possible to isolate each filter-bank via polarisation specific measurements and the detectors can be characterised by their mm-wave spectral peak. The mapping from millimetre ν_0 and microwave f_0 to physical location is mostly important if capacitor trimming is required. This is where the capacitor geometry is edited to alter detector f_0 s, after the initial fabrication run, once the device has been characterised. Trimming has demonstrated clear reductions in resonator scatter and collisions¹¹⁰. However, since optical measurements are required to identify the detectors, conducting further fabrication steps on released OMT membranes was deemed to risky. One advantage of this multiplexing method is that the nearest frequency neighbours on the same side of the mm-wave feedline (the ones prone to cross-coupling) will be separated by $2G$ filter-channels, thus it would be obvious that the two detectors are cross-coupling as their mm-wave peaks would be separate and identifiable even in the regime of overlapping spectral profiles.

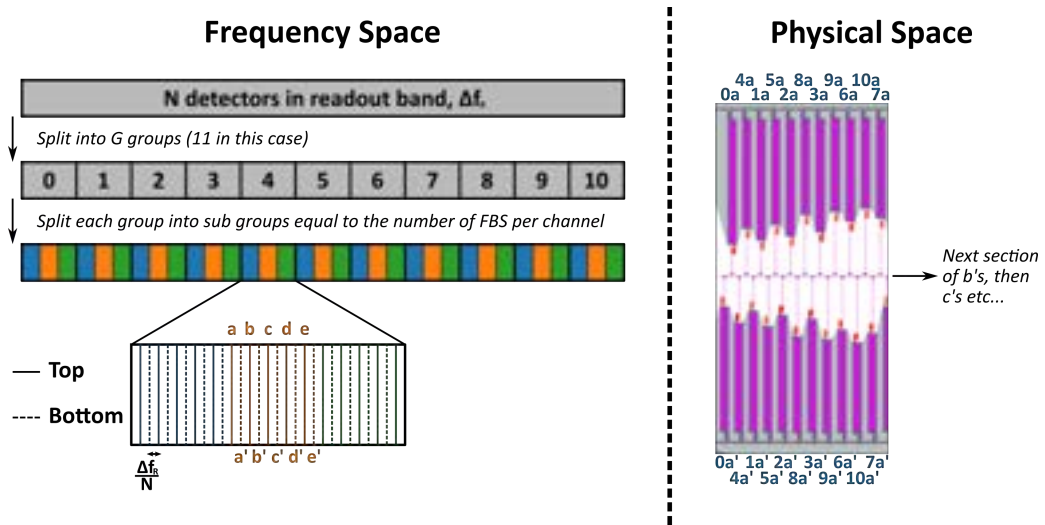


Figure 4.16. Diagram explaining how the resonant frequencies within the readout band, Δf_R , for a Trio spectrometer group are split up and arranged in frequency space then assigned in physical space along a filter-bank to avoid cross-coupled detectors. This examples shows how a Trio of $R = 200$ spectrometers was multiplexed within 500 MHz of bandwidth.

A Python script was used to find the minimum required number of groups and the best mixing sequence which provided the most uniform frequency spacing. The logic of this script is visualised in Figure 4.17. First the variables defining the problem are declared: the number of filter-banks on a channel, N_{FBS} , the FBS resolution, R , filter spacing, dx (either $\frac{1}{4}\lambda$ or $\frac{3}{8}\lambda$), oversampling, Σ , and frequency groups, G . This is used to calculate the number of filter channels/readout frequencies and then generate the array of frequencies and split into G groups. Then, for every permutation

of arranging G groups ($G!$ permutations) the frequency array is mixed as per the logic shown in Figure 4.16. For each filter-bank's array, the frequency separation, δf between every m -th neighbour for the Tops and Bottoms for $1 \leq m \leq G$ is compared to the required frequency separation as per the plots in Figure 4.12. If all separations are greater than the required separations, the permutation is given a score based on the ratio of each neighbour separation to its required separation. Hence, the bigger the total score the further the average neighbour frequency separation is from the minimum frequency separation. The permutation with the best score would be the one used to multiplex to detector frequencies. However it was possible that some combinations were not possible to multiplex. This is explored further in Section 4.4.2.

Typically, the minimum number of groups was equivalent to or greater than the NFNPs. Therefore, for the combinations that required large NFNPs, the computation required quickly became impractical as the number of permutations scaled as a factorial of G . Variations of $G \geq 15$ were not attempted and where situations that had no solution below this were therefore considered to not work.

4.4.2 Focal plane variations

With the limitations on the microwave side (detector cross-coupling) of the filter-bank characterised and using the help of the filter-bank simulation tool, we were able to compare possible variations in the focal plane design. Following the cross-coupling study of the IDC LEKIDs it was apparent that the nominal 12 pixel, $R = 300$ design was not possible since this required two Trio channels per sub-module, which at $\frac{1}{2}\lambda$ needed $\text{NFPN} = 19$ when the NFNPs was suitable at $\frac{3}{8}\lambda$ the filter-banks were too large when combined with four pixels per filter-bank. In this section, three focal plane variations will be presented and compared, one at each resolution ($R = 100, 200, 300$) as this will convey most of what was considered when deciding on a design. It is worth noting that the end goal of performing line intensity mapping will choose higher spectrometer resolutions and more pixels whenever possible, however, as will become apparent, these choices have ramifications on the efficiency of the device.

The three focal plane variations can be viewed in Figure 4.18 and the key attributes and efficiency metrics are summarised in Table 4.1. The variations consider changing the following attributes in the focal plane:

1. FBS Resolution, R - Controls the number of filters per FBS.

- Changes length of the lossy filter-bank feedline.
- Changes the single filter loss due to the inverse relationship between filter resolution and filter efficiency (see Figure 3.10b).

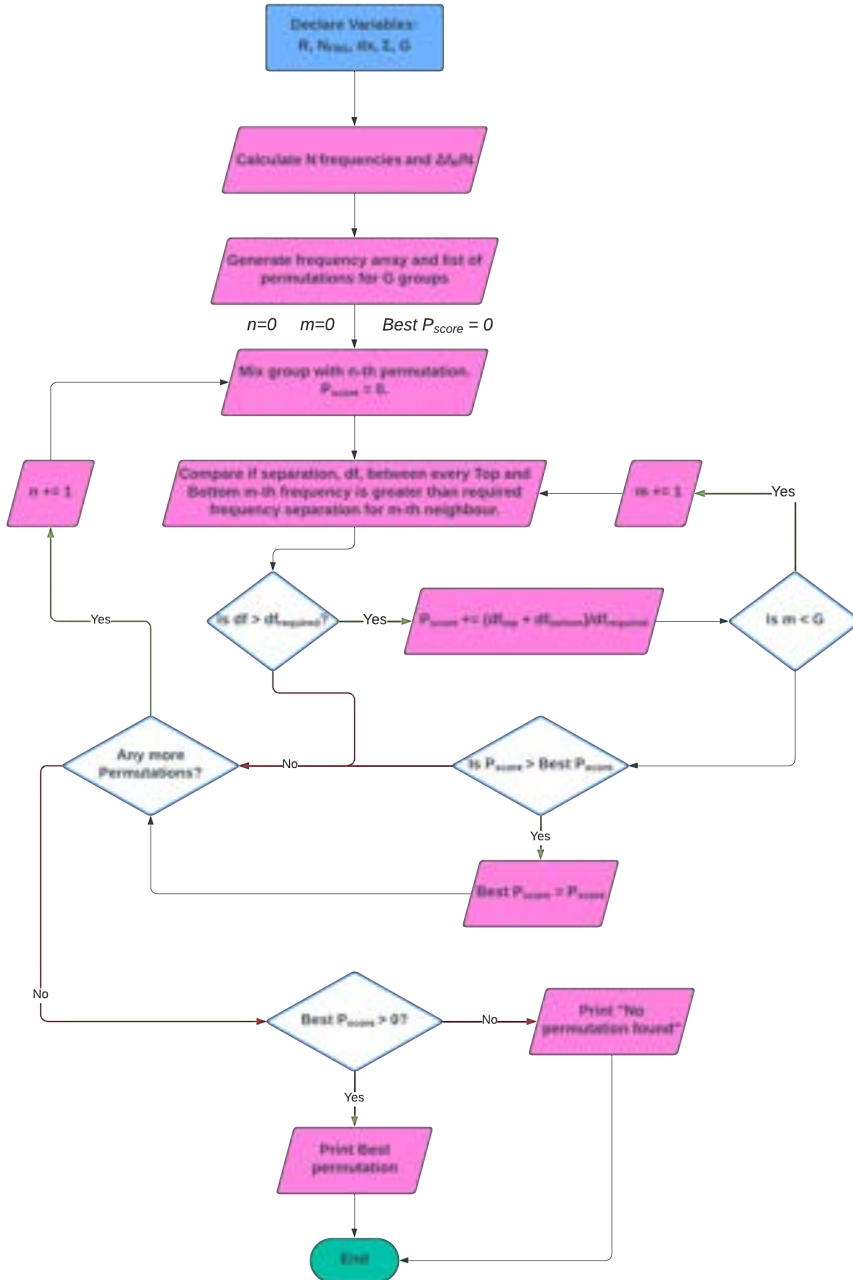


Figure 4.17. Flow chart visualising the logic used in the Python script to find suitable mixing sequences for a given number of filter-banks on a channel, N_{FBS} , the FBS resolution, R , filter spacing, dx (either $\frac{1}{4}\lambda$ or $\frac{3}{8}\lambda$), oversampling, Σ , and frequency groups, G . All permutations of arranging G groups are tested and if successful given a score, P_{score} . The permutation with the best score is printed at the end unless no successful permutations are found.

- The number of mm-filters changes the number of detectors within the readout band, hence changing the NNP.
2. Number of pixels (9 or 12) - Controls the distance between the OMT and the start of the

FBS.

- Changes the amount of loss due to the lossy microstrip between OMT and FBS (feedline efficiency).
- Since the number of readout lines is fixed at 9, changing the number of pixels determines how many filter-banks per channel and thus also controls the frequency spacing and NFNP.

3. Filter spacing

- Changes length of the lossy filter-bank feedline.
- Changes the degree of cross-coupling between resonators, hence changing the NFNP.

The difference between the feedline efficiencies of the 9 pixel and 12 pixel options can be seen as the black dashed line in Figure 4.19. There is around a 9% increase in throughput when dropping to 3 pixels per sub-module. It is also worth noting that there is a slope due to the electrical length increasing at higher frequencies and therefore increasing the total loss through the feedline. It is also one of the reasons that the highest frequency filter will have a smaller single filter efficiency and hence is placed at the start of the FBS as an attempt to balance the total FBS throughput.

The three variations we will consider are shown in Figure 4.18 and a dielectric loss tangent of 1.0×10^{-3} is assumed. The first design is the 9 pixel, $R = 300$, $\frac{3}{8}\lambda$ spaced focal plane. Removing a pixel was the only viable option to realise a $R = 300$ FBS due to the cross-coupling constraints, as such this is dubbed “the high resolution” option. Secondly, the compromise option keeps the 12 pixels but reduces the resolution to $R = 200$ yet still requiring $\frac{3}{8}\lambda$ filter spacing in order to bring the NFNP down to a suitable value. Finally, a “low risk” option has 9 pixels with $R = 100$ filter-banks. It would have been possible from a cross-coupling point of view to space this spectrometer at $\frac{1}{4}\lambda$, however when this design was later implemented and better estimates for material parameters at millimetre frequencies were known, it became apparent that the width of the IDC capacitors (parallel to the millimetre feedline) were too large for $\frac{1}{4}\lambda$ spacing. As a result, $\frac{3}{10}\lambda$ spacing was the smallest spacing that could be used and this is therefore what is presented in this section.

The various efficiency metrics for each variation are tabulated in Table 4.1 along with the key attributes, they can also be visualised in Figure 4.20a. These values and uncertainties were obtained from the simulation model described in Section 3.6 and the simulated FBS power transmission is shown in Figure 4.19. In these plots, the OMT to FBS feedline has been included in the simulation. Here, the feedline efficiency, η_{feedline} is, as previously mentioned, the signal throughput from

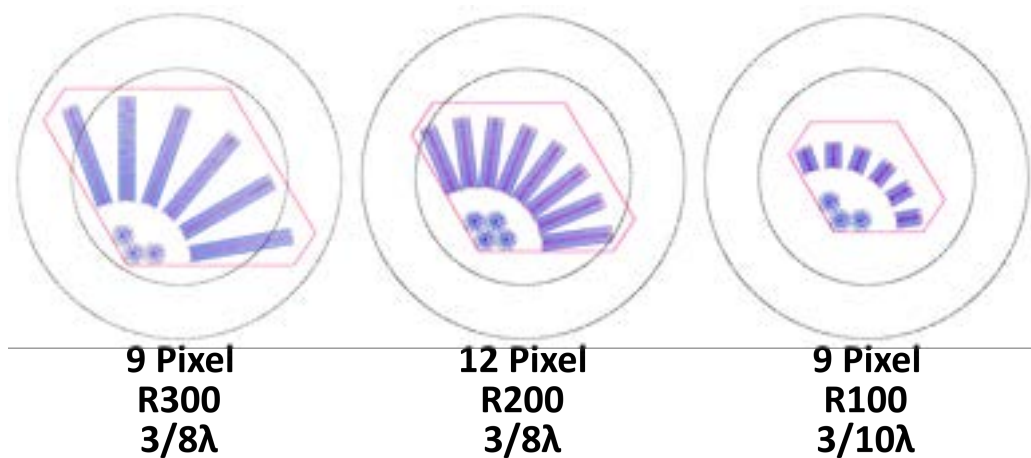


Figure 4.18. Approximate sub-module layouts for the three considered focal plane variations defined by the spectrometer resolution, number of OMT pixels and filter spacing. The outermost black circle indicates a 6-inch silicon wafer and the inner circle a 4-inch.

the OMT to the start of the FBS, the uncertainty is the half range due to the variation across frequencies. The single filter efficiency, η_{filt} , is the average peak throughput across all channels with the standard deviation as the uncertainty. The end to end single filter efficiency, $\eta_{\text{total, filt}}$, is simply the aforementioned efficiencies combined ($\eta_{\text{total, filt}} = \eta_{\text{feedline}} \times \eta_{\text{filt}}$) and the total FBS efficiency represents the total end-to-end throughput across the filter-bank band (total across all channels), accounting for the OMT to FBS feedline loss.

Attribute	The High Resolution	The Compromise	The Low Risk
Resolution	300	200	100
N pixels	9	12	9
Filter spacing	$\frac{3}{8}\lambda$	$\frac{3}{8}\lambda$	$\frac{3}{10}\lambda$
N channels per FBS	195	130	65
Filterbanks per channel	2	2 or 3	2
NFNP	8	6	7
Feedline efficiency	$(79.3 \pm 3.7)\%$	$(70.3 \pm 5.0)\%$	$(79.3 \pm 3.7)\%$
Single filter efficiency	$(10.1 \pm 4.7)\%$	$(12.9 \pm 6.0)\%$	$(25.2 \pm 8.5)\%$
End-to-end single filter efficiency	$(7.99 \pm 3.60)\%$	$(9.07 \pm 4.11)\%$	$(20.0 \pm 6.7)\%$
Total FBS efficiency	$(32.6 \pm 9.75)\%$	$(34.9 \pm 7.7)\%$	$(51.2 \pm 8.2)\%$

Table 4.1. A table of attributes that describe the three different focal plane variations and the resulting mean simulated efficiencies across the frequency band assuming a loss tangent of 1×10^{-3} . See text for definitions/descriptions of each efficiency metric.

Considering these efficiency results, the collaboration initially chose to pursue the compromise option since the efficiencies were slightly higher than the $R = 300$ option with a more consistent throughput across the frequency band whilst also maintaining three extra pixels. Remember,

from the perspective of line intensity mapping, the higher resolution is important for improved constraints on spectral lines and the more pixels allows for faster mapping speeds via increased instantaneous sensitivity which is ultimately the advantage that this technology offers.

An additional point of comparison to consider is that in the ideal simulated results shown in Figure 4.19, we see that the $R = 200$ and $R = 300$ simulation shows significant fringing effects towards the higher frequencies where the $R = 100$ design does not. This is not to do with the resolution of the filter-bank but rather is due to the filter spacing. As discussed in Section 3.6.3, there is a stop band created by the interference of the parasitic off-resonance filter stubs which enters into the filter-bank spectrum as the filter spacing approaches $\frac{1}{2}\lambda$. Therefore the higher resolution designs utilising the reduced microwave cross-coupling at $\frac{3}{8}\lambda$ will be closer in frequency to the stop band and thus the beginnings of the fringing effects can be seen. Furthermore, this is also why the average ideal in-band total throughput for the $\frac{3}{8}\lambda$ FBS is lower than for the $\frac{3}{10}\lambda$ FBS as there is more destructive interference.

During the development of the $R = 200$ focal plane, multiple devices were not seeing any discernible mm-wave spectra. A potential cause of this was that the dielectric loss tangent was higher than expected with potential values ranging between 1×10^{-3} to 3×10^{-3} that were measured using the test devices presented in Pan et. al.⁹⁰ that shared the carrier wafer of the sub-modules under test. The efficiency implications on the focal plane due to the upper bound on the loss tangent is shown in Figure 4.20b when compared to the lower loss bound in 4.20a. This suggested that only $2.1 \pm 0.7\%$ of the light that couples to the OMT was reaching the detector, whereby the signal could have very easily been hidden within the noise. With this in mind and deployment date on the horizon, it was decided to move to the low risk option to ensure something could be deployed since it is clearly more robust to dielectric loss. On top of the efficiency argument we were also seeing significant reductions in yield due to detector collisions, this would therefore also improve with the low risk option since the frequency spacing is larger between detectors. Further information on collisions is presented in Section 6.1.

4.5 Microwave perspective conclusion

The main goal of this chapter was to convey the developments and considerations which lead to the final focal plane design presented in Chapter 2 and the corresponding results presented in Chapter 7.

This chapter presented the design of a microstrip-coupled LEKID suitable for an on-chip spectrometer. The design uses an inductor geometry which was predicted to result in a photon noise limited detector with the maximal power coupling achieved understanding the impedance

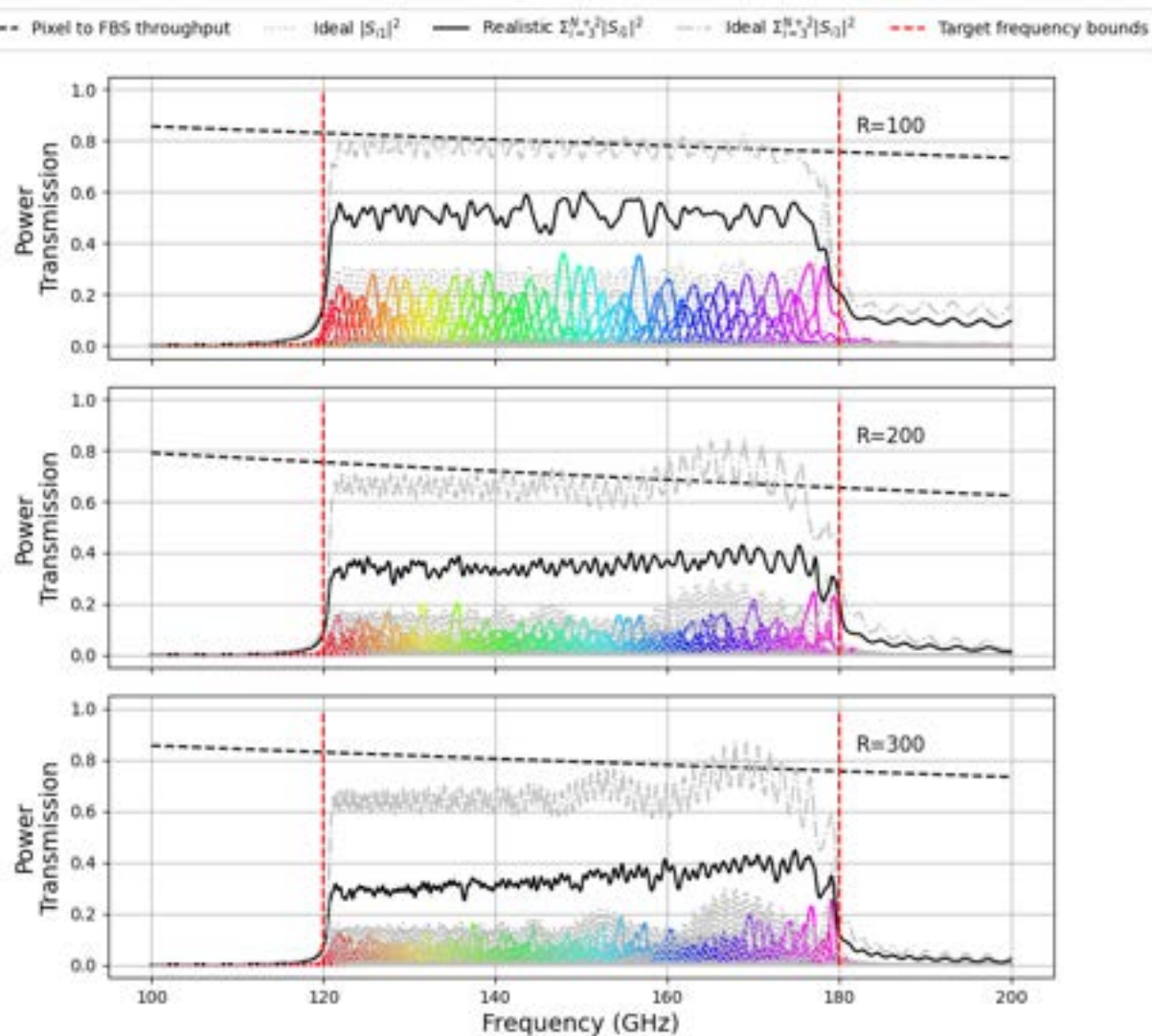


Figure 4.19. Simulated filter-bank power transmission for the three focal plane variations including the feedline from the OMT to the start of the FBS. The sloping black dashed line indicates the input feedline throughput. The top plot is the “low risk” option, middle “the compromise” and bottom “the high resolution”.

matching at the signal input. An inter-digital capacitor geometry was first presented, where the capacitive region is surrounded only by the crystal silicon of the handle wafer with the intention to minimise TLS noise. Results from an in-depth study on the degree of electromagnetic cross-coupling between detectors was shown which indicated these IDC resonators exhibited significant cross-coupling such that for a resonator to shift in frequency less than 1 % of a 2 linewidth shift in its nearest horizontal neighbour, there would need to be a separation of 173 MHz if they were to be used in a $\lambda/4$ wave spaced FBS. This ultimately meant that the nominal instrument design of $R = 300 \lambda/4$ wave spaced filter-banks, requiring a resonator spacing of ≈ 850 kHz within

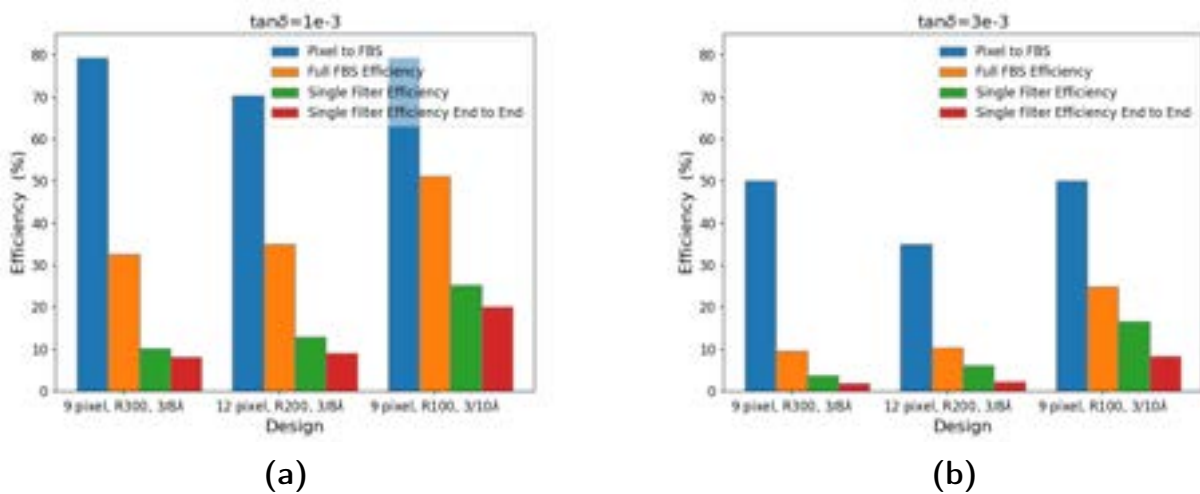


Figure 4.20. Bar plots showing the average values for the various efficiency metrics used to help evaluate each focal plane variation. The plots show the simulated values using a dielectric loss tangent of 1×10^{-3} (left) and 3×10^{-3} (right).

500 MHz was not possible when considering a suitable frequency multiplexing scheme. Increasing the physical separation of detectors by changing to a $3\lambda/8$ spacing was shown to reduce cross-coupling to a more manageable level, but with a sacrifice to the millimetre performance. The strong cross-coupling between these IDC resonators imposed significant constraints on the entire focal plane design and ultimately the instrument performance due to the interplay between the implications of the physical separation of the filter channels on the millimetre performance (larger spacing results in worse efficiency and increased destructive interference), the microwave circuit (smaller spacing increases detector cross-coupling leading to impossibilities in multiplexing) and the focal plane layout (larger spacing increases the filter-bank footprint leading to exceeding the dimensions of current fabrication techniques). Furthermore, the number of detectors per readout channel as impacted by the desired FBS resolution and pixel count was also important to consider as sharing a limited readout bandwidth with more detectors forces further multiplexing constraints. Three possible focal plane variations which considered various compromises were presented, whereby a 12 pixel $R = 200$, $3\lambda/8$ spaced configuration was initially chosen as the middle ground. This was later de-scoped further to a 9 pixel, $R = 100$, 0.3λ spaced focal plane over concerns regarding detector collisions which is evidenced in Chapter 6.

A parallel plate capacitor LEKID was also introduced as an alternative design. A PPC resonator would significantly relax many of the constraints that the IDC LEKID imposes in a filter-bank setting. Firstly, since the PPC was shown to have effectively negligible cross-coupling, $\lambda/4$ wave spaced filter-banks or even smaller spacing would be possible with a frequency scheduling that could be substantially easier to decipher, e.g. grouped in frequency based on the filter-bank group.

Furthermore, the footprint of the FBS would be smaller for an equivalent readout frequency range due to the higher capacitance per unit area, hence it would be easier to achieve a more densely packed focal plane which would lead to faster mapping speeds. Another advantage is that the a more responsive detector can be achieved as there is minimal geometric inductance in the parallel plate relative to the long IDC geometries. The parallel plate was also shown to have a smaller resonant frequency sensitivity to lithography variation relative to the IDC, however the larger kinetic inductance fraction of the PPC resulted in an increased sensitivity to the inductor linewidth. Despite these clearly beneficial improvements, the main reason parallel plates are yet to be used in the majority of MKID detector arrays is their requirement for a dielectric material in order to form the parallel plates. Since deposited dielectrics are known to be responsible for significant TLS noise in detectors, until further developments in dielectric processing as has been the focus of recent studies with amorphous silicon carbide for example^{107,111}, or innovations in parallel plate fabrication are made, such as using the Si handle wafer as the dielectric, PPCs are likely to always fall short when compared to the noise performance of the IDC LEKID unless a very small inductor volume is used to counter the increased noise with increased responsivity¹⁰⁸. This is an avenue currently being explored for SPT-SLIM at the time of writing.

Chapter 5

Fabrication

This section aims to firstly provide a reference to aid in understanding the architecture of the IDC and PPC resonators as well as other key components of both the microwave and millimetre circuitry and secondly, to present the details of the fabrication processes. Whilst the fabrication masks were created as part of the work from this thesis, the processes and realisation were developed and conducted at the Center for Nanoscale Materials at Argonne National Laboratory. One can find further details on the various recent and on-going works from the ANL group in literature¹¹². The design uses an inverted microstrip on the millimetre circuit and CPW microwave readout. The inverted design reduces the number of steps prior to depositing the sensitive aluminium inductors in an effort to minimise microwave loss and noise, whilst also giving the added benefit of protecting the sensitive inductors from stray light with the superconducting Nb ground plane.

It was necessary to implement a step-down at some point in the circuitry in order to grow the IDC directly onto the silicon of the handle wafer, as discussed in Section 4.1, whilst also enabling the use of an OMT on a membrane. Given the thickness of the low stress SiN_x membrane layer ($2\text{ }\mu\text{m}$), there was concern around line breaks if this step-down occurred on the millimetre feedline as this feedline linewidth is $2.5\text{ }\mu\text{m}$. We therefore chose to implement the step-down between the LEKID inductor and IDC where niobium linewidths are $6\text{ }\mu\text{m}$. To further reduce the risk of line breaks the niobium sheet thickness for the device layer was targeted to 300 nm (including the NbN cap as discussed later). This in turn resulted in a concern that the thin aluminium layer would also struggle to step down off the niobium at the galvanic contact where the Nb microstrip feeds the detector input. Thus, a thicker than desired Al thickness of 50 nm was used instead of 30 nm . This would of course impact the responsivity of the detectors as well as the impedance matching (see Section 4.2 for more details), however mitigating total device failures was a priority over performance reductions until a working design was realised and enough devices were in cache to ensure there was something to deploy. Figure 5.2 shows a region of an FBS, with zoomed views

around the step-down, LEKID and filter geometries.

The fabrication process is detailed as follows with reference to the process flow cartoons shown in Figure 5.1. However, note that whilst this process flow is focused on the fabrication of an IDC SPT-SLIM sub-module device, it is also compatible for PPC devices providing the microwave readout circuit does not undergo the step-down processes (steps 2 and 3 below):

1. To begin, high resistivity ($> 10 \text{ k}\Omega \text{ cm}$) silicon wafers are obtained with a pre-grown $2 \mu\text{m}$ thick low-stress ($(150 \pm 50) \text{ MPa}$) SiN_x layer on top of a 450 nm SiO_2 layer.
2. The low stress SiN_x layer is first etched by a reactive ion etch (RIE) to remove material around the IDC capacitors and microwave readout.
3. The buried SiO_2 layer is then also removed in the same regions as the low stress SiN layer via a HF wet etch.
4. Then, a relatively thick layer of Nb ($\approx 170 \text{ nm}$) for the millimetre and microwave circuitry is deposited with a 30 nm NbN capping layer. Thick Nb is desirable as this keeps the sheet resistance and kinetic inductance low whilst also making it robust to the step-down. This layer is then patterned via a flourine-based ion etch.
5. 30 nm to 50 nm Al is then deposited for the LEKID inductors and lossy terminations and patterned with a bi-layer lift-off process.
6. The dielectric layer is then deposited, at the time this used the baseline of 300 nm thick Si-rich SiN_x ion beam assisted sputtering (IBAS) at a temperature of 20°C to avoid damaging the aluminium inductors. The dielectric is patterned with via an etch such that the IDCs are free of any dielectric.
7. The last deposition is for the Nb ground plane and is patterned via lift-off. This is necessary as otherwise the ground plane would be deposited directly onto the niobium IDC layer since the dielectric is removed.
8. The back side membrane layers are then etched using the same process as the frontside by RIE. For the sake of simplicity in the diagram below, these layers are completely removed in steps 8 and 9.
9. Finally, the OMT membrane is released by removing the Si and SiO_2 from the backside of the handle wafer. This is achieved with a deep reactive ion etch (DRIE) to remove the Si then a wet etch consisting of 10% HF buffered oxide is used to remove the buried SiO_2 layer.

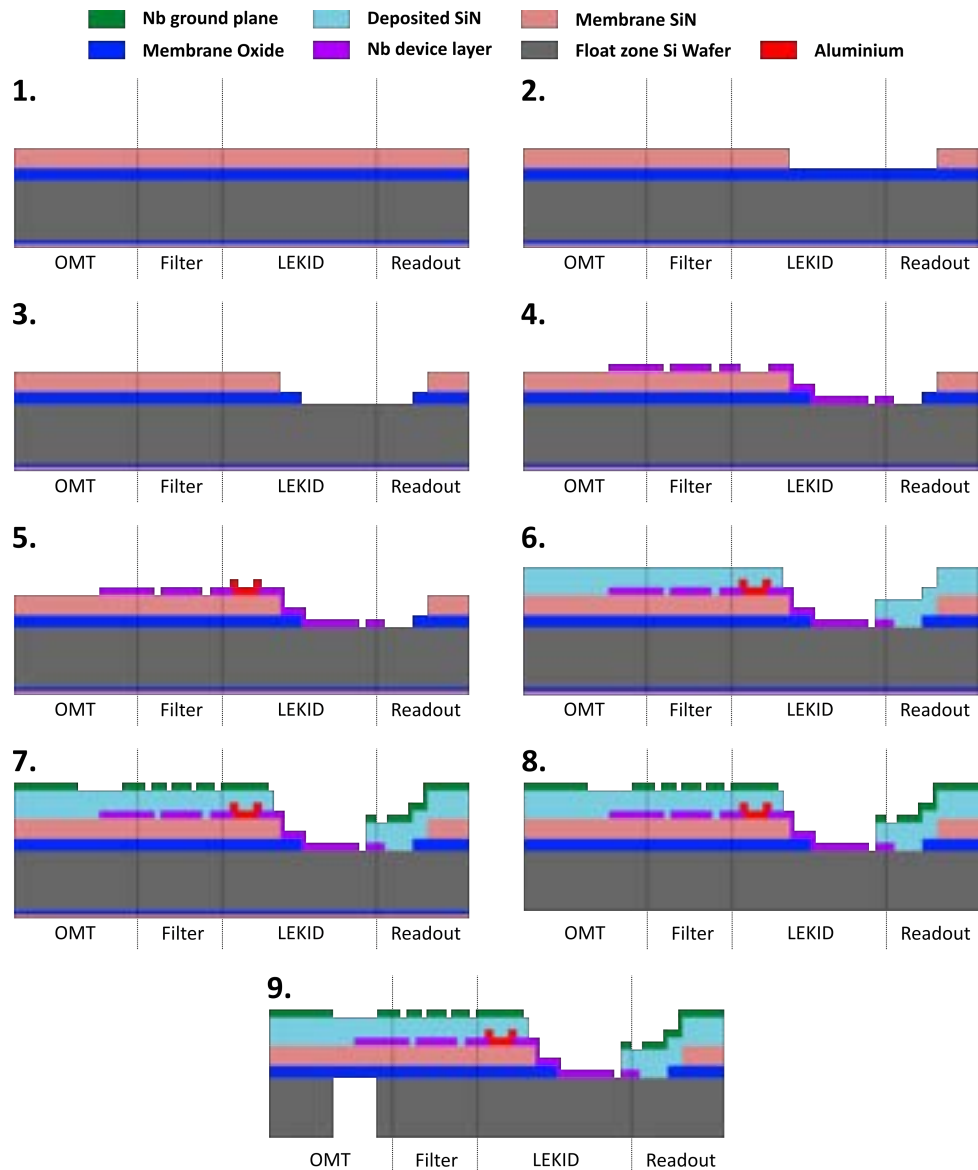


Figure 5.1. Wafer cross-section cartoons demonstrating the process flow used to fabricate the SPT-SLIM devices as per the description in the text. The cross-sections are split into approximate zones of key regions of the circuitry. Also note, the backside membrane layers should be the same thickness as the front side layers, but here are minimised for simplicity.

To ensure the quality of the aluminium film, it would ideally be the first material to be deposited as there are many studies that suggest the morphology of deposition surface has a significant impact on the quality of superconducting films^{113–116}, particularly for thin films (<50 nm), i.e. cleaner and smoother surfaces produce better films. However, the hybrid Al-Nb LEKID design (see Section 4.1) required a galvanic contact between the aluminium and niobium, but devices fabricated with the niobium layer following the aluminium yielded poor and inconsistent or open DC contacts between the two layers¹¹², even with the use of an ion mill. Instead, a solution was found by depositing the niobium first then adding an additional 30 nm of NbN which appeared to prevent oxidisation and thus allowing good galvanic contact without degrading the internal quality factors of the resonators.

Another one of the main difficulties with this architecture from a fabrication point of view was finding a dielectric that would work with the process flow with suitable electrical properties, namely loss tangent (at both microwave and millimetre frequencies). The importance for which is shown throughout this thesis with particular emphasis on limitations on the resolution and efficiency of half-wave filter-banks at millimetre wave, and less responsive and more noisy detectors at microwave. Studies have found a range of materials that show promise for low loss, for example, there is particular interest in amorphous silicon (a-Si) deposited via PECVD with measured loss tangents of $\tan \delta = 4 \times 10^{-5}$ to 5×10^{-5} at microwave frequencies^{111,112,117–119} and 2×10^{-4} at 350 GHz^{111,119}. Though clearly desirable properties, these high quality dielectrics typically involve temperatures above 150 °C which have been found to degrade the aluminium quality¹¹². Therefore, to improve the quality of the critical aluminium inductors by having aluminium as one of the first processes whilst enabling other features of the fabrication, such as the Al-Nb galvanic contact, a dielectric with low loss and low temperature deposition was needed. Si-rich SiN_x deposited at 100 °C deposited with PECVD showed promising results with a loss tangent of $\tan \delta = 2 \times 10^{-4}$ at ≈ 1 GHz. Unfortunately, this dielectric had adhesion issues such that the dielectric films were often peeling off after deposition. Hence, the more consistent Si-rich SiN_x dielectric deposited via an IBAS process was eventually favoured. At microwave frequencies, the loss tangent for this material was measured to be $\tan \delta = 2 \times 10^{-4}$ ¹¹². This is not as low as amorphous silicon and does not leave much or any room for the up to a factor of 10 increase in loss tangent at mm-wave as is typically observed¹¹⁹, however considering the deployment time constraints and its conformity with the aluminium requirements, this was taken as the baseline dielectric with further measurements at mm-wave to be conducted along with continuing dielectric study in parallel.

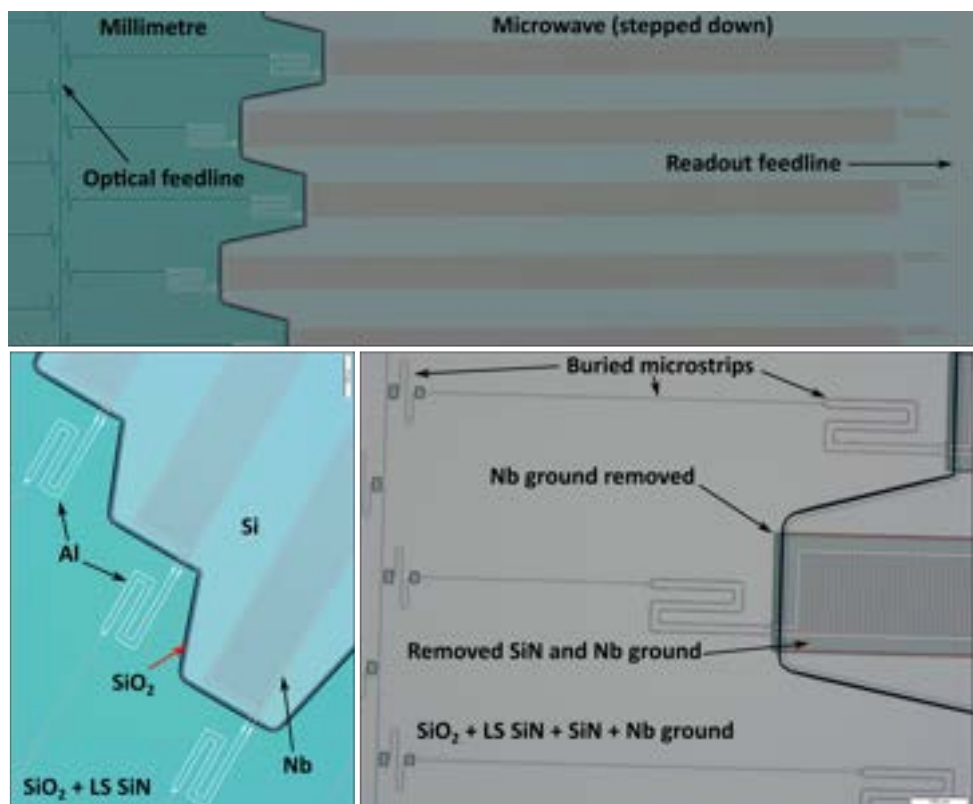


Figure 5.2. Micrographs of a SPT-SLIM device in an FBS region (top and lower left) before the SiN dielectric and Nb ground layers were deposited (up to step 6 in Figure 5.1) and (lower right) at the end of the fabrication process. To clarify, “LS SiN” refers to the low stress SiN_x membrane layer.

Dark Detector Characterisation

In this Chapter, a dark characterisation of LEKID architectures with three variations on the capacitor geometry is presented. Here, all resonators use the exact same aluminium inductor geometry. The device tested is of an $R = 200$ sub-module design with unreleased OMT membranes and hence has no optical capabilities and is from the tenth SPT-SLIM fabrication run at Argonne National Laboratory (SLIM10). This device, shown in Figure 6.1, consists of a Trio channel of nominal IDC resonators with a membrane step-down as presented in 4.1.3, these will be referred to as “IDC”. There is also a Duo channel of IDC resonators without a step-down, “IDC NS”, and finally a Trio of parallel plate capacitor resonators as were presented in Section 4.3, “PPC”. It is worth also observing the size difference between the IDC capacitor filter-banks and the PPC filter-banks, whereby the PPC filter-banks occupy almost half the physical space perpendicular to the mm-wave feedline. These three designs were of interest because the IDC design was the nominal design with the best anticipated noise performance, however this required the step-down off the membrane layers, hence if the IDC NS showed good noise performance then the step down would be unnecessary and simplify fabrication. Furthermore, as discussed in Chapter 4, the PPC provides many possible improvements such as negligible cross-coupling, reduced footprint, higher kinetic inductance fraction and also no step-down processes. Thus, the PPC would be a much better option if the noise performance was suitable.

Since all resonators are fabricated at the same time (same deposition layers) and the inductor geometries are identical, we can assume that the material parameters should be consistent (for example quasiparticle lifetime, sheet resistivity, dielectric constant etc.) and any differences in the performance of the resonators should purely be due to the architecture.

The goal of these measurements is to ascertain the suitability of each architecture as filter-bank detectors and compare the validity of the detector simulations. We have already seen that according to simulation, the PPC resonator should be more responsive than the IDC due to the

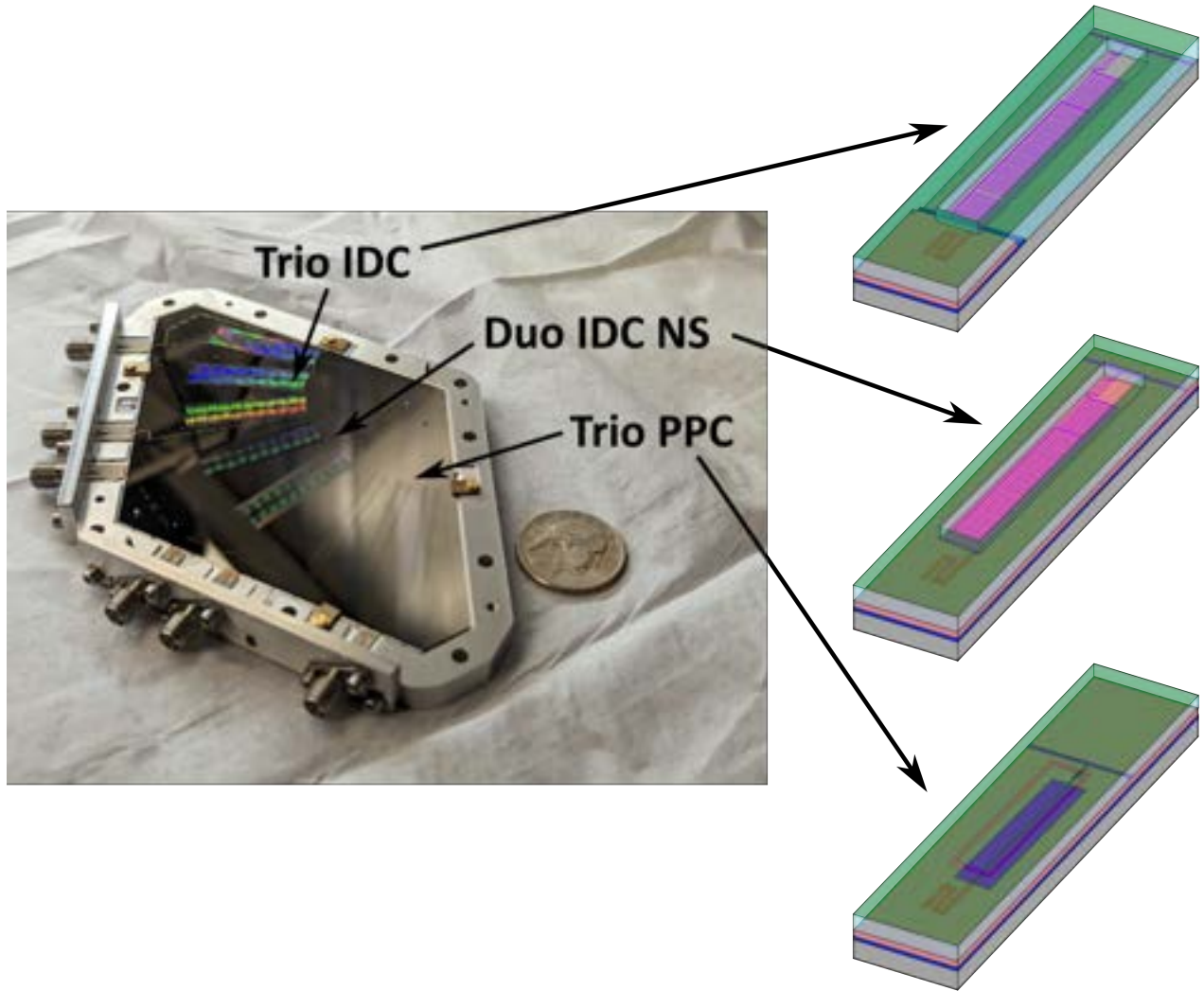


Figure 6.1. (Left) The SLIM10 prototype device installed in its testing box. The arrows indicate the three channels, a Trio of nominal IDC resonators with a step-down, “IDC”, a Duo of IDC resonators without a step-down, “IDC NS”, and a Trio of parallel plate capacitor resonators, “PPC”. The cartoons show roughly what each architecture looks like with layer colours matching the material stack shown in Chapter 5.

smaller geometric inductance resulting in a higher kinetic inductance fraction ($\alpha_k = 0.419$ compared to $\alpha_k = 0.117$) as well as having extremely small cross-coupling compared to the IDC. However, if the resonator noise in the frequency range of the observation band is too high such that the noise equivalent power (NEP) is above the photon noise limit then it is simply not possible to instantaneously tell the difference between the generation-recombination of quasiparticles due to noise fluctuations such as TLS or thermal changes to that of an incident photon. If the detectors are not photon noise-limited, this issue can be overcome by increased integration time, however, to some extent, this would negate the technology advantages of the on-chip spectrometer. By the end of this section we aim to present the noise equivalent power spectrum for each architecture,

whilst also presenting the end-to-end dark characterisation of the microwave circuit for each SPT-SLIM readout channel. The observing band is yet to be fully defined for SPT-SLIM, however, we will consider the NEP within the approximate observing band under typical SPT operation¹²⁰ between ≈ 1 Hz to 20 Hz, where the lower bound corresponds to the lowest source modulation frequencies for the largest scales, and the higher bound for the smallest scales.

For the measurements presented in this section, the device was installed into a BlueFors cryostat with a base temperature of 24mK. The RF-line configuration can be seen in the left hand side of Figure 6.2. The VNA measurements used the same warm RF chain to that shown for the homodyne schematic shown in the right hand-side of the figure. The IDC and PPC channels actually needed a second warm amplifier which was placed after the output variable attenuator since their bifurcation powers were approximately 10dB lower than for the IDC NS. Some measurements use the well established single tone or homodyne, readout technique to measure the on and off resonance noise spectrum. Here, a signal is generated with a synthesizer at the desired frequency. This signal is split into two via a 6dB splitter, one side passing through the cryostat chain before connecting to the RF port of the IQ mixer and the other directly connecting to the LO port. The mixer then outputs the In-phase (I) and Quadrature (Q) component voltages which are read with an ADC NI PXI-4461. Multi-tone measurements for noise were also taken using the RF-ICE board, which in very basic terms is effectively the described single tone procedure, just executed at multiple frequencies simultaneously. For further detail on this system, the reader is advised to see works by M. Rouble⁹⁴.

6.1 Detector yield, scatter and quality factors

Typically, the first set of measurements taken on any MKID readout channel when it is fresh out of fabrication will be to take an S_{21} VNA sweep and identify all the resonators on the feedline, generally using a peak finding algorithm. The broadband VNA S_{21} sweep for each device is shown in Figure 6.3.

Once identified, each resonator can then be swept individually to allow the fitting of a Lorentzian to extract measurements of the resonator f_0 and quality factors, Q_r , Q_c , and Q_t (total resonator Q , feedline coupling Q and dissipative losses Q respectively). The description of the forward transfer function of superconducting micro-resonators such as an MKID has been extensively derived and presented throughout literature in the field for both operation in the linear regime^{4,64,85,102,121} and also accounting for non-linearities^{122–124}. In the linear regime one can achieve good agreement by fitting Equation 6.1 to S_{21} data as a function of frequency, f .

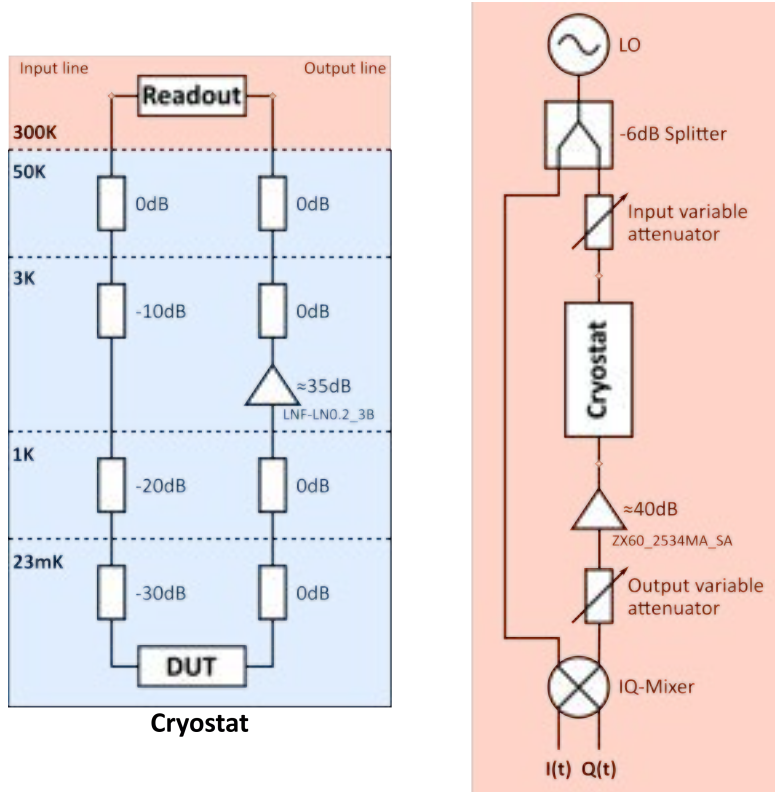


Figure 6.2. RF readout system schematic showing the RF component gains used in the cryostat (left) for attenuating thermal noise before the device at the sub-kelvin stage and then the low noise 4K amplifier on the output line. When taking measurements with the RF-ICE board, to enable enough power to bias multiple resonators close to bifurcation within the 0dBm maximum combined tone output, the 1K input attenuator was swapped for a 0dBm and the sub-kelvin attenuator changed was to 20dBm

$$S_{21}(x) = 1 - \frac{Q_r}{Q_c} \frac{1}{1 + 2jQ_r x} \quad \text{where} \quad x = \frac{f - f_0}{f_0} \quad (6.1)$$

However, since MKIDs are typically operated close to bifurcation¹²³, it is often more robust to fit a function that includes the non-linearities by applying the following parameterisation, $x = \frac{y}{Q_r}$ to Equation 6.1 where the parameter y is a cubic function expressed as¹²³,

$$4y^3 + 4y_0y^2 + y_0 + a = 0 \quad \text{where} \quad y_0 = \frac{f - f_0}{f_0} Q_r, \quad (6.2)$$

and has a single root solution (monotonic) in the linear regime, corresponding to when the non-linearity parameter, a is below $4\sqrt{3}/9$ and otherwise is multi-valued where the smallest real solution should be taken in the case of a sweep of increasing frequencies. This fitting method is used in the data presented in this section and example fits of an IDC and PPC resonator from

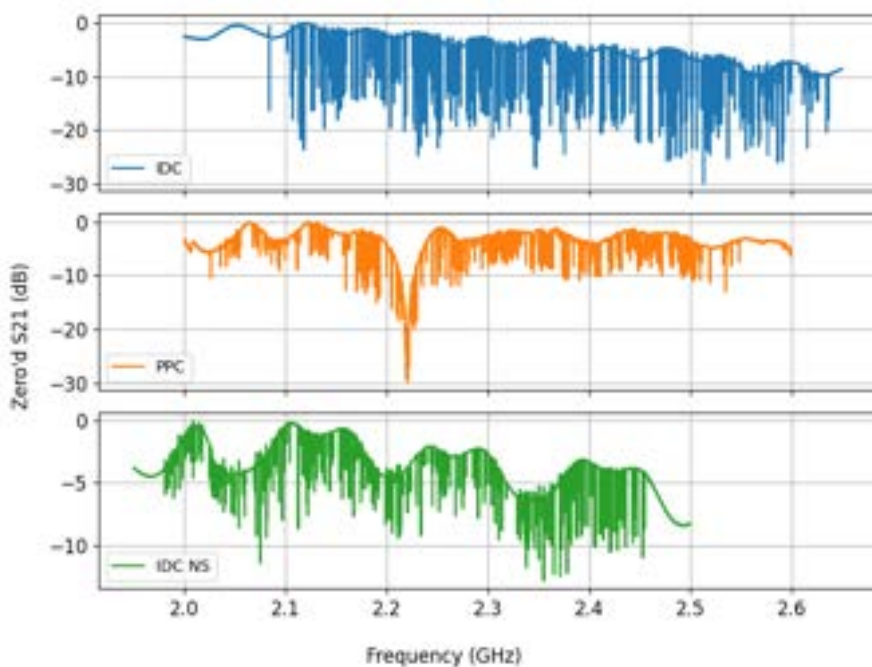


Figure 6.3. Broadband S_{21} sweeps for each device channel of the SLIM10 prototype. The IDC and PPC channels were designed to have 390 resonators yet yielded 361 and 355 respectively and the IDC NS yielded 247 resonators out of the designed 260.

SLIM10 at 200 mK with a range of bias powers is shown in Figure 6.4. Here, as expected, we can see that for the IDC resonator, Q_c is approximately constant with carrier power as is Q_i until bifurcation at which point Q_i begins to drop due to the readout power generating enough lossy quasiparticles to carry the resonating current. A slightly different trend is seen in the the PPC data where Q_i noticeably improves up to bifurcation as the readout power saturates TLS states as is seen in Pan et. al.⁹⁰ and then we see Q_i drop as losses in the metal occur in the bifurcated regime.

We define the “Full yield” as the percentage of resonators compared to the expected total that are present in the full band S_{21} sweep, this includes collided resonators as long as the peaks are clearly distinguishable. We will later constrain the yield to a “Useful yield” which represents the number of resonators that have at least a 10 linewidth separation from its neighbouring resonators. The value of 10 linewidths was chosen here as this is significantly above the cross-coupling threshold of a 2 linewidth shift and it allows for a large enough frequency window for baseline subtraction during Lorentzian fitting along with ensuring an off-resonance tone can be placed suitably far from the tone during noise measurements. It would be possible to use a smaller linewidth separation and this would improve the useful yield, however, given that the intended spacing for an $R = 200$ Trio channel with resonators of $Q_r = 5 \times 10^4$ is equivalent to approximately 30 linewidths, using increasingly packed resonators would increase the degree of

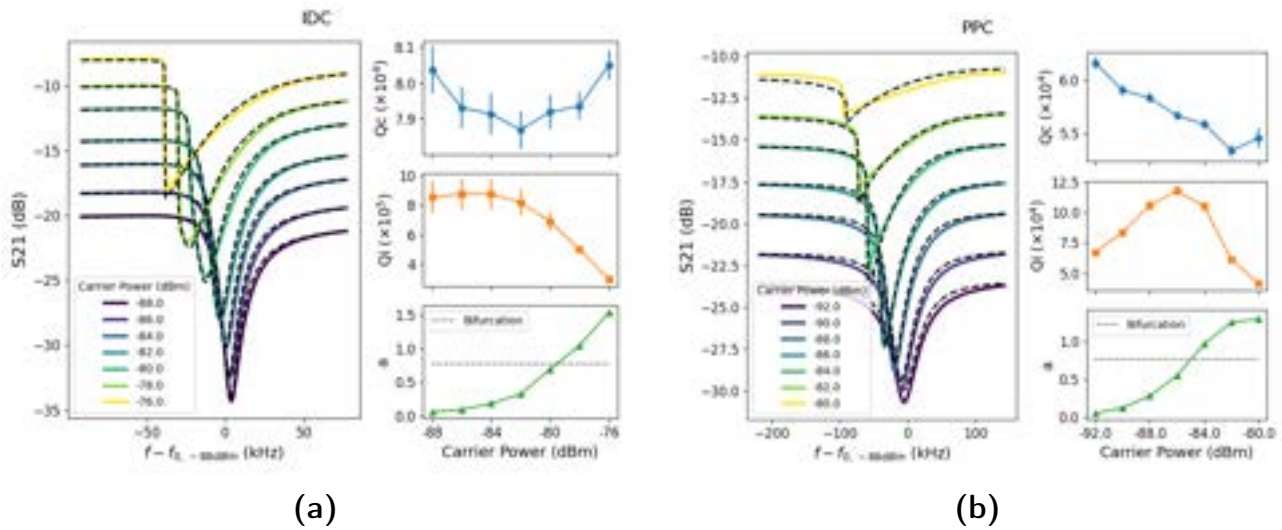


Figure 6.4. Demonstration of fitting the non-linear Lorentzian model to an IDC (left) and PPC (right) resonator from the SLIM10 device at 200mK for a variety of approximate bias powers at the device.

cross-coupling, especially for the IDC designs.

The three channels each had a very good full yield of 92.6 %, 95.0 % and 91.0 % for the IDC, IDC NS and PPC channels respectively. Plots of measured and expected resonant frequencies against the resonator index (ascending frequency order) can be seen in the left hand plots of shown in Figure 6.5.

One of the main issues that can arise when multiplexing resonators in the frequency domain within a limited readout bandwidth is when resonators collide. Collisions can render detectors unusable due to electrical cross-talk whereby carrier currents of a target resonator tone become modulated by the impedance changes in a nearby resonator. Effectively, a tone on one resonator would “see” a change in I and Q due to a change in another resonator, simply because of overlapping Lorentzian lineshapes. Varying frequency spacing will also impact the electromagnetic cross-coupling as described in Section 4.2. Since we were unable to identify each resonance to the physical location on the mask, it was not possible to map each measured f_0 to the expected. Thus preventing a direct measurement of the fractional scatter. We therefore first measured the f_0 separation and obtained the mean and standard deviations to be (1.53 ± 1.73) MHz, (1.66 ± 1.10) MHz and (1.48 ± 1.70) MHz for IDC, IDC NS, and PPC, respectively, the expected separation was designed to be 1.22 MHz. These results are shown in the right hand plots of Figure 6.5. Despite the mean separation being larger than the expected, there is a large standard deviation to the mean which results in a significant number of collisions as the frequency separation is on the same order of magnitude as the frequency scatter. It is often common to define the scatter as a fractional frequency scatter, we can obtain this by halving the separation standard deviation (as

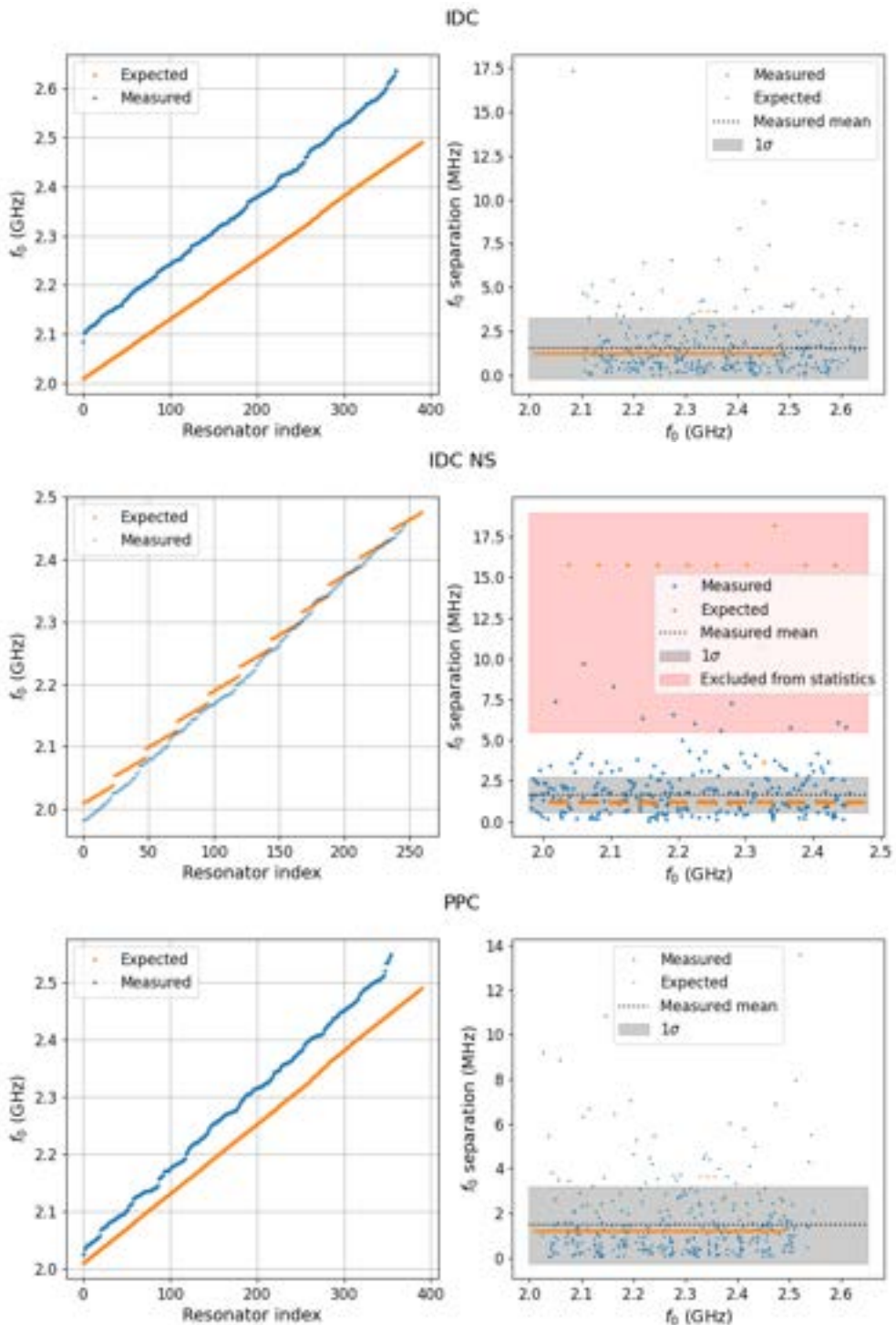


Figure 6.5. SLIM10 frequency scatter results: (Left column) Resonator f_0 compared to the designed frequencies. (Right column) The frequency separation of the resonators

the f_0 separation combines the scatter of two resonators) and then divide by a resonant frequency. Hence, for a resonator with $f_0 = 2.25$ GHz, the three channels each suggest a fractional frequency shift of 3.84×10^{-4} for IDC, 2.44×10^{-4} for IDC NS and 3.79×10^{-4} for PPC. The Duo IDC

NS channel consists of two thirds of the resonant frequencies seen in the Trio channels, for this reason there are several f_0 separation data points which are significantly higher than the rest and these frequencies are removed from the statistics as indicated by the red region in Figure 6.5. Surprisingly, these values for scatter are approximately two orders of magnitude smaller than the expected fractional shift obtained from simulation as per Figure 4.15 in Section 4.3, which could suggest our expected random linewidth variation is lower than anticipated. However, an alternative, and more likely interpretation of this data is that the expected frequency scatter on the order of 20 MHz (0.01 fractional shift) for these resonators from the tolerance analysis is approximately ten times larger than the designed frequency separation and would therefore result in the observed scatter being limited to the average tone separation. Therefore, the collision rate will be a probabilistic function such that smaller designed frequency separations and wider resonances (lower Q) will result in more collisions. This may explain why the scatter appears roughly the same between the various architectures, despite the differences in capacitor geometries. This would therefore suggest a true fractional scatter closer to 0.01, however other devices of different architectures yet similar fabrication processes demonstrated a similar order of magnitude of fractional frequency shifts to these measured values such as McGeehan et. al., 2016¹¹⁰.

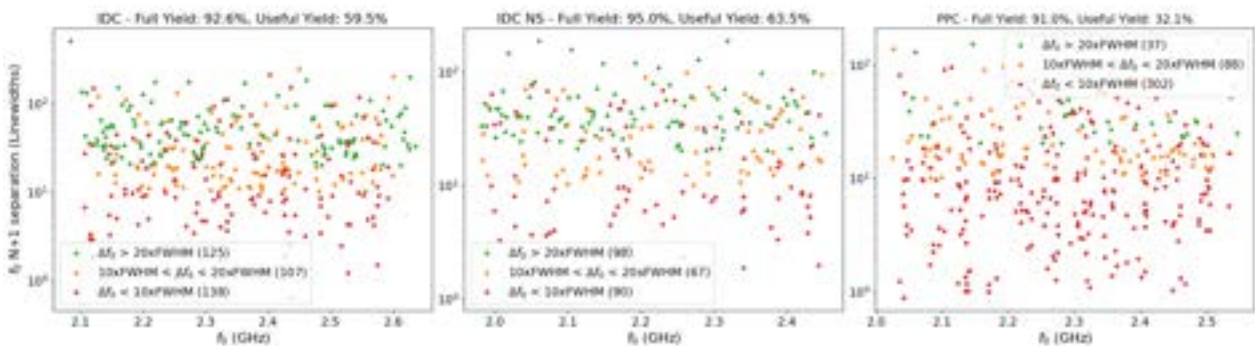


Figure 6.6. (left) IDC, (centre) IDC NS and (right) PPC. Scatter plots of the f_0 separation between each resonator and its next frequency neighbour ($N+1$). Each plot shows the results for one of the SLIM10 channels split into three groupings of linewidth separations indicated by the colours. These groups account for the $N - 1$ spacing as well.

As a result of the scatter and the resonator quality factors, we further reduce our device yield to the “Useful Yield” as described above. The outcomes are presented in Figure 6.6, showing the useful yields as 59.5 %, 63.5 %, 32.1 % for the IDC, IDC NS and PPC channels respectively. The linewidth separation is obviously dependent on the resonator Q_r distribution (shown in Figure 6.7), hence why, compared to the IDC channel, the IDC NS with a lower Q_r has a similar useful yield despite having less detectors within the readout bandwidth and the PPC has much lower useful yield as this channel has approximately the same number of resonances as the IDC but also wider Lorentzians. Regardless, a useful yield of around 60 % is undesirable and this number

of collisions relative to the full yield was one of the motivators for moving to a lower detector count via reducing the filter-bank resolution to $R = 100$ until a better handle on resonator scatter would be achieved. Of course, there has been demonstrated success in literature with post fabrication resonator trimming to recover the resonators lost to collisions^{110,125}, however, as mentioned previously, we initially chose to avoid this due to concern over the fragility of the OMT membrane or logistic concerns with taking dark measurements prior to the final fabrication processes (membrane release and releasing the device from it's carrier wafer).

Taking a closer look at the quality factor distributions, it is apparent that the differences in Q_r stem from the resonator losses since the Q_c distributions are relatively similar, yet Q_i is an order of magnitude smaller for the IDC NS and PPC compared to the IDC, resulting in the former architectures being Q_i dominated where it is more desirable to be Q_c dominant as in the IDC case. This is not unexpected since the PPC will experience dielectric loss through the capacitor plates, as would the IDC NS given the IDC fingers reside on a lossy dielectric which conversely is not the case for the IDC that steps down on to the bulk silicon of the handle wafer.

6.2 Homodyne noise measurement

The dark noise power spectral density (PSD) of a resonator is a useful tool for probing the resonator characteristics. To create a resonator with a sensitivity limited by the photon noise (photon limited), one must understand the components contributing to the detector noise of which typically falls into three categories. Firstly, MKIDs typically exhibit a low frequency noise component that exhibits an inverse frequency relation ($1/f^n$). This is commonly considered to be caused by the excitation of two-level system states¹²⁶ by the readout microwaves in a surface layer^{85,127} within the region of strong electric fields around the resonator⁹³. Whilst a microscopic theory for TLS is yet to be developed, multiple studies have been able to characterise the magnitude of the TLS noise via observing the excessive low frequency noise^{128–130}.

Secondly, when the $1/f$ noise is sufficiently suppressed at higher frequencies it is possible to observe a shelf in the PSD due to the generation-recombination rate of quasiparticles within the superconductor^{102,127}. In dark thermal equilibrium the number of quasiparticles in a superconducting volume, V at a temperature, T such that the thermal energy is lower than the superconducting energy gap, Δ_{sc} is given by

$$N_{qp} = 2N_0 \sqrt{2\pi k_B T \Delta_{sc}} e^{-\frac{\Delta_{sc}}{k_B T}}, \quad (6.3)$$

where N_0 is the single spin density of states typically quoted as $N_0 = 1.72 \times 10^{10} \mu\text{m}^{-3} \text{ eV}^{-1}$ for

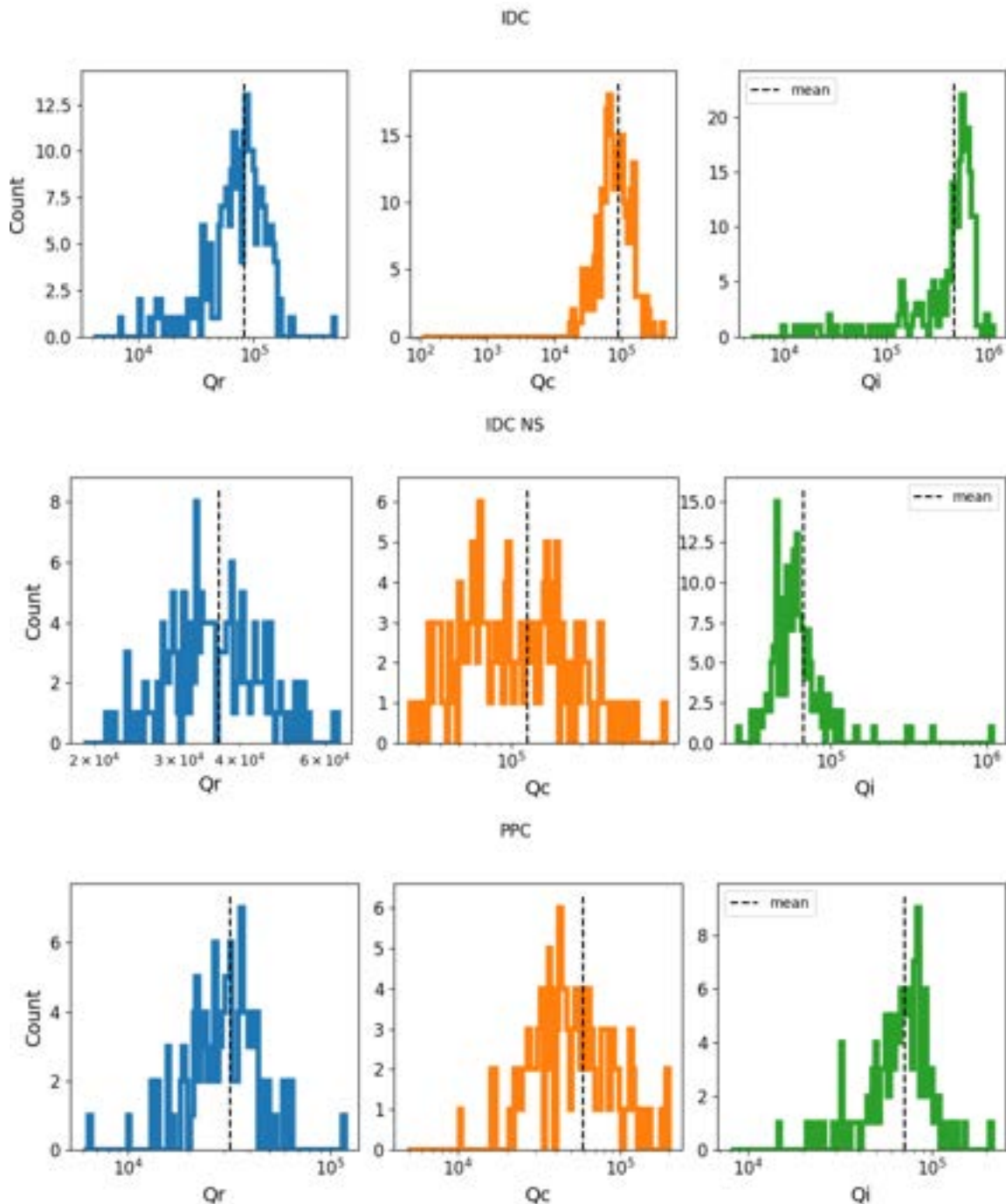


Figure 6.7. SLIM10 quality factor distributions for (top row) IDC, (middle row) IDC NS and (bottom row) PPC with mean Q_r values of $(8.26 \pm 4.13) \times 10^4$, $(3.07 \pm 0.75) \times 10^4$, $(3.22 \pm 1.39) \times 10^4$ respectively and Q_i 's $(4.55 \pm 2.05) \times 10^5$, $(4.48 \pm 1.11) \times 10^4$, $(7.07 \pm 2.71) \times 10^4$ respectively.

aluminium¹²⁷. We use the superconducting properties for aluminium as they will be dominant over the niobium since the Al quasiparticle lifetime is significantly longer^{131,132}. Of course, in practice there are constant thermal fluctuations that cause fluctuations in the quasiparticle population

which can therefore be observed as a modulation of the I and Q signal with a homodyne-like readout for frequencies up to the dominating time constant of the resonator. The power spectral density of these number fluctuations is given by a lorentzian spectrum as¹³¹

$$S_N(f) = \frac{4N_{\text{qp}}\tau_{\text{qp}}}{1 + (2\pi f\tau_{\text{qp}})^2}, \quad (6.4)$$

where τ_{qp} is the quasiparticle lifetime in the superconductor. Furthermore, the PSD of a resonator observable such as fractional frequency shift, x can be expressed as

$$S_x(f) = S_N(f) \frac{(dx/dN_{\text{qp}})^2}{1 + (2\pi f\tau_{\text{res}})^2}. \quad (6.5)$$

Here, τ_{res} is the resonator ringdown time given by the $\tau_{\text{res}} = \frac{Q_r}{\pi f_0}$. Hence, if the power spectrum of the observable is dominated by the quasiparticle fluctuations, the G-R portion of the PSD will present a “knee” at which the noise rolls off according to τ_{qp} , otherwise the roll-off would occur at τ_{res} . Thus, it is possible to use this roll-off feature to fit for the time constant of the resonator and ideally probe the quasiparticle lifetime as first demonstrated by de Visser 2011¹³¹.

Finally, the noise spectrum will then roll off to the next dominating noise source which is typically due to the thermal noise of the 4 K low noise amplifier.

Studies^{110,130} have shown it is possible to fit a general expression for the fractional frequency shift power spectrum S_{xx} that accounts for these three contributing terms and is given by

$$S_{xx}(f) = \left(\frac{A + Bf^{-n}}{1 + (2\pi f\tau)^2} + C \right). \quad (6.6)$$

In this expression, the coefficient A is the G-R component, the Bf^{-n} term is the low frequency noise term and C accounts for the system noise level. This expression using values on a similar order of magnitude as the PSDs shown later in this section can be seen in Figure 6.8 along with the PSD of the three separate components which is obtained by setting the other coefficients to zero.

There are many resources that describe in detail the process of taking a noise measurement of an MKID resonator^{102,121,127}, the reader is directed to these for further, in depth detail. As described above, we place a tone via a signal generator either on resonance (determined by sweeping I and Q around resonance and obtaining the frequency at the maximum in $\frac{dI_{\text{sweep}}}{df}^2 + \frac{dQ_{\text{sweep}}}{df}^2$) or off resonance. I and Q are then sampled at a given sampling rate for some specified duration to obtain the timestreams of $I(t)$ and $Q(t)$. In the following homodyne measurements we used

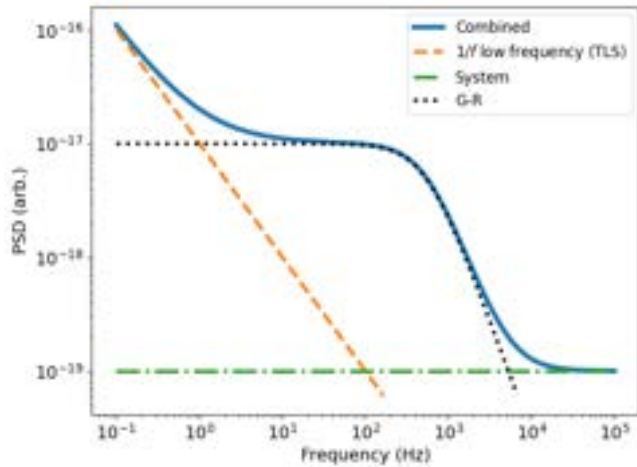


Figure 6.8. Example breakdown of the three components contributing to the on-resonance detector noise power spectrum using the model expressed by Equation 6.6. The combined series uses $A = 1 \times 10^{-17}$, $B = 1 \times 10^{-17}$, $n = 1$, $C = 1 \times 10^{-19}$, $\tau = 300 \times 10^{-6}$, then all coefficients (A, B, C) are set to zero excluding A for the G-R term, B for the low frequency term and C for the system noise term.

a sampling rate of 1 kHz for 10 s to sample the lower frequency spectrum and 0.2 MHz for 1.5 s to sample the high frequency spectrum, with three and 20 repeats, respectively. For high signal-to-noise resonances it is possible to use the following expression to obtain the perturbation in resonant frequency, $\delta f(t)$ as a function of time, t , for each IQ pair¹⁰²,

$$\delta f(t) = \frac{I(t)dl_0 + Q(t)dQ_0}{dl_0^2 + dQ_0^2} - j \frac{I(t)dQ_0 - Q(t)dl_0}{dl_0^2 + dQ_0^2}. \quad (6.7)$$

The variables denoted with a 0 subscript are the values of the I and Q frequency derivatives from the resonator sweep at the resonant or synthesizer frequency. e.g. $dl_0 = \frac{dl_{\text{sweep}}}{df}(f = f_0)$. The fractional frequency timestream is then obtained by dividing the f_0 perturbation by the resonant frequency ($x(t) = \delta f(t)/f_0$). Finally, the power spectrum is then obtained by taking the Fourier transform of $x(t)$ and taking the mean PSD across the repeats to reduce the variance at each frequency. The real and imaginary component provides the frequency and dissipation power spectrum respectively. An additional processing step was performed on the I and Q timestreams in the case where a glitch or step was observed. These are commonly due to electrical glitches or the arrival of high energy cosmic particles such as muons being absorbed in the wafer and breaking Cooper pairs. These glitches were removed by setting a window of data around the glitch to the mean timestream value. Figure 6.9 presents the data from an IDC resonator from SLIM10 at base temperature. A clear feature in the PSD shown is the various peaks at particular frequencies. Excluding the peak at mains electricity frequency of 50 Hz, we are confident that the root cause of these microphonics is vibrational pick-up since the peaks are no longer present when

the pulse tube cooler (PTC) and driver are switched off or exacerbated if the cryostat is knocked. We also saw some improvement by altering the wafer clamping scheme to include MUSCAT style pogo pins¹³³. Curiously this was only an issue with our IDC step-down resonators, however this will be discussed further in this section. The noise spikes caused some difficulties when trying to fit Equation 6.6 to the PSDs. Since the white noise level did not change when the PTC was switched off, the noise spikes were therefore attempted to be processed out of the spectra for fitting.

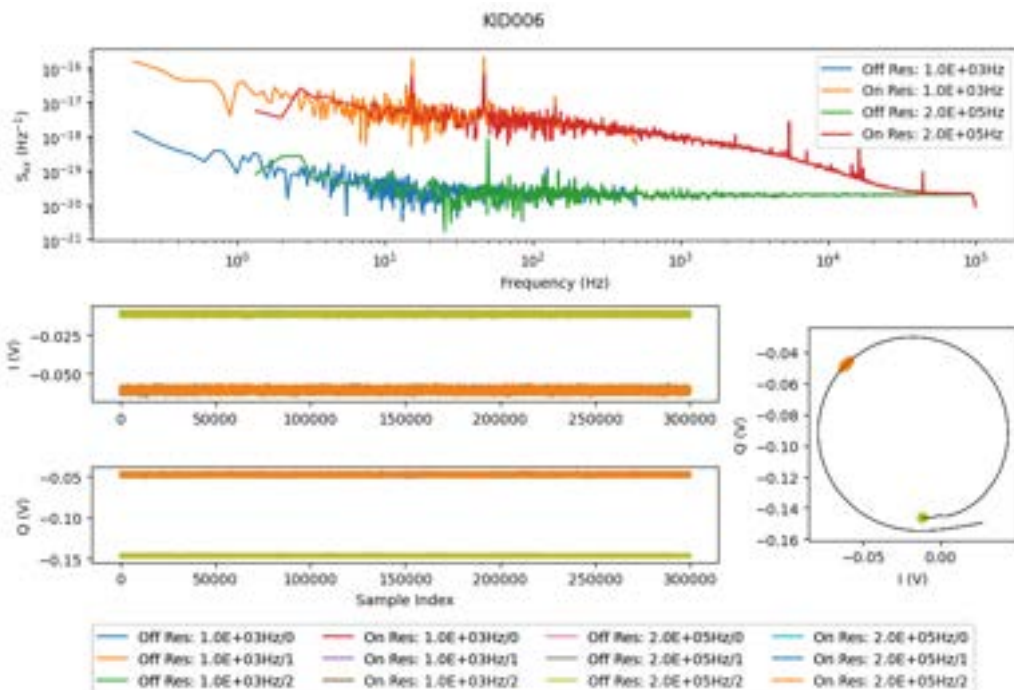


Figure 6.9. Example noise data for a resonator with $f_0 = 2.114$ GHz and $Q_r = 7.7 \times 10^4$ from the SLIM10 IDC device at the base temperature of 24 mK. The black line in the figure in the bottom right is the I/Q sweep data and the coloured “balls” show the entire on and off resonance timestream values. The legend labels state whether the data is on or off resonance, followed by the sampling rate. The S_{xx} spectra have been logarithmically re-sampled into 2000 bins.

The same noise measurements were taken at a range of temperatures for a handful of detectors from each channel. The on-resonance PSD temperature sweep for the same resonator as that shown in Figure 6.9 is shown in Figure 6.10. Here, the noise spikes have been somewhat removed by applying a similar window averaging technique as implemented to the timestreams, the high and low sampling rate spectra have been combined and re-sampled into 500 bins. At around 500 Hz there is a notch due to the anti-aliasing filter from the low sampling rate timestreams which should therefore be ignored.

Regarding the quasiparticle lifetime, as temperature decreases it is expected that τ_{qp} increases due to the decrease in quasiparticle density, i.e. there are fewer quasiparticles and it takes longer

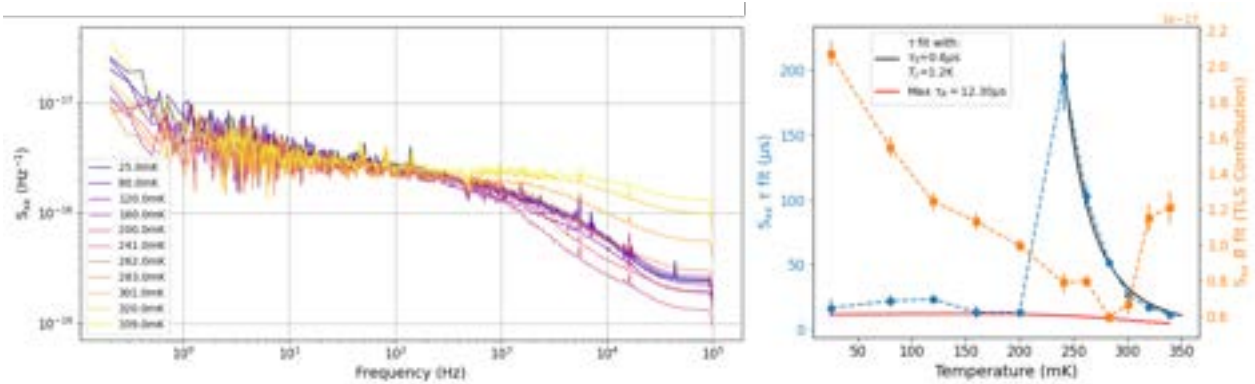


Figure 6.10. (Left) Fractional frequency noise spectra as a function of temperature for an IDC resonator from the SLIM10 device. (Right) Fit values of τ and B from Equation 6.6 for the S_{xx} spectra to the left as a function of temperature. Also shown by the red line is the ring down time of the resonator as calculated from fit values of Q_r and f_0 at each temperature which reaches a maximum value of $12.8\text{ }\mu\text{s}$. Finally, the black line is a fit to the quasiparticle lifetime with Equation 6.8, finding good agreement with $\tau_0 = 0.6\text{ }\mu\text{s}$ and $T_c = 1.2\text{ K}$.

for one to find another and form a Cooper pair. This increase is in τ_{qp} is expected to be exponential as per Equation 6.8 until becoming limited by other relaxation mechanisms^{134,135} and will therefore present a saturation plateau¹³⁶ at lower temperatures. As a result, for a noise spectrum dominated by quasiparticle fluctuations, we expect to see the roll-off occur at higher modulation frequencies and then decrease with temperature to a certain value in line with the saturation of τ_{qp} . However, an interesting phenomena presented itself in all of the resonators we measured, regardless of being of IDC, IDC NS or PPC architecture (see Figure 6.11). As shown in the left hand side of Figure 6.10, we do see a roll-off at high frequencies which appears to decrease in frequency with temperature until around 200 mK where below this temperature it appears that the roll-off snaps back to a higher frequency value and is approximately constant thereafter. This is further demonstrated in the right panel of Figure 6.10, showing values for τ and B extracted from a fit to Equation 6.6. Here, we see the expected exponential increase in τ , then the dominant time constant drops to be within the range $13.1\text{ }\mu\text{s}$ to $23.4\text{ }\mu\text{s}$. The resonator ringdown time as calculated from fit values of Q_r and f_0 at each temperature is also shown in red which is approximately constant at $\tau_{\text{res}} = (12.0 \pm 1.7)\text{ }\mu\text{s}$ in the low temperature range, which is within 1 standard deviation of the lower bound for the low temperature time constant from the PSD fits.

Furthermore, to validate that the increasing time constant at the higher temperatures is in fact the quasiparticle lifetime we can fit this data to the following expression¹³⁷,

$$\tau_{\text{qp}} = \frac{\tau_0 N_0 (k_B T_c)^3}{4 n_{\text{qp}} \Delta_{\text{sc}}^2}, \quad (6.8)$$

and obtain a value for the superconducting critical temperature, T_c and the electron-phonon interaction time τ_0 . Here, n_{qp} is the quasiparticle number density (N_{qp}/V). We find good agreement with a value of $\tau_0 = (0.6 \pm 0.1) \mu\text{s}$ with a $T_c = 1.2 \text{ K}$, which is consistent with other studies¹³⁰ using similarly fabricated aluminium. Therefore, it is reasonable to conclude that the measurements show two regimes, one where the resonator time constant is dominated by quasiparticle fluctuations at higher temperatures and the other which is dominated by the resonator ringdown time. As shown in Figure 6.11, the three architectures show similar trends yet with a slight difference around the regime switch. The largest value we were able to measure for the aluminium quasiparticle lifetime was $(647 \pm 86) \mu\text{s}$ with an IDC NS resonator. It became increasingly difficult to measure timestreams above 300 mK for PPC resonators as the amplitudes became very suppressed, resulting in large signal-to-noise.

The exact cause for this switching behaviour remains to be understood, however the fact that this is seen for all three architectures suggests the source is likely a common feature in all three, i.e. linked to the inductor. Furthermore, given the values of B from the fits, a qualitative conclusion could be drawn that at the lower temperatures, the resonator is operating in a regime of higher low frequency noise which sufficiently “hides” the G-R plateau whilst the roll-off is at lower modulation frequencies. Then, when the quasiparticle lifetime decreases such that the roll-off is pushed to higher frequencies and the level of low frequency noise is sufficiently reduced, the G-R plateau and quasiparticle lifetime roll-off becomes visible. This result is also indicative that the fitting model and method presented here should be further extended to include both time constants. As previously mentioned, it is commonly considered that the low frequency noise is caused by TLS states, however, the next section will present evidence that the different architectures show noticeably different degrees of TLS behaviour.

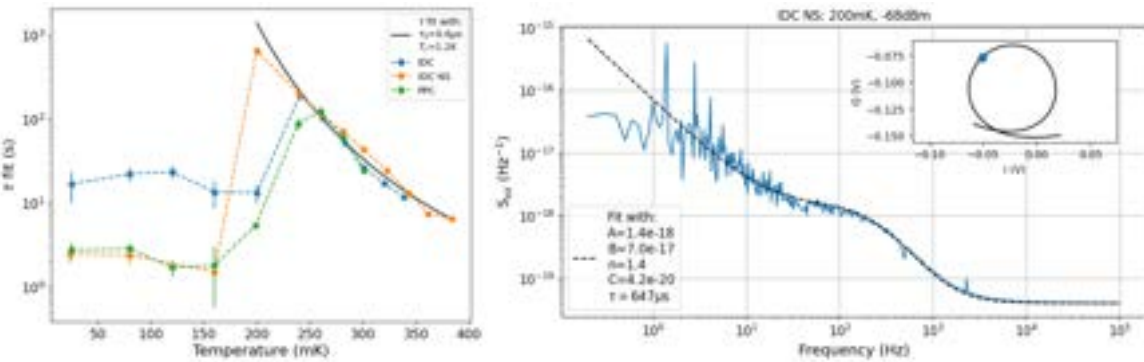


Figure 6.11. (Left) Noise PSD time constant fit results for IDC, IDC NS and PPC resonators with base temperature $Q_r = 7.7 \times 10^4$, 1.53×10^4 , and 3.96×10^4 and $f_0 = 2.114 \text{ GHz}$, 2.171 GHz , and 2.234 GHz respectively. (Right) Plot showing the fit to the IDC NS noise spectrum at a temperature of 200 mK.

6.3 Kinetic inductance fraction and dark responsivity

Another parameter that is necessary to determine in order to be able to calculate the dark NEP is the responsivity of a detector. Here, we define the responsivity of a detector as the fractional frequency shift, x per Watt of power, P , which can be calculated by recognising that

$$R = \frac{dx}{dP} = \frac{dx}{dN_{qp}} \frac{dN_{qp}}{dP}. \quad (6.9)$$

The latter product of the above expression can be calculated providing the quasiparticle lifetime is known since the power absorbed for pair breaking has been derived as^{102,127}

$$P = \frac{\eta_{pb}\tau_{qp}}{\Delta_{sc}} \rightarrow \frac{dN_{qp}}{dP} = \frac{\eta_{pb}\tau_{qp}}{\Delta_{sc}}, \quad (6.10)$$

where η_{pb} is the pair breaking efficiency associated with the absorbed power which for photon energies in the range of $2\Delta_{sc} < h\nu < 4\Delta_{sc}$ can be approximated as $2\Delta_{sc}/h\nu$ ¹³⁸, where ν is the photon frequency.

Therefore, it is then possible to calculate the dark responsivity by measuring the fractional frequency shift as a function of the number of quasiparticles which in the dark setting can be obtained as a function of temperature given Equation 6.3.

The following results were obtained by taking VNA sweeps around each resonator at a range of temperatures. The list of resonators used for each channel in these measurements were derived from those that contributed to the “useful yield” presented in Section 6.1. This was simply because these resonators would be easiest to track over a temperature range as they were suitably spaced from other resonators. This was not perfectly executed, particularly at higher temperatures where resonances become increasingly shallow such that the measurement program would mistake noise glitches or other non-resonator features for the resonator. Representative examples for each architecture can be seen in Figure 6.12. Despite this, after discarding the poorly tracked resonators, suitably large sample sizes of 154, 128, and 58 for the IDC, IDC NS and PPC channels respectively were obtained. Interestingly, as evident from the dip depths in Figure 6.12, the internal losses of these resonators appears to continuously improve all the way down to base temperature without presenting the commonly observed improvement in Q_i due to TLS saturation before the temperature increases sufficiently for the quasiparticle losses to dominate¹³⁹. This is particularly expected for resonators with a large presence of two level systems, which is the case for the PPC resonators as indicated by the large back-bending in Figure 6.13a, a trait associated with the presence of TLS⁹³. This could be caused by the quasiparticle losses dominating even at

low temperatures due to the small inductor volume or simply that insufficiently small temperature steps were used.

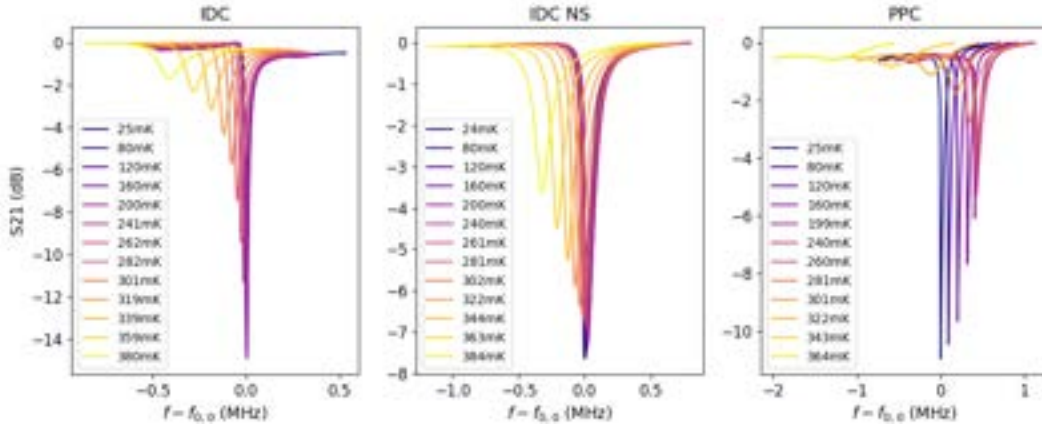


Figure 6.12. Example S_{21} measurements for resonators from each SLIM10 channel over a range of temperatures. To easily compare between resonators, the S_{21} values have been offset by the maximum value to “zero” the spectrum.

Here, we define the fractional frequency shift as the difference between the resonant frequency at a given temperature, $f_{0,T}$, and the lowest temperature resonant frequency measurement, $f_{0,0K}$, hence, $x = \frac{f_{0,T}}{f_{0,0K}} - 1$. Figure 6.13 shows the mean fractional frequency shift for each architecture population as a function of temperature or the number of quasiparticles in the inductor volume of $135 \mu\text{m}^3$ (50 nm thick film) as calculated by Equation 6.3. Using these results, values for the kinetic inductance fraction, α_k as well as the dx/dN_{qp} term of Equation 6.9 can be obtained.

The first MKID demonstration⁴ shows that an increase in surface inductance of a superconductor, L_s , due to increase quasiparticles will result in a reduction in the resonant frequency as a function of the kinetic inductance fraction ($x = 0.5\alpha_k\delta L_s/L_s$). Various works^{95,102,121,127} present in detail how the Mattis-Bardeen theory can be used to equate the perturbation in surface impedance to superconductor properties (N_0 , Δ_{sc} , n_{qp} , T etc.). The model was taken further to include the effect of a modification to the dielectric constant due to TLS state coupling to resonator electric fields as argued by Gao et. al. 2008¹⁴⁰. As with the data shown in Figure 6.13a, this model, as expressed in Equation 6.11, has shown good agreement with various results^{90,93,141,142}. We fit the $x(t)$ with the following expression,

$$x(T) = -\frac{\alpha_k n_{\text{qp}} S_2(f = f_0)}{4\Delta_{\text{sc}} N_0} + \frac{F\delta_{\text{TLS}}^0}{\pi} \left[\Re \Psi \left(\frac{1}{2} - \frac{\hbar f_0}{jk_B T} \right) - \log \left(\frac{\hbar f_0}{jk_B T} \right) \right], \quad (6.11)$$

where the second term is the TLS component consisting of the real part of the digamma function, Ψ , the intrinsic TLS loss term δ_{TLS}^0 and the energy filling factor in amorphous dielectrics, F . The

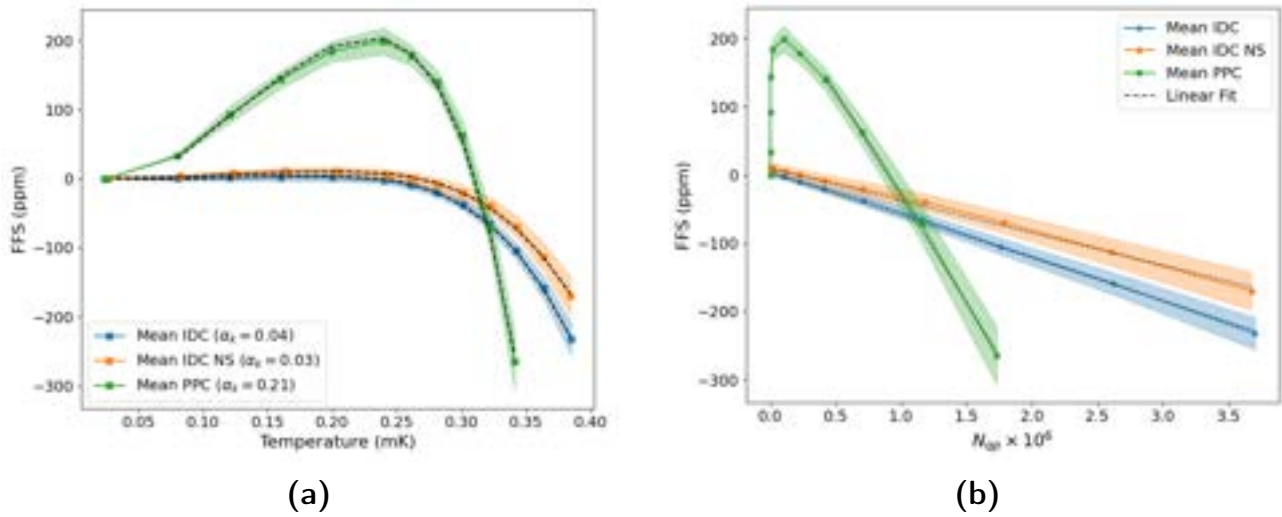


Figure 6.13. Mean fractional frequency shift for populations of IDC, IDC NS and PPC resonators with the coloured regions representing one standard deviation. (Left) Showing FFS as a function of temperature with the dashed lines showing the fits for the kinetic inductance fraction, α_k accounting for the TLS contribution to the so called “backbending” as per Equation 6.11. (Right) Straight line fits to the linear portions of the FFS as a function of quasiparticle number to obtain values for the term dx/dN_{qp} .

first term is from the Mattis-Bardeen derived expression for a perturbation in surface impedance and contains the parameter S_2 which is expressed as¹⁰²,

$$S_2 = 1 + \sqrt{\frac{2\Delta_{sc}}{\pi k_B T}} I_0(\xi) e^{-\xi} \quad \text{where} \quad \xi = \frac{\hbar\pi f_0}{k_B T}, \quad (6.12)$$

containing the zeroth order Bessel function of the first kind, I_0 . We fit to Equation 6.11 using $F\delta_{\text{TLS}}^0$ as a single value since we are only interested in extracting the kinetic inductance fraction and F and δ_{TLS}^0 are degenerate in $x(T)$ vs. T . We measure the mean values and standard deviation for α_k as 0.042 ± 0.004 , 0.033 ± 0.005 , and 0.216 ± 0.015 for the IDCs IDC NSs and PPCs, respectively. These values are substantially lower than the simulated values presented in Section 4.1.3 for the IDC (0.117) and Section 4.3 for the PPC (0.419), suggesting the values used for L_k in simulation were incorrect. However, the relative difference between IDC and PPC is roughly consistent. The distributions for α_k throughout the sampled populations can be seen in the right panel of Figure 6.14.

Returning to measuring responsivity, we can fit a straight line to the linear portion of the $x(N_{qp})$ data as demonstrated in Figure 6.13b. The start of the linear section the fit can use depends on the degree of TLS contribution, for the IDC this is effectively the full data range, however the TLS states only begin to saturate from around 280 mK for the PPC, hence only the last four data points are used. With the value of the gradients as dx/dN_{qp} and the expression for dN_{qp}/dP from

Equation 6.10 with the values $\eta_{pb} = 0.6$, $\tau_{qp} = 647 \mu\text{s}$ and $\Delta_{sc} \approx 1.764 k_B T_c$ with $T_c = 1.2 \text{ K}$, the measured responsivity mean and standard deviation for the three architectures were $(834 \pm 80) \text{ FFS } \mu\text{W}^{-1}$, $(645 \pm 90) \text{ FFS } \mu\text{W}^{-1}$, and $(3816 \pm 313) \text{ FFS } \mu\text{W}^{-1}$, respectively. The distribution for the population is shown in the left handside of Figure 6.14.

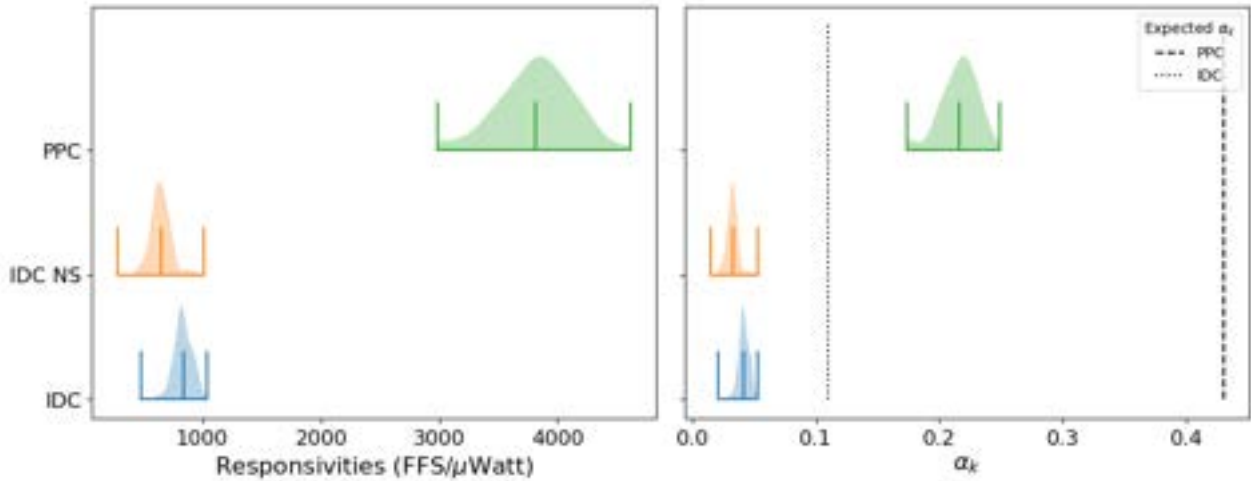


Figure 6.14. One sided violin plots for the measured resonator dark responsivities (left) and kinetic inductance fraction α_k (right). The mean and standard deviation for the responsivities were measured as $(834 \pm 80) \text{ FFS } \mu\text{W}^{-1}$, $(645 \pm 90) \text{ FFS } \mu\text{W}^{-1}$, and $(3816 \pm 313) \text{ FFS } \mu\text{W}^{-1}$ for the IDC, IDC NS and PPC respectively, and α_k was measured as 0.042 ± 0.004 , 0.033 ± 0.005 , and 0.216 ± 0.015 respectively. The black dotted line indicates the α_k value from simulation for the IDC and the dashed for the PPC.

Given the significant contribution to geometric inductance by the capacitor of the IDC design, it is unsurprising that we see a medium to high positive correlation for both the responsivity and α_k with resonant frequency as shown by Figure 6.15. Since we suspect the long IDC fingers and rails are the contributors to the geometric inductance, it makes sense that as the resonator increases in frequency and the capacitor gets smaller, so will the geometric inductance, hence improving the kinetic inductance fraction.

6.4 Multitone Dark NEP

The sources that contribute to the noise power spectrum of an MKID resonator have been extensively covered in various works in literature^{18,64,85,102}. As discussed, the sensitivity of a detector is typically quantified by the noise equivalent power (NEP), which is the amount of power with a Signal-to-Noise Ratio (SNR) of 1 that the device can detect in 0.5 seconds. In an optical setting, the total NEP, $\text{NEP}_{\text{total}}$, will be given by the quadrature sum of the independent noise mechanisms, as

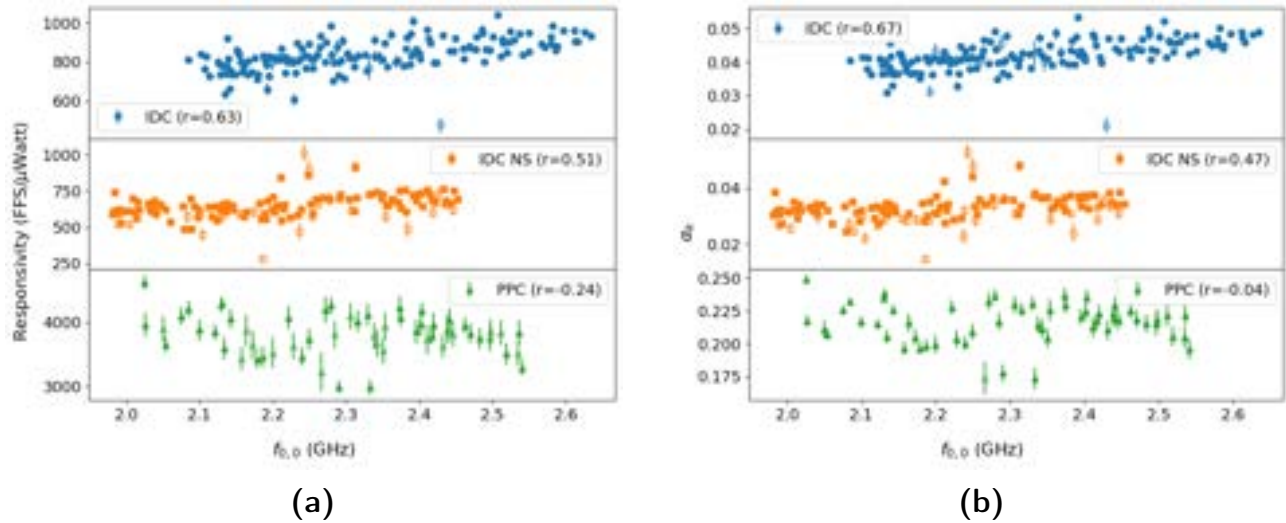


Figure 6.15. Scatter plot of measured responsivity and kinetic inductance fractions for SLIM10 resonators plotted against the resonant frequency at base temperature. Each subplot shows the Spearman's rank correlation coefficient, demonstrating a frequency correlation for the IDC and IDC NS geometries but not for the PPC geometry. Hollow markers were removed from the statistics as they had larger than 5% uncertainties.

$$\text{NEP}_{\text{total}}^2 = \text{NEP}_{\text{GR}}^2 + \text{NEP}_{\gamma}^2 + \text{NEP}_{\text{system}}^2 + \text{NEP}_{1/f}^2, \quad (6.13)$$

where the “ γ ” term represents the photon shot noise, “GR” term is due to generation-recombination noise, the “system” term is the dominating noise source of the readout system, and the “ $1/f$ ” term represents all low frequency noise sources such as TLS. As previously mentioned, for a photon noise limited detector, NEP_{γ} should be the dominant term in Equation 6.13. We can make the assumption that the latter three noise terms are the same in a dark setting as they would be in the optical setting^{143,144}. We can calculate the dark NEP by taking the noise power spectrum of a resonator (here we will use the fractional frequency noise spectrum, S_{xx}) and accounting for the detector responsivity as

$$\text{NEP} = \frac{\sqrt{S_{xx}}}{R}. \quad (6.14)$$

To obtain a representative result for each architecture, the noise spectra of multiple resonators for each architecture were measured using the RF-ICE readout system (the same type of system as will be used for SPT-SLIM deployment)⁹⁴. A subset of the tone frequencies from the “useable” resonator list were used for each of the three SLIM10 channels (as mentioned in Section 6.1). The control software has built-in methods that, with reasonably good success, are able to automate finding the most suitable bias power for each resonator, i.e. the largest readout power without

bifurcating within a user-defined step size. The tone frequency is also adjusted to the frequency at the maximum rate of change for I and Q. The methods were still in development at the time of measurements and occasionally resonators were biased beyond bifurcation or off of resonance; attempts were made to remove these from the following results. The fractional frequency power spectrum for each measured resonator was calculated in the same way as described in Section 6.2. The noise spectra for all the multitone measured IDC and PPC resonators at 160 mK (the approximate base temperature planned for on-sky operation) are shown in Figure 6.16, along with the median at each frequency shown in black compared with an equivalent homodyne tone noise spectrum in red, demonstrating reasonably good agreement. The offset in the off resonance floor is explained by a difference in bias powers. The discontinuity in the multitone noise data between low and high frequencies is because the ICE board uses a polyphase filter-bank to process the high frequency noise data, which is an entirely different process to what is used at lower frequencies, however details of this are beyond the scope of this thesis. Details of the ICE readout system can be found in Rouble, 2022⁹⁴.

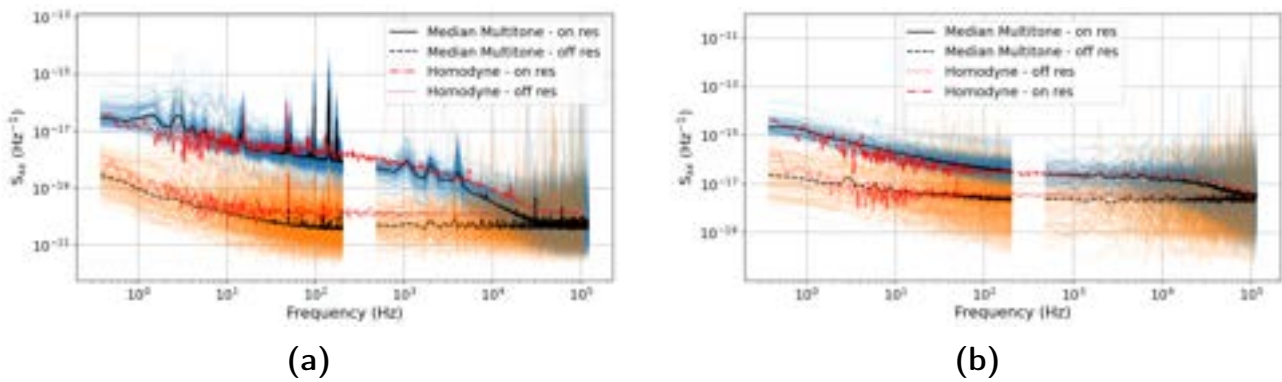


Figure 6.16. Multitone fractional frequency noise measurements for 125 IDC resonators (Left) and 85 PPC resonators (right). Black lines show the median value and red shows a homodyne PSD for both the on (solid line) and off (dashed line) resonance.

The previously mentioned frequency noise spikes are particularly more noticeable in the multitone data compared to the homodyne, however the frequency peaks do line up. Given the larger responsivity of the PPC resonators compared to IDC, it is unsurprising that the noise power is larger for the PPC, hence by considering Equation 6.14, one can understand why it is necessary to compare the sensitivity of these detectors with the NEP. The median noise spectra for the IDC and PPC architectures are compared in the top panel of Figure 6.17 along with a homodyne S_{xx} spectrum from the IDC NS. Measurements for the IDC NS channel with the ICE board were unsuccessful and were not pursued due to time constraints, however given the agreements between the homodyne and multitone, the IDC NS spectrum is likely representative. Note, the IDC NS resonators required approximately 10dB higher drive powers than the IDC and PPC resonators, hence, despite similar architecture and responsivity to the IDC, the S_{xx} spectrum is higher in magnitude. The on resonance

S_{xx} are then used along with the values for responsivity from Section 6.3 to calculate the dark NEP shown in the bottom panel of Figure 6.17 accounting for the resonator roll-off via,

$$\text{NEP} = \frac{\sqrt{S_{xx}}}{R} (1 + [2\pi f \tau_{qp}]^2) (1 + [2\pi f \tau_{res}]^2), \quad (6.15)$$

where we assume that the three architectures have the same quasiparticle lifetime of 647 μs as they were all fabricated in the same processing steps and then the resonator ringdown time is calculated from an f_0 of 2.25 GHz (as the centre of the readout band) the mean Q_r from Section 6.1 for the IDC and PPC NEP, then the resonator values for the IDC NS resonator ($Q_r = 3.07 \times 10^4$, $f_0 = 2.234$ GHz).

The photon noise limit shown here, $\text{NEP}_\gamma = 2.08 \times 10^{-18} \text{ W}/\sqrt{\text{Hz}}$, is calculated as described in Section 4.1.2 using Equation 4.2 with updated values as per the $R = 100$ design described in Section 4.4.2: the expected optical power, $P_{\text{opt}} \approx 70 \text{ fW}$ as each detector now receives a wider bandwidth and the optical efficiency, $\eta_{\text{opt}} = 0.25$ taken from the simulated single filter efficiency. For a quantitative comparison consider the NEP at $\approx 15 \text{ Hz}$. Unfortunately, noise spikes for the IDC resonators fall within our observing band which does bring the NEP slightly above the photon noise around 15 Hz where it would otherwise be below. As mentioned, we are yet to understand the exact mechanism for how this noise couples to the resonator, however we have observed that this particular peak (along with many others) is exacerbated by intentional knocks to the cryostat as well as disappearing when the PTC and driver are turned off. Along with the fact that other SLIM devices measured in different cryostats see similar microphonics but at different frequencies, this all suggests that the source of the noise is a vibrational mode of the specific cryostat configuration. If so, it may not be such an issue in the SPT-SLIM cryostat and if it is it should be possible move the frequency of the mode, for example, by adding mass to the cryostat similar to the physics of a mass on a spring. One would expect this frequency noise to be correlated in time across the resonator timestreams measured with the multitone at the same time. If true, the noise should be easily identified and removed via principal component analysis (PCA)¹⁴⁵, as demonstrated in Figure 6.18 where the median NEP spectrum for the IDC between 10 Hz and 100 Hz is shown for a different orders of PCA. Here, a group of simultaneous timestreams from 40 resonators are passed through a PCA pipeline and N principal components are removed, the S_{xx} spectrum is then calculated for each resonator and the median value is taken to then convert into NEP as above.

Whilst the first principal component appears to make a clear reduction in the 15 Hz noise spike, even after nine principal components the peaks are still present.

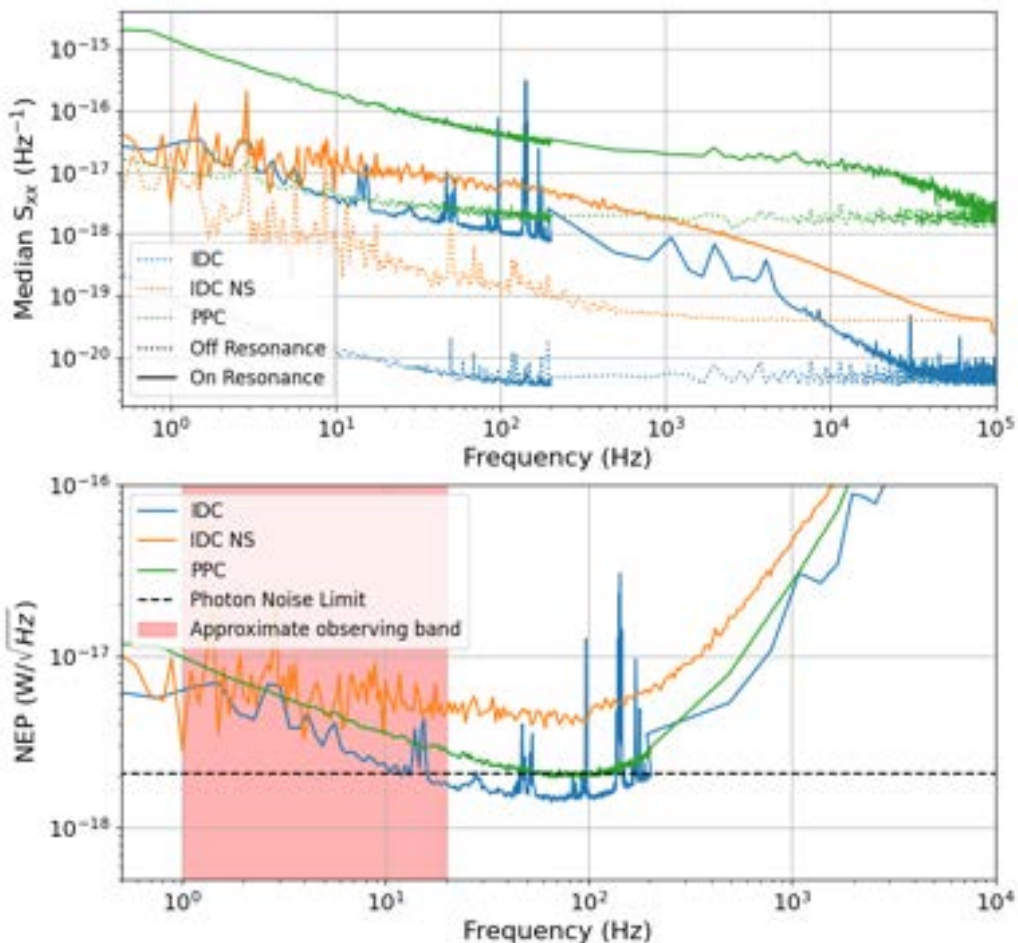


Figure 6.17. (Top) Multitone median S_{xx} spectra for the IDC and PPC and a homodyne S_{xx} spectrum for an IDC NS resonator. (Bottom) NEP calculated from the on resonance noise spectra shown in the top panel and calculated using Equation 6.15, see text for details. The photon noise limit shown is taken from the value shown in Section 4.1.2 and the approximate observing band between 1 Hz and 20 Hz. The approximate NEPs at 15 Hz (excluding noise spikes) are $2.1 \times 10^{-18} \text{ W}/\sqrt{\text{Hz}}$, $4.4 \times 10^{-18} \text{ W}/\sqrt{\text{Hz}}$, and $3.0 \times 10^{-18} \text{ W}/\sqrt{\text{Hz}}$ for IDC, IDC NS and PPC respectively compared to the photon noise limit at $2.08 \times 10^{-18} \text{ W}/\sqrt{\text{Hz}}$.

6.5 Summary and discussion

In this section, microwave detectors from an early SPT-SLIM-like submodule prototype were characterised in a dark setting. Using a combination of VNA, homodyne and multitone measurements, detector properties from three different architectures were obtained and compared, these key resonator properties are summarised in Table 6.1 for each of the architectures, IDC, IDC NS and PPC.

Whilst all channels showed similarly high yields ($> 90\%$), the useful yield, as defined by the number of resonators with more than 10 linewidth spacing to its neighbouring resonators, varied

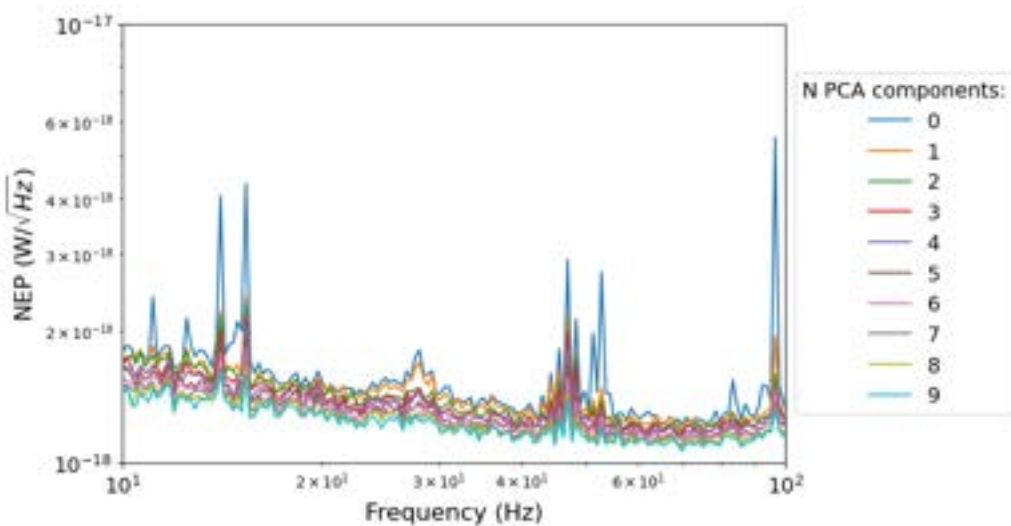


Figure 6.18. Median NEP spectrum for the IDC architecture for a variety of N th order PCA processes on a group of simultaneous timestreams from 40 resonators. $N=0$ indicates the NEP spectrum without PCA.

across the architectures despite the measured fractional frequency scatter being very similar. It was concluded that this was due to the combination of the number of resonators within the readout bandwidth and the differences in resonator quality factor Q_r as the PPC and IDC NS resonators were not largely Q_c dominated unlike the IDC resonators. The higher values of Q_r for the IDC are testament to the intended design of minimising loss through dielectric loss tangents in the regions of high electric field around the capacitor by depositing the IDC only on top of the bulk silicon wafer.

Furthermore, there was a moderate degree of success in measuring the quasiparticle lifetime of the aluminium by fitting to the roll-off of the fractional frequency noise spectrum. It was possible to extract the quasiparticle lifetime at higher temperatures, which was verified by finding good agreement between the measured τ_{qp} and theoretical as a function of temperature for an aluminium superconductor with a $T_c = 1.2\text{ K}$ and a electron-phonon interaction time of $\tau_0 = 0.6\text{ }\mu\text{s}$. However, below 200 mK it appeared that the noise spectrum became dominated by some low frequency noise which caused the resonator to operate in a regime whereby the noise roll-off was limited by the resonator ringdown time. This behaviour was seen across the three different architectures. Low frequency noise such as this is typically associated with TLS states. However, given the difference in Q_r between the three architectures and varying degrees of the so-called “backbending” in f_0 vs. temperature sweeps (IDC showing minimal relative to the PPC), which is another common trait that suggests the presence of TLS, it is possible that this noise originates from another source that is common across the designs, such as the inductor. This would be an interesting area for further study.

	IDC	IDC NS	PPC
Full yield	92.6 %	95.0 %	91.0 %
Useful yield	59.5 %	63.5 %	32.1 %
f_0 fractional scatter	3.84×10^{-4}	2.44×10^{-4}	3.79×10^{-4}
Mean Q_r	$(8.26 \pm 4.13) \times 10^4$	$(3.07 \pm 0.75) \times 10^4$	$(3.22 \pm 1.39) \times 10^4$
Mean Q_i	$(4.55 \pm 2.05) \times 10^5$	$(4.48 \pm 1.11) \times 10^4$	$(7.07 \pm 2.71) \times 10^4$
τ_{qp} (μ s)	647 ± 86	647 ± 86	647 ± 86
Al T_c (K)	1.2	1.2	1.2
Mean α_k	0.042 ± 0.004	0.033 ± 0.005	0.216 ± 0.015
Mean R (FFS μW$^{-1}$)	834 ± 80	645 ± 90	3816 ± 313
Dark NEP (W/$\sqrt{\text{Hz}}$)	2.1×10^{-18}	4.4×10^{-18}	3.0×10^{-18}

Table 6.1. Table summarising the dark characterisation results present in this section from the SLIM10 device for each resonator architecture: the nominal inter-digital capacitor design (IDC), the inter-digital capacitor design without a step-down (IDC NS) and the parallel plate (PPC).

The kinetic inductance fraction for each design were also measured along with the responsivity. The measured results for α_k were approximately half of what simulations suggested. This is most likely because the deposited aluminium was thicker than we would ideally like to have (50 nm), thus the sheet resistance and kinetic inductance will be reduced. This thicker aluminium was chosen as a risk reducing measure until full-scale working devices were realised to confirm the design actually worked. This lower than intended kinetic inductance will also impact the responsivity and therefore the sensitivity (NEP) of the detectors. That said, the IDC geometry, was shown to be on the cusp of the photon limited sensitivity at 15 Hz, with an NEP of approximately 2.1×10^{-18} W/ $\sqrt{\text{Hz}}$ (if one ignores the noise microphonic noise), whereas the PPC came in at $\approx 3.0 \times 10^{-18}$ W/ $\sqrt{\text{Hz}}$ and the IDC NS higher again at $\approx 4.4 \times 10^{-18}$ W/ $\sqrt{\text{Hz}}$. It was for this reason that the IDC was chosen as the deployment detector, along with the order of magnitude higher Q_i leading to smaller linewidths reducing collisions, and the minimal TLS excitations near the operational temperature (160 mK). The IDC was also considered as a safer option from a fabrication point of view due to its lower dependence on the dielectric, a fabrication process which is prone to drifting. However, it is worth noting that there are substantial benefits to using a parallel plate resonator, such as its higher tolerance capacitor linewidth variations, negligible cross coupling which would dramatically simplify the multiplexing scheme (providing high Q_i s are attainable to reduce linewidths). Furthermore, the reduced footprint of the PPC would firstly allow filter-banks to be much smaller allowing more filter-banks on a focal plane (assuming no readout limitations), thus improving mapping speeds. Secondly, with smaller detectors (currently the limiting dimension between filter channels), it should be possible to space filter-channels by $\lambda/4$ or even smaller, ensuring that the stop-band at half wavelength spacing is further away in frequency space which was shown previously to have a significant impact on the filter-bank. Since SPT-SLIM is a technological pathfinder for LIM on-chip filter-bank spectrometry and low

loss/noise dielectrics for parallel plates are still to be developed, the IDC is a suitable detector for now. There is however, a new version of the PPC design with shorter inductor and thinner aluminium sheet thickness currently being fabricated with the hope that a further increased responsivity will overcome the excess noise, allowing for photon limited detection.

Optical Filter-Bank Characterisation

This Chapter presents optical measurements of filter-banks. Firstly, the measurement set-up and procedure of using Fourier transform spectroscopy to obtain the spectral response of the detectors with the set-up at Cardiff University is covered in Section 7.1. This methodology is then applied to an SPT-SLIM test device used for measuring the dielectric loss tangent at mm-wave in Section 7.2. Finally in Section 7.3 results of multiple filter banks from deployment grade sub-modules are presented as measured with a similar procedure at The University of Chicago. Regarding the chronology of the measurements presented here, the loss tangent measurements were actually the last measurements of the work included in this thesis and were useful for understanding the lower-than-designed resolutions of the sub-module results. It would have of course been beneficial to measure this sooner in the instruments progression however various logistics, time constraints, and limited resources placed a higher priority on measurements of deployable devices.

7.1 Experimental set-up and procedure

7.1.1 Martin-Puplett interferometer set-up

Interferometry has an extensive history with the first interferometer dating back to the early 1800s. As such, there is a wealth of existing information spanning from the basic principles and Fourier theory^{146,147} to a range of specific applications in various fields of Engineering, Physics and other sciences. Sub-mm astronomy is one of these fields, with numerous existing and planned instruments employing an FTS^{12,13,30,31,148,149}. Here, we focus on the use of a Martin-Puplett Interferometer¹⁵⁰ (MPI) as a means of characterising both the wide band and narrow band spectral response of detectors, i.e, how the detectors respond as a function of millimetre frequency. Similar

to the well-known Michelson interferometer, one can obtain an interferogram, a modulated detector response as a function of distance, specifically optical path difference is obtained via a configuration of mirrors and a beam splitter. In contrast to the Michelson interferometer, the MPI takes advantage of the polarisation properties of light, hence polarisers are also included in the MPI. The main advantage of the MPI over other conventional interferometers is that the polarising wire grid beam-splitter has minimal variation in throughput efficiency across millimetre and sub-millimetre wavelengths, unlike common dielectric based beam-splitters such as the half-silvered mirror^{33,150,151}.

The right hand side of Figure 7.1 shows a simplified schematic of a MPI. Detailed explanations of the operation of a MPI can be found in Naylor et. al. 1994¹⁵¹ and Barry 2014¹⁰². Briefly, an incoherent and unpolarised source such as a black body emits radiation through an input polarising wire grid (P1). In the case of a non-beam filling or point-like source a collimating lens or mirror (C1) can be used to form a collimated beam. The polarised light is then incident on a wire grid polarising beam-splitter (BS) oriented at 45° to the input polariser (P1) such that components parallel to the beam-splitter will be reflected (undergoing a phase shift of π), whilst the perpendicular component is transmitted, maintaining its phase. Each of the two branches/paths are then reflected by a rooftop mirror, changing the polarisation by 90°, such that the phase of each branch switch whereby the originally reflected wave now transmits through the beam-splitter and the originally transmitted wave gets reflected. The two beams combine to create a circularly polarised wave with the total electric field as the sum of the two electric fields. A second polariser (P2) is then placed on the output to select one component of the circular field which then is then focused onto a detector/focal plane via a second collimator (C2).

In the case where the mirrors of each path are placed equidistant from the beam-splitter such that the optical path difference is zero, known as the Zero Path Difference (ZPD), will result in maximal power at the detector as all frequencies constructively interfere resulting in the white light fringe. As one of the mirrors moves, thus changing the Optical Path Difference (OPD), the output and measured electric field is then modulated as a function of the mirror position or OPD, forming the interferogram. In the case of MKIDs, at each mirror position, *I* and *Q* can be sampled with a similar procedure as that described for on-resonance noise timestreams (Section 6.2). These *IQ* values can then be converted to fractional frequency shift, df/f (using the calibration sweep taken at the start of the measurement), as a measure of detector response and will produce the interferogram when plotted against the fractional frequency shift. The frequency spectrum of the response can be obtained by taking the forward Fourier transform of the interferogram and OPD axis. A useful resource for building an intuition for interferogram patterns and their corresponding spectra is Davis, S. P., Abrams, M. C., & Brault, J. W. (2001)¹⁴⁷. The analysis of the interferograms from detectors responding to narrow-band spectral inputs, such as those connected to the half-wave filters in an FBS, is detailed in Section 7.1.2.

The two main parameters that define the performance of an MPI are the maximum OPD and the accuracy to which the mirror position is known, i.e, the mechanical step size or OPD sampling.

The maximum operating frequency of an FTS is governed by the Nyquist sampling theorem, which states the sampling rate of any analog signal must be at least twice that of the maximum frequency. The maximum frequency, ν_{\max} , for an FTS is therefore given by¹⁵²

$$f_{\max} = \frac{c}{2 \times \text{FF} \times ds}, \quad (7.1)$$

where c is the speed of light in air/vacuum, ds is the mechanical step size and FF is the FTS Fold Factor. The FF is simply the ratio of the optical path difference change to a given change in mirror position (ds). In the single mirror per branch case $FF = 2$ however it is possible to have other designs that have more mirrors resulting in a larger FF, such as the FTS configuration designed for the PIXIE experiment³³.

The maximum frequency resolution, $\Delta\nu$ of an FTS is set by the largest path difference, OPD_{\max} , since the envelopes of the longest wavelengths (smallest frequencies) require a large OPD in order to be observed in the interferogram. This is calculated by¹⁵²

$$\Delta\nu = \frac{c}{2 \times \text{OPD}_{\max}}. \quad (7.2)$$

A schematic of the experimental set-up used at Cardiff for the results presented in Section 7.2 is shown in Figure 7.1. A thermally-isolated, temperature controlled carbon-filled epoxy plate with a heater and thermometer (PT100) is used as a black body source and the MPI has a maximum mirror travel that corresponds to an maximum OPD of 20 cm and mechanical step size of 8 μm . Hence, $\nu_{\max} \approx 9.4 \text{ THz}$, which is significantly greater than the requirements of the devices in this thesis and the frequency resolution $\Delta\nu = 0.75 \text{ GHz}$. This frequency resolution is larger than the bandwidth of some of the higher resolution filters presented in Section 7.2, however, in Section 7.1.2 it will be shown that the filter resolution, R / quality factor, Q_{filt} can be accurately extracted by fitting to the interferogram, even when $\Delta\nu$ is an order of magnitude larger than the filter bandwidth.

7.1.2 Interferogram analysis of a Lorentzian spectrum

The spectral profile of a half-wavelength filter is known to result in a Lorentzian profile as a function of frequency as is demonstrated through simulation in Section 3.6.4. The Fourier

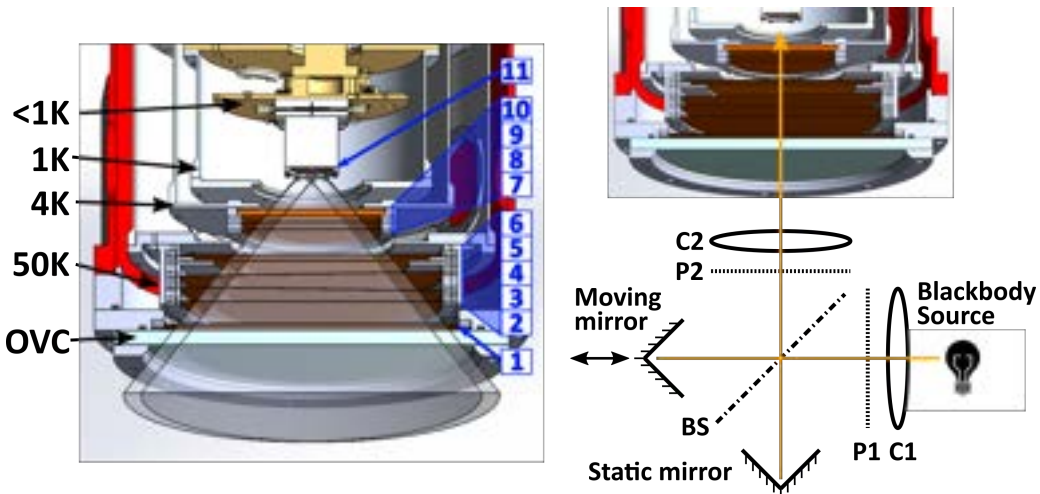


Figure 7.1. (Left) Cross-section CAD model of the cryostat optical configuration used to take FTS measurements at Cardiff indicating the temperature stages in black. The pass band is defined through a set of infrared blockers (thermals) and metal-mesh quasi-optical low-pass edge filters indicated by blue text and is as follows: 1 to 8 are thermals then 9 and 10 are 13 cm^{-1} and 12 cm^{-1} low pass edges respectively at 4 K followed finally by a 6.8 cm^{-1} low pass edge immediately in front of the horn block at $\approx 250\text{ mK}$. (Right) A schematic of a Martin-Puplett FTS relative to the optical cryostat set-up.

transform of a Lorentzian is given by an exponentially damped co-sinusoid where the maximum at ZPD will correspond to the white light fringe. The interferogram as a function of OPD, $g(\text{OPD})$, is expressed as follows^{102,147}

$$g(\text{OPD}) = Ae^{-\frac{\text{OPD}}{\tau}} \cos(2\pi k_0 \text{OPD}), \quad (7.3)$$

where A is a scaling parameter in units of the detector's response (i.e., df/f), k_0 is the wavenumber corresponding to the resonant frequency ($\nu_0 = ck_0$) and τ is the decay constant of the damped resonator relating to the filter quality factor (filter resolution) via $Q_{\text{filt}} = R = k_0\pi\tau$. Figure 7.2 shows generated interferograms using Equation 7.3 for $Q_{\text{filt}} = 100, 200$, and 300 with an added normally distributed random noise at a signal-to-noise ratio of 10 . The left hand column shows the approximate interferograms we might measure with the FTS described above with an $8\text{ }\mu\text{m}$ step size and $\approx 20\text{ cm}$ maximum OPD. The middle column shows these same interferograms but in this case they were “measured” using an FTS with a maximum OPD of 5 cm ($\Delta\nu = 3\text{ GHz}$), which is approximately an order of magnitude larger than the full-width half-maximum of a Lorentzian filter profile with $Q_{\text{filt}} = 500$: FWHM = 0.36 GHz . The right hand column then shows a zoom in of the fits for the middle column. Fitting a Lorentzian profile in the frequency domain would struggle to get accurate fits since possibly only one data point would lie within the spectral band. However, fitting the model from Equation 7.3 to this OPD range still yields

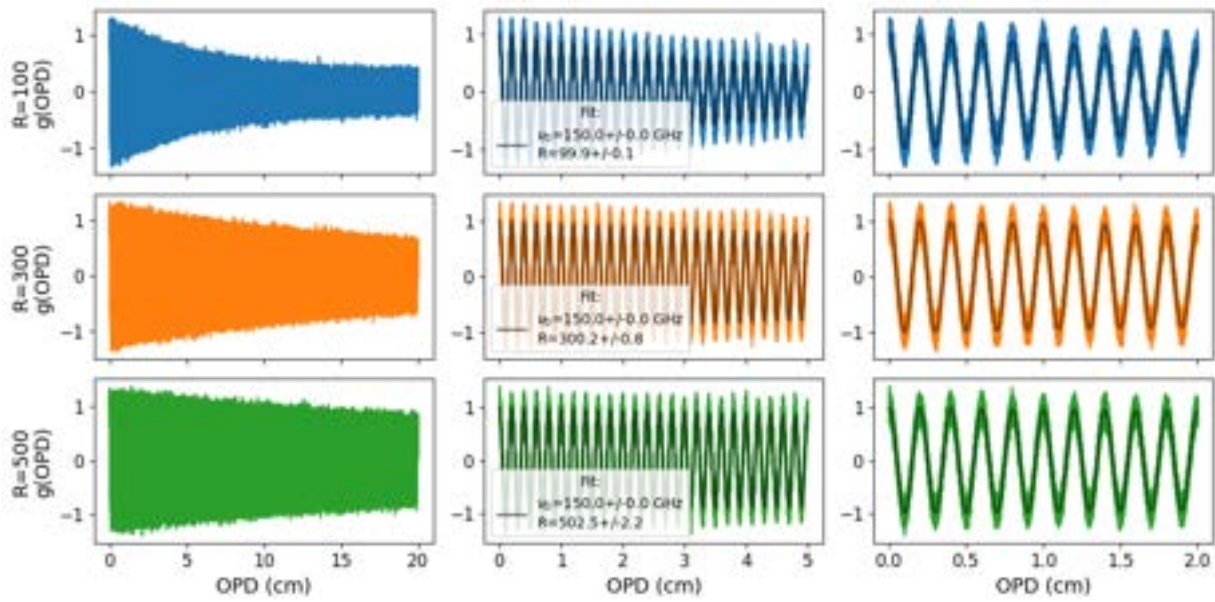


Figure 7.2. Generated Lorentzian interferogram data of arbitrary units with a signal-to-noise ratio of 10 for quality factors of $Q = 100$ (top row), 200 (middle row) and 300 (bottom row). The middle column shows fits of Equation 7.3 to the interferogram between $0 \text{ cm} < \text{OPD} < 5 \text{ cm}$ and the right hand column shows a futher zoom in of these fits.

fit values for ν_0 and Q_{filt} within 1 % of the true value despite relatively small SNR compared to what is measured in the results of Sections 7.2 and 7.3 which are typically in the range of $100 < \text{SNR} < 1000$. Note, for this to be true, the step size must be suitably small, as is the case here.

We therefore conclude that our measurements of spectral resolution and resonant frequency of the filters to be characterised in the following sections should not be limited by the measurement apparatus nor the analysis procedure.

7.2 Loss tangent measurement at mm-wave

As is clear throughout this thesis, the loss tangent of the dielectric material at millimetre wave is a crucial parameter to quantify in order to understand the performance of the on-chip FBS. A test chip, dubbed the “Mini FBS”, was designed to occupy a portion of the same handle wafer as a sub-module, and serve the purpose of troubleshooting the mm-wave circuit if the accompanying sub-module failed to detect spectra. A diagram of the design and a mounted device (prior to installing the horn block) is shown in Figure 7.3. The device consists of four OMT antennas the probes connected to “Direct” detectors probe each stage of the mm-wave circuit before the FBS, i.e, a direct single probe coupling, a detector connected to the difference port of a 180°

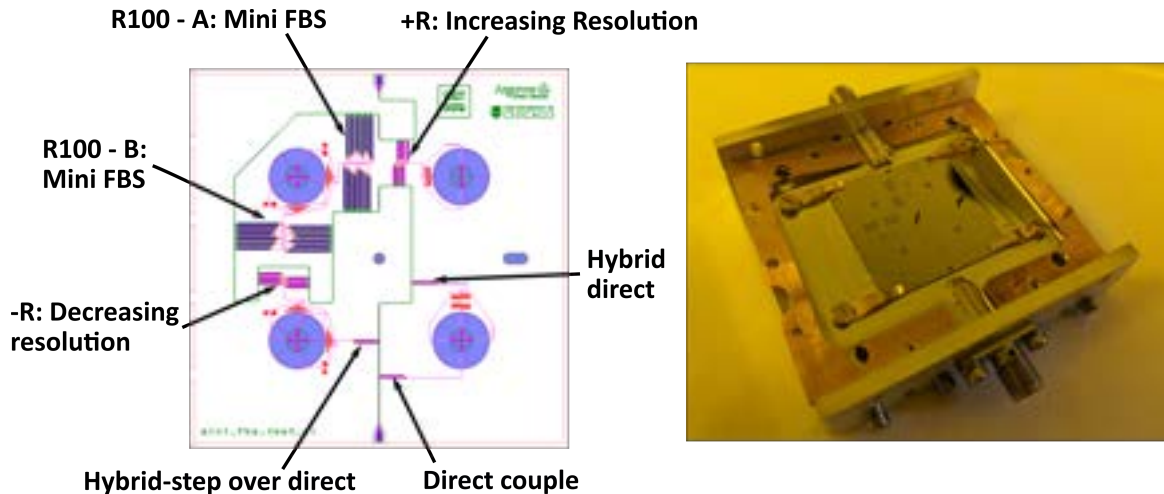


Figure 7.3. (Left) Diagram detailing the key components of the Mini FBS test chip design. See text for further details. (Right) Image of the mounted SLIM30 Mini FBS device in its test box before the horn block is installed on top.

hybrid, and another connected to the hybrid but also including a step-over. The top left OMT is connected to two $11 R = 100$ spectral channel filter-banks using IDC detectors creating a miniature version of an FBS found on the sub-module. All other detectors in this design are parallel plate resonators to enable the use of the 1 GHz to 2 GHz readout range without the detectors becoming too large. Finally, connected to the vertical polarisation in the top right OMT and the horizontal polarisation in the bottom left OMT are two small FBS structures which have each have 5 spectral channels of varying resolution and one broadband resonator connected to the end of the filter-bank. The “+R” FBS has increasing filter resolutions relative to the filter ν_0 i.e., starting at $R \approx 100$ with $\nu_0 = 130$ GHz at the start of the FBS, then rising to $R \approx 550$ with $\nu_0 = 170$ GHz. The “-R” FBS is the reverse, see the orange data points in Figure 7.6 for further details on the designed Q_{filt} and spectral ν_0 . This section will focus only on the results of these variable resolution filter-banks (from the SLIM30 fabrication run) as it is possible to extract the dielectric loss tangent at mm-wave with these structures.

The fractional frequency interferograms shown in Figure 7.4 were obtained using the procedure described in the previous section measured with a homodyne readout system whilst aligning the output polarisation close to the orientation of the rising resolution FBS OMT probes. The interferogram plots each show two interferograms, in this case, the only difference between the original and processed interferograms is that a linear trend is fit and then removed from the data to zero the interferogram. This would also remove any slope to the data from systematics such as temperature drifts. The interferograms show a clear difference between the broadband detector (000) and the “turned off” polarisation (001 to 005), indicated by the red titles compared with the spectral channels indicated by green. Note, the broadband detector from the rising

resolution group was missing. For each polarisation the interferograms were fit with the model from Equation 7.3 as shown by the black lines, where the inset plots demonstrate the agreement of the fits more clearly.

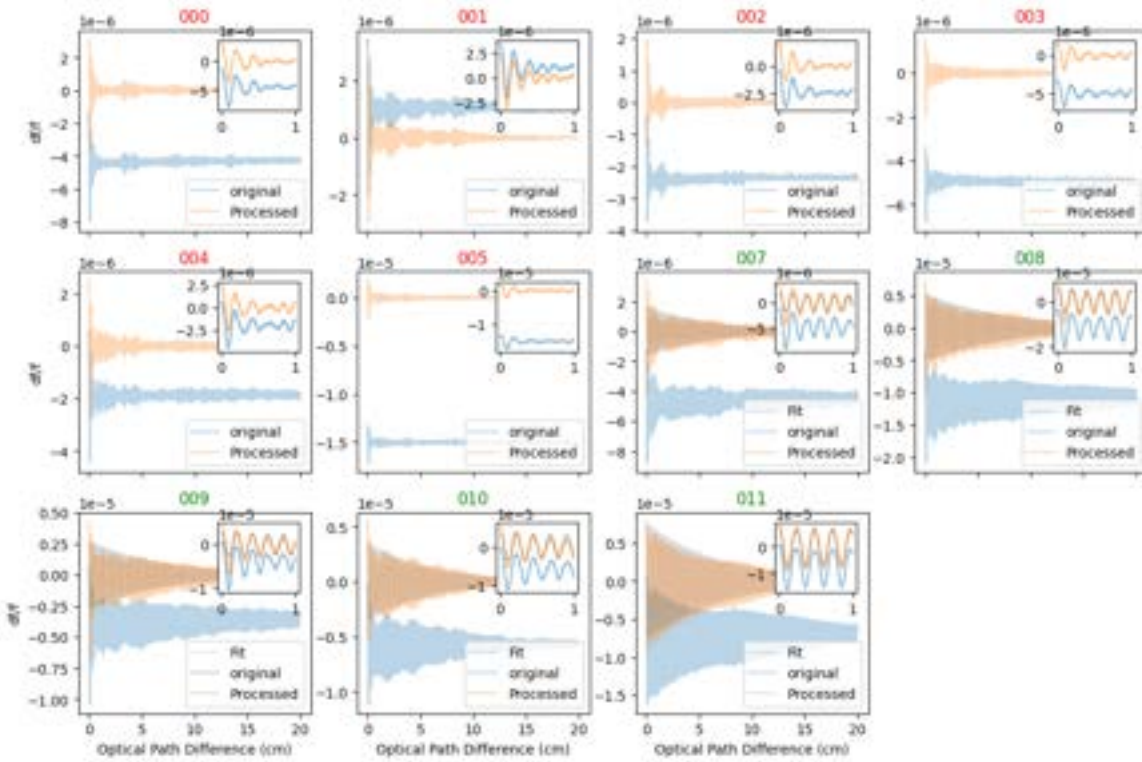


Figure 7.4. Interferograms of the fractional frequency response for the SLIM30 Mini FBS variable resolution detectors with the FTS polarisation aligned to the rising resolution FBS OMT probes. Red and green titles indicate whether the interferogram is considered as broadband/dark or spectral respectively. Spectral interferograms are fit with the model expressed by Equation 7.3 shown by the black lines. See text for details of the difference between the original and processed interferograms.

Taking the Fourier transform of these interferograms then yields the spectra in the frequency domain. The spectra presented in Figure 7.5, were obtained by dividing the spectral response by standard deviation of the response within the FBS out-of-band region defined between 190 GHz to 200 GHz in order to obtain the signal to noise plots. Then the bottom plots show the spectral response normalised by the peak values. Observing the broadband detector response clearly shows the circular waveguide cut-off operating as expected at ≈ 110 GHz. In both FBSs there is a detector which shows noticeably more response (particularly in the normalised plots) at frequencies outside of the distinct spectral peak. This is the green profile in the rising resolution group and red profile in the falling resolution group. Observing these spectra in the signal to noise plot shows that these correspond to the lowest SNR measurements, which are also the highest designed quality factor filters as is shown in Figure 7.6. Referring back to Section 3.4.2,

particularly Figure 3.10b, we would expect the Q_{filt} filter to have the lowest throughput efficiency due to dielectric loss, hence the lowest detector response and SNR. This is particularly true in the case of large dielectric loss tangents which is corroborated below by the measurement of the loss tangent.

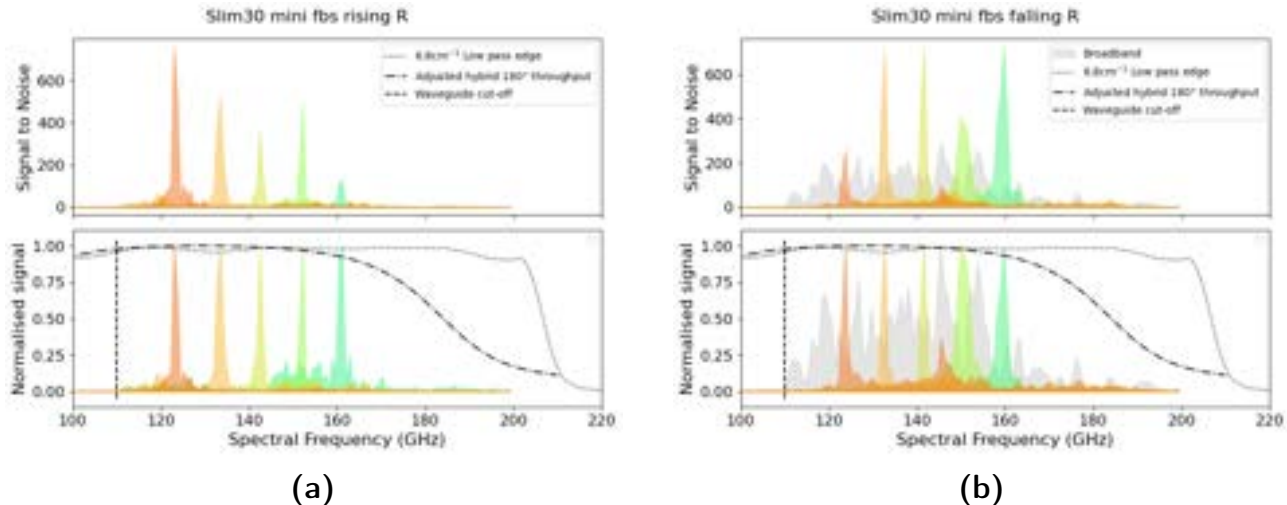


Figure 7.5. Measured spectra from the SLIM30 Mini FBS $+R$ (left) and $-R$ (right) filter-banks measured in the Elmo cryostat at Cardiff. The top row shows the df/f response of the resonators divided by the standard deviation of the response out of band (190 GHz to 200 GHz) whereas the top row shows the spectra divided by the peak value. Also shown on the bottom plots are the frequency cut-off for the $D = 1.6$ mm circular waveguide, the limiting low pass edge normalised transmission, and finally the normalised simulated transmission for the 180° hybrid accounting for a frequency shift of ≈ -8 GHz.

By comparing the difference between the designed spectral ν_0 to the measured values, dubbed the spectral ν_0 deviation (left of Figure 7.7), one can obtain an indication for the accuracy of the values used for the material parameters that affect the wave velocity in the microstrip, namely the kinetic inductance, L_k of the niobium and the relative permittivity of the dielectric ε_r . The measured ν_0 values appear to have shifted down in frequency by approximately 8 GHz. Furthermore, a very rough estimate of the stochastic variation of the filter ν_0 can be quantified by calculating the difference between each $+R$ and $-R$ pair at each frequency since the two FBSs were designed to have identical frequency scheduling. As shown in the right hand side of Figure 7.7, a value on the order of 1.0 GHz to 1.5 GHz is obtained which suggests an impact of stochastic fabrication variation of near 1% which is similar to the values derived from the design tolerancing in Figure 3.11 for a feature size uncertainty of ± 0.2 μm . It is not understood why the falling resolution deviation appears to be systematically larger than the rising ν_0 deviation.

These variable resolution filter-banks were designed with the intention of using the relation of the total filter quality factor, Q_{filt} to the coupling quality factors, Q_c and the losses (of which

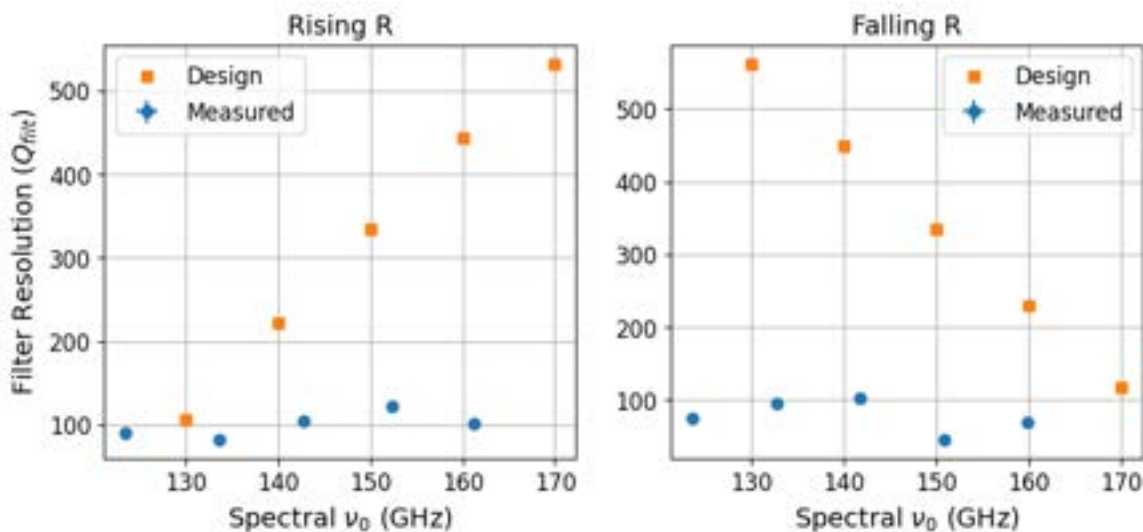


Figure 7.6. SLIM30 Mini FBS Comparison of measured spectral ν_0 and Q_{filt} to the designed values for the rising resolution FBS (left) and the falling resolution FBS (right). Error bars on the measured data are from the fitting uncertainty and are effectively negligible.

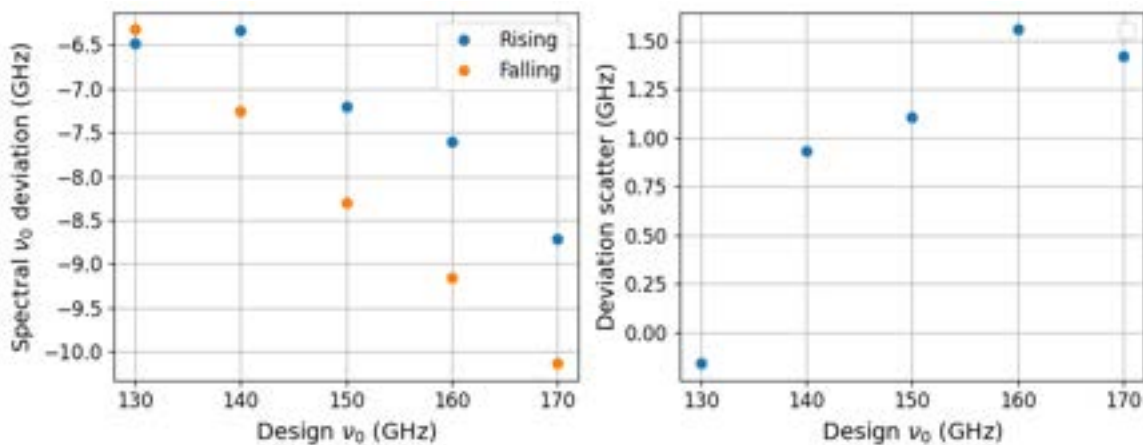


Figure 7.7. (Left) The difference between measured spectral ν_0 values and the designed values, i.e., the deviation from design. (Right) The difference between the ν_0 deviation from the falling resolution group to that from the rising resolution group as an approximate gauge for stochastic variation on the spectral frequency placement.

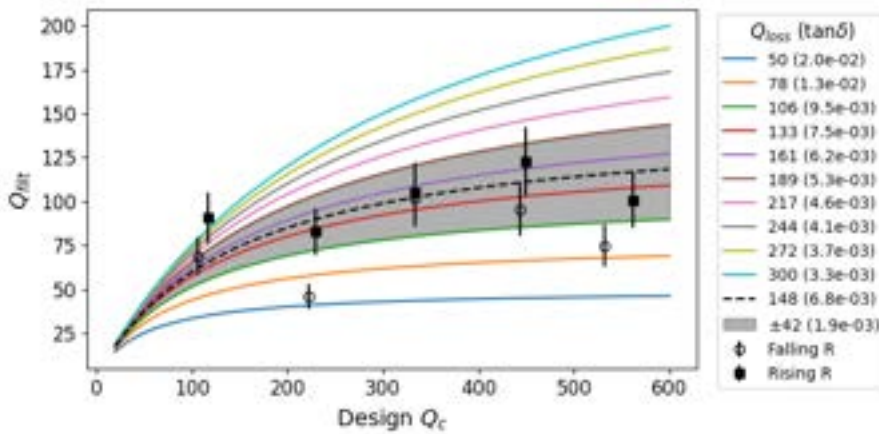


Figure 7.8. A scatter plots of the measured Q_{filt} from the SLIM30 variable resolution filter-banks as a function of the designed Q_c

are expected to be dominated by the dielectric loss tangent) $Q_i = 1/\tan \delta$, in order to obtain a measurement of the loss tangent. Recalling that

$$\frac{1}{Q_{\text{filt}}} = \frac{1}{Q_c} + \frac{1}{Q_i}, \quad (7.4)$$

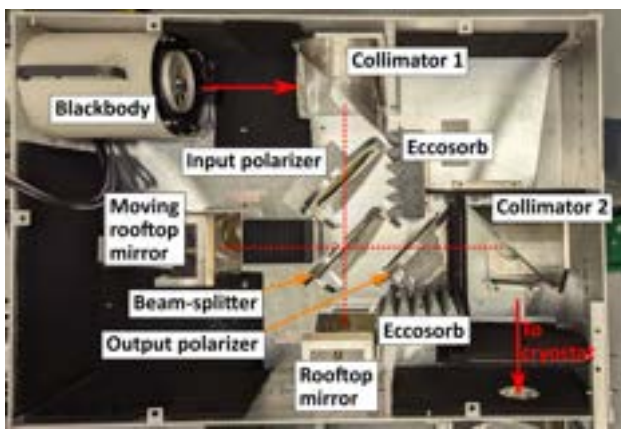
where in the case of a negligible loss tangent ($Q_c \gg Q_i$) the measured $Q_{\text{filt}} = Q_c$. However, in the regime of $Q_i \gtrsim Q_c$, as Q_i decreases (loss tangent increases) Q_{filt} will also decrease relative to Q_c . This relationship is shown in Figure 7.8 for a range of plausible Q_c and Q_i values relative to the designed Q_c and measured Q_{filt} values from the variable resolution filter-banks. The uncertainties in the plot represent a approximate 16 % confidence interval which is derived from the percentage uncertainty of the standard deviation of measured Q_{filt} values from six $R = 100$ sub-module filter-banks (see Section 7.3). The bulk spectral ν_0 downshift suggests a variation in either L_k or ε_r or both. If L_k is incorrect, then we would not expect any detuning of the resonator couplings as this does not effect the capacitance of a parallel plate (this is indicated by the minimal impact on Q_{filt} shown in Figure 3.11). If in the case that ε_r is incorrect, we would expect some detuning as this is analagous to any change in capacitance, e.g., an oversized coupling capacitor or a decrease in dielectric thickness, however it is unlikely to explain the decrease of approximately 60 % to 80 % for the high resolution filters. Instead, there is a much more compelling explanation from a dielectric loss tangent of $\tan \delta = (6.8 \pm 1.9) \times 10^{-3}$ as shown by the black dashed line and grey region in Figure 7.8. These results will be used further in this section to ascertain values for niobium L_k and the effective relative permittivity, ε_r .

7.3 Optical sub-module measurements

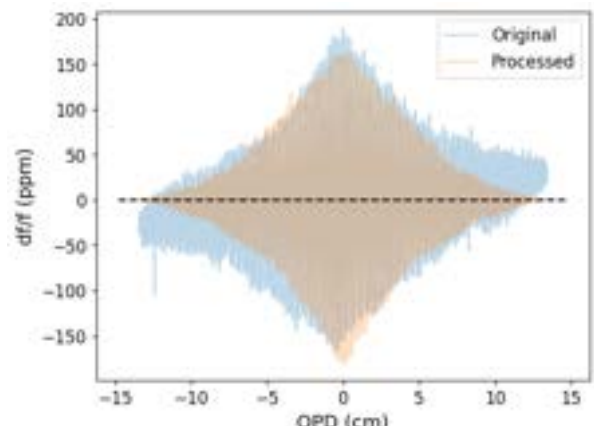
In this section, the optical FTS measured results for three $R = 100$ sub-module readout channels are presented (refer to Figure 2.3). These correspond to two channels from the SLIM23 (Slim23-1 and Slim23-3) fabrication run and one channel from the SLIM24 (Slim24-1) fabrication run. Since these were $R = 100$ sub-modules (3 pixels, 6 filter-banks, 65 channels, 0.3λ spaced, $\Sigma = 1.6$), each readout channel consists of two filter-banks, each connected to orthogonal OMT polarisations. The sub-modules were measured at the University of Chicago by K. Dibert, K. Fichman and T. Natoli using a similar cryostat configuration to that shown in Figure 7.1 and also the Blue Sky¹⁵³ Martin-Puplett FTS shown in Figure 7.9a. The FTS has a mechanical step size of $\approx 2\mu\text{m}$ ($\nu_{\text{max}}=3.7\text{ THz}$) and a maximum OPD of 13.8 cm ($\Delta\nu = 1.08\text{ GHz}$), which was sufficient for accurately fitting filter interferograms. A difference between the Blue Sky FTS and the FTS used for the loss tangent measurements of Section 7.2 is that the ZPD of the Blue Sky FTS is in the center of the moving track, thus allowing both the positive and negative OPD sides of the interferogram to be measured. The measurements were taken using a similar procedure as described in Section 7.2, however the multi-tone RF-ICE readout system was used to simultaneously take measurements on the full tones list at each mirror position (and involved the automated tone placement and biasing algorithms as mentioned in Section 6.4).

Since each filter-bank could be distinguished on the readout line by the polarisation of the OMT, for each readout channel two FTS scans were conducted, once with the output polariser approximately aligned to each polarisation. These will be referred to as “Horizontal” and “Vertical” referring to the orientation of the polarisation grid. Often, a single resonator showed the Lorentzian profile in both polarisations, therefore suggesting the grid was not perfectly aligned with the OMT probes. To avoid double counting, for each “cross-pol” resonator, the magnitude of the peak in fractional frequency response in frequency space was compared between the two scans and the smallest valued spectrum was ignored.

The interferograms were processed with a similar procedure as described in Section 7.2 with one additional step, where an example original interferogram is shown in blue in Figure 7.9b compared with the fully processed interferogram ready for fitting is in orange. As before, a slope (if there is one) is removed and the interferogram is identified as spectral if the SNR is greater than 300. In frequency space the peak region is identified, then utilising increase phase resolution due to the double sided nature of the interferogram, a linear phase correction was carried out. As shown in the left plot of Figure 7.10, a linear trend is fit to the peak region, weighted by spectral amplitude, representing the phase offset at each frequency, ϕ . As explained in Spencer and Naylor, 2005¹⁵⁴, an ideal FTS frequency spectrum should have no imaginary component, yet many of the measured spectra did, as exampled in the uncorrected series in the right hand plot of Figure



(a)



(b)

Figure 7.9. (Left) Blue Sky Martin-Puplett FTS set-up used at the University of Chicago to measure the SLIM23 and SLIM24 sub-module channels. (Right) An example of a measured interferogram before and after processing. See text for details.

7.10. This therefore implies an offset in the used ZPD from the true ZPD. Hence, by removing the phase offset using the Forman et. al. correction¹⁵⁵ from the complex spectral amplitudes (fractional frequency shift), $x(\nu) = \frac{df}{f}(\nu)$, via

$$x_{\text{corrected}}(\nu) = x(\nu)e^{-i\phi}. \quad (7.5)$$

The impact of this phase correction is clearly demonstrated in the right hand plot of Figure 7.10 where the corrected spectrum has zero imaginary component and maximised real component as should be the case in an ideal FTS measured spectrum. Finally, following the phase correction, the spectral amplitudes corresponding to positive frequencies are converted back to the interferogram domain via an inverse Fourier transform to allow the interferogram to be fit for the filter characteristics. Note, by taking only the positive frequencies a symmetric interferogram is forced in the processed result shown in Figure 7.9b.

All the measured spectra from channel 3 of the SLIM23 sub-module are shown in Figure 7.11. Starting from the top, the first tile shows the standard deviation of the df/f spectrum (i.e. the noise) between 190 GHz to 200 GHz for each spectral tone. The second tile shows the fractional frequency spectrum, where the spectra of the tones considered to be not spectral are shown in grey. The third is the SNR spectrum obtained by dividing the df/f spectrum by the corresponding noise standard deviation value and finally the bottom tile shows only the spectral tone spectra normalised by the peak value. The black dashed line dubbed the “normalised spectral coverage” is calculated by taking the mean value at each frequency across all normalised spectra and dividing by the maximum value. This effectively shows the spectral weight in a normalised

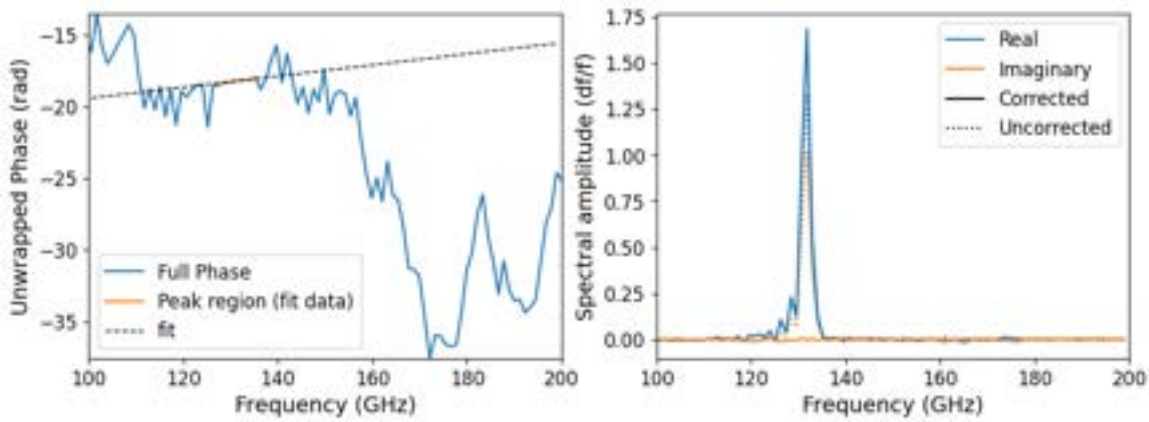


Figure 7.10. (Left) Plot of the phase spectrum of a measured spectral interferogram with a linear fit to the peak region for a phase correction to the real and imaginary components of the spectral amplitude (right).

sense since filter channels overlap in frequency. Plotting this against the spectrum of the broadband detector at the end of the filter-bank yields the plots shown in Figure 7.12 which nicely demonstrate how the frequencies between the waveguide cut-off and the start of the FBS channels pass down the length of the filter-bank before being absorbed in the termination detector. Furthermore, the start of the band is close to the designed 120 GHz, which implies the values used for L_k and ε_r used to simulate the filters were close. This is explored further in this section. A 5.7 cm^{-1} LPE was used which can be seen to cut-off some of the higher frequency detectors.

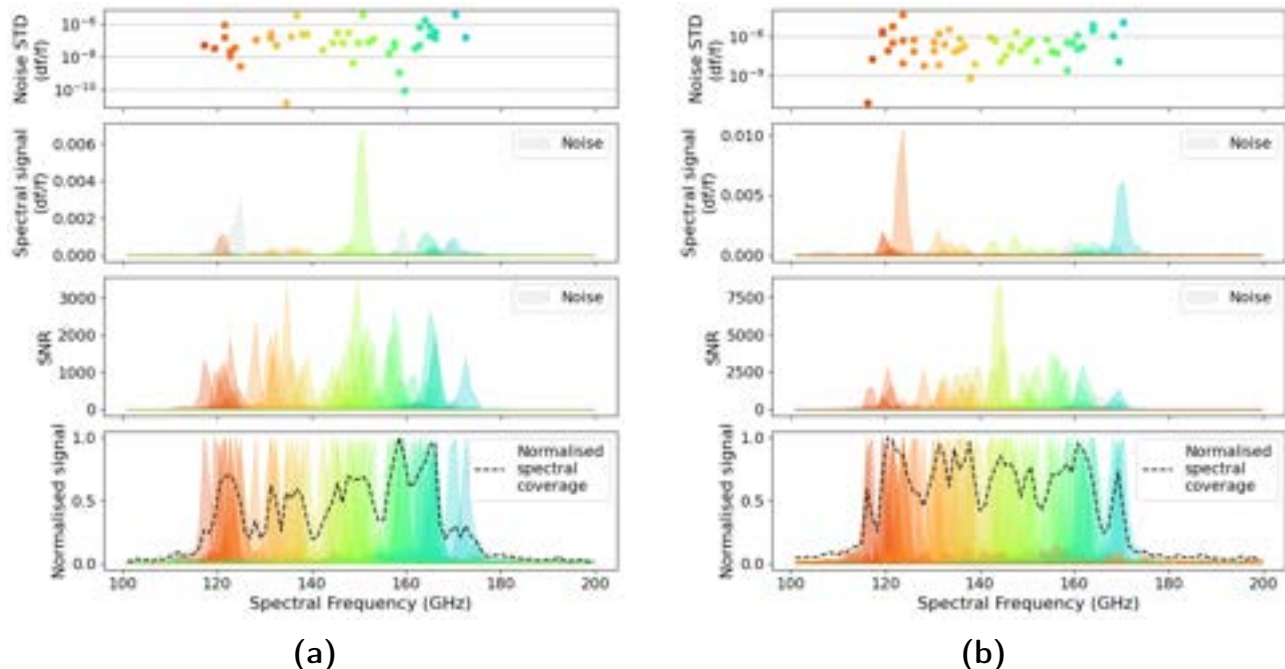


Figure 7.11. Vertical (left) and horizontal (right) polarisation coupled filter-bank spectra from SLIM23 channel 3 visualised in three different ways. See text for details.

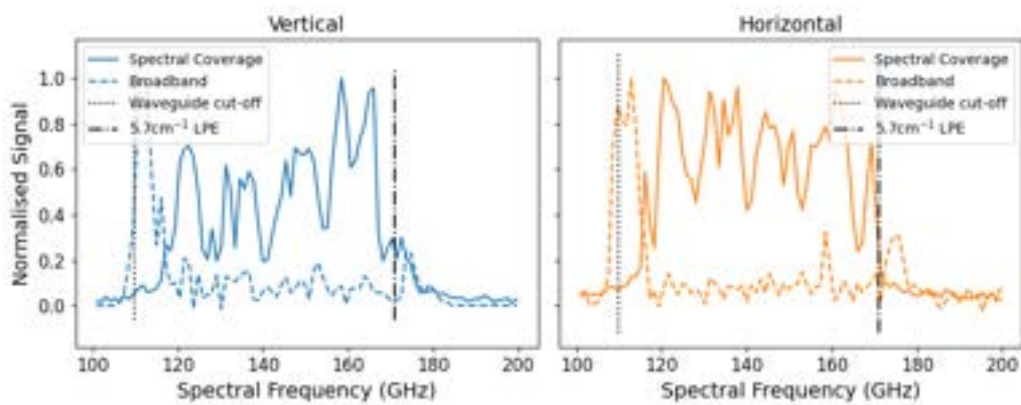


Figure 7.12. Spectral coverage of both vertical and horizontal polarisation filter-banks from channel 3 of SLIM23 compared to their corresponding broadband detector spectrum relative to the waveguide cut-off and band-pass limiting low pass edge.

Given that the expected variation in detector responsivity is less than 10 % (as per results from Chapter 6) and there is no clear spectral frequency dependence, i.e., position dependence down the filter-bank, it is therefore expected that the orders of magnitude variation in the noise is due to deviations in tone placement and bias power relative to the true resonant frequency and optimal bias power. This is further supported by large variety of the peak amplitude in the df/f spectrum compared to the more consistent SNR spectrum.

The fit results from both the vertical and horizontally coupled polarisation filter-bank detectors are shown in Figure 7.13a. An identical plot from fits to channel spectra from a simulated filter-bank with realistic fabrication errors and a dielectric loss tangent of $\tan \delta = 7 \times 10^{-3}$ is also shown Figure 7.13b. A total of 42 and 52 channels out of 65 yielded for the vertical and horizontal filter-banks with mean channel resolutions of 66.0 ± 13.5 and 67.5 ± 8.2 , respectively, where the uncertainties are one standard deviation. The combined spectral yield across the two filter-banks was 73 %, where 11 % was already lost in the microwave yield either due to collisions, non-functional/unyielded detectors or because of detectors being outside the RF-ICE readout bandwidth. A further 9 % (6 channels per FBS) can be accounted for as being lost above the 5.7 cm^{-1} LPE cut-off assuming a down shift of $\approx 2.4 \text{ GHz}$. This leaves roughly a further 7 % unaccounted for, which is likely to be a combination of failed mm-wave circuitry or incorrect tone placement/bias.

A similar reduction in Q_{filt} from the designed $Q_{\text{filt}} = 100$ is observed, as was seen with the Mini FBS results from Section 7.2. In fact, this was observed consistently with all measured filter-banks from both the SLIM23 and SLIM24 fabrication runs as is shown by the results in Table 7.1. Across the six filter-banks, the average Q_{filt} was found to be 66.6 ± 10.9 . This mean value was within 1σ of the simulated mean value when using the loss tangent measured from the SLIM30

Mini FBS. The fact that the degree of scatter, which is representative of the stochastic variation, is similar to the simulated expectation (16.4 % compared to the simulated 10.6 %), suggests that our model is reasonably accurate.

	Spectral tones			Total tones measured	Spectral Yield (%)		Lowest spectral f_0 (GHz)		Mean Q_{filt}	
	H	V	T		H	V	H	V	H	V
Slim23-1	35	50	85	124	54	77	118.1	117.6	67.5 ± 8.8	67.8 ± 8.0
Slim23-3	52	43	95	116	80	65	116.7	118.0	67.5 ± 8.2	66.0 ± 13.5
Slim24-1	40	47	87	129	58	72	119.7	117.6	63.7 ± 16.8	67.0 ± 9.9
Average					67.7 ± 9.5		117.6 ± 0.9		66.6 ± 10.9	

Table 7.1. Summary of measured results from FTS data taken from 6 filter-banks from the SLIM23-1, SLIM23-3 and SLIM24-1 channels. “H” refers to the horizontal filter-bank, “V” the vertical and “T” is the total between the two. Spectral tones refers to the total number of channels identified as spectral. Total tones measured is the number of microwave resonators that yielded and were within the total readout bandwidth of the RF-ICE board. Spectral yield is the number of spectral tones relative to the designed 65. The Lowest spectral f_0 is the f_0 of the lowest spectral channel. Mean Q_{filt} shows the average filter channel quality factor with it’s corresponding standard deviation. The “Averages” row is obtained by taking the corresponding mean across all 6 filter-banks.

It is possible and quite likely that the deposited SiN_x dielectric differs slightly between the SLIM23 and SLIM24 sub-modules compared to that from the SLIM30 Mini FBS as is evidenced from the difference in the the approximate ν_0 shift in the SLIM30 results (≈ 8 GHz) compared to the sub-module results (≈ 2.4 GHz). However, it is unlikely that the loss tangent is much different as the designed $Q_c = 107$ from the rising resolution group was measured as $Q_{\text{filt}} = 69.0$ with a fitting uncertainty of 0.2, which falls well within the middle of the uncertainty range from the sub-module results.

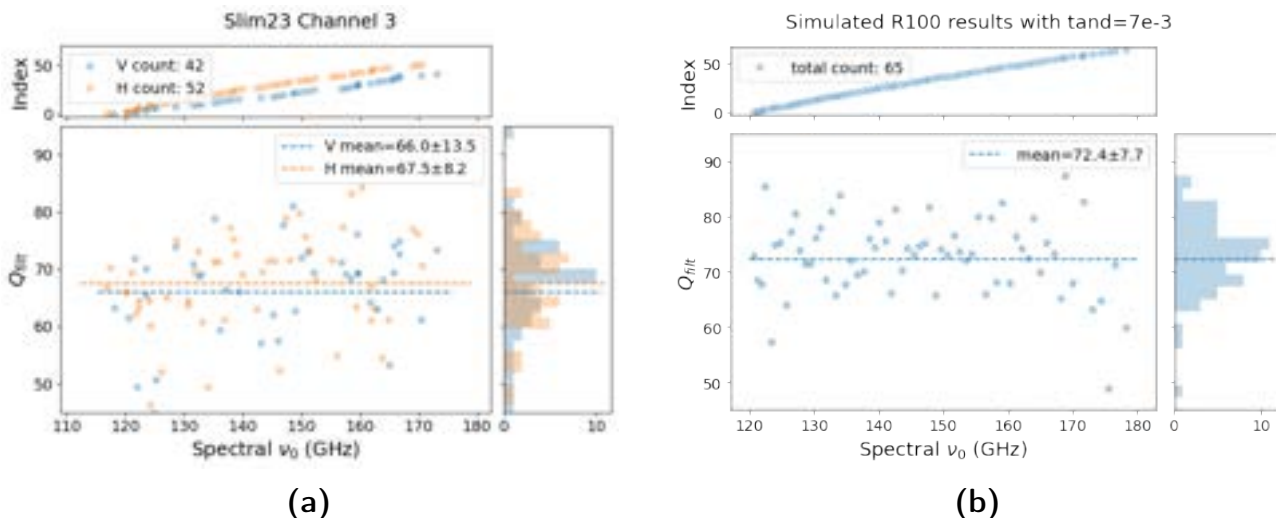


Figure 7.13. Fit values for the Q_{filt} and spectral f_0 for the measured FTS from SLIM23-3 (left) and a simulated filter-bank with $\tan \delta = 7e-3$ (right).

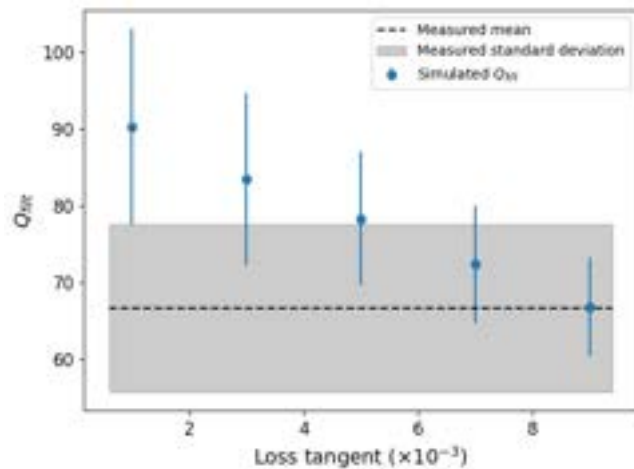


Figure 7.14. Mean simulated FBS Q_{filt} as a function of dielectric loss tangent compared to the measured result from six filter-banks.

A further comparison between the simulated mean Q_{filt} and standard deviation as a function of dielectric loss tangent compared to the measured values is shown in Figure 7.14. This plot largely supports the uncertainty range of the loss tangent measured with the SLIM30 Mini FBS ($(6.8 \pm 1.9) \times 10^{-3}$) however it does suggest $\tan \delta = 9 \times 10^{-3}$. It is probable that a global increase in feature size across the device could explain the discrepancy as this was not included in the simulation. This would increase the parallel plate capacitance, therefore reducing the coupling quality factor.

7.4 Summary and discussion

This section began by presenting the methodology of characterising filter channels of a filter bank via measurements from a Martin-Puplett FTS and showed that even in the case of a low resolution FTS, it is possible to get accurate fits to the filter resolution/quality factor, Q_{filt} , and resonant frequency by fitting an exponentially decaying cosine to the interferogram. However, it is worth noting that this is in the case of a very high precision and sampling of the mirror position, and the point at which this is not true was not explored.

This procedure was used to measure spectra firstly, of a SLIM30 test device consisting of two 5 channel filter-banks with variable resolutions aimed at measuring the dielectric loss tangent and secondly of six different sub-module $R = 100$ filter-banks from the SLIM23 and SLIM24 fabrication runs. The sub-module filter-banks showed an average spectral yield of $(67.7 \pm 9.5) \%$ out of 65 filters per filter-bank where approximately 6 channels per FBS (9 %) were likely cut-off by a limiting LPE filter and the impact of the microwave useful yield had an impact ranging

ranging between 1% to 7%. Across the six sub-modules, the mean filter Q_{filt} was measured to be 66.6 ± 10.9 , where the uncertainty is the standard deviation.

All devices were designed using simulations with values of the niobium L_k and dielectric ε_r set as $0.1 \text{ pH} \square^{-1}$ and 10 respectively. The spectral ν_0 s were found to differ from the design by $\approx -8 \text{ GHz}$ for the SLIM30 device and $\approx (-2.4 \pm 0.9) \text{ GHz}$ for the SLIM23 and SLIM24 sub-modules. This indicated that there is a difference between the SLIM23/24 and SLIM30 devices. All devices showed a similar reduction in Q_{filt} for filters designed for $R \approx 100$, suggesting that the dielectric loss tangent is likely to be still be similar. Assuming this to be the case, the dielectric loss tangent was measured as $(6.8 \pm 1.9) \times 10^{-3}$. However, one of the main issues with the measurement of the dielectric loss tangent in the millimetre spectrum with the method shown in Section 7.2 is the difficulty in distinguishing a the difference between a change in Q_{filt} because of the loss tangent (Q_i) or a detuning caused by something altering the capacitance of the parallel plate coupling capacitors. It is clear that the filters are affected by stochastic lithography variation as evidenced from the 16% standard deviation of quality factor. There will be further variation from the design if the material parameters, namely the L_k and ε_r , are not correct. Ideally, the kinetic inductance of the niobium would be measured at microwave frequencies as this would be an easier measurement to make and L_k should not vary with frequency. The value of $0.1 \text{ pH} \square^{-1}$ is a historic and potentially outdated value for the NbN-capped niobium used in these devices.

That said, it is possible to make an attempt at constraining these values with the measurements made and comparing to simulation. First, a filter is simulated in Sonnet with $\nu_0 = 153 \text{ GHz}$ that is optimally tuned for $Q_{\text{filt}} = 100$ with a lossless dielectric and $L_k = 0.1 \text{ pH} \square^{-1}$, $\varepsilon_r = 10.0$. Then, varying L_k , ε_r and $\tan \delta$, fitting the filter channel throughput (S_{31} in accordance with the simulations shown in Section 3.4) for the ν_0 and Q_{filt} , the parameter space can be mapped out. Taking the loss tangent to be 7×10^{-3} from the SLIM30 device, and the measured Q_{filt} with standard error ($\sigma/\sqrt{6}$) as 66.6 ± 4.4 and change in ν_0 as $(-2.4 \pm 0.9) \text{ GHz}$, the percentage difference between the measured and simulated values can be used to score each parameter combination where a 0% difference indicates a possible solution. The top left of Figure 7.15 shows the possible solutions that satisfy the measured Q_{filt} when fixing $\tan \delta = 7 \times 10^{-3}$. The combinations that satisfy the measured ν_0 deviation with $\tan \delta = 7 \times 10^{-3}$ are then shown in the lower left plot and then calculating a combined score by taking the sum of the magnitudes for the Q_{filt} and ν_0 percentage differences results in the top right plot. The fact the combined score does not show a zero region on the color bar is likely just a parameter resolution issue, however, there is a clear (dark) region where the score tends towards zero and the ν_0 and Q_{filt} zero score contours cross. As such, a likely solution for the kinetic inductance was found to be $L_k = (0.103 \pm 0.018) \text{ pH} \square^{-1}$ and the relative permittivity as $\varepsilon_r = 10.1 \pm 0.6$ where the uncertainties arise from the 6.6% contour as the Q_{filt} standard error is dominant. Indicated by the

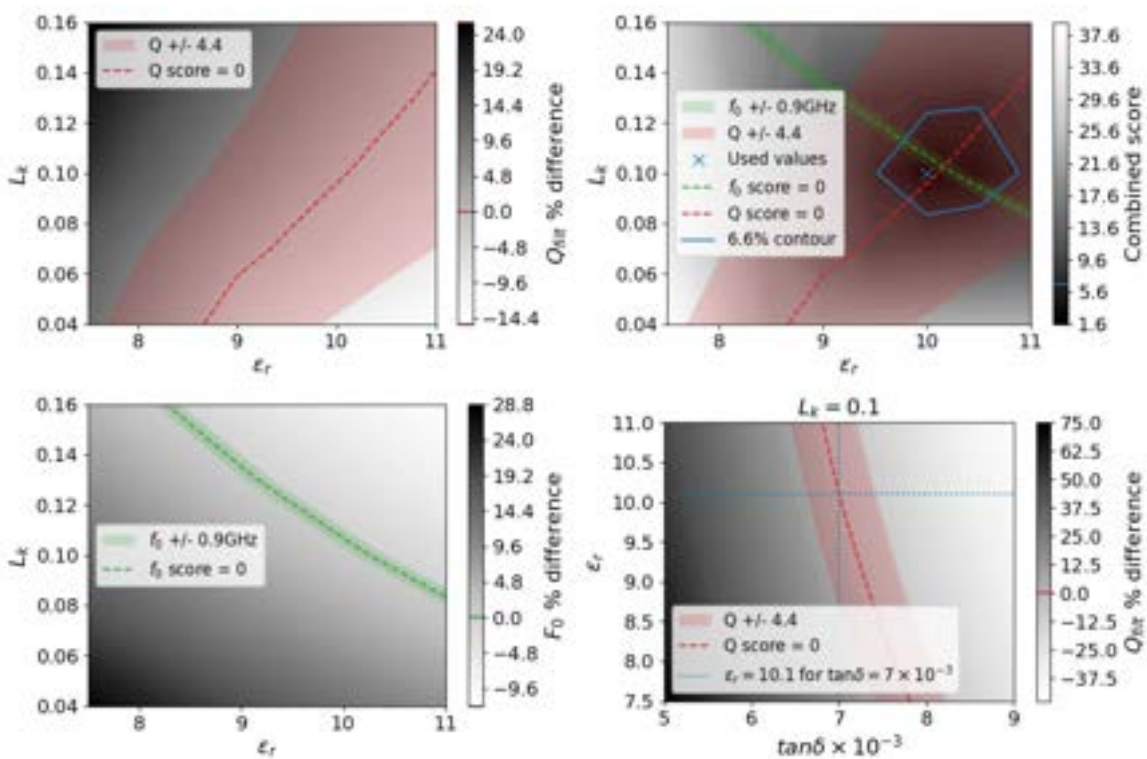


Figure 7.15. Colormaps showing the difference between simulated and measured filter quality factors and resonant frequencies for a variety of possible material parameter combinations. The top and lower left plots have the dielectric loss tangent constrained to 7×10^{-3} and the lower right has the niobium kinetic inductance constrained to (0.103 ± 0.018) . Further details of the plots are described in the text.

blue cross in the combined score plot, these values are indeed close to the values used to initially optimise the design. A further demonstration of the degeneracies and ambiguity around these three parameters is shown in the lower right plot, where instead the kinetic inductance has been constrained to $L_k = 0.1 \text{ pH} \square^{-1}$. It does also show quite clearly that the problem can be single valued if L_k and ϵ_r are precisely known (within the uncertainty of the filter quality factor).

To summarise, the method used to measure the dielectric loss tangent proved difficult to obtain an accurate and precise result as it isn't possible to distinguish between the effects of the loss tangent and that of the coupler detuning with the current design. A value can be determined by assuming the impact of detuning is substantially small relative to the loss tangent, however from the tolerance analysis of the filter geometry we know this to not be the case. This inability to distinguish between Q_c and Q_i does not disappear entirely with precise knowledge of L_k and ϵ_r , it just further minimises the degree of detuning, improving the accuracy of the measured result. Nevertheless it is still important to know these values in order to maximise the efficiency of the filter. Instead, it would be preferable to measure the millimetre wave loss with methods which do not suffer this distinguishing issue such as using on-chip Fabry-Pérot resonators with the technique

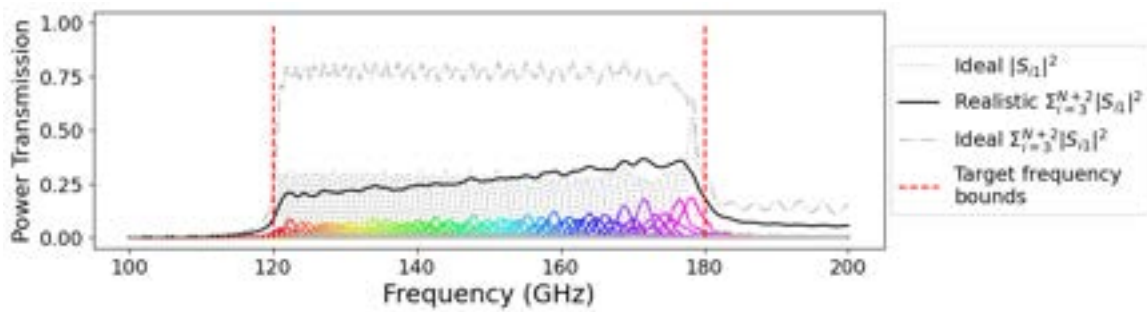


Figure 7.16. Simulated spectrum of a realistic $R = 100$, 0.3λ spaced, $\Sigma = 1.6$ filter-bank with the expected loss tangent of 7×10^{-3} .

described in Hähnle et. al. 2021¹¹⁹, the differential transmission line measurements detailed in Pan et. al. 2023, or the on-chip “ S_{21} ” method used by Superspec⁷⁶.

Finally, despite the uncertainty, it is clear that the dielectric loss tangent is significantly larger than originally anticipated which will therefore have a significant impact on the performance of the device. As per the filter-bank simulation shown in Figure 7.16, with a loss tangent of 7×10^{-3} a mean single channel efficiency of $(7.8 \pm 3.0)\%$ and an approximate total efficiency of 25% across the band is expected. Of course, the end-to-end efficiency will be even lower given the antenna to FBS feedline and other losses related to the OMT. Although, to conclude on a positive note, multiple working filter-bank spectrometers have been demonstrated despite a high loss tangent and worst case, at least four (two sub-modules not shown in this thesis) functional sub-modules with a reasonable forecast throughput efficiency can be deployed to the South Pole Telescope following further device characterisation (with the assumption the channels not presented in this Chapter show a similar functionality and yield).

Chapter 8

Conclusion

This Chapter aims to summarise the work presented in this thesis of which was carried out over four years at Cardiff University within the SPT-SLIM collaboration. First, the structure and content of this thesis is summarised, then the key results are highlighted, followed finally by a discussion on the future outlook implicated by this work.

8.1 Thesis Overview

In Chapter 1, I introduce the current landscape of millimetre wave spectrometers and provide a surface level description of the scientific potential of line intensity mapping and the technological requirements to truly exploit the measurements. I argue why the sensitivity and scalability of superconducting on-chip filter-bank spectrometers positions them as a compelling technology to provide fast, low to medium resolution intensity maps over large areas of the sky.

Chapter 2 provides an overview of SPT-SLIM highlighting it as a technology pathfinder yet still a cutting-edge instrument that will provide beneficial measurements. The SPT-SLIM cryostat details and position on the telescope are briefly covered before introducing the various subsystems of the focal plane.

Details of the focal plane are split into two chapters using the natural separation between the millimetre (spectral) circuit in Chapter 3, and the microwave (readout) circuit in Chapter 4. Firstly, from the millimetre perspective, the circular waveguide is shown to set the high pass edge of the optical throughput which after the OMT antenna, is used in conjunction with a 180° Hybrid to disregard all but the TE_{11} mode, ensuring only this Gaussian beam mode is delivered to the filter-bank. Then the concept of a filter-bank is introduced, followed by the details of the $\lambda/2$ resonating filter and the motivations for the design choices. The process of filter tuning is

also shown, where an iterative process is used to enable maximum efficiency at the desired filter quality factor/resolution. The dielectric loss tangent is then introduced as well as its impact on the single filter efficiency where a trade-off between filter efficiency and resolution is evident. The process used to build an accurate, realistic filter-bank simulation was shown which enabled a tolerance analysis of the filter design as well as an insight into the impact certain design choices had on the filter-bank performance in the absence of devices.

Secondly, the microwave perspective begins by presenting the constraints imposed on the detector design and then details the nominal IDC LEKID and focuses on each lumped component separately. For the aluminium microstrip coupled inductor, there exists a fundamental trade-off between throughput and responsivity. Reducing the aluminium thickness and superconducting volume and therefore increasing the responsivity and kinetic inductance as well as the sheet resistance which then causes an impedance mismatch between the reactance of the superconducting niobium at the inductor input. Furthermore, the motivation for the inductor volume in a $Q_r = 5 \times 10^4$ resonator was provided given the results from the detector model used to forecast the performance to aid the design of a photon noise limited detector. Requirements on the frequency scheduling and footprint on the IDC were shown to lead to a long and narrow design causing a significant dilution of the kinetic inductance fraction with geometric inductance, a design which compromised between being able to tune the filter within the FBS geometry and maximises the kinetic inductance fraction (simulated as $\alpha_k = 0.117$) was adopted. A cross-coupling study for these IDC resonators was presented which characterised the cross coupling by finding the necessary frequency spacing between two detectors separated in various configurations which resulted in a frequency shift of less than 1% in the neighbouring resonator due to a two linewidth shift in the detecting resonator. The parallel plate capacitor LEKID was then also presented, showing negligible cross-coupling, noticeably larger α_k at 0.419 when simulated, and improved f_0 scatter tolerance to linewidth variations in the capacitor. The method applied to manage the cross-coupling between IDC detectors when frequency multiplexing was also shown, followed by the implications these constraints had on the focal plane design which, along with efficiency concerns due to high dielectric loss tangent, ultimately lead to de-scoping the spectrometer design to the 9 pixel, $R = 100$ spectrometer design presented in Chapter 2.

Chapter 6 presents dark measurements of a non-optical prototype device from the SLIM10 fabrication run. Here, VNA and both single tone and multi-tone noise measurements to characterise various parameters of the readout circuit for three detector capacitor architectures, the IDC on the Si substrate, the IDC on the membrane SiN and the parallel plate. Measurements included detector scatter, collisions and yield as well as detector properties such as the responsivity, α_k , quasiparticle lifetime, detector noise spectra, and dark NEP.

Finally, Chapter 7 presents the method by which devices were optically characterised utilising

a Martin-Puplett interferometer in front of a black body as well as the analysis technique for fitting to the interferogram in order to extract the filter properties: resolution, R , and millimetre resonant frequency, ν_0 . The experimental data, analysis and results from a “Mini FBS” prototype device with variable resolution filters from the SLIM30 fabrication run was presented and was used to measure the dielectric loss tangent at millimetre wave. Following this, optical measurements taken at the University of Chicago of three device channels from the SLIM23 and SLIM24 sub-modules were shown and the results were compared to simulated data. Lastly, using these results, an attempt was made with moderate success to constrain the relative permittivity of the dielectric and kinetic inductance of the niobium in order to improve filter ν_0 placement and resolution tuning.

8.2 Key Results

An important result from the filter-bank simulations in the millimetre perspective was that a small section of microstrip in the filter geometry, acts as a small stub off-resonance. When multiple stubs are positioned along a feedline, interference results in a large stop-band-like feature with a frequency response determined by the spacing between the filters. This, along with increased dissipation due to dielectric losses, motivates for shorter spacing between filters relative to the millimetre wavelength of the spectral channels, with optimal efficiencies for spacing at $\lambda/4$ or likely smaller. Conversely, due to the large IDC capacitors, a larger spacing between filters is preferable since the IDC LEKID design suffers significantly from electromagnetic cross-coupling. So much so that within the constraints from the cryostat (spectrometers per readout channel) and readout system (readout bandwidth), to ensure a $Q_r = 5e4$ detector has less than 1% shift in frequency for a two linewidth shift in a neighbouring detector, the nearest frequency neighbour (≈ 850 kHz) must be physically located 19 resonators away in the case of three $R = 300$, $\lambda/4$ spaced filter-bank. Therefore, maximising the FBS technology for efficiency, focal plane packing and resolution is ultimately limited in this detector design without increasing the readout bandwidth, and therefore the required frequency spacing between detectors. For this reason, the negligible cross-coupling for the PPC as well as around a factor of two reduction in capacitor footprint makes the PPC LEKID an attractive option.

From dark measurements of resonant frequency as a function of temperature, the mean values for α_k were measured as 0.042 ± 0.004 , 0.033 ± 0.005 , and 0.216 ± 0.015 for the IDCs, IDC NSs, and PPCs, respectively. These were approximately half of what was anticipated from simulation and this discrepancy is attributed to the increase in aluminium thickness in order to mitigate fabrication risks, therefore reducing the kinetic inductance, hence α_k . The IDC and IDC NS resonators were therefore found to have rather low responsivities of $R = (834 \pm 80) \text{ FFS } \mu\text{W}^{-1}$

and $(645 \pm 90) \text{ FFS } \mu\text{W}^{-1}$, respectively, compared to that of the PPC measured at $(3816 \pm 313) \text{ FFS } \mu\text{W}^{-1}$. This ultimately lead to the PPC having a lower dark NEP at $\approx 3.0 \times 10^{-18} \text{ W}/\sqrt{\text{Hz}}$ at 15 Hz than the IDC NS ($\text{NEP} \approx 4.4 \text{ W}/\sqrt{\text{Hz}}$) and only slightly higher than that of the nominal IDC design with $\text{NEP} \approx 2.1 \text{ W}/\sqrt{\text{Hz}}$ despite the PPC suffering from a large low frequency TLS noise contribution. However, whilst the nominal IDC was close, none of the detectors were below the photon noise at an approximate value of $\approx 2.08 \times 10^{-18} \text{ W}/\sqrt{\text{Hz}}$ for an $R = 100$ spectrometer under typical load at the South Pole. This will be sufficient for SPT-SLIM as a technology pathfinder as it can be overcome by larger integration times, however it does reduce the impact of the demonstration as this will reduce achievable mapping speeds, one of the key advantages of the on-chip FBS.

Furthermore, the noise spectra for all detector architectures exhibited a roll-off type feature that seemed to correspond to the quasiparticle lifetime at higher temperatures ($> 200 \text{ mK}$) but switch to being dominated by the ring-down time of the resonator at lower temperatures. As such, it was not possible to clearly see the lifetime plateau towards lower temperatures with the longest lifetime measured at $(647 \pm 86) \mu\text{s}$. The cause of this is as yet unknown, but given all three capacitor architectures demonstrated similar behaviour it is possibly due to noise contributed by the inductor which was a consistent geometry in all three geometries. An additional issue also presented itself in the IDC noise spectrum whereby large frequency spikes were observed. Whilst the exact coupling mechanism is still to be determined, it is known that these spikes are likely due to vibrational modes of the cryostat, hence to evaluate the extent of this issue noise spectra must be measured within the SPT-SLIM cryostat.

The millimetre dielectric loss tangent for the SiN was measured to have a much larger value than what was anticipated throughout the development process of focal plane where most simulations were carried out expecting close to $\tan \delta = 1 \times 10^{-3}$. Instead through measurements of comparing the measured filter Q_{filt} to varying designed Q_c s, a value of $\tan \delta = (6.8 \pm 1.9) \times 10^{-3}$ was measured. An issue with this measurement technique however is that it is difficult to decouple the reduction in quality factor due loss tangent from that of filter de-tuning via inaccurate material parameters used in simulation of fabrication errors. As such, alternative methods^{90,119} of measuring dielectric loss at millimetre wavelengths will likely be preferable, or at least complementary.

Despite the large dielectric loss, multiple functioning antenna coupled, $R = 100$ spectrometers were still realised. Of the three devices measured across two separate sub-modules spectra within the correct frequency band ($\approx 120 \text{ GHz}$ to 180 GHz) were measured, with a mean spectral yield of $(67.7 \pm 9.5) \%$ and mean filter resolution of $R = Q_{\text{filt}} = 66.6 \pm 10.9$. Note, the spectral yield would likely be slightly higher as approximately 9 % of channels were cut off by a low pass edge in the filter stack. Simulated results, $R = 72.4 \pm 7.7$ for a filter-bank with $\tan \delta = 7 \times 10^{-3}$ showed good agreement with the measured results, further corroborating the loss tangent measurement

and the accuracy of the simulations. Therefore, the simulated spectrum of a realistic $R = 100$, 0.3λ spaced, $\Sigma = 1.6$ filter-bank with the expected loss tangent of 7×10^{-3} implied an approximate average total filter-bank efficiency of $\approx 25\%$ with a single filter efficiency of $(7.8 \pm 3.0)\%$.

8.3 Future work and concluding remarks

As was intended for SPT-SLIM, the work presented in this thesis lays the groundwork for future improvements to SPT-SLIM and similar devices on the path to kilo-pixel, on-chip filter-bank spectrometer devices. Whilst the current sub-modules set for deployment will be sufficient for the first demonstration, there are both short and long term changes that will make significant improvements.

The dielectric loss tangent remains the aspect where the largest gains will come from by improving. This is the dominant limiting factor for both the filter efficiency and resolution where at least one order of magnitude improvement is required from the current dielectric used for SPT-SLIM. However, if resolutions on the order of 1×10^3 are to be achieved, utilising materials with loss tangents similar to those seen with a-Si¹¹⁹ for example, ($\lesssim 1 \times 10^{-4}$) are crucial. Yet current dielectric deposition techniques for these materials are unsuitable to follow the patterning of the sensitive aluminium inductors of which has shown improved detector quality factors with fewer fabrication processes beforehand¹¹². Hence it is a non-trivial amount of work to incorporate these lower loss materials into the design if aluminium is desired for the inductor of a LEKID. One solution would be to move away from the inverted microstrip structure if the gains from reduced dielectric loss outweigh the reduced aluminium quality. A promising result to further boost millimeter efficiencies is the directional filter design developed a SRON¹⁵⁶ which can theoretically reach 100 % filter efficiencies compared to the maximum of 50 % with filter-bank designs used so far.

Additionally, it is largely an obvious statement, the results presented throughout this thesis clearly shows the necessity of having precise and accurate values for the material properties at both microwave and millimetre wavelengths. Without this, results and conclusions become ambiguous and it will not be possible to fully optimise an on-chip FBS and reach the technologies true potential.

Whilst the current detectors satisfy many of the design requirements there are necessary improvements to be made. Whilst the IDC geometry demonstrates minimal TLS noise contributions, the large capacitors dilute the kinetic inductance fraction significantly, resulting in a very low responsivity. To address this, we intend to reduce the aluminium film thickness now we are in a position with deployable sub-modules to take increased risks. Increased responsivity could also come from

Conclusion

moving the readout band to higher frequencies since the capacitors and therefore the geometric inductance will reduce. However, this would have to have a greater improvement to responsivity compared to the inherent reduction to the response tangent by moving to higher frequencies¹⁸. This would also allow the inductor length to be reduced to what it was initially intended to be, further improving responsivity.

Further characterisation and understanding of the current devices is also required. The microphonics in the IDC noise spectrum could pose significant issues with photon sensitivity depending on the frequency they will occur at when devices are installed in the SPT-SLIM cryostat. Improved clamping schemes have shown minor improvements but by no means are they removed. Furthermore, the inability to measure the quasiparticle lifetime at low temperatures with these resonators is a concern.

In the filter-bank configuration, due to the cross-coupling, the IDC LEKID in its current form will ultimately limit the potential of the on-chip spectrometer within limited readout bandwidths relative to the number of detectors per readout line. This and the aforementioned issues with the IDC responsivity and noise spectrum imply that moving to an alternative detector geometry is necessary. The distributed MKID as employed by DESHIMA⁴⁴ and DESHIMA 2.0⁴⁵ is unlikely to suffer from many of these issues, but also the parallel plate capacitor could provide the benefits of LEKID, without the microphonics and the many issues that come from excessively large IDC capacitors. Given how close the PPC detectors were to the photon noise limit, it will likely be possible to overcome the higher TLS noise purely by reducing the detector volume and gaining responsivity. However, the PPC will become a much more versatile and compelling architecture if they can be constructed with low noise dielectrics, where amorphous silicon is a promising candidate¹⁵⁷.

Bibliography

- [1] PG Pérez-González, GH Rieke, and M Blaylock. The cosmic infrared background resolved by spitzer. *arXiv preprint astro-ph/0603208*, 2008.
- [2] Gerhard Ulbricht, Mario De Lucia, and Eoin Baldwin. Applications for microwave kinetic induction detectors in advanced instrumentation. *Applied Sciences*, 11(6):2671, 2021.
- [3] KD Irwin. An application of electrothermal feedback for high resolution cryogenic particle detection. *Applied Physics Letters*, 66(15):1998–2000, 1995.
- [4] Peter K. Day, Henry G. Leduc, Benjamin A. Mazin, Anastasios Vayonakis, and Jonas Zmuidzinas. A broadband superconducting detector suitable for use in large arrays. *Nature*, 425(6960):817–821, 2003.
- [5] Kevork Abazajian, Arwa Abdulghafour, Graeme E Addison, Peter Adshead, Zeeshan Ahmed, Marco Ajello, Daniel Akerib, Steven W Allen, David Alonso, Marcelo Alvarez, et al. Snowmass 2021 cmb-s4 white paper. *arXiv preprint arXiv:2203.08024*, 2022.
- [6] Shawn W Henderson, Jason R Stevens, Mandana Amiri, Jason Austermann, James A Beall, Saptarshi Chaudhuri, Hsiao-Mei Cho, Steve K Choi, Nicholas F Cothard, Kevin T Crowley, et al. Readout of two-kilopixel transition-edge sensor arrays for advanced actpol. In *Millimeter, Submillimeter, and Far-Infrared Detectors and Instrumentation for Astronomy VIII*, volume 9914, pages 346–362. SPIE, 2016.
- [7] Christine Goodwin Pappas et al. Assembly, characterization, and operation of large-scale tes detector arrays for actpol. 2016.
- [8] A Suzuki, Peter Ade, Y Akiba, C Aleman, K Arnold, M Atlas, D Barron, J Borrill, S Chapman, Y Chinone, et al. The polarbear-2 experiment. *Journal of Low Temperature Physics*, 176:719–725, 2014.

BIBLIOGRAPHY

- [9] Brian G Keating, Peter AR Ade, James J Bock, Eric Hivon, William L Holzapfel, Andrew E Lange, Hien Nguyen, and Ki Won Yoon. Bicep: a large angular-scale cmb polarimeter. In *Polarimetry in Astronomy*, volume 4843, pages 284–295. SPIE, 2003.
- [10] Bradford A Benson, PAR Ade, Z Ahmed, SW Allen, K Arnold, JE Austermann, AN Bender, LE Bleem, JE Carlstrom, CL Chang, et al. Spt-3g: a next-generation cosmic microwave background polarization experiment on the south pole telescope. In *Millimeter, Submillimeter, and Far-Infrared Detectors and Instrumentation for Astronomy VII*, volume 9153, pages 552–572. SPIE, 2014.
- [11] BICEP Collaboration II. Experiment and three-year data set. *Astrophys. J.*, 792:62, 2014.
- [12] Martino Calvo, Alain Benoit, A Catalano, J Goupy, Alessandro Monfardini, N Ponthieu, E Barria, G Bres, Michel Grollier, G Garde, et al. The nika2 instrument, a dual-band kilopixel kid array for millimetric astronomy. *Journal of Low Temperature Physics*, 184:816–823, 2016.
- [13] Wayne Holland, Michael MacIntosh, Alasdair Fairley, Dennis Kelly, David Montgomery, David Gostick, Eli Atad-Ettedgui, Maureen Ellis, Ian Robson, Matthew Hollister, et al. Scuba-2: a 10,000-pixel submillimeter camera for the james clerk maxwell telescope. In *Millimeter and Submillimeter Detectors and Instrumentation for Astronomy III*, volume 6275, pages 437–451. SPIE, 2006.
- [14] Nicholas Galitzki, Peter AR Ade, Francesco E Angilè, Peter Ashton, James A Beall, Dan Becker, Kristi J Bradford, George Che, Hsiao-Mei Cho, Mark J Devlin, et al. The next generation blast experiment. *Journal of Astronomical Instrumentation*, 3(02):1440001, 2014.
- [15] M Griffin, J Baselmans, A Baryshev, Simon Doyle, M Grim, Peter Hargrave, T Klapwijk, J Martin-Pintado, A Monfardini, A Neto, et al. Spacekids: kinetic inductance detectors for space applications. In *Millimeter, Submillimeter, and Far-Infrared Detectors and Instrumentation for Astronomy VIII*, volume 9914, pages 10–20. SPIE, 2016.
- [16] Sunil R Golwala, Clint Bockstiegel, Spencer Brugger, Nicole G Czakon, Peter K Day, Thomas P Downes, Ran Duan, Jiansong Gao, Amandeep K Gill, Jason Glenn, et al. Status of music, the multiwavelength sub/millimeter inductance camera. In *Millimeter, Submillimeter, and Far-Infrared Detectors and Instrumentation for Astronomy VI*, volume 8452, pages 33–53. SPIE, 2012.
- [17] Thomas LR Brien, Peter AR Ade, Peter S Barry, Edgar Castillo-Domínguez, Daniel Ferrusca, Thomas Gascard, Victor Gómez, Peter C Hargrave, Amber L Hornsby, David Hughes, et al. Muscat: The mexico-uk sub-millimetre camera for astronomy. In *Millimeter, Submillimeter,*

- and Far-Infrared Detectors and Instrumentation for Astronomy IX*, volume 10708, pages 173–181. SPIE, 2018.
- [18] Jonas Zmuidzinas. Superconducting microresonators: Physics and applications. *Annual Review of Condensed Matter Physics*, 3(1):169–214, 2012.
 - [19] Jochem Baselmans. Kinetic inductance detectors. *Journal of Low Temperature Physics*, 167:292–304, 2012.
 - [20] Benjamin A Mazin. Microwave kinetic inductance detectors: The first decade. In *AIP Conference Proceedings*, volume 1185, pages 135–142. American Institute of Physics, 2009.
 - [21] Philip Mauskopf, Jin Zhang, Peter Ade, Stafford Withington, and Paul Grime. Clover polarimetric detector - a novel design of an ortho-mode transducer at 150 and 225 ghz. In *2008 33rd International Conference on Infrared, Millimeter and Terahertz Waves*, pages 1–2, 2008.
 - [22] Paul F Goldsmith. Sub-millimeter heterodyne focal-plane arrays for high-resolution astronomical spectroscopy. *URSI Radio Science Bulletin*, 2017(362):53–73, 2017.
 - [23] ESO European Southern Observatory. Alma basics, 2024. <https://almascience.eso.org/about-alma/alma-basics>, journal=ALMA Science Portal at ESO [Accessed: 30/08/2024].
 - [24] Jonas Zmuidzinas, Jacob W Kooi, Jonathan Kawamura, Goutam Chattopadhyay, Bruce Bumble, Henry G LeDuc, and Jeffry A Stern. Development of sis mixers for 1 thz. In *Advanced Technology MMW, Radio, and Terahertz Telescopes*, volume 3357, pages 53–62. SPIE, 1998.
 - [25] Duncan Farrah, Kimberly Ennico Smith, David Ardila, Charles M Bradford, Michael Dipirro, Carl Ferkinhoff, Jason Glenn, Paul Goldsmith, David Leisawitz, Thomas Nikola, et al. Far-infrared instrumentation and technological development for the next decade. *Journal of Astronomical Telescopes, Instruments, and Systems*, 5(2):020901–020901, 2019.
 - [26] Alwyn Wootten. Alma capabilities for observations of spectral line emission. In *Science with the Atacama Large Millimeter Array: A New Era for Astrophysics*, pages 9–12. Springer, 2008.
 - [27] L. Earle, P. Ade, J. Aguirre, R. Aikin, J. Battle, J. Bock, C. M. Bradford, M. Dragovan, L. Duband, J. Glenn, G. Griffin, V. Hristov, P. Maloney, H. Matsuura, B. Naylor, H. Nguyen, M. Yun, and J. Zmuidzinas. Z-Spec: a broadband direct-detection millimeter-wave spectrometer – instrument status and first results. In Jonas Zmuidzinas, Wayne S.

BIBLIOGRAPHY

- Holland, Stafford Withington, and William D. Duncan, editors, *Millimeter and Submillimeter Detectors and Instrumentation for Astronomy III*, volume 6275, pages 311 – 319. International Society for Optics and Photonics, SPIE, 2006.
- [28] Chao-Te Li, C. M. Bradford, Abigail Crites, Jonathon Hunacek, Tashun Wei, Jen-Chieh Cheng, Tzu-Ching Chang, and James Bock. TIME millimeter wave grating spectrometer. In *Millimeter, Submillimeter, and Far-Infrared Detectors and Instrumentation for Astronomy IX*, volume 10708, pages 540 – 547. International Society for Optics and Photonics, SPIE, 2018.
- [29] Jonathon Hunacek. *Time: A Millimeter-Wavelength Grating Spectrometer Array for [CII]/CO Intensity Mapping*. PhD thesis, California Institute of Technology, 2020.
- [30] A Fasano, M Aguiar, A Benoit, A Bideaud, O Bourrion, M Calvo, A Catalano, AP de Taoro, G Garde, A Gomez, et al. Kiss: a spectrometric imager for millimetre cosmology. In *EPJ Web of Conferences*, volume 228, page 00010. EDP Sciences, 2020.
- [31] Concerto Collaboration et al. A wide field-of-view low-resolution spectrometer at apex: instrument design and scientific forecast. *Astron. Astrophys.*, 642:A60, 2020.
- [32] Griffin, M. J., Abergel, A., Abreu, A., Ade, P. A. R., André, P., Augueres, J.-L., Babbedge, T., Bae, Y., Baillie, T., Baluteau, J.-P., Barlow, M. J., Bendo, G., Benielli, D., Bock, J. J., Bonhomme, P., Brisbin, D., Brockley-Blatt, C., Caldwell, M., Cara, C., Castro-Rodriguez, N., Cerulli, R., Chanial, P., Chen, S., Clark, E., Clements, D. L., Clerc, L., Coker, J., Communal, D., Conversi, L., Cox, P., Crumb, D., Cunningham, C., Daly, F., Davis, G. R., De Antoni, P., Delderfield, J., Devin, N., Di Giorgio, A., Diduschuns, I., Dohlen, K., Donati, M., Dowell, A., Dowell, C. D., Duband, L., Dumaye, L., Emery, R. J., Ferlet, M., Ferrand, D., Fontignie, J., Fox, M., Franceschini, A., Frerking, M., Fulton, T., Garcia, J., Gastaud, R., Gear, W. K., Glenn, J., Goizel, A., Griffin, D. K., Grundy, T., Guest, S., Guillemet, L., Hargrave, P. C., Harwit, M., Hastings, P., Hatziminaoglou, E., Herman, M., Hinde, B., Hristov, V., Huang, M., Imhof, P., Isaak, K. J., Israelsson, U., Ivison, R. J., Jennings, D., Kiernan, B., King, K. J., Lange, A. E., Latter, W., Laurent, G., Laurent, P., Leeks, S. J., Lellouch, E., Levenson, L., Li, B., Li, J., Lilienthal, J., Lim, T., Liu, S. J., Lu, N., Madden, S., Mainetti, G., Marliani, P., McKay, D., Mercier, K., Molinari, S., Morris, H., Moseley, H., Mulder, J., Mur, M., Naylor, D. A., Nguyen, H., O'Halloran, B., Oliver, S., Olofsson, G., Olofsson, H.-G., Orfei, R., Page, M. J., Pain, I., Panuzzo, P., Papageorgiou, A., Parks, G., Parr-Burman, P., Pearce, A., Pearson, C., Pérez-Fournon, I., Pinsard, F., Pisano, G., Podosek, J., Pohlen, M., Polehampton, E. T., Poulquin, D., Rigopoulou, D., Rizzo, D., Roseboom, I. G., Roussel, H., Rowan-Robinson, M., Rownd, B., Saraceno, P., Sauvage, M.,

- Savage, R., Savini, G., Sawyer, E., Scharnberg, C., Schmitt, D., Schneider, N., Schulz, B., Schwartz, A., Shafer, R., Shupe, D. L., Sibthorpe, B., Sidher, S., Smith, A., Smith, A. J., Smith, D., Spencer, L., Stobie, B., Sudiwala, R., Sukhatme, K., Surace, C., Stevens, J. A., Swinyard, B. M., Trichas, M., Tourette, T., Triou, H., Tseng, S., Tucker, C., Turner, A., Vaccari, M., Valtchanov, I., Vigroux, L., Virique, E., Voellmer, G., Walker, H., Ward, R., Waskett, T., Weilert, M., Wesson, R., White, G. J., Whitehouse, N., Wilson, C. D., Winter, B., Woodcraft, A. L., Wright, G. S., Xu, C. K., Zavagno, A., Zemcov, M., Zhang, L., and Zonca, E. The herschel-spire instrument and its in-flight performance*. *A&A*, 518:L3, 2010.
- [33] Zhaodi Pan, Mira Liu, Ritoban Basu Thakur, Bradford A. Benson, Dale J. Fixsen, Hazal Goksu, Eleanor Rath, and Stephan S. Meyer. Compact millimeter-wavelength fourier-transform spectrometer. *Applied Optics*, 58(23):6257, August 2019.
- [34] Vidi Saptari. *Fourier transform spectroscopy instrumentation engineering*. SPIE Optical Engineering Press Bellingham Washington, DC, 2003.
- [35] David Naylor, Brad Gom, Anthony Huber, Alicia Anderson, Adam Christiansen, Willem Jellema, Bram Lap, Ian Veenendaal, Alain Cournoyer, Frederic Grandmont, et al. Development of a cryogenic far-infrared post-dispersed polarizing fourier transform spectrometer: a demonstrator for the spica safari instrument. In *Millimeter, Submillimeter, and Far-Infrared Detectors and Instrumentation for Astronomy X*, volume 11453, pages 117–127. SPIE, 2020.
- [36] Brad Gom and David Naylor. Testing results and current status of fts-2, an imaging fourier transform spectrometer for scuba-2. In *Proc. SPIE*, volume 7741, page 2E, 2010.
- [37] Amil Patel, Ari-David Brown, Wen-Ting Hsieh, Thomas Stevenson, S Harvey Moseley, U Kongpop, Negar Ehsan, Emily Barrentine, George Manos, Edward J Wollack, et al. Fabrication of mkids for the microspec spectrometer. *IEEE transactions on applied superconductivity*, 23(3):2400404–2400404, 2013.
- [38] Giuseppe Cataldo, Emily M Barrentine, Berhanu T Bulcha, Negar Ehsan, Larry A Hess, Omid Noroozian, Thomas R Stevenson, Edward J Wollack, Samuel H Moseley, and Eric R Switzer. Second-generation micro-spec: A compact spectrometer for far-infrared and submillimeter space missions. *Acta Astronautica*, 162:155–159, 2019.
- [39] Giuseppe Cataldo, EM Barrentine, BT Bulcha, N Ehsan, LA Hess, O Noroozian, TR Stevenson, K U-Yen, EJ Wollack, and SH Moseley. Second-generation design of micro-spec: a medium-resolution, submillimeter-wavelength spectrometer-on-a-chip. *Journal of Low Temperature Physics*, 193:923–930, 2018.

- [40] Mona Mirzaei, Emily M. Barrentine, Berhanu T. Bulcha, Giuseppe Cataldo, Jake A. Connors, Negar Ehsan, Thomas M. Essinger-Hileman, Larry A. Hess, Jonas W. Mugge-Durum, Omid Noroozian, Trevor M. Oxholm, Thomas R. Stevenson, Eric R. Switzer, Carolyn G. Volpert, and Edward J. Wollack. μ -spec spectrometers for the EXCLAIM instrument. In Jonas Zmuidzinas and Jian-Rong Gao, editors, *Millimeter, Submillimeter, and Far-Infrared Detectors and Instrumentation for Astronomy X*. SPIE, dec 2020.
- [41] Carolyn G Volperta Switzera and Edward J Wollacka. μ -spec spectrometers for the exclaim instrument. *arXiv preprint arXiv:2101.11741*, 2021.
- [42] Giuseppe Cataldo, Wen-Ting Hsieh, Wei-Chung Huang, S Harvey Moseley, Thomas R Stevenson, and Edward J Wollack. Micro-spec: an ultracompact, high-sensitivity spectrometer for far-infrared and submillimeter astronomy. *Applied optics*, 53(6):1094–1102, 2014.
- [43] Omid Noroozian, EM Barrentine, AD Brown, Giuseppe Cataldo, Negar Ehsan, Wen-Ting Hsieh, Thomas Stevenson, Kongpop U-yen, Edward Wollack, and Samuel Harvey Moseley. μ -spec: An efficient compact integrated spectrometer for submillimeter astrophysics. In *26th International Symposium On Space Terahertz Technology*, 2015.
- [44] A Endo, P Van der Werf, RMJ Janssen, PJ De Visser, TM Klapwijk, JJA Baselmans, L Ferrari, AM Baryshev, and SJC Yates. Design of an integrated filterbank for deshima: On-chip submillimeter imaging spectrograph based on superconducting resonators. *Journal of low temperature physics*, 167:341–346, 2012.
- [45] Akio Taniguchi, Tom JLC Bakx, Jochem JA Baselmans, Robert Huiting, Kenichi Karatsu, Nuria Llombart, Matus Rybak, Tatsuya Takekoshi, Yoichi Tamura, Hiroki Akamatsu, et al. Deshima 2.0: Development of an integrated superconducting spectrometer for science-grade astronomical observations. *Journal of Low Temperature Physics*, 209(3):278–286, 2022.
- [46] Akira Endo, Kenichi Karatsu, Yoichi Tamura, Tai Oshima, Akio Taniguchi, Tatsuya Takekoshi, Shin'ichiro Asayama, Tom J. L. C. Bakx, Sjoerd Bosma, Juan Bueno, and et al. First light demonstration of the integrated superconducting spectrometer. *Nature Astronomy*, 3(11):989–996, Aug 2019.
- [47] Tatsuya Takekoshi, Kenichi Karatsu, Junya Suzuki, Yoichi Tamura, Tai Oshima, Akio Taniguchi, Shin'ichiro Asayama, Tom JLC Bakx, Jochem JA Baselmans, Sjoerd Bosma, et al. Deshima on aste: on-sky responsivity calibration of the integrated superconducting spectrometer. *Journal of Low Temperature Physics*, 199:231–239, 2020.
- [48] P. S. Barry, E. Shirokoff, A. Kovács, T. J. Reck, S. Hailey-Dunsheath, C. M. McKenney, L. J. Swenson, M. I. Hollister, H. G. Leduc, S. Doyle, R. O'Brient, N. Llombart, D. Marrone,

- G. Chattopadhyay, P. K. Day, S. Padin, C. M. Bradford, P. D. Mauskopf, and J. Zmuidzinas. Electromagnetic design for SuperSpec: a lithographically-patterned millimetre-wave spectrograph. In Wayne S. Holland, editor, *Millimeter, Submillimeter, and Far-Infrared Detectors and Instrumentation for Astronomy VI*, volume 8452, page 84522F. International Society for Optics and Photonics, SPIE, 2012.
- [49] S. Hailey-Dunsheath, E. Shirokoff, P. S. Barry, C. M. Bradford, G. Chattopadhyay, P. Day, S. Doyle, M. Hollister, A. Kovacs, H. G. LeDuc, and et al. Status of superspec: a broadband, on-chip millimeter-wave spectrometer. *Millimeter, Submillimeter, and Far-Infrared Detectors and Instrumentation for Astronomy VII*, Aug 2014.
- [50] KS Karkare, PS Barry, CM Bradford, S Chapman, S Doyle, J Glenn, S Gordon, S Hailey-Dunsheath, RMJ Janssen, A Kovács, et al. Full-array noise performance of deployment-grade superspec mm-wave on-chip spectrometers. *Journal of Low Temperature Physics*, 199(3):849–857, 2020.
- [51] Ritoban Basu Thakur, A Steiger, S Shu, F Faramarzi, N Klimovich, PK Day, E Shirokoff, PD Mauskopf, and PS Barry. Development of superconducting on-chip fourier transform spectrometers. *Journal of Low Temperature Physics*, 211(5):227–236, 2023.
- [52] David A. Naylor, Brad G. Gom, Alicia M. Anderson, Adam J. Christiansen, Alain Cournoyer, Frederic Grandmont, Ben Louwerse, Peter A. R. Ade, Willem Jellema, Bram Lap, and Stafford Withington. Development of a cryogenic far-infrared post-dispersed polarising fourier transform spectrometer. In *2022 47th International Conference on Infrared, Millimeter and Terahertz Waves (IRMMW-THz)*, pages 1–2, 2022.
- [53] Ely D Kovetz, Marco P Viero, Adam Lidz, Laura Newburgh, Mubdi Rahman, Eric Switzer, Marc Kamionkowski, James Aguirre, Marcelo Alvarez, James Bock, et al. Line-intensity mapping: 2017 status report. *arXiv preprint arXiv:1709.09066*, 2017.
- [54] Kirit S Karkare, Azadeh Moradinezhad Dizgah, Garrett K Keating, Patrick Breysse, and Dongwoo T Chung. Snowmass 2021 cosmic frontier white paper: Cosmology with millimeter-wave line intensity mapping. *arXiv preprint arXiv:2203.07258*, 2022.
- [55] Andrej Obuljen, Emanuele Castorina, Francisco Villaescusa-Navarro, and Matteo Viel. High-redshift post-reionization cosmology with 21cm intensity mapping. *Journal of Cosmology and Astroparticle Physics*, 2018(05):004–004, May 2018.
- [56] ER Switzer, CJ Anderson, AR Pullen, and S Yang. Intensity mapping in the presence of foregrounds and correlated continuum emission. *The Astrophysical Journal*, 872(1):82, 2019.

BIBLIOGRAPHY

- [57] Azadeh Moradinezhad Dizgah, Garrett K. Keating, Kirit S. Karkare, Abigail Crites, and Shouvik Roy Choudhury. Neutrino properties with ground-based millimeter-wavelength line intensity mapping, 2021.
- [58] Joaquin Vieira, James Aguirre, C Matt Bradford, Jeffrey Filippini, Christopher Groppi, Dan Marrone, Matthieu Bethermin, Tzu-Ching Chang, Mark Devlin, Oliver Dore, et al. The terahertz intensity mapper (tim): A next-generation experiment for galaxy evolution studies. *arXiv preprint arXiv:2009.14340*, 2020.
- [59] Manuel Aravena, Jason E Austermann, Kaustuv Basu, Nicholas Battaglia, Benjamin Beringue, Frank Bertoldi, Frank Bigiel, J Richard Bond, Patrick C Breysse, Colton Broughton, et al. Ccat-prime collaboration: science goals and forecasts with prime-cam on the fred young submillimeter telescope. *The Astrophysical Journal Supplement Series*, 264(1):7, 2022.
- [60] K. S. Karkare, A. J. Anderson, P. S. Barry, B. A. Benson, J. E. Carlstrom, T. Cecil, C. L. Chang, M. A. Dobbs, M. Hollister, G. K. Keating, and et al. Spt-slim: A line intensity mapping pathfinder for the south pole telescope. *Journal of Low Temperature Physics*, 209(5–6):758–765, 2022.
- [61] John Ruhl, Peter A. R. Ade, John E. Carlstrom, Hsiao-Mei Cho, Thomas Crawford, Matt Dobbs, Chris H. Greer, Nils w. Halverson, William L. Holzapfel, Trevor M. Lanting, Adrian T. Lee, Erik M. Leitch, Jon Leong, Wenyang Lu, Martin Lueker, Jared Mehl, Stephan S. Meyer, Joe J. Mohr, Steve Padin, T. Plagge, Clem Pryke, Marcus C. Runyan, Dan Schwan, M. K. Sharp, Helmuth Spieler, Zak Staniszewski, and Antony A. Stark. The South Pole Telescope. In Jonas Zmuidzinas, Wayne S. Holland, and Stafford Withington, editors, *Millimeter and Submillimeter Detectors for Astronomy II*, volume 5498, pages 11 – 29. International Society for Optics and Photonics, SPIE, 2004.
- [62] J. E. Carlstrom, P. A. R. Ade, K. A. Aird, B. A. Benson, L. E. Bleem, S. Busetti, C. L. Chang, E. Chauvin, H.-M. Cho, T. M. Crawford, A. T. Crites, M. A. Dobbs, N. W. Halverson, S. Heimsath, W. L. Holzapfel, J. D. Hrubes, M. Joy, R. Keisler, T. M. Lanting, A. T. Lee, E. M. Leitch, J. Leong, W. Lu, M. Lueker, D. Luong-Van, J. J. McMahon, J. Mehl, S. S. Meyer, J. J. Mohr, T. E. Montroy, S. Padin, T. Plagge, C. Pryke, J. E. Ruhl, K. K. Schaffer, D. Schwan, E. Shirokoff, H. G. Spieler, Z. Staniszewski, A. A. Stark, C. Tucker, K. Vanderlinde, J. D. Vieira, and R. Williamson. The 10 meter south pole telescope. *Publications of the Astronomical Society of the Pacific*, 123(903):568, apr 2011.
- [63] Junhan Kim, Daniel P. Marrone, Christopher Beaudoin, John E. Carlstrom, Shepherd S. Doeleman, Thomas W. Folkers, David Forbes, Christopher H. Greer, Eugene F. Lauria,

- Kyle D. Massingill, Evan Mayer, Chi H. Nguyen, George Reiland, Jason SooHoo, Antony A. Stark, Laura Vertatschitsch, Jonathan Weintroub, and André Young. A VLBI receiving system for the South Pole Telescope. In Jonas Zmuidzinas and Jian-Rong Gao, editors, *Millimeter, Submillimeter, and Far-Infrared Detectors and Instrumentation for Astronomy IX*, volume 10708, page 107082S. International Society for Optics and Photonics, SPIE, 2018.
- [64] Simon Doyle. *Lumped element Kinetic Inductance Detectors*. PhD thesis, Cardiff School of Physics and Astronomy, 2008.
- [65] David M. Pozar. *Microwave engineering*. John Wiley & Sons, 2012.
- [66] Johannes Hubmayr, Jason E. Austermann, James A. Beall, Daniel T. Becker, Steven J. Benton, A. Stevie Bergman, J. Richard Bond, Sean Bryan, Shannon M. Duff, Adri J. Duivenvoorden, H. K. Eriksen, Jeffrey P. Filippini, A. Fraisse, Mathew Galloway, Anne E. Gambrel, K. Ganga, Arpi L. Grigorian, Riccardo Gualtieri, Jon E. Gudmundsson, John W. Hartley, M. Halpern, Gene C. Hilton, William C. Jones, Jeffrey J. McMahon, Lorenzo Moncelsi, Johanna M. Nagy, C. B. Netterfield, Benjamin Osherson, Ivan Padilla, Alexandra S. Rahlin, B. Racine, John Ruhl, T. M. Rudd, J. A. Shariff, J. D. Soler, Xue Song, Joel N. Ullom, Jeff Van Lanen, Michael R. Vissers, I. K. Wehus, Shyang Wen, D. V. Wiebe, and Edward Young. Design of 280 ghz feedhorn-coupled tes arrays for the balloon-borne polarimeter spider. In Wayne S. Holland and Jonas Zmuidzinas, editors, *Millimeter, Submillimeter, and Far-Infrared Detectors and Instrumentation for Astronomy VIII*. SPIE, 2016.
- [67] S. M. Stanchfield, P. A. Ade, J. Aguirre, J. A. Brevik, H. M. Cho, R. Datta, and M. J. and Devlin. Development of a microwave squid-multiplexed tes array for mustang-2. *Journal of Low Temperature Physics*, 184(1–2), 2016.
- [68] J. E. Austermann, K. A. Aird, J. A. Beall, D. Becker, A. Bender, B. A. Benson, L. E. Bleem, J. Britton, J. E. Carlstrom, C. L. Chang, H. C. Chiang, H.-M. Cho, T. M. Crawford, A. T. Crites, A. Datesman, T. de Haan, M. A. Dobbs, E. M. George, N. W. Halverson, N. Harrington, J. W. Henning, G. C. Hilton, G. P. Holder, W. L. Holzapfel, S. Hoover, N. Huang, J. Hubmayr, K. D. Irwin, R. Keisler, J. Kennedy, L. Knox, A. T. Lee, E. Leitch, D. Li, M. Lueker, D. P. Marrone, J. J. McMahon, J. Mehl, S. S. Meyer, T. E. Montroy, T. Natoli, J. P. Nibarger, M. D. Niemack, V. Novosad, S. Padin, C. Pryke, C. L. Reichardt, J. E. Ruhl, B. R. Saliwanchik, J. T. Sayre, K. K. Schaffer, E. Shirokoff, A. A. Stark, K. Story, K. Vanderlinde, J. D. Vieira, G. Wang, R. Williamson, V. Yefremenko, K. W. Yoon, and O. Zahn. SPTpol: an instrument for CMB polarization measurements with the South Pole Telescope. In Wayne S. Holland, editor, *Millimeter, Submillimeter, and*

BIBLIOGRAPHY

Far-Infrared Detectors and Instrumentation for Astronomy VI, volume 8452, page 84521E. International Society for Optics and Photonics, SPIE, 2012.

- [69] M. D. Niemack, P. A. R. Ade, J. Aguirre, F. Barrientos, J. A. Beall, J. R. Bond, J. Britton, H. M. Cho, S. Das, M. J. Devlin, S. Dicker, J. Dunkley, R. Dünner, J. W. Fowler, A. Hajian, M. Halpern, M. Hasselfield, G. C. Hilton, M. Hilton, J. Hubmayr, J. P. Hughes, L. Infante, K. D. Irwin, N. Jarosik, J. Klein, A. Kosowsky, T. A. Marriage, J. McMahon, F. Menanteau, K. Moodley, J. P. Nibarger, M. R. Nolta, L. A. Page, B. Partridge, E. D. Reese, J. Sievers, D. N. Spergel, S. T. Staggs, R. Thornton, C. Tucker, E. Wollack, and K. W. Yoon. ACTPol: a polarization-sensitive receiver for the Atacama Cosmology Telescope. In Wayne S. Holland and Jonas Zmuidzinas, editors, *Millimeter, Submillimeter, and Far-Infrared Detectors and Instrumentation for Astronomy V*, volume 7741, page 77411S. International Society for Optics and Photonics, SPIE, 2010.
- [70] Thomas Essinger-Hileman, Aamir Ali, Mandana Amiri, John W. Appel, Derek Araujo, Charles L. Bennett, Fletcher Boone, Manwei Chan, Hsiao-Mei Cho, David T. Chuss, Felipe Colazo, Erik Crowe, Kevin Denis, Rolando Dünner, Joseph Eimer, Dominik Gothe, Mark Halpern, Kathleen Harrington, Gene C. Hilton, Gary F. Hinshaw, Caroline Huang, Kent Irwin, Glenn Jones, John Karakla, Alan J. Kogut, David Larson, Michele Limon, Lindsay Lowry, Tobias Marriage, Nicholas Mehrle, Amber D. Miller, Nathan Miller, Samuel H. Moseley, Giles Novak, Carl Reintsema, Karwan Rostem, Thomas Stevenson, Deborah Towner, Kongpop U-Yen, Emily Wagner, Duncan Watts, Edward J. Wollack, Zhilei Xu, and Lingzhen Zeng. CLASS: the cosmology large angular scale surveyor. In Wayne S. Holland and Jonas Zmuidzinas, editors, *Millimeter, Submillimeter, and Far-Infrared Detectors and Instrumentation for Astronomy VII*, volume 9153, page 91531I. International Society for Optics and Photonics, SPIE, 2014.
- [71] Shibo Shu, Shigeyuki Sekiguchi, Masakazu Sekine, Yutaro Sekimoto, Tom Nitta, Agnes Dominjon, Takashi Noguchi, Masato Naruse, and Wenlei Shan. Development of octave-band planar ortho-mode transducer with kinetic inductance detector for LiteBIRD. In Wayne S. Holland and Jonas Zmuidzinas, editors, *Millimeter, Submillimeter, and Far-Infrared Detectors and Instrumentation for Astronomy VIII*, volume 9914, page 99142C. International Society for Optics and Photonics, SPIE, 2016.
- [72] Johannes Hubmayr, Jason E. Austermann, James A. Beall, Jake A. Connors, Shannon M. Duff, and Jeffrey J. McMahon. Tolerance analysis of octave bandwidth millimeter-wave planar orthomode transducer, 2022.
- [73] Karwan Rostem, Aamir Ali, John W. Appel, Charles L. Bennett, Ari Brown, Meng-Ping

- Chang, David T. Chuss, Felipe A. Colazo, Nick Costen, Kevin L. Denis, Tom Essinger-Hileman, Ron Hu, Tobias A. Marriage, Samuel H. Moseley, Thomas R. Stevenson, Kongpop U-Yen, Edward J. Wollack, and Zhilei Xu. Silicon-based antenna-coupled polarization-sensitive millimeter-wave bolometer arrays for cosmic microwave background instruments. In Wayne S. Holland and Jonas Zmuidzinas, editors, *Millimeter, Submillimeter, and Far-Infrared Detectors and Instrumentation for Astronomy VIII*. SPIE, 2016.
- [74] R. Gualtieri, P. S. Barry, T. Cecil, A. N. Bender, C. L. Chang, J. C. Hood, M. Lisovenko, and V. G. Yefremenko. Optical leakage mitigation in ortho-mode transducer detectors for microwave applications. *Journal of Low Temperature Physics*, 209(3–4):314–321, 2022.
- [75] Kaushik Debbarma, Nhat Truong, Satish Kumar Sharma, and Jia-Chi Samuel Chieh. 2-d beam steering performance of a triple mode horn antenna integrated with risley prism and phase correcting surface. *IEEE Open Journal of Antennas and Propagation*, 3:752–761, 2022.
- [76] Jordan Wheeler. *Millimeter-wave galaxy spectroscopy: SuperSpec on-Chip Spectrometer Technology Development and ALMA observations of molecular gas in the ARP 220 nucleus*. PhD thesis, University of Colorado, 2015.
- [77] Attila Kovács, Peter S. Barry, Charles M. Bradford, Goutam Chattopadhyay, Peter Day, Simon Doyle, Steve Hailey-Dunsheath, Matthew Hollister, Christopher McKenney, Henry G. LeDuc, and et al. Superspec: design concept and circuit simulations. *Millimeter, Submillimeter, and Far-Infrared Detectors and Instrumentation for Astronomy VI*, Sep 2012.
- [78] Alejandro Pascual Laguna, Kenichi Karatsu, David Thoen, Vignesh Murugesan, Bruno Buijtendorp, Akira Endo, and Jochem Baselmans. Terahertz band-pass filters for wideband superconducting on-chip filter-bank spectrometers. *IEEE Transactions on Terahertz Science and Technology*, pages 1–1, 2021.
- [79] S. Hailey-Dunsheath, E. Shirokoff, P. S. Barry, C. M. Bradford, G. Chattopadhyay, P. Day, S. Doyle, M. Hollister, A. Kovacs, H. G. LeDuc, and et al. Status of superspec: a broadband, on-chip millimeter-wave spectrometer. *Millimeter, Submillimeter, and Far-Infrared Detectors and Instrumentation for Astronomy VII*, Aug 2014.
- [80] E. Shirokoff, P. S. Barry, C. M. Bradford, G. Chattopadhyay, P. Day, S. Doyle, S. Hailey-Dunsheath, M. I. Hollister, A. Kovács, C. McKenney, H. G. Leduc, N. Llombart, D. P. Marrone, P. Mauskopf, R. O'Brient, S. Padin, T. Reck, L. J. Swenson, and J. Zmuidzinas. MKID development for SuperSpec: an on-chip, mm-wave, filter-bank spectrometer. In Wayne S. Holland, editor, *Millimeter, Submillimeter, and Far-Infrared Detectors and Instrumentation for Astronomy VI*, volume 8452, pages 209 – 219. International Society for Optics and Photonics, SPIE, 2012.

BIBLIOGRAPHY

- [81] A. Endo, C. Sfiligoj, S. J. C. Yates, J. J. A. Baselmans, D. J. Thoen, S. M. H. Javadzadeh, P. P. van der Werf, A. M. Baryshev, and T. M. Klapwijk. On-chip filter bank spectroscopy at 600–700 ghz using nbtin superconducting resonators. *Applied Physics Letters*, 103(3):032601, 2013.
- [82] Akira Endo, Kenichi Karatsu, Alejandro Pascual Laguna, Behnam Mirzaei, Robert Huiting, David J Thoen, Vignesh Murugesan, Stephen JC Yates, Juan Bueno, Nuri van Marrewijk, et al. Wideband on-chip terahertz spectrometer based on a superconducting filterbank. *Journal of Astronomical Telescopes, Instruments, and Systems*, 5(3):035004–035004, 2019.
- [83] Sonnet Software, Inc. Sonnet suites.
- [84] Moe S Khalil, FC Wellstood, and Kevin D Osborn. Loss dependence on geometry and applied power in superconducting coplanar resonators. *IEEE Transactions on Applied Superconductivity*, 21(3):879–882, 2010.
- [85] Jiansong Gao. *The physics of superconducting microwave resonators*. PhD thesis, California Institute of Technology, Department of Physics, Caltech, Pasadena, CA, USA, 2008.
- [86] David P. Pappas, Michael R. Vissers, David S. Wisbey, Jeffrey S. Kline, and Jiansong Gao. Two level system loss in superconducting microwave resonators. *IEEE Transactions on Applied Superconductivity*, 21(3):871–874, 2011.
- [87] John M. Martinis, K. B. Cooper, R. McDermott, Matthias Steffen, Markus Ansmann, K. D. Osborn, K. Cicak, Seongshik Oh, D. P. Pappas, R. W. Simmonds, and Clare C. Yu. Decoherence in josephson qubits from dielectric loss. *Phys. Rev. Lett.*, 95:210503, Nov 2005.
- [88] Hanhee Paik and Kevin D Osborn. Reducing quantum-regime dielectric loss of silicon nitride for superconducting quantum circuits. *Applied physics letters*, 96(7):072505–072505–3, 2010.
- [89] S Hailey-Dunsheath, P S Barry, C M Bradford, G Chattopadhyay, P Day, S Doyle, M Hollister, A Kovacs, H G LeDuc, N Llombart, P Mauskopf, C McKenney, R Monroe, H T Nguyen, R O'Brient, S Padin, T Reck, E Shirokoff, L Swenson, C E Tucker, and J Zmuidzinas. Optical measurements of superspec: A millimeter-wave on-chip spectrometer. *Journal of low temperature physics*, 176(5):841–847, 2014.
- [90] Z. Pan, P. S. Barry, T. Cecil, C. Albert, A. N. Bender, C. L. Chang, R. Gualtieri, J. Hood, J. Li, J. Zhang, M. Lisovenko, V. Novosad, G. Wang, and V. Yefremenko. Measurement of dielectric loss in silicon nitride at centimeter and millimeter wavelengths. *IEEE Transactions on Applied Superconductivity*, 33(5):1–7, 2023.

- [91] George Che. *Advancements in Kinetic Inductance Detector, Spectrometer, and Amplifier Technologies for Millimeter-Wave Astronomy*. PhD thesis, Department of Physics, Arizona State University, 2018.
- [92] Byeong Ho Eom, Peter K. Day, Henry G. LeDuc, and Jonas Zmuidzinas. A wideband, low-noise superconducting amplifier with high dynamic range. *Nature Physics*, 8(8):623–627, 2012.
- [93] A. L. Hornsby, P. S. Barry, S. M. Doyle, Q. Y. Tang, and E. Shirokoff. Reducing the susceptibility of lumped-element kids to two-level system effects. *Journal of Low Temperature Physics*, 200(5-6):239–246, 2020.
- [94] M. Rouble, G. Smecher, A. Anderson, P. S. Barry, K. Dibert, M. Dobbs, K. S. Karkare, and J. Montgomery. RF-ICE: large-scale gigahertz readout of frequency-multiplexed microwave kinetic inductance detectors. In Jonas Zmuidzinas and Jian-Rong Gao, editors, *Millimeter, Submillimeter, and Far-Infrared Detectors and Instrumentation for Astronomy XI*, volume 12190, page 1219024. International Society for Optics and Photonics, SPIE, 2022.
- [95] S. Doyle, P. Mauskopf, J. Naylor, A. Porch, and C. Duncombe. Lumped element kinetic inductance detectors. *Journal of Low Temperature Physics*, 151(1–2):530–536, Jan 2008.
- [96] Henry G. Leduc, Bruce Bumble, Peter K. Day, Byeong Ho Eom, Jiansong Gao, Sunil Golwala, Benjamin A. Mazin, Sean McHugh, Andrew Merrill, David C. Moore, Omid Noroozian, Anthony D. Turner, and Jonas Zmuidzinas. Titanium nitride films for ultrasensitive microresonator detectors. *Applied Physics Letters*, 97(10):102509, 09 2010.
- [97] P. Szypryt, S. R. Meeker, G. Coiffard, N. Fruitwala, B. Bumble, G. Ulbricht, A. B. Walter, M. Daal, C. Bockstiegel, G. Collura, N. Zobrist, I. Lipartito, and B. A. Mazin. Large-format platinum silicide microwave kinetic inductance detectors for optical to near-ir astronomy. *Opt. Express*, 25(21):25894–25909, Oct 2017.
- [98] Nicholas Zobrist, Grégoire Coiffard, Bruce Bumble, Noah Swimmer, Sarah Steiger, Miguel Daal, Giulia Collura, Alex B. Walter, Clint Bockstiegel, Neelay Fruitwala, Isabel Lipartito, and Benjamin A. Mazin. Design and performance of hafnium optical and near-IR kinetic inductance detectors. *Applied Physics Letters*, 115(21):213503, 11 2019.
- [99] Kevin Kouwenhoven, Daniel Fan, Enrico Biancalani, Steven A.H. de Rooij, Tawab Karim, Carlas S. Smith, Vignesh Murugesan, David J. Thoen, Jochem J.A. Baselmans, and Pieter J. de Visser. Resolving power of visible-to-near-infrared hybrid β –Ta/Nb–Ti–N kinetic inductance detectors. *Phys. Rev. Appl.*, 19:034007, Mar 2023.

BIBLIOGRAPHY

- [100] Robert M Fano. Theoretical limitations on the broadband matching of arbitrary impedances. *Journal of the Franklin Institute*, 249(1):57–83, 1950.
- [101] Hendrik W Bode. Network analysis and feedback amplifier design. (*No Title*), 1945.
- [102] Peter Barry. *On the development of SuperSpec: A fully integrated On-chip spectrometer for Far-infrared astronomy*. PhD thesis, Cardiff School of Physics and Astronomy, 2014.
- [103] Karia Dibert, Pete Barry, Zhaodi Pan, Adam Anderson, Bradford Benson, Clarence Chang, Kirit Karkare, Juliang Li, Tyler Natoli, Maclean Rouble, et al. Development of mkids for measurement of the cosmic microwave background with the south pole telescope. *Journal of Low Temperature Physics*, 209(3):363–371, 2022.
- [104] P. S. Barry, A. Anderson, B. Benson, J. E. Carlstrom, T. Cecil, C. Chang, M. Dobbs, M. Hollister, K. S. Karkare, G. K. Keating, and et al. Design of the spt-slim focal plane: A spectroscopic imaging array for the south pole telescope. *Journal of Low Temperature Physics*, 209(5–6):879–888, Sep 2022.
- [105] Omid Noroozian, Peter K. Day, Byeong Ho Eom, Henry G. Leduc, and Jonas Zmuidzinas. Crosstalk reduction for superconducting microwave resonator arrays. *IEEE Transactions on Microwave Theory and Techniques*, 60(5):1235–1243, may 2012.
- [106] Shiling Yu, Shibo Shu, Ran Duan, Lihui Yang, and Di Li. Design of microstrip-line coupled kinetic inductance detectors for near infrared astronomy, 2022.
- [107] K Kouwenhoven, GPJ Van Doorn, BT Buijtendorp, SAH De Rooij, D Lamers, DJ Thoen, V Murugesan, JJA Baselmans, and PJ De Visser. Geometry dependence of two-level-system noise and loss in a-si c: H parallel-plate capacitors for superconducting microwave resonators. *Physical Review Applied*, 21(4):044036, 2024.
- [108] Nicholas F. Cothard, Christopher Albert, Andrew D. Beyer, Charles M. Bradford, Pierre Echternach, Byeong-Ho Eom, Logan Foote, Marc Foote, Steven Hailey-Dunsheath, Reinier M. J. Janssen, Elijah Kane, Henry LeDuc, Joanna Perido, Jason Glenn, and Peter K. Day. Parallel plate capacitor aluminum kids for future far-infrared space-based observatories, 2023.
- [109] Joanna Perido, Peter K Day, Andrew D Beyer, Nicholas F Cothard, Steven Hailey-Dunsheath, Henry G Leduc, Byeong H Eom, and Jason Glenn. Parallel-plate capacitor titanium nitride kinetic inductance detectors for infrared astronomy. *Journal of Low Temperature Physics*, pages 1–11, 2024.

- [110] R. McGeehan, P. S. Barry, E. Shirokoff, C. M. Bradford, G. Che, J. Glenn, S. Gordon, S. Hailey-Dunsheath, M. Hollister, A. Kovács, and et al. Low-temperature noise performance of superspec and other developments on the path to deployment. *Journal of Low Temperature Physics*, 193(5–6):1024–1032, Sep 2018.
- [111] BT Buijtendorp, S Vollebregt, K Karatsu, DJ Thoen, V Murugesan, K Kouwenhoven, S Hähnle, JJA Baselmans, and A Endo. Hydrogenated amorphous silicon carbide: A low-loss deposited dielectric for microwave to submillimeter-wave superconducting circuits. *Physical Review Applied*, 18(6):064003, 2022.
- [112] T Cecil, C Albert, AJ Anderson, PS Barry, B Benson, C Cotter, C Chang, M Dobbs, K Dibert, R Gualtieri, et al. Fabrication development for spt-slim, a superconducting spectrometer for line intensity mapping. *IEEE Transactions on Applied Superconductivity*, 33(5):1–6, 2023.
- [113] M Tarasov, A Chekushkin, M Fominsky, D Zakharov, A Lomov, O Devitsky, A Gunbina, E Sohina, and V Edelman. Superconducting thin films and tunnel junctions based on aluminum. *Phys. Solid State*, 64:1352–1355, 2022.
- [114] Yanfu Wu, Zengqian Ding, Kanglin Xiong, and Jiagui Feng. High-quality superconducting α -ta film sputtered on the heated silicon substrate. *Scientific Reports*, 13(1):12810, 2023.
- [115] Jianshe Liu, Jinyang Li, Tianzong Li, Tiefu Li, Wei Wu, and Wei Chen. Study of stress and morphology of superconducting niobium thin films. *IEEE Transactions on Applied Superconductivity*, 19(3):245–248, 2009.
- [116] R.B. Bass, L.T. Lichtenberger, and A.W. Lichtenberger. Effects of substrate preparation on the stress of nb thin films. *IEEE Transactions on Applied Superconductivity*, 13(2):3298–3300, 2003.
- [117] Benjamin A Mazin, Daniel Sank, Sean McHugh, Erik A Lucero, Andrew Merrill, Jiansong Gao, David Pappas, David Moore, and Jonas Zmuidzinas. Thin film dielectric microstrip kinetic inductance detectors. *Applied Physics Letters*, 96(10), 2010.
- [118] Bruno T Buijtendorp, Juan Bueno, David J Thoen, Vignesh Murugesan, Paolo M Sberna, Jochem JA Baselmans, Sten Vollebregt, and Akira Endo. Characterization of low-loss hydrogenated amorphous silicon films for superconducting resonators. *Journal of Astronomical Telescopes, Instruments, and Systems*, 8(2):028006–028006, 2022.
- [119] S Hähnle, K Kouwenhoven, B Buijtendorp, A Endo, K Karatsu, DJ Thoen, V Murugesan, and JJA Baselmans. Superconducting microstrip losses at microwave and submillimeter wavelengths. *Physical Review Applied*, 16(1):014019, 2021.

BIBLIOGRAPHY

- [120] JA Sobrin, AJ Anderson, AN Bender, BA Benson, D Dutcher, A Foster, N Goeckner-Wald, J Montgomery, A Nadolski, A Rahlin, et al. The design and integrated performance of spt-3g. *The Astrophysical Journal Supplement Series*, 258(2):42, 2022.
- [121] B. Mazin. *Microwave kinetic inductance detectors*. PhD thesis, California Institute of Technology, 2004.
- [122] PJ de Visser, S Withington, and D Goldie. Readout-power heating and hysteretic switching between thermal quasiparticle states in kinetic inductance detectors. *Journal of Applied Physics*, 108(11):114504–1–114504–9, 2010.
- [123] LJ Swenson, P.K. Day, B.H. Eom, H.G. Leduc, N Llombart Juan, C.M. Mckenney, O Noroozian, and J Zmuidzinas. Operation of a titanium nitride superconducting microresonator detector in the nonlinear regime. *Journal of Applied Physics*, 113(10, May 2013):1–11, 2013.
- [124] C N Thomas, S Withington, Z Sun, T Skyrme, and D J Goldie. Nonlinear effects in superconducting thin film microwave resonators. *New Journal of Physics*, 22(7):073028, jul 2020.
- [125] X. Liu, W. Guo, Y. Wang, M. Dai, L. F. Wei, B. Dober, C. M. McKenney, G. C. Hilton, J. Hubmayr, J. E. Austermann, J. N. Ullom, J. Gao, and M. R. Vissers. Superconducting micro-resonator arrays with ideal frequency spacing. *Applied Physics Letters*, 111(25):252601, 12 2017.
- [126] W. A. Phillips. Tunneling states in amorphous solids. *Journal of Low Temperature Physics*, 7(3–4):351–360, May 1972.
- [127] Jiansong Gao, Miguel Daal, Anastasios Vayonakis, Shwetank Kumar, Jonas Zmuidzinas, Bernard Sadoulet, Benjamin A. Mazin, Peter K. Day, and Henry G. Leduc. Experimental evidence for a surface distribution of two-level systems in superconducting lithographed microwave resonators. *Applied Physics Letters*, 92(15):152505, 04 2008.
- [128] Omid Noroozian, Jiansong Gao, Jonas Zmuidzinas, Henry G. LeDuc, Benjamin A. Mazin, Betty Young, Blas Cabrera, and Aaron Miller. Two-level system noise reduction for microwave kinetic inductance detectors. In *AIP Conference Proceedings*. AIP, 2009.
- [129] Y Sueno, S Honda, H Kutsuma, S Mima, C Otani, S Oguri, J Suzuki, and O Tajima. Characterization of two-level system noise for a microwave kinetic inductance detector comprising niobium film on a silicon substrate. *Progress of Theoretical and Experimental Physics*, 2022(3):033H01, 02 2022.

- [130] Z. Pan, K. R. Dibert, J. Zhang, P. S. Barry, A. J. Anderson, A. N. Bender, B. A. Benson, T. Cecil, C. L. Chang, R. Gualtieri, J. Li, M. Lisovenko, V. Novosad, M. Rouble, G. Wang, and V. Yefremenko. Noise optimization for mkids with different design geometries and material selections. *IEEE Transactions on Applied Superconductivity*, 33(5):1–8, 2023.
- [131] P. J. de Visser, J. J. A. Baselmans, P. Diener, S. J. C. Yates, A. Endo, and T. M. Klapwijk. Number fluctuations of sparse quasiparticles in a superconductor. *Phys. Rev. Lett.*, 106:167004, Apr 2011.
- [132] P.A. Warburton and M.G. Blamire. Quasiparticle lifetimes in epitaxial niobium and tantalum films. *IEEE Transactions on Applied Superconductivity*, 5(2):3022–3025, 1995.
- [133] T. L. R. Brien, P. A. R. Ade, P. S. Barry, E. Castillo-Domínguez, D. Ferrusca, V. Gómez-Rivera, P. Hargrave, J. L. Hernández Rebollar, A. Hornsby, D. H. Hughes, J. M. Jáuregui-Garcia, P. Mauskopf, D. Murias, A. Papageorgiou, E. Pascale, A. Pérez, S. Rowe, M. W. L. Smith, M. Tapia, C. Tucker, M. Velázquez, S. Ventura, and S. Doyle. Pre-deployment verification and predicted mapping speed of MUSCAT. In Jonas Zmuidzinas and Jian-Rong Gao, editors, *Millimeter, Submillimeter, and Far-Infrared Detectors and Instrumentation for Astronomy X*, volume 11453, page 1145303. International Society for Optics and Photonics, SPIE, 2020.
- [134] Gianluigi Catelani, Jens Koch, Luigi Frunzio, RJ Schoelkopf, Michel H Devoret, and LI Glazman. Quasiparticle relaxation of superconducting qubits in the presence of flux. *Physical review letters*, 106(7):077002, 2011.
- [135] John M Martinis, M Ansmann, and J Aumentado. Energy decay in superconducting josephson-junction qubits<? format?> from nonequilibrium quasiparticle excitations. *Physical review letters*, 103(9):097002, 2009.
- [136] R Barends, JJA Baselmans, SJC Yates, JR Gao, JN Hovenier, and TM Klapwijk. Quasiparticle lifetime and noise in tantalum high q superconducting resonators. *Journal of Low Temperature Physics*, 151:518–523, 2008.
- [137] Steven B Kaplan, CC Chi, DN Langenberg, Jhy-Jiun Chang, S Jafarey, and DJ Scalapino. Quasiparticle and phonon lifetimes in superconductors. *Physical Review B*, 14(11):4854, 1976.
- [138] T Guruswamy, DJ Goldie, and S Withington. Quasiparticle generation efficiency in superconducting thin films. *Superconductor Science and Technology*, 27(5):055012, 2014.

BIBLIOGRAPHY

- [139] H McCarrick, D Flanigan, G Jones, BR Johnson, P Ade, D Araujo, K Bradford, R Cantor, G Che, P Day, et al. Horn-coupled, commercially-fabricated aluminum lumped-element kinetic inductance detectors for millimeter wavelengths. *Review of Scientific Instruments*, 85(12), 2014.
- [140] Jiansong Gao, Miguel Daal, Anastasios Vayonakis, Shwetank Kumar, Jonas Zmuidzinas, Bernard Sadoulet, Benjamin A Mazin, Peter K Day, and Henry G Leduc. Experimental evidence for a surface distribution of two-level systems in superconducting lithographed microwave resonators. *Applied Physics Letters*, 92(15), 2008.
- [141] R Barends, HL Hortensius, T Zijlstra, JJA Baselmans, SJC Yates, JR Gao, and TM Klapwijk. Contribution of dielectrics to frequency and noise of nbtin superconducting resonators. *Applied Physics Letters*, 92(22), 2008.
- [142] R Barends, N Vercruyssen, A Endo, PJ De Visser, T Zijlstra, TM Klapwijk, and JJA Baselmans. Reduced frequency noise in superconducting resonators. *Applied Physics Letters*, 97(3), 2010.
- [143] RMJ Janssen, A Endo, PJ De Visser, TM Klapwijk, and JJA Baselmans. Equivalence of optical and electrical noise equivalent power of hybrid nbtin-al microwave kinetic inductance detectors. *Applied Physics Letters*, 105(19), 2014.
- [144] JJA Baselmans, F Facchin, A Pascual Laguna, J Bueno, DJ Thoen, V Murugesan, Nuria Llombart, and PJ De Visser. Ultra-sensitive thz microwave kinetic inductance detectors for future space telescopes. *Astronomy & Astrophysics*, 665:A17, 2022.
- [145] I.T. Jolliffe. *Principal Component Analysis*. Springer Series in Statistics. Springer, 2002.
- [146] Jean Baptiste Joseph Fourier. *Théorie analytique de la chaleur*, volume 1. Gauthier-Villars, 1888.
- [147] Sumner P Davis, Mark C Abrams, and James W Brault. *Fourier transform spectrometry*. Academic press, 2001.
- [148] Stephen T Ridgway. Fourier transform spectroscopy in astrophysics. In *IN: Observational astrophysics with high precision data; Proceedings of the Twenty-seventh Liege International Astrophysical Colloquium, Liege, Belgium, June 23-26, 1987 (A88-52251 22-89)*. Cointe-Ougree, Belgium, Universite de Liege, 1987, p. 91-101; *Discussion*, p. 102., volume 27, pages 91–101, 1987.

- [149] Locke Dean Spencer et al. *Imaging Fourier transform spectroscopy from a space based platform: the Herschel/SPIRE Fourier transform spectrometer*. PhD thesis, Lethbridge, Alta.: University of Lethbridge, Dept. of Physics and Astronomy, 2009.
- [150] DH Martin and E Puplett. Polarised interferometric spectrometry for the millimetre and submillimetre spectrum. *Infrared Physics*, 10(2):105–109, 1970.
- [151] David A Naylor, TA Clark, and Gary R Davis. Polarizing fourier transform spectrometer for astronomical spectroscopy at submillimeter and mid-infrared wavelengths. In *Instrumentation in Astronomy VIII*, volume 2198, pages 703–714. SPIE, 1994.
- [152] M Bin, DJ Benford, MC Gaidis, TH Büttgenbach, J Zmuidzinas, E Serabyn, and TG Phillips. A large throughput high resolution fourier transform spectrometer for submillimeter applications. *International journal of infrared and millimeter waves*, 20:383–400, 1999.
- [153] Blue Sky Spectroscopy. Blue sky spectroscopy, inc. <https://blueskyspectroscopy.com/>, 2024. Accessed: 2024-09-22.
- [154] Locke D Spencer and David A Naylor. Optimization of fts phase correction parameters. In *Fourier Transform Spectroscopy*, page FTuD12. Optica Publishing Group, 2005.
- [155] Michael L Forman, W Howard Steel, and George A Vanasse. Correction of asymmetric interferograms obtained in fourier spectroscopy. *JOSA*, 56(1):59–63, 1966.
- [156] Louis H Marting, Kenichi Karatsu, Akira Endo, Jochem JA Baselmans, and Alejandro Pascual Laguna. Directional filter design and simulation for superconducting on-chip filter-banks. *Journal of Low Temperature Physics*, pages 1–10, 2024.
- [157] Fabien Defrance, Andrew D Beyer, Shibo Shu, Jack Sayers, and Sunil R Golwala. Characterization of the low electric field and zero-temperature two-level-system loss in hydrogenated amorphous silicon. *Physical Review Materials*, 8(3):035602, 2024.